

# Imaging of the three-dimensional quark-gluon structure of the proton via analysis of deeply virtual electron scattering

---

Čuić, Marija

Doctoral thesis / Doktorski rad

2024

Degree Grantor / Ustanova koja je dodijelila akademski / stručni stupanj: **University of Zagreb, Faculty of Science / Sveučilište u Zagrebu, Prirodoslovno-matematički fakultet**

Permanent link / Trajna poveznica: <https://um.nsk.hr/um:nbn:hr:217:414762>

Rights / Prava: [In copyright](#) / [Zaštićeno autorskim pravom.](#)

Download date / Datum preuzimanja: **2025-03-11**



Repository / Repozitorij:

[Repository of the Faculty of Science - University of Zagreb](#)





University of Zagreb  
Faculty of Science  
Department of Physics

Marija Čuić

**Imaging of the three-dimensional  
quark-gluon structure of the proton via  
analysis of deeply virtual electron scattering**

DOCTORAL THESIS

Zagreb, 2023



University of Zagreb  
Faculty of Science  
Department of Physics

Marija Čuić

**Imaging of the three-dimensional  
quark-gluon structure of the proton via  
analysis of deeply virtual electron scattering**

DOCTORAL THESIS

Supervisor:  
prof. dr. sc. Krešimir Kumerički

Zagreb, 2023



Sveučilište u Zagrebu  
Prirodoslovno-matematički fakultet  
Fizički odsjek

Marija Čuić

**Oslikavanje trodimenzijske  
kvarkovsko-gluonske strukture protona  
analizom duboko virtualnih raspršenja  
elektrona**

DOKTORSKI RAD

Mentor:  
prof. dr. sc. Krešimir Kumerički

Zagreb, 2023.

## Supervisor information

Krešimir Kumerički is a full professor at the University of Zagreb, Faculty of Science, Department of Physics. He defended his doctoral dissertation "Rare decays of  $K$  mesons" under the supervision of professor Ivica Picek in 1998 at the same university. The focus of his research then was the interplay of electroweak and chromodynamic effects in various decays that include a change in the quark flavor. In the meantime, after longer stays at the Universities of Oslo and Regensburg, his interest focused on research of the quark-gluon structure of the nucleon, described by the so-called generalized parton distributions. This provides a new three-dimensional view of the nucleon structure. He also introduced the application of neural networks to these studies. Their application in the calculation of the pressure inside the proton was published in the prestigious journal *Nature* under the sole authorship of prof. Kumerički. He is the author of 36 peer-reviewed papers which have 3676 citations, and 27 conference proceedings, according to the INSPIRE-HEP database. He was the head of several projects, including "MIAU – Matter and Interactions at Accelerators and in Universe" granted by the Croatian Science Foundation under the number IP-2013-11-8799, "Revealing Generalized Parton Distributions" with M. Polyakov, granted by the German Research Foundation under the project number DFG 436 KRO 113/11/0-1, and "The strong interaction at the frontier of knowledge: fundamental research and applications (STRONG-2020)", granted by European Union's Horizon 2020 research and innovation program under the grant agreement No. 824093, where he is the representative for Croatia alongside prof. D. Bosnar.

# Acknowledgements

I would like to extend my gratitude to my supervisor, prof. Krešimir Kumerički, for his patience and guidance through this challenging time. A special thanks goes to my coworkers, Ana, Ante and Lucija, for their invaluable insights during our regular "trač" meetings. Thank you to all of my fellow PhD students for sharing our joys and miseries in the blue room. I am grateful for the opportunity to teach so many students and be a part of their education.

Most of all, I would like to thank my dear husband for his infinite patience, love and support. Thank you for shielding me from most of the responsibilities of being an adult so that I can pursue this PhD.

# Abstract

The study of the structure of the proton has been an ongoing effort ever since its first experimental discovery in 1917 by Rutherford. As experimental methods progressed, and the properties of the proton, such as its mass, spin and charge, were uncovered, the question of its underlying structure arose. Experiments conducted in 1969 at SLAC undoubtedly confirmed the fact that the proton is not an elementary particle, but that it consists of smaller particles, which we now recognize as quarks and gluons. From that point on, physicists tried to understand how exactly the interplay of quarks and gluons inside the proton gives rise to its properties.

One of the ways we can experimentally study the proton is through hard exclusive processes, such as deeply virtual Compton scattering (DVCS) and deeply virtual meson production (DVMP), which give access to a class of functions called generalized parton distributions (GPDs). GPDs describe the three dimensional structure of the proton, and they are a potential solution to the proton spin puzzle. It is currently not possible to extract GPDs from measurements directly, since they are convoluted with hard scattering amplitudes inside cross sections, and deconvolution is in itself an ill-posed problem. These functions are also not possible to calculate from first principles due to the non-perturbative nature of QCD, so we rely on modeling and machine learning methods in order to extract them from measurements. In this work we present recent results on the extraction of GPDs and relevant form factors from DVCS and DVMP data. Using the more recent proton DVCS data, we extract the set of leading Compton form factors (CFFs) with uncertainties and, by adding neutron DVCS data, we separate the contributions of up and down quarks to the CFF  $\mathcal{H}$ . We make simultaneous fits to high energy deep inelastic scattering, DVCS and DVMP data at low  $x$  and study the impact of next-to-leading order (NLO) corrections, as well as the possibility of a unique description of these processes with twist-2 GPDs. We demonstrate a sizeable impact of NLO corrections and that extraction of unique GPDs becomes possible at NLO.

Keywords: proton, generalized parton distributions, deeply virtual Compton scattering, Compton form factors

# Prošireni sažetak

Proučavanje strukture protona započelo je prije više od 100 godina. Od prvog Rutherfordovog otkrića 1917., kada se smatralo da je proton točkasta čestica, preko razumijevanja da ipak ima podstrukturu, pa do mjerenja dubokog neelastičnog raspršenja 1969. na SLAC-u, gdje se potvrdilo da je ta podstruktura netrivialna, proučavanje protona, osnovne građevne jedinice svemira, predstavlja uzbudljivo i rastuće područje u fizici.

U ovom radu bavit ćemo se strukturom protona kroz proučavanje generaliziranih partonskih distribucija (GPD-ova). GPD-ovi predstavljaju interesantno područje istraživanja utoliko što objašnjavaju trodimenzijsku raspodjelu kvarkova i gluona u protonu, daju rješenje zagonetke protonskog spina, kao i mnoga druga svojstva.

Povijesni tijek eksperimentalnog ispitivanja svojstava protona krenuo je s elastičnim raspršenjem. Nabijena proba, tipično elektron, sudara se s protonom i raspršuje se na njemu. Elektromagnetska interakcija probe s protonom, koja se prenosi virtualnim fotonima, daje nam uvid u raspodjelu električnog naboja protona. Već se ovakvim eksperimentom može vidjeti da proton nije točkasta čestica, nego da posjeduje prostornu protežnost. Povećavanjem energije elektrona dolazimo u režim neelastičnog raspršenja, gdje struktura protona apsorbira dio energije elektrona. Elektromagnetska svojstva protona razotkrivena ovim eksperimentom ne mogu doći od elementarne čestice, čime se nazire netrivialna podstruktura protona.

Prvi konkretniji uvid u sastavnice protona dobivamo putem dubokog neelastičnog raspršenja (DIS, od engleskog *deep inelastic scattering*). Pri njemu je prijenos energije s elektrona na proton toliko veliki da se proton razbije, što nam u konačnici ograničava koliko možemo saznati o njegovoj podstrukturi. Ovaj proces simbolično pišemo kao

$$e^-(k_1) + N(P_1) \rightarrow e^-(k_2) + X(P_2),$$

gdje nam  $X$  označava sve čestice nađene u konačnom stanju. Ovakvi procesi, gdje se ne detektiraju pojedinačno čestice koje nastaju u reakciji, nazivaju se inkluzivima. Varijable koje nam

govore koliko je ovaj proces neelastičan nazivaju se Bjorkenov  $x$ , definiran kao

$$x_B = \frac{Q^2}{2P_1 \cdot q},$$

gdje je  $q = k_2 - k_1$ , tj.  $Q^2 = -q^2$  virtualnost fotona, i neelastičnost, definirana kao

$$y = \frac{P_1 \cdot q}{P_1 \cdot k_1}.$$

U naivnom Feynmanovom modelu, proton se sastoji od čestica skupnog naziva partoni, i u prvom redu računa smetnje elektron međudjeluje s jednim od tih partona, za koje danas znamo da odgovaraju kvarkovima, i izbija ga iz protona. U kinematičkom režimu u kojem se odvija DIS, pokazuje se da  $x_B$  odgovara frakciji longitudinalnog impulsa protona koju nosi udareni parton  $x$ . Diferencijalni udarni presjek za ovakav opis DIS-a može se napisati kao

$$\frac{d^2\sigma}{dQ^2 dx} = \frac{4\pi\alpha^2}{Q^4} \left[ (1-y) + \frac{y^2}{2} \right] \sum_i Q_i^2 q_i^p(x),$$

gdje je  $Q_i$  naboj udarenog kvarka, a  $q_i^p(x)$  je partonska distribucijska funkcija (PDF). Prethodno navedeni udarni presjek sastoji se od dva dijela. Prvi je udarni presjek raspršenja elektrona na kvarku okusa  $i$ , a drugi je vjerojatnost da kvark s kojim elektron međudjeluje ima udio longitudinalnog impulsa protona  $x$ . U ovom izrazu vidimo faktorizaciju, moćan alat koji nam omogućava proučavanje ovih procesa. U kvantnoj kromodinamici (QCD, od engleskog *quantum chromodynamics*) konstanta vezanja  $\alpha_s$  ima takvu ovisnost o energetske skali procesa da raste što je energija manja, odnosno pada kako energija raste, pa na dovoljno visokim energijama QCD postaje efektivno slobodna teorija. Faktorizacija nam u suštini govori da DIS možemo promatrati kao proces koji se sastoji od dijela definiranog na visokim energetske skalama, što znači da ga se može tretirati perturbativno, i od dijela koji je definiran na niskim skalama te se ne može tretirati perturbativno. Dio na visokim, odnosno tvrdim skalama opisuje raspršenje elektrona na kvarku, dok PDF odgovara dijelu na mekim skalama i objašnjava raspodjelu partona u protonu. Budući da je PDF definiran na mekoj energetske skali, ne možemo ga izračunati alatima perturbativne teorije polja, te nam je jedini način da pristupimo takvim funkcijama fenomenološki, odnosno da pokušamo pretpostaviti nekakvu funkcionalnu ovisnost o kinematičkim varijablama, pri čemu će takva funkcija imati nekolicinu slobodnih parametara koji se određuju numerički pri usporedbi s eksperimentalnim podacima, ili da se poslužimo metodama strojnog učenja. Važno je napomenuti da, kako se odmičemo od prvog reda računa smetnje, PDF-ovi ovise i o skali procesa, što je u ovom slučaju virtualnost fotona  $Q^2$ . Fizikalno nam to govori da

pri većim energijama virtualnog fotona imamo finiju probu za promatranje strukture protona, koja vidi izmjene virtualnih čestica među valentnim kvarkovima. Te izmjene događaju se na kratkim vremenskim skalama i stvaraju u protonu more virtualnih kvarkova, antikvarkova i gluona. Dakle, u protonu se ne nalaze samo tri statična valentna kvarka, već je situacija mnogo kompleksnija, što nas potiče da istražujemo procese koji nam daju bogatiji pristup unutrašnjosti protona.

U svrhu kompleksnijeg istraživanja protonske strukture, proučavamo u smislu strukture dva ekvivalentna procesa, duboko virtualno komptonско raspršenje (DVCS, od engleskog *deeply virtual Compton scattering*) i duboko virtualnu mezonsku produkcija (DVMP, od engleskog *deeply virtual meson production*). Ti su procesi ekvivalentni jer nam daju pristup istim funkcijama mekane energetske skale, generaliziranim partonskim distribucijama. GPD-ovi su funkcije koje ovise o tri kinematičke varijable, te daju uvid u trodimenzijsku strukturu protona. DVCS simbolično definiramo kao

$$\ell(k_1) + N(P_1) \rightarrow \ell(k_2) + N(P_2) + \gamma(q_2),$$

pri čemu je odlika procesa da se izlazni foton emitira iz samog protona, a ne iz ulaznog ili izlaznog leptona. Kvadrat amplitude ovog procesa može se napisati kao

$$|\mathcal{T}_{\text{DVCS}}|^2 = \frac{2(2-2y+y^2)}{y^2 Q^2 (2-x_B)^2} \left[ 4(1-x_B) \left( |\mathcal{H}|^2 + |\tilde{\mathcal{H}}|^2 \right) - \left( x_B^2 + (2-x_B)^2 \frac{\Delta^2}{4M^2} \right) |\mathcal{E}|^2 \right. \\ \left. - x_B^2 \left( \mathcal{H}\mathcal{E}^* + \mathcal{E}\mathcal{H}^* + \tilde{\mathcal{H}}\tilde{\mathcal{E}}^* + \tilde{\mathcal{E}}\tilde{\mathcal{H}}^* \right) - x_B^2 \frac{\Delta^2}{4M^2} |\tilde{\mathcal{E}}|^2 \right],$$

i dan je pomoću funkcija koje nazivamo komptonски form faktori (CFF-ovi, od engleskog *Compton form factors*), ovdje označeni kao  $\mathcal{H}$ ,  $\mathcal{E}$ ,  $\tilde{\mathcal{H}}$  i  $\tilde{\mathcal{E}}$ . U CFF-ovima se primjenom faktORIZACIJE mogu odvojiti aspekti procesa koji se odvijaju na tvrdoj, odnosno mekoj skali. Shodno tome, CFF-ove možemo pisati kao

$$\mathcal{F}^A(\xi, \Delta^2, Q^2) = \int_{-1}^1 \frac{dx}{2\xi} {}_A T \left( \frac{\xi+x-i\epsilon}{2(\xi-i\epsilon)}, \xi \middle| \alpha_s(\mu_R), \frac{Q^2}{\mu_F^2} \right) F^A(x, \xi, \Delta^2, \mu_F^2),$$

gdje nam je tvrdi dio procesa dan koeficijentima raspršenja  $T$ , dok je mekani dio procesa dan GPD-ovima  $F^A \in \{H^A, E^A, \tilde{H}^A, \tilde{E}^A\}$ ,  $A \in \{q, G\}$ . GPD-ovi su dani preko tri varijable, za koje odabiremo  $x$ , koji se sada definira kao prosječni udio longitudinalnog impulsa koji nosi udareni parton,  $t = (P_1 - P_2)^2$ , koji daje prijenos impulsa na proton, i  $\xi = -\Delta \cdot q / P \cdot q$  (uz  $P = P_1 + P_2$  i  $q = (q_1 + q_2)/2$ ), koji se naziva eng. *skewness* i mjeri koliko je proces nesimetričan u smislu

početnog i konačnog impulsa udarenog partona. GPD-ovi također ovise o skali procesa, što je opet odraz toga da se slika unutrašnjosti protona mijenja s energijom probe.

DVMP je simbolično dan izrazom

$$\ell(k_1) + N(P_1) \rightarrow \ell(k_2) + N'(P_2) + M(q_2),$$

gdje se sada umjesto fotona u konačnom stanju nalazi mezon  $M$ . Ukoliko se u ovom procesu proizvode longitudinalno polarizirani vektorski mezoni, kvadrat amplitude dan je kao

$$|\mathcal{T}^{\text{VL}}|^2 = 16 \frac{1-y}{y^2(2-x_B)^2} \left[ 4(1-x_B)|\mathcal{H}|^2 - x_B^2(\mathcal{H}\mathcal{E}^* + \mathcal{E}\mathcal{H}^*) - \left( x_B^2 + (2-x_B)^2 \frac{\Delta^2}{4M^2} \right) |\mathcal{E}|^2 \right],$$

gdje se sada pojavljuju takozvani tranzicijski form faktori (TFF-ovi, od engleskog *transition form factors*). TFF-ovi se faktoriziraju kao i CFF-ovi i možemo ih pisati kao

$$\mathcal{F}^A(\xi, \Delta^2, Q^2) = \frac{f_{\text{CF}}}{Q N_c} \int_{-1}^1 \frac{dx}{2\xi} \int_0^1 dv \varphi(v)^A T \left( \frac{\xi+x-i\epsilon}{2(\xi-i\epsilon)}, v, \xi \left| \alpha_s(\mu_R), \frac{Q^2}{\mu_F^2}, \frac{Q^2}{\mu_\Phi^2}, \frac{Q^2}{\mu_R^2} \right. \right) F^A(x, \xi, \Delta^2).$$

Za razliku od CFF-ova, osim koeficijenata raspršenja na tvrdoj skali  $T$  i GPD-ova  $F$ , ovdje se javljaju nove funkcije mekane skale  $\varphi(v)$ , koje nazivamo distribucijske amplitude.

Formalno definiramo GPD-ove kao Fourierove transformate matričnih elemenata prijelaza protona iz stanja impulsa  $P_1$  u stanje impulsa  $P_2$ , odnosno

$$\begin{aligned} \langle P_2 | \mathcal{O}^{qq}(-z^-, z^-) | P_1 \rangle &= \int_{-1}^1 dx e^{-ixP^+z^-} [h^+ H^q(x, \xi, \Delta^2) + e^+ E^q(x, \xi, \Delta^2)], \\ \langle P_2 | \tilde{\mathcal{O}}^{qq}(-z^-, z^-) | P_1 \rangle &= \int_{-1}^1 dx e^{-ixP^+z^-} [\tilde{h}^+ \tilde{H}^q(x, \xi, \Delta^2) + \tilde{e}^+ \tilde{E}^q(x, \xi, \Delta^2)], \\ \langle P_2 | \mathcal{O}^{gg}(-z^-, z^-) | P_1 \rangle &= \frac{1}{4} P^+ \int_{-1}^1 dx e^{-ixP^+z^-} [h^+ H^G(x, \xi, \Delta^2) + e^+ E^G(x, \xi, \Delta^2)], \\ \langle P_2 | \tilde{\mathcal{O}}^{gg}(-z^-, z^-) | P_1 \rangle &= \frac{1}{4} P^+ \int_{-1}^1 dx e^{-ixP^+z^-} [\tilde{h}^+ \tilde{H}^G(x, \xi, \Delta^2) + \tilde{e}^+ \tilde{E}^G(x, \xi, \Delta^2)]. \end{aligned}$$

Na ovoj razini preciznosti imamo četiri kvarkovska i četiri gluonska GPD-a koji su definirani u tzv. sustavu svjetlosnog stošca. Faktori uz GPD-ove u gornjim definicijama su elementi baze bilinearnih spinornih kovarijanti.

GPD-ovi imaju mnoga svojstva, od kojih ćemo istaknuti povezanost s PDF-ovima, koja se

definira u režimu kada vrijedi  $P_1 = P_2$ , odnosno  $\Delta = 0 = \xi$ . Tada imamo

$$\begin{aligned} H^q(x, \xi = 0, \Delta^2 = 0) &= f^q(x) = q(x)\theta(x) - \bar{q}(-x)\theta(-x), \\ \tilde{H}^q(x, \xi = 0, \Delta^2 = 0) &= \Delta f^q(x) = \Delta q(x)\theta(x) + \Delta \bar{q}(-x)\theta(-x), \end{aligned}$$

i ekvivalentno za gluone ( $H^G, \tilde{H}^G$ ). Također dajemo definiciju distribucije partona u trodimenzijskom prostoru protona

$$q(x, \mathbf{b}_\perp) = \int \frac{d^2\Delta_\perp}{(2\pi)^2} e^{-i\mathbf{b}_\perp \cdot \Delta_\perp} H^q(x, 0, t = -\Delta_\perp^2),$$

koja se dobiva Fourierovim transformatom GPD-ova, kao i Jijevo sumacijsko pravilo koje govori kako kvarkovi i gluoni doprinose spinu protona

$$\langle J_3^q \rangle = \frac{1}{2} \int dx x [H^q(x, \xi, t) + E^q(x, \xi, t)], \quad \langle J_3^G \rangle = \frac{1}{2} \int dx [H^G(x, \xi, t) + E^G(x, \xi, t)].$$

Spomenuli smo da GPD-ovi ovise o skali procesa. Makar je ta ovisnost poznata i jednadžbe koje opisuju tu ovisnost računaju se perturbativno, komplicirane su za implementirati numerički i dovode do kompliciranog miješanja raznih GPD-ova. U svrhu pojednostavljenja transformiramo GPD-ove, pa posljedično i CFF-ove i TFF-ove, u bazu konformnih momenata, odnosno gradimo reprezentacije kolinearne podgrupe konformne grupe. U praktičnom smislu to uključuje razvoj GPD-ova u bazi Gegenbauerovih polinoma, tj.

$$\begin{aligned} F_n^q(\xi, \Delta^2) &= \int_{-1}^1 dx c_n^{3/2}(x, \xi) F^q(x, \xi, \Delta^2), \\ F_n^G(\xi, \Delta^2) &= \int_{-1}^1 dx c_{n-1}^{5/2}(x, \xi) F^G(x, \xi, \Delta^2). \end{aligned}$$

Koristeći Mellin-Barnesovu reprezentaciju, pišemo CFF-ove i TFF-ove u sektoru singletnih kvarkova mora i gluona

$$\begin{aligned} \mathcal{F}^S(\xi, \Delta^2, Q^2) &= \frac{1}{2i} \int_{c-i\infty}^{c+i\infty} dj \xi^{-j-1} \begin{bmatrix} \tan \\ \cot \end{bmatrix} \bar{T}_j^I(Q^2, \mu_0^2) \mathbf{F}_j(\xi, \Delta^2, \mu_0^2), \\ \mathcal{F}_{V_L}^S(\xi, \Delta^2, Q^2) &= \frac{C_F f_{V^0}}{N_c Q} \frac{1}{2i} \int_c dj \xi^{-j-1} \begin{bmatrix} \tan \\ \cot \end{bmatrix} \varphi_k(\mu_0^2) \bigoplus_{\text{even}}^k \bar{T}_{jk}^I(Q^2, \mu_0^2) \mathbf{F}_j(\xi, \Delta^2, \mu_0^2). \end{aligned}$$

Za GPD-ove koristimo razvoj po SO(3) parcijalnim valovima

$$F_j^a(\xi, t) = \sum_{\substack{J=j+1 \\ \text{even}}}^{j+1} F_{j,J}^a(t) \xi^{j+1-J} \hat{d}_{\alpha,\beta}^J(\xi), \quad J = j+1, j-1, j-3, \dots, \quad a \in \{q, G\},$$

gdje koristimo aproksimaciju  $\hat{d}_{\alpha,\beta}^J \approx 1$ , prekidamo razvoj na trećem članu i pretpostavljamo da su amplitude drugog i trećeg parcijalnog vala proporcionalne amplitudi prvog parcijalnog vala.

Tada imamo

$$F_j^a(\xi, t) = (1 + s_2^a \xi^2 + s_4^a \xi^4) f_j^a(t),$$

gdje je

$$F_{j,j+1}^a(t) \equiv f_j^a(t) = N_a \frac{B(1 - \alpha_0^a + j, \beta^a + 1)}{B(2 - \alpha_0^a, \beta^a + 1)} \frac{1 + j - \alpha_0^a}{1 + j - \alpha_0^a - \alpha'^a t} \left(1 - \frac{t}{m_a^2}\right)^{-2}.$$

Prvi faktor u ovoj definiciji je standardni ansatz za PDF-ove, dok je  $t$  ovisnost potaknuta razmatranjima iz Regge teorije.

Gornju reprezentaciju koristimo za istovremeni opis DIS, DVCS i DVMP procesa na malim vrijednostima  $x_B$ , odnosno na velikim vrijednostima  $Q^2$ , što je standardna kinematika eksperimentalnog postrojenja HERA u Njemačkoj. Slične analize provedene su u [1], gdje je pokazano da GPD-ovi dobiveni prilagodbom na DVMP podatke daju dobre predikcije za DVCS podatke, te u [2, 3, 4], gdje je napravljena istovremena prilagodba na DVCS i DVMP podatke u vodećem i drugom redu računa smetnje. U ovom kinematičkom režimu dominiraju kvarkovi mora i gluoni, stoga zanemarujemo valentni sektor i provodimo analizu do drugog reda računa smetnje. Udarni presjeci su tada dani samo CFF-om, odnosno TFF-om  $\mathcal{H}$ , pri čemu se efektivno zanemaruje doprinos distribucijske amplitude. Rutinom najmanjih kvadrata MINUIT provodi se prilagodba na podatke H1 i ZEUS kolaboracija, pri čemu se za DVMP uzima samo produkcija  $\rho^0$  mezona. Ovom analizom testirala se mogućnost opisa sva tri procesa na razini gore spomenuta četiri CFF-a, odnosno TFF-a, kao i mogućnost dobivanja istih GPD-ova u tim procesima. Također se ispitivao doprinos drugog reda računa smetnje i kvarkovsko-gluonska struktura protona. U ovoj analizi napravljeno je 6 modela, od kojih su tri u vodećem redu, a tri u drugom redu računa smetnje. Za oba reda računa smetnje napravljen je jedan model prilagođen na mjerenja sva tri procesa, jedan model prilagođen na DIS i DVCS, i jedan prilagođen na DIS i DVMP. Kvaliteta tih modela kvantificirana je izračunom vrijednosti  $\chi^2/N_{\text{pts}}$ , gdje je  $N_{\text{pts}}$  broj točaka mjerenja koju taj model pokušava opisati. Prilagodba na drugom redu računa smetnje dobro opisuje podatke i pokazuje značajnu razliku od prilagodbe na vodećem redu računa smetnje kod DVCS i DVMP procesa. Vrijednost  $\chi^2/N_{\text{pts}}$  za najbolji model je 1.1. Univerzalnost GPD-

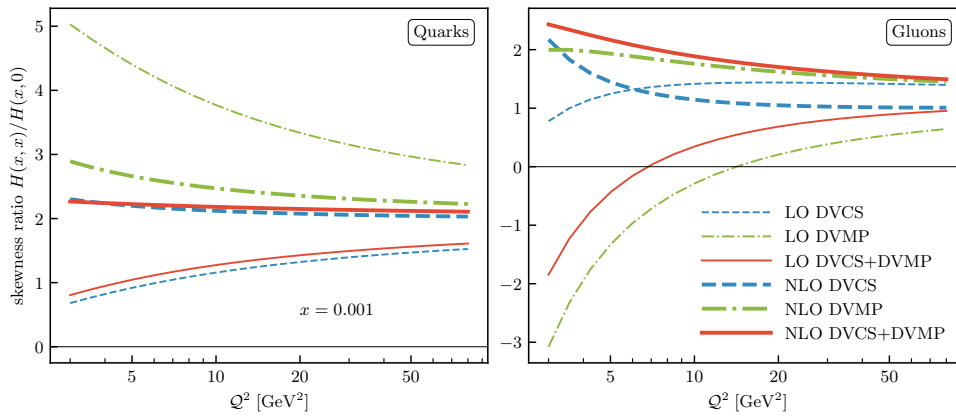
ova i važnost implementacije drugog reda računa smetnje potvrđena je računom takozvanog *skewness* omjera

$$r^a(Q^2) = \frac{H^a(x, \xi = x, t = 0, Q^2)}{H^a(x, \xi = 0, t = 0, Q^2)},$$

za kojeg se očekuje da poprma vrijednosti

$$r^{\text{Quark}} \approx 1.65, \quad r^{\text{Gluon}} \approx 1.0.$$

Prikaz ovog omjera dan je na slici niže.



Slika 1: Prikaz *skewness* omjera za  $x = 0.001$  za kvarkove (lijevo) i gluone (desno) na vodećem redu (tanke linije) i drugom redu računa smetnje (debele linije).

Svi kodovi potrebni za provedbu analize dostupni su javno u obliku softverskog paketa Gepard, opisanog na <https://gepard.phy.hr/index.html>.

Drugi alat kojeg koristimo u analizi DVCS-a je strojno učenje, tj. neuronske mreže koje se sastoje od više slojeva perceptrona. Učenje neuronskim mrežama provedeno je na DVCS podacima, gdje se raspršenje elektrona odvijalo na protonu i neutronu. Cilj ove analize bio je izdvajanje GPD-ova za gornje i donje kvarkove, što je moguće dodavanjem neutronske podatka i korištenjem izospinske simetrije, koja kaže  $F_{u, \text{proton}} = F_{d, \text{neutron}} \equiv F_u$ . Prvo je analiza provedena samo na protonskim podacima, bez razmatranja različitih okusa. Zanimljivo je evolucija u skali i analiza je implementirana na vodećem redu računa smetnje. U modele su prvi puta uvedene disperzijske relacije, koje povezuju realni i imaginarni dio CFF-ova na način

$$\Re \mathcal{H}(\xi, t, Q^2) = \frac{1}{\pi} \text{P.V.} \int_0^1 d\xi' \Im \mathcal{H}(\xi', t, Q^2) \left( \frac{1}{\xi - \xi'} - \frac{1}{\xi + \xi'} \right) + \Delta_{\mathcal{H}}(t, Q^2),$$

gdje je  $\Delta_{\mathcal{H}}(t, Q^2)$  suptrakcijska konstanta koja ne ovisi o  $\xi$ . Implementacijom disperzijskih

relacija možemo modelirati samo imaginarne dijelove CFF-ova i jednu suptrakcijsku konstantu, jer vrijedi  $\Delta_{\mathcal{H}} = -\Delta_{\mathcal{E}}$  i  $\Delta_{\tilde{\mathcal{H}}} = \Delta_{\tilde{\mathcal{E}}} = 0$ . Ovom metodom za sada nismo u mogućnosti izračunati GPD-ove, pa računamo samo CFF-ove.

Radi usporedbe napravljena je i standardna prilagodba najmanjih kvadrata na podatke, gdje je valentni sektor implementiran u  $x$  prostoru

$$H_q^{\text{val}}(x, x, t) = \frac{n_q r_q}{1+x} \left( \frac{2x}{1+x} \right)^{-\alpha_v(t)} \left( \frac{1-x}{1+x} \right)^{b_q} \frac{1}{1 - \frac{1-x}{1+x} \frac{t}{M_q^2}}, \quad q = u, d,$$

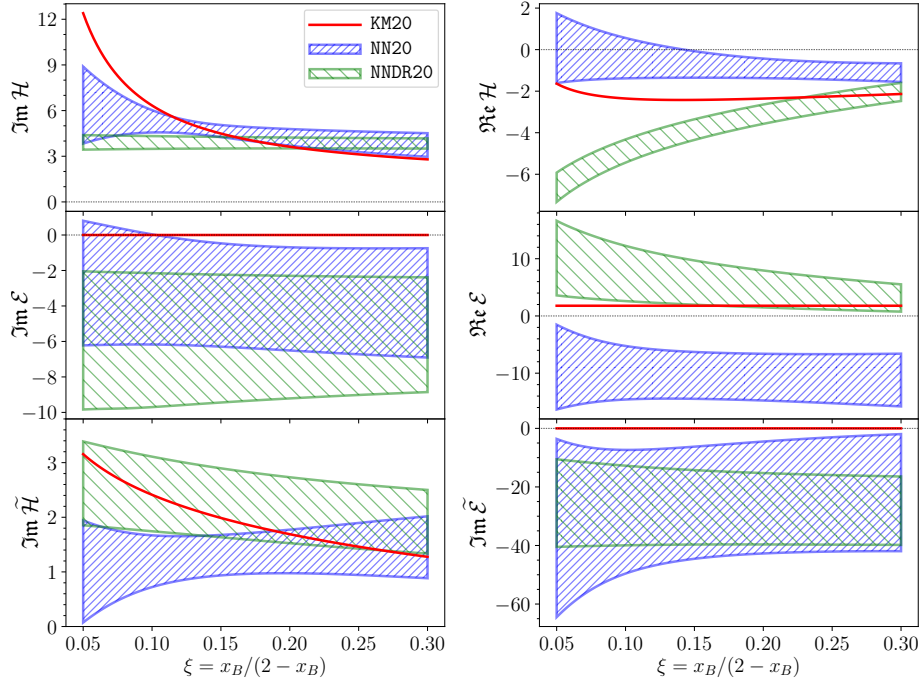
s CFF-ovima

$$\Im \mathcal{H}^{\text{val}}(\xi, t) = \pi \sum_{q=u,d} Q_q^2 \left[ H_q^{\text{val}}(\xi, \xi, t) - H_q^{\text{val}}(-\xi, \xi, t) \right].$$

Prethodne formule vrijede ekvivalentno za sve GPD-ove i CFF-ove. Suptrakcijska konstanta dana je modelom

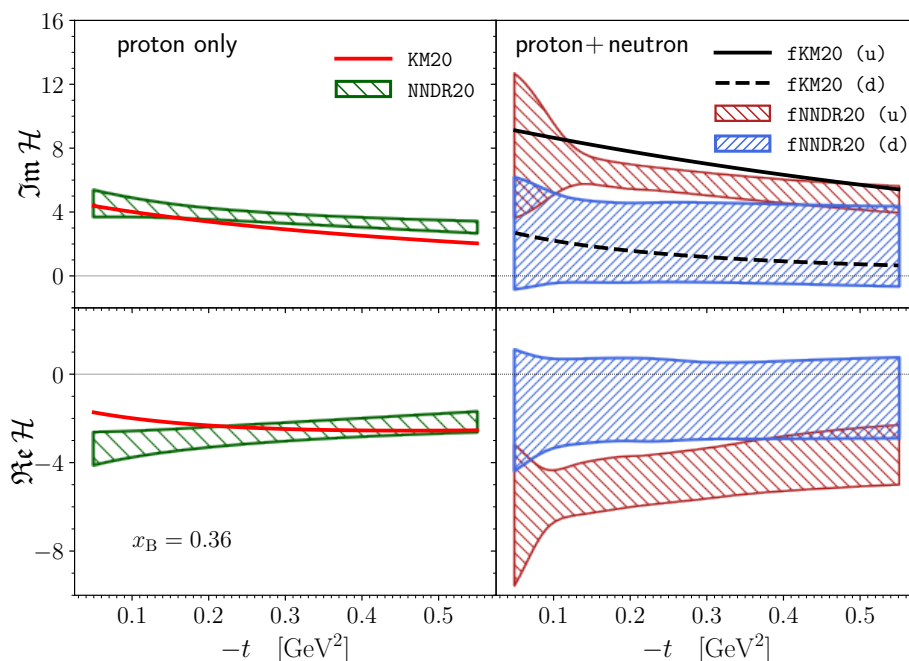
$$\Delta_{\mathcal{F}}(t) = \frac{C}{\left( 1 - \frac{t}{M_C^2} \right)^2}.$$

CFF-ovi kvarkova mora i gluona dani su u konformnom prostoru, pa ovaj model nazivamo hibridnim. Analiza je u ovom slučaju provedena na vodećem redu računa smetnje i evolucija u skali zanemarena je za valentni sektor. Ovaj model nazivamo  $\text{KM20}$ . Vrijednosti  $\chi^2/N_{\text{pts}}$  za sve modele su između 1.1 i 1.3, što smatramo vjernom reprezentacijom izmjerenih podataka. Ekstrakcija 6 od 8 komponenti CFF-ova prikazana je na slici niže.



Slika 2: Ekstrakcija CFF-ova na  $Q^2 = 4 \text{ GeV}^2$  i  $t = -0.2 \text{ GeV}^2$  s modelima neuronskih mreža treniranim na protonskim podacima s postrojenja JLab, NN20 i NNDR20, i s modelom dobivenim prilagodbom najmanjih kvadrata na podatke s postrojenja JLab i HERA KM20 [5].

Za okusno razdvojene CFF-ove korišten je model dobiven prilagodbom na podatke gdje se oslobađaju zasebni parametri za okuse kvarkova u valentnom sektoru. Ovaj model nazivamo  $f_{\text{KM20}}$  i prilagođen je na protonske i neutronske podatke s postrojenja JLab. Iskorišten je model neuronskih mreža s disperzijskim relacijama gdje su zasebno modelirane komponente CFF-ova za svaki okus, dakle  $\text{Im}\mathcal{H}^u$ ,  $\text{Im}\mathcal{H}^d$ , itd. Rezultati okusno razdvojenog CFF-a  $\mathcal{H}$  dani su na slici niže. Za ostale CFF-ove nije postignuta separacija okusa, no nada je da će se i to postići s više mjerenja.



Slika 3: Ekstrakcija (lijevo) i okusno razdvojeni (desno) imaginarni i realni dio CFF-a  $\mathcal{H}$  dobiveni okusnim modelima  $f_{\text{KM20}}$  i  $f_{\text{NNDR20}}$  [5].

Budući da je u planu izgradnja novog postrojenja EIC (od engleskog *Electron-Ion Collider*), kao i nadogradnja postojećih postrojenja JLab i Brookhaven, nadolazeća mjerenja će biti sve preciznija, stoga će biti iznimno važno eliminirati što više neodređenosti prisutnih u našim modelima. Neodređenosti uvedene raznim izborima i aproksimacijama nije lako kvantificirati, zbog čega se u ovom radu za sve modele dobivene prilagodbom najmanjih kvadrata ni ne prikazuju neodređenosti.

Ključne riječi: proton, generalizirane partonske distribucije, duboko virtualno komptonsko raspršenje, komptonski form faktori

# Contents

<b>1</b>	<b>Introduction</b>	<b>1</b>
<b>I</b>	<b>Hadron structure</b>	<b>4</b>
<b>2</b>	<b>Probing the structure of the proton</b>	<b>5</b>
2.1	Elastic electron-proton scattering . . . . .	5
2.2	Deep inelastic scattering . . . . .	8
2.3	Deeply virtual Compton scattering . . . . .	14
2.4	Deeply virtual meson production . . . . .	19
<b>3</b>	<b>Generalized parton distributions</b>	<b>23</b>
3.1	Operator product expansion . . . . .	23
3.2	Formal definition . . . . .	26
3.3	Partonic interpretation . . . . .	28
3.4	Basic properties . . . . .	30
3.4.1	Symmetry properties . . . . .	30
3.4.2	Forward limit . . . . .	31
3.4.3	Link to elastic form factors . . . . .	32
3.4.4	Domain and positivity bounds . . . . .	33
3.4.5	Distribution amplitudes . . . . .	34
3.4.6	Polynomiality . . . . .	35
3.5	Energy-momentum tensor . . . . .	37
3.5.1	Sum rules and the spin puzzle . . . . .	38
3.5.2	Hadron tomography . . . . .	39
3.5.3	Evolution of GPDs . . . . .	40
3.5.4	Other parton distributions . . . . .	42
3.5.5	Dispersion relations . . . . .	45
3.6	Status of experiments . . . . .	46
3.6.1	Observables . . . . .	47
<b>4</b>	<b>Conformal symmetry and conformal moments</b>	<b>51</b>
4.1	Conformal group and conformal towers . . . . .	51
4.2	Conformal operator product expansion . . . . .	55

4.3	Conformal partial wave expansion . . . . .	57
4.3.1	Generalized parton distributions . . . . .	57
4.4	Mellin-Barnes representation of scattering amplitudes . . . . .	65
4.4.1	Structure functions . . . . .	65
4.4.2	Compton form factors . . . . .	67
4.4.3	Transition form factors . . . . .	70
<b>5</b>	<b>Machine learning methods</b>	<b>72</b>
5.1	Artificial neuron . . . . .	72
5.2	Neural networks . . . . .	74
5.2.1	Backpropagation . . . . .	76
5.2.2	Network training . . . . .	79
<b>II</b>	<b>Global fits</b>	<b>82</b>
<b>6</b>	<b>Conformal partial wave parametrization</b>	<b>83</b>
6.1	Hard-scattering amplitudes . . . . .	85
6.1.1	DVCS . . . . .	85
6.1.2	DVMP . . . . .	86
6.2	Evolution of GPDs and DAs . . . . .	88
6.3	Modeling GPDs . . . . .	92
<b>7</b>	<b>Multichannel fits</b>	<b>97</b>
7.1	L/T separation . . . . .	98
7.2	Results . . . . .	100
7.2.1	Fits and parameters . . . . .	100
7.2.2	Data representation . . . . .	104
7.2.3	Quark and gluon contributions . . . . .	110
7.2.4	Gepard . . . . .	115
<b>III</b>	<b>Neural network parametrization</b>	<b>117</b>
<b>8</b>	<b>Neural network extraction of CFFs</b>	<b>118</b>
8.1	Neural network framework . . . . .	118
8.2	Extraction of CFFs . . . . .	121
8.2.1	Model fits . . . . .	121
8.2.2	Neural network models . . . . .	123
8.2.3	Experimental data and results . . . . .	124
8.3	Flavor separation of CFFs . . . . .	128
<b>9</b>	<b>Closure tests</b>	<b>133</b>
9.1	Testing the extraction of CFFs . . . . .	134
9.2	Testing the flavor separation of CFFs . . . . .	142

<b>10 Thesis summary and outlook</b>	<b>144</b>
<b>References</b>	<b>146</b>
<b>Curriculum vitae</b>	<b>153</b>

# List of Figures

1	Prikaz <i>skewness</i> omjera za $x = 0.001$ za kvarkove (lijevo) i gluone (desno) na vodećem redu (tanke linije) i drugom redu računa smetnje (debele linije). . . .	vii
2	Ekstrakcija CFF-ova na $Q^2 = 4 \text{ GeV}^2$ i $t = -0.2 \text{ GeV}^2$ s modelima neuronskih mreža treniranim na protonskim podacima s postrojenja JLab, NN20 i NNDR20, i s modelom dobivenim prilagodbom najmanjih kvadrata na podatke s postrojenja JLab i HERA KM20 [5]. . . . .	ix
3	Ekstrakcija (lijevo) i okusno razdvojeni (desno) imaginarni i realni dio CFF-a $\mathcal{H}$ dobiveni okusnim modelima $f_{\text{KM20}}$ i $f_{\text{NNDR20}}$ [5]. . . . .	x
2.1	Deep inelastic scattering. . . . .	9
2.2	Deeply virtual Compton scattering and Bethe-Heitler process. . . . .	15
2.3	BKM reference frame. Adapted from [23]. . . . .	17
2.4	Deeply virtual Compton scattering at leading order of perturbation theory. . . .	18
2.5	Deeply virtual meson production. . . . .	20
2.6	Deeply virtual meson production at leading order of perturbation theory. . . . .	20
3.1	Partonic definition of GPDs for various values of $x$ and $\xi \geq 0$ . In a) the struck parton is a quark which is emitted and reabsorbed by the hadron. In b) a quark-antiquark pair are emitted. In c) the struck parton is an antiquark which is also emitted and reabsorbed by the hadron. . . . .	29
3.2	Hierarchy of parton distributions. Inspired by [82]. . . . .	44
3.3	Depiction of kinematic dependences of various distributions. . . . .	45
3.4	Kinematic coverage of DVCS measurements. Taken from [86]. . . . .	47
4.1	Integral contour of the Mellin-Barnes representation of the GPD. . . . .	61
4.2	Deformed integral contour of the Mellin-Barnes integral. . . . .	64
5.1	Model of a perceptron. . . . .	73
5.2	Sigmoid activation function. . . . .	74
5.3	Example of a neural network architecture. . . . .	75
5.4	Black line represents the full-batch gradient descent, and the green line represents the stochastic gradient descent. . . . .	77
5.5	Example of an underfitted network, a good fit and an overfitted network. . . . .	80
5.6	Example of loss function for an overfitted model. . . . .	80

7.1	Comparison of $R(W, Q^2)_{\text{H1}}$ to measurements from [134] (left) and $R(W, Q^2)_{\text{ZEUS}}$ to measurements in [135] (right). Both measurements are compared to the function $R(Q^2)$ from [2], which is plotted in green. . . . .	100
7.2	Description of H1 measurements [129] of the structure function $F_2(x_B, Q^2)$ at LO (thin line) and NLO (thick line). . . . .	104
7.3	Description of H1 [130, 131] and ZEUS [132, 133] measurements of the cross section dependence on $t$ , $W$ and $Q^2$ . The LO (thin lines) and NLO (thick lines) models fitted to DIS+DVCS (blue dashed), and DIS+DVCS+DVMP (red solid) are compared to the data. The three H1 lines on the left panels correspond, from top to bottom, to $Q^2 = 8, 15.5$ and $25 \text{ GeV}^2$ , respectively. . . . .	105
7.4	Description of H1 DVMP measurements [134] of the cross section dependence on $Q^2$ and $W$ by LO (thin lines) and NLO (thick lines) models fitted to H1 and ZEUS DVMP data (green dot-dashed), as well as DVCS data (red solid). . . . .	106
7.5	Description of ZEUS DVMP measurements [135] of the cross section dependence on $Q^2$ and $W$ by LO (thin lines) and NLO (thick lines) models fitted to H1 and ZEUS DVMP data (green dot-dashed), as well as DVCS data (red solid). . . . .	106
7.6	Description of H1 DVMP measurements of $\phi$ production [134] of the cross section dependence on $Q^2$ and $W$ by LO (thin lines) and NLO (thick lines) models fitted to H1 and ZEUS DVMP data (green dot-dashed), as well as DVCS data (red solid). . . . .	107
7.7	Prediction for the H1 longitudinal cross section from [134] at fixed $x = 0.0018$ by LO-DVMP (thin) and NLO-DVMP (thick) models. . . . .	108
7.8	Prediction for the H1 longitudinal cross section from [134] at fixed $W$ by LO (thin) and NLO (thick) models, specifically the models fit to DIS+DVMP data (green dot-dashed), and the models fit to all datapoints (red full). The data and the model predictions have been rescaled by the approximate $Q^{-5}$ scaling, and the $\phi$ production data and predictions have been rescaled by the factor from (7.1). . . . .	109
7.9	Depiction of the H1 $t$ -dependent cross section from [134] at fixed $x$ for each line. The data are compared to LO (thin) and NLO (thick) models, specifically the models fit to DIS+DVMP data (green dot-dashed), and the models fit to all datapoints (red full). . . . .	109
7.10	Separation of quark (blue dot-dashed) and gluon (red dashed) contributions to the DIS structure function $F_2$ (black solid) at LO (left) and NLO (right) for $x = 0.001$ . . . . .	111
7.11	Separation of quark (blue dot-dashed) and gluon (red dashed) contributions to the real (top) and imaginary (bottom) CFF $\mathcal{H}$ (black solid) with models LO-DVCS-DVMP (left) and NLO-DVCS-DVMP (right) for $x = 0.001$ and $t = 0$ . . . . .	112
7.12	Separation of quark (blue dot-dashed) and gluon (red dashed) contributions to the real (top) and imaginary (bottom) TFF $\mathcal{H}^p$ (black solid) with models LO-DVCS-DVMP (left) and NLO-DVCS-DVMP (right) for $x = 0.001$ and $t = 0$ . . . . .	113
7.13	Depiction of skewness ration at $x = 0.001$ for quark (left) and gluon (right) GPD $H$ for three LO (thin) and three NLO (thick) models from Table 7.1. . . . .	114

8.1	Example of a neural network architecture that parametrizes CFFs as functions of $x_B$ and $t$ . . . . .	119
8.2	Extraction of CFFs at $Q^2 = 4 \text{ GeV}^2$ and $t = -0.2 \text{ GeV}^2$ by two neural network models fitted to JLab proton data, NN20 and NNDR20, as well as a standard model fit KM20 [5]. . . . .	127
8.3	Predictions of Hall A proton (red) and neutron (blue) cross section (up) and its first cosine harmonic (down) by models $f_{\text{KM20}}$ (black line) and $f_{\text{NNDR20}}$ (green band) at beam energies 4.45 GeV (left) and 5.55 GeV (right) [5]. . . . .	130
8.4	Extraction (left) and flavor separation (right) of the real and imaginary components of the CFF $\mathcal{H}$ predicted by the flavored models $f_{\text{KM20}}$ and $f_{\text{NNDR20}}$ [5]. . . . .	131
8.5	Extraction (left) and flavor separation (right) of the real and imaginary components of the CFF $\mathcal{E}$ predicted by the flavored models $f_{\text{KM20}}$ and $f_{\text{NNDR20}}$ . . . . .	132
9.1	Kinematics of the simulated data in comparison to CLAS data kinematics. . . . .	134
9.2	Simulated data for the helicity-dependent cross section $X_{\text{LU}}$ . . . . .	135
9.3	Prediction of simulated data for the helicity-dependent cross section $X_{\text{LU}}$ by a neural net model, which is depicted as a red band. . . . .	136
9.4	Comparison of $\Im\mathcal{H}(t)$ obtained by the KM15 model (green line) and the neural net model (red band) trained on simulated data at $x_B = 0.1$ (left) and 0.2 (right), and $Q^2 = 4 \text{ GeV}^2$ . . . . .	136
9.5	Prediction of simulated data for the helicity-dependent cross section $X_{\text{LU}}$ with added noise by a neural net model. . . . .	137
9.6	Comparison of $\Im\mathcal{H}(t)$ modeled by the KM15 model (green line) and extracted by the neural net model (red band) from simulated $X_{\text{LU}}$ data with noise at $x_B = 0.1$ (left) and 0.2 (right), and $Q^2 = 4 \text{ GeV}^2$ . . . . .	138
9.7	Comparison of simulated $X_{\text{LU}}$ and $A_{\text{C}}$ data and the neural network predictions. . . . .	138
9.8	Comparison of $\Im\mathcal{H}(x_B, t)$ and $\Re\mathcal{E}(x_B, t)$ modeled by the KM15 model and extracted by the neural net model trained on simulated $X_{\text{LU}}$ and $A_{\text{C}}$ data with noise at $Q^2 = 4 \text{ GeV}^2$ and $x_B = 0.1$ (left) and $x_B = 0.2$ (right). . . . .	139
9.9	Extrapolation of CFFs extracted in Figure 9.8 to the entire domain of $\xi$ at $t = -0.2 \text{ GeV}^2$ . . . . .	140
9.10	Comparison of simulated $X_{\text{LU}}$ , $A_{\text{C}}$ and $A_{\text{UT}}$ data and the neural network predictions. . . . .	140
9.11	Comparison of $\Im\mathcal{H}$ , $\Re\mathcal{H}$ , $\Im\mathcal{E}$ , $\Re\mathcal{E}$ modeled by the KM15 model (green line) and extracted by the neural net model (red band) trained on simulated $X_{\text{UU}}$ , $X_{\text{LU}}$ , $X_{\text{UL}}$ , $A_{\text{C}}$ and $A_{\text{UT}}$ data with noise at $Q^2 = 4 \text{ GeV}^2$ , and $x_B = 0.1$ (left) and $x_B = 0.2$ (right). . . . .	141
9.12	Comparison of the extraction of flavor separated imaginary and real components of the CFF $\mathcal{H}$ obtained by a neural network fit (red band) and a random single net extraction (green line) at $Q^2 = 4 \text{ GeV}^2$ , and $x_B = 0.1$ (left) and $x_B = 0.2$ (right). . . . .	143

# List of Tables

3.1	Typical kinematics used for experiments. Taken from [1]. . . . .	49
3.2	Dependence of observables on CFFs, normalized to the highest coefficient. The coefficients are evaluated at the kinematics from Table 3.1. Coefficients smaller than 1% are not kept, except for the Hall A cross section. Taken from [1]. . . .	50
4.1	Charge parity, signature, conformal momenta and Mellin-Barnes representation factors for all GPDs occurring in CFFs and TFFs. . . . .	68
7.1	List of models used in this work, order of perturbation theory, and datasets to which the model was fitted. References to used DIS, DVCS and DVMP experimental data are given in Table 7.2. . . . .	101
7.2	Values of $\chi^2/N_{\text{pts}}$ for all of the six models described in this section (columns) tested against four different datasets (rows). The values denoted by $\gg 1$ are greater than 10. . . . .	102
7.3	The initial values of the parameters and their limits are given in the first two rows. The final fitted values and their uncertainties (one standard deviation) of the best NLO-DVCS-DVMP model are given in the last two rows. The values of $\chi^2/n_{\text{pts}}$ are given in the last column of Table 7.2. . . . .	103
8.1	Values of $\chi^2/N_{\text{pts}}$ for presented models and for each set of JLab DVCS measurements used in this study ( $\phi$ -space). First row specifies the number of real independent CFFs plus the number of subtraction constants. Second row gives the total value for leading harmonics of Fourier-transformed data, to which we actually fit. . . . .	126
8.2	Values of $\chi^2/N_{\text{pts}}$ for flavor separated models. See the caption of Table 8.1 for details. . . . .	129

# Chapter 1

## Introduction

Visualization of objects not visible to the naked eye has been one of the biggest pursuits of physics. Be it the objects that are too far away from us, such as distant galaxies and black holes, or objects that are too small in comparison to everyday life, we have been developing technology that would allow us to bring these objects closer to us. From telescopes to microscopes, our desire to uncover the world around us has yielded many technical and scientific discoveries. One of the bigger technical advantages of modern physics is the building of particle accelerators, which represent the next step in observing very small objects, i.e. they are in some sense very large microscopes. They allow us to enter the very building blocks of all matter in our universe, that is, they allow us to enter the proton.

So far we know most of the fundamental properties of the proton, such as its mass, electric charge and spin. But what we do not know, is how these properties came to be. The proton is not an elementary particle, but one that consists of many elementary particles, quarks and gluons, and their interaction is described by quantum chromodynamics (QCD). The picture of the proton has for a long time been the one of three static valence quarks, but adding up their mass recovers only 1% of the total mass of the proton. For this reason we had to reject the idea of the proton as having a static underlying structure, but as a dynamical system where the quarks interact strongly, and this binding energy is what results in the mass of the proton. It is also this interaction that gives rise to a sea of quark and antiquark pairs, and gluons as well. The image of the proton now becomes much more complicated, not only due to so many interacting particles, but also due to the nature of their interaction. QCD is a non-Abelian force with an SU(3) color symmetry, and a coupling constant which becomes large at small energies, which makes most calculations regarding strong interactions extremely difficult to carry out. Given that the proton is a stable particle, it represents a perfect testing ground for various tenets of QCD, such as confinement, which is still largely a mystery from a theoretical standpoint. Given

that a lot of current research in the field of particle physics deals with the physics beyond the standard model, it is paramount that the physics described by the standard model is described very precisely, which is still not the case for many aspects of QCD.

One of the points of interest that drives our area of research is that it is unclear how the spins and orbital angular momenta of partons inside the proton make up its spin. It was experimentally confirmed that the spin of all of the quarks, antiquarks and gluons makes up less than half of the total spin of the proton. Ideally we would want to obtain a full description of the phase space inside the proton, which would be enabled through the knowledge of Wigner distributions, but since this object is currently almost completely unknown, we settle for simpler distributions, which would illuminate the three-dimensional structure of partons, and how the quarks and gluons individually contribute to the total spin of the proton. These distributions are called generalized parton distributions (GPDs), and they are the main focus of this work. Unfortunately, they are currently not directly accessible from experiments, but are hidden inside an integral which goes into observables directly. The reason we are able to introduce GPDs in the first place is owed to the so-called factorization theorems, which allow us to separate the processes of interest into a part that can be described using perturbative field theory, the hard part, and into a part that cannot be calculated perturbatively, the soft part. This soft part represents the various parton distributions of interest, GPDs included. Since we cannot calculate GPDs from first principles, we approach this problem by modeling them in various ways and fitting them to data. In this work, we will describe two main approaches we take in analyzing processes that contain GPDs, which are deeply virtual Compton scattering (DVCS) and deeply virtual meson production (DVMP).

This work is divided into three parts. The first part contains the description of the processes we study, including also deep inelastic scattering (DIS), since GPDs reduce to parton distribution functions (PDFs), which are the soft part of DIS, in a certain limit. This is detailed in Chapter 2. In Chapter 3 we give all of the properties of GPDs necessary for our analysis, and for understanding our motivation in studying them, such as Ji's sum rule, their connection to PDFs and elastic form factors, and how to obtain a three-dimensional distribution function from them. In Chapter 4 we detail the conformal moments representation of GPDs, which allows us to more easily implement QCD evolution of GPDs. Here we also give the Mellin-Barnes representation of Compton form factors (CFFs), which are the convolutions of GPDs and the hard part of DVCS, as well as transition form factors (TFFs), which are the equivalent convolutions present in DVMP. Finally, in Chapter 5 we give a brief overview of the machine learning methods used in this work, mainly focusing on neural networks.

In the second part we present our high energy simultaneous analysis of DIS, DVCS and

DVMP using the conformal momentum representation of CFFs, TFFs and GPDs with an  $SO(3)$  partial wave expansion in the singlet quark and gluon sector. We give the details of our GPD and CFF/TFF model in Chapter 6. Through this analysis we test the twist-2 collinear description of these processes. We also study the quark-gluon content of these two processes at leading order (LO) and next-to-leading order (NLO). We test whether the twist-2 GPD description of these processes is universal by calculating the skewness ratio. All of our models have been fit to data taken at the HERA collider by the H1 and ZEUS collaborations. The analysis is presented in Chapter 7.

In the last part we present our machine learning approach to the description of DVCS. In Chapter 8 we extract CFFs from the proton DVCS data measured at Jefferson National Laboratory (JLab). This analysis is still not at the level of extracting GPDs, but it has proven successful in extracting 6 out of 8 twist-2 CFFs at LO. By adding the neutron DVCS data, we are able to separate the up and down quark contribution to the leading CFF  $\mathcal{H}$ . In this analysis we also perform standard hybrid model fits, where we also introduce a flavored model fit for comparison to the neural network extractions. In Chapter 9 we test the reliability of our neural network extractions of CFFs by performing closure tests.

# **Part I**

## **Hadron structure**

# Chapter 2

## Probing the structure of the proton

There are many inclusive and exclusive processes that probe the structure of the proton in some way, the most common being those where a lepton is scattered off the proton, and the interaction between the two is mediated by a virtual photon. Historically, one of the first processes that studied the structure of the proton is electron-proton elastic scattering, which is the dominant process at lower energies. As technology advanced, higher energy lepton beams were being produced at accelerators, which allowed for deeper probing of the structure of the proton. Some of these processes are deep inelastic scattering, semi-inclusive deep inelastic scattering, deeply virtual Compton scattering, deeply virtual meson production and many more. In this chapter we will try to provide an intuitive and historical overview of the first processes that probed the structure of the proton. Many books have been written on this subject and we refer the reader to [6] and [7] for the introduction.

### 2.1 Elastic electron-proton scattering

As we know from quantum mechanics, the higher the energy of a particle, the smaller their de Broglie wavelength, which means that we can probe the structure of matter more deeply. By comparing the wavelength of the electron  $\lambda_e$  to the radius of the proton  $R_p$ , we can classify the process  $e^- p \rightarrow e^- p$  into four categories:

- i) when the wavelength of the electron is much larger than the radius of the proton, i.e.  $\lambda_e \gg R_p$ , which occurs at lower electron energies, the proton looks essentially as a point-particle. This kinematic regime does not provide much insight into the structure of the proton;
- ii) when the wavelength of the electron is similar in size to the radius of the proton, i.e.  $\lambda_e \sim$

$R_p$ , we cannot treat the proton as a point-particle and have to include the non-localized nature of the electric charge and magnetic moment distributions;

- iii) when the wavelength of the electron is smaller than the radius of the proton, i.e.  $\lambda_e < R_p$ , inelastic scattering becomes the dominant process;
- iv) when the wavelength of the electron is much smaller than the radius of the proton, i.e.  $\lambda_e \ll R_p$ , we can uncover the dynamical properties of the proton structure. We call this regime deep inelastic scattering. This regime is described by an interaction of the virtual photon with a spin 1/2 point-particle inside the proton.

In regime i), depending if we treat the electron as a relativistic particle or not, we obtain the Mott or Rutherford scattering, respectively. In both of these we ignore the recoil of the proton. The differential cross section for Mott scattering is given as

$$\left(\frac{d\sigma}{d\Omega}\right)_{\text{Mott}} = \frac{\alpha^2}{4E^2 \sin^4(\theta/2)} \cos^2 \frac{\theta}{2}, \quad (2.1)$$

where  $E$  is the energy of the electron, and  $\theta$  is the scattering angle. In this regime any spin-spin interaction between the electron and the proton is negligible.

As we decrease the wavelength of the electron, we can no longer ignore the extended charge and magnetic moment distributions and the proton does not look like a point-particle. The fact that the proton has an extended charge distribution affects the wavefunction of the virtual photon in the sense that various waves scatter off of various points on the proton, which results in phase differences and the waves do not add up constructively, as they would when the wavelength is much larger than the radius of the proton. In order to account for these phase differences, one introduces a *form factor* so that the scattering amplitude can be written as the amplitude for Mott scattering multiplied by the form factor, or in terms of the cross section

$$\frac{d\sigma}{d\Omega} = \left(\frac{d\sigma}{d\Omega}\right)_{\text{Mott}} |F(\mathbf{q}^2)|^2, \quad (2.2)$$

where the form factor is defined as the Fourier transform of the charge distribution

$$F(\mathbf{q}^2) = \int \rho(\mathbf{r}) e^{i\mathbf{q}\cdot\mathbf{r}} d^3\mathbf{r}. \quad (2.3)$$

Here  $\mathbf{q} = \mathbf{p}_1 - \mathbf{p}_3$  is the momentum transfer from the electron to the proton.

The form factor has to satisfy  $F(0) = 1$ , since the charge distribution is assumed to be normalized. This value should also be recovered in the limit of a point-particle since there is

no charge distribution to discern, and the process is reduced to Mott scattering. We expect the same when the wavelength of the electron is very large, since we also effectively cannot see the charge distribution of the proton. In both of these cases  $\mathbf{q} \cdot \mathbf{r} \approx 0$ . When the wavelength of the electron is very small, the phase differences between the scattered waves will tend to cancel, and in this regime we expect  $F(\mathbf{q}^2 \rightarrow \infty) = 0$ . Equivalently, if the momentum transfer is infinite, then the electron energy has to be infinite so no scattering will occur, the electron will not feel the presence of the proton so the form factor has to vanish. This reflects the fact that the elastic cross section drops off as  $\mathbf{q}^2$  increases and inelastic scattering becomes dominant.

The next step in uncovering the structure of the proton would be to include the proton recoil and its spin into the calculation of the cross section. If we write the most general Lorentz covariant form of the current that describes the propagation of the proton in the scattering, taking into account hermiticity and parity, we have

$$J^\mu \propto F_1(q^2) \gamma^\mu + \frac{\kappa}{2M} F_2(q^2) i\sigma^{\mu\nu} q_\nu. \quad (2.4)$$

The first term of the current is the helicity-conserving part, and the second is the helicity-flip part.  $F_1$  is called the Dirac form factor, and  $F_2$  the Pauli form factor. They describe the spatial charge distribution inside the proton and they depend on the four-momentum of the virtual photon squared. For high energy transfer,  $q^2 < 0$  so we introduce  $Q^2 = -q^2$ . The limiting values for the proton and neutron form factors are

$$F_1^p(0) = 1 \quad (2.5)$$

$$F_1^n(0) = 0 \quad (2.6)$$

$$F_2^p(0) = \kappa_p = \mu_p - 1 \quad (2.7)$$

$$F_2^n(0) = \kappa_n = \mu_n, \quad (2.8)$$

where  $\mu_{p,n}$  are the anomalous magnetic moments of the proton and the neutron.

The cross section in the laboratory frame can be written as

$$\frac{d\sigma}{dQ^2} = \frac{4\pi\alpha^2}{Q^4} \left[ \left( 1 - y - \frac{m_p^2 y^2}{Q^2} \right) F_2(Q^2) + \frac{1}{2} y^2 F_1(Q^2) \right] \quad (2.9)$$

We can introduce a new set of form factors,  $G_E(Q^2)$  and  $G_M(Q^2)$ , known as Sachs form factors,

which are connected to  $F_{1,2}$  as

$$G_E(Q^2) = F_1(Q^2) - \tau F_2(Q^2) \quad (2.10)$$

$$G_M(Q^2) = F_1(Q^2) + F_2(Q^2), \quad (2.11)$$

where

$$\tau = \frac{Q^2}{4M^2}. \quad (2.12)$$

The cross section can then be written as

$$\frac{d\sigma}{d\Omega} = \frac{\alpha^2}{4E_1^2 \sin^4(\theta/2)} \frac{E_3}{E_1} \left( \frac{G_E^2 + \tau G_M^2}{(1 + \tau)} \cos^2 \frac{\theta}{2} + 2\tau G_M^2 \sin^2 \frac{\theta}{2} \right), \quad (2.13)$$

which is known as the Rosenbluth formula. All of these form factors depend on  $Q^2$ , which means that we can no longer simply interpret them as in the case of elastic scattering. Sachs form factors are more intuitive because they can be interpreted as Fourier transforms of charge and magnetic moment distributions in the limit when the time-like component of  $Q^2$  is very small, that is when  $Q^2 \approx \mathbf{q}^2$ . Both form factors can be measured in experiments and their value at  $Q^2 = 0$  can be extrapolated. This showed that  $G_M(0) = 2.79$ , which is directly connected to the fact that the magnetic moment of the proton is not that of a Dirac point particle. From this we can conclude that the proton possesses an underlying structure.

As we increase  $Q^2$ , we expect the cross section to drop off because the proton has a finite size. Even in the inelastic regime, where the proton is broken up, we would expect a steep decrease in the cross section if the virtual photon still interacted with the proton as a whole, not seeing its underlying structure. But experiments did not demonstrate this, which also confirmed the fact that the proton has an underlying structure and that the virtual photon interacts with the constituents inside the proton. In order to go deeper into the structure of the proton, we now study deep inelastic scattering (DIS).

First experiments on this topic were conducted at Stanford in 1953 by Robert Hofstadter [8, 9, 10]. For reviews on this matter see [11, 12, 13].

## 2.2 Deep inelastic scattering

As we increase the energy, electron-proton scattering is dominated by inelastic scattering, where the proton is excited and or broken up into various particles, denoted symbolically by  $X$ . In the case where we do not know all final products of the scattering, the scattering is denoted as

*inclusive*, and we sum over all possible final states. This process is symbolically written as

$$e^-(k_1) + N(P_1) \rightarrow e^-(k_2) + X(P_2), \quad (2.14)$$

and is depicted in figure 2.1 below.

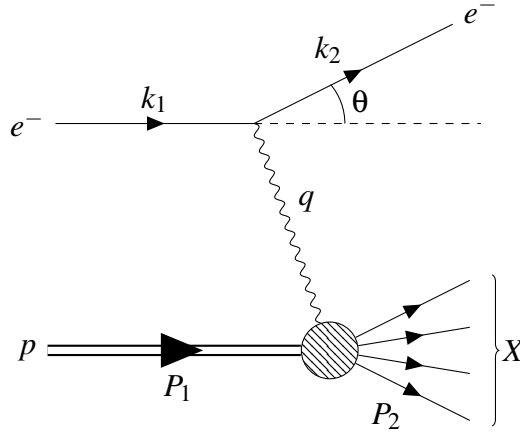


Figure 2.1: Deep inelastic scattering.

The first measurements of DIS were performed in 1969 at Stanford [14], and a Nobel prize was awarded in 1990 to Freedman [15], Kendall [16], and Taylor [17].

The invariant mass of the hadronic system  $X$  is denoted as  $W$ , and from conservation of energy and momentum we have

$$W^2 = P_2^2 = (P_1 + q)^2. \quad (2.15)$$

Since now the final state is not just one particle, the invariant mass  $W$  is not fully determined and the final cross section will depend on two variables, the angle of scattering and  $W^2 \neq M^2$ , as opposed to elastic scattering, where we only had one degree of freedom. We can choose a variety of variables, one of which is typically  $Q^2$ , with the same definition as in the case of elastic scattering. The other variable could be the invariant mass  $W$ , Bjorken  $x$ , defined as

$$x_B = \frac{Q^2}{2P_1 \cdot q}, \quad (2.16)$$

inelasticity  $y$ , defined as

$$y = \frac{P_1 \cdot q}{P_1 \cdot k_1}, \quad (2.17)$$

or the variable

$$\mathbf{v} = \frac{P_1 \cdot q}{M}. \quad (2.18)$$

Only two out of these variables are independent. For example, we can write  $x_B$  as

$$x_B = \frac{Q^2}{Q^2 + W^2 - m_p^2}. \quad (2.19)$$

Since we have a proton in the initial state, we need to have a baryon in the final state due to baryon number conservation. The proton is the lightest baryon, so we always have  $W^2 \geq M^2$ . Therefore  $x_B$  can take on the values

$$0 \leq x_B \leq 1. \quad (2.20)$$

In the limit of elastic scattering,  $W^2 = M^2$ , and  $x_B = 1$ . So the smaller the variable  $x_B$ , the more inelastic the scattering.

In the frame where the proton is at rest, the inelasticity can be written as

$$y = 1 - \frac{E'_e}{E_e}, \quad (2.21)$$

which is the fractional loss of the electron energy. In this frame we have to have  $E'_p \geq M$ , which implies, similarly as for  $x_B$ , that  $y$  is in the range

$$0 \leq y \leq 1. \quad (2.22)$$

The scattering is more inelastic as  $y$  approaches 1. In this frame we can also write

$$\mathbf{v} = E_e - E'_e, \quad (2.23)$$

which is just the loss of electron energy. Clearly  $y$  and  $\mathbf{v}$  cannot be independent. We can choose any two of the previously defined variables, aside from  $y$  and  $\mathbf{v}$ , to describe inelastic scattering, and we will choose  $x_B$  as our second variable.

The final state  $X$  in inelastic scattering can be an excited state of the proton, such as the baryon  $\Delta^+$ , which will subsequently decay into the proton, among other products. The kinematic regime where the invariant mass is higher than the mass of excited proton states and the proton is broken up into a multitude of particles is called *deep inelastic scattering*.

The total cross section for DIS, which is the sum over all possible states  $X$ , can be written

as

$$d\sigma^{ep \rightarrow eX} = \frac{1}{4ME_e} \frac{d^3k_2}{(2\pi)^2 2E'_e} \sum_X \int d\Pi_n |\mathcal{M}(ep \rightarrow eX)|^2 (2\pi)^4 \delta^{(4)}(k_1 + P_1 - k_2 - P_2). \quad (2.24)$$

At leading order in QED we describe this process as a single photon exchange, so we can write the cross section as

$$d\sigma \propto L^\mu L^{\nu\dagger} W_{\mu\nu}, \quad (2.25)$$

where  $L^\mu$  is the leptonic current

$$L^\mu = \frac{-i}{q^2 + i\epsilon} \bar{u}(k_2) \gamma^\mu u(k_1), \quad (2.26)$$

and  $W^{\mu\nu}$  is the hadronic tensor

$$W_{\mu\nu}(p_1, q) = \frac{1}{2\pi} \sum_X \int d\Pi_n \langle P_1 | j_\nu^\dagger(q) | P_2 \rangle \langle P_2 | j_\mu(q) | P_1 \rangle \cdot (2\pi)^4 \delta^{(4)}(k_1 + P_1 - k_2 - P_2). \quad (2.27)$$

Using the optical theorem, we can write the hadronic tensor as the imaginary part of the forward Compton tensor

$$W_{\mu\nu}(p_2, q) = \frac{1}{\pi} \Im T_{\mu\nu}(P_1, q), \quad (2.28)$$

where the forward Compton tensor, which describes the scattering  $\gamma(k)p(P) \rightarrow \gamma(k)p(P)$ , is given as

$$T_{\mu\nu}(p_2, q) = i \int d^4z e^{iq \cdot z} \langle P_1 | T \{ j_\mu(z) j_\nu(0) \} | P_1 \rangle. \quad (2.29)$$

It can be shown that the cross section can be written in the same form as the elastic cross section (2.9)

$$\frac{d^2\sigma}{dx_B dQ^2} \approx \frac{4\pi\alpha^2}{Q^4} \left[ (1-y) \frac{F_2(x_B, Q^2)}{x_B} + y^2 F_1(x_B, Q^2) \right], \quad (2.30)$$

where we additionally use the approximation  $Q^2 \gg M^2 y^2$ . We can notice one key difference, and that is that the new form factors,  $F_{1,2}$ , now depend on two variables,  $x_B$  and  $Q^2$ . These functions are called *structure functions*, and we can no longer interpret them as the Fourier transform of the electric and magnetic moment distributions. In order to interpret the meaning of the structure functions, we observe DIS through the partonic model, developed by Feynman [18].

At first order of perturbation theory, assuming that we have a very large energy and momentum transfer, we can describe this process as a virtual photon elastically scattering off a parton that has been separated from the broken proton. For ease of calculation, one typically

introduces the frame where the proton energy is very large, i.e.  $E_p \gg M$ , which is referred to as the infinite momentum frame. In this frame the proton moves along the  $z$ -axis, and this allows us to ignore the momentum components of the partons that are perpendicular to the  $z$ -axis. We parametrize the momenta of the partons using the momentum of the proton

$$p_q = xP_1 + p_\perp \approx xP_1, \quad (2.31)$$

where  $x$  is the longitudinal momentum fraction of the proton. We can use energy and momentum conservation to write the 4-momentum of the final quark as  $p'_q = p_q + q \approx xP_1 + q$ . If we ignore the mass of the quark, we have

$$p'^2_q \approx 0 \approx 2xq \cdot P_1 - Q^2. \quad (2.32)$$

Therefore, the definition of the momentum fraction  $x$  is

$$x = \frac{Q^2}{2q \cdot P_1} = x_B. \quad (2.33)$$

This means that in the infinite momentum frame the struck parton has the momentum fraction equal to Bjorken  $x$ . The cross section for elastic electron-quark scattering at leading order is given as

$$\frac{d\sigma}{dQ^2} = \frac{4\pi\alpha^2 Q_q^2}{Q^4} \left[ (1-y) + \frac{y^2}{2} \right]. \quad (2.34)$$

We can see that this expression has a similar structure to (2.30). In order to get the full picture, that is, to include the hadronic part of the process, we must recognize that the partons inside the proton interact via the strong nuclear force, i.e. through the exchange of gluons, which means that the partons do not have a precisely determined momentum, but rather that the momenta of the partons are given by probability distribution functions, called *parton distribution functions* (PDFs). These distributions are defined in the sense that  $u^P(x)\delta x$  gives the number of up quarks within the proton that have a momentum fraction between  $x$  and  $x + \delta x$ . They represent the hadronic part of this process and at this point we do not have a way of calculating them from first principles. This is because they describe the so-called *soft* part of the process, which is the interaction of partons through QCD at low energies that does not allow for a description using perturbation theory, since the strong coupling constant increases as the momentum transfer decreases. The scattering of the virtual photon off the quark is the *hard* part of the process, because it involves transfers of very large momenta, and it can be described using perturbation theory, which gives us expression (2.34). The hard part of the process occurs at much higher

energies, or equivalently at much smaller time-scales in comparison to the soft part. This means that, at least at leading order (LO), the hard part does not interfere with the soft part, and we can take them into consideration separately. This phenomenon is called *factorization*, and it is a powerful tool that allows us to make calculations and predictions about DIS and similar processes that probe the structure of nucleons, and it will be explained in more details later. The fact that we can factorize DIS and other processes involving the structure of the proton is due to the property of QCD called *asymptotic freedom*. This means that the strong coupling constant tends to zero as the momentum transfer tends to infinity, so for high momentum transfer we can expand the hard part of the process in terms of  $\alpha_S$ .

In order to write the full leading-order cross section, we need to multiply the  $e^-q$  cross section (2.34) by the number of quarks  $q_i$  that have the momentum fraction  $x$  in the interval  $[x, x + \delta x]$ , which gives us

$$\frac{d\sigma}{dQ^2} = \frac{4\pi\alpha^2}{Q^4} \left[ (1-y) + \frac{y^2}{2} \right] \times Q_i^2 q_i^p(x) \delta(x), \quad (2.35)$$

where  $Q_i$  is the charge of the struck quark. Now the full double-differential cross section, which sums over all quark flavors, is given as

$$\frac{d^2\sigma}{dQ^2 dx} = \frac{4\pi\alpha^2}{Q^4} \left[ (1-y) + \frac{y^2}{2} \right] \sum_i Q_i^2 q_i^p(x). \quad (2.36)$$

If we compare to (2.30), we can identify the structure functions of the proton

$$F_2^{\text{ep}}(x, Q^2) = 2xF_1^{\text{ep}}(x, Q^2) = x \sum_i Q_i^2 q_i^p(x). \quad (2.37)$$

We can make two conclusions from the partonic model. The first is that the structure functions do not depend on two variables, but only on  $x$ . This is called Bjorken scaling, and it reflects the assumption that the proton consists of point-like particles that carry its charge, rather than being a continuous spatial charge distribution. The second conclusion is that the structure functions are related to one another, which is called the Callan-Gross relation. This is a reflection of the quarks being point-like spin-half Dirac particles, whose electric and magnetic contribution to the interaction is fixed with respect to one another through the Dirac magnetic moment.

These two relations are only approximate. If we observe the static model of the proton, it would appear that it only consists of two up and one down quarks, called the valence quarks, in which case the PDFs would just be the delta function centered on  $x = 1/3$ . But this is of course not the case, because the valence quarks interact via the exchange of gluons, which can also

form quark-antiquark pairs, so in reality the proton consists of valence quarks, but also a sea of virtual quarks, antiquarks and gluons. Since high energy partons are suppressed by the  $1/q^2$  factor coming from the propagator, they can only be resolved at higher momentum transfers, or equivalently at low  $x_B$ . This is when the PDFs are more smeared and the dominating process is not elastic scattering off a point-like particle. This is why we need a  $Q^2$  dependence in the structure functions.

For reviews on this topic, see [19, 20].

## 2.3 Deeply virtual Compton scattering

Deeply virtual Compton scattering (DVCS) [21, 22] is a hard *exclusive* process, symbolically written as

$$\ell(k_1) + N(P_1) \rightarrow \ell(k_2) + N(P_2) + \gamma(q_2). \quad (2.38)$$

Hard means that there is a large momentum transfer from the initial lepton to the nucleon, and exclusive means that we detect all of the products in the final state. This process represents the next step in our pursuit of uncovering the structure of the proton. Like DIS, this process also relies on factorization to the hard and soft part in order to extract the functions that describe the structure of the proton. In this instance, the soft functions are called *generalized parton distributions* (GPDs), which describe the transition from the initial nucleon to the final nucleon state. The fact that we can access a richer description of the structure of nucleons is owed to the fact that DVCS is an off-forward process, meaning that the initial and final nucleon do not have the same impulse.

In DVCS the final state photon is emitted from the nucleon, but since the detectors only measure the products of the scattering, this process interferes with another process with the same initial and final state, called the Bethe-Heitler process. In the Bethe-Heitler process, the final state photon is emitted from either the initial or the final lepton through Bremsstrahlung, and the interaction between the virtual photon and the nucleon is described by the electromagnetic form factors  $F_{1,2}(Q^2)$ . Both of these processes are depicted in figure 2.2 below.

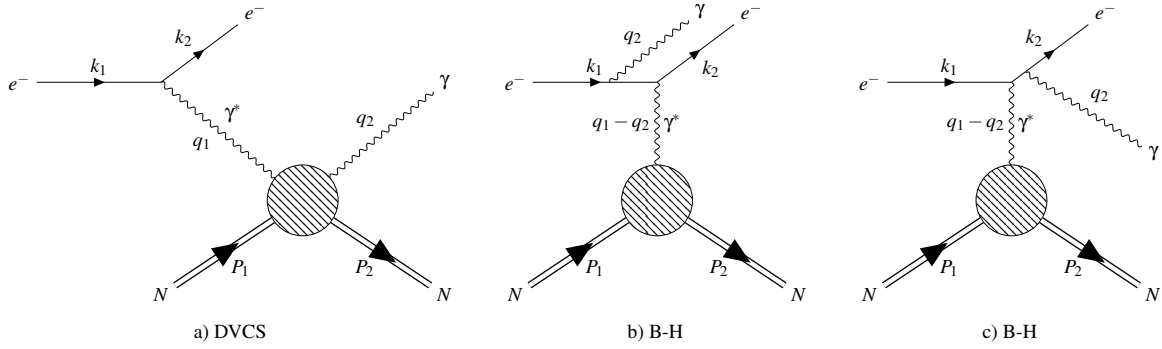


Figure 2.2: Deeply virtual Compton scattering and Bethe-Heitler process.

The amplitude for the process  $\ell N \rightarrow \ell N \gamma$  is the sum of the amplitudes for DVCS and the Bethe-Heitler process, which means that the differential cross section is written as

$$\frac{d\sigma}{dx_B dy d|\Delta^2| d\phi d\varphi} = \frac{\alpha^3 x_B y}{16\pi^2 Q^2 \sqrt{1+\epsilon^2}} \left| \frac{\mathcal{T}}{e^3} \right|^2, \quad (2.39)$$

where the amplitude is

$$|\mathcal{T}|^2 = |\mathcal{T}_{\text{DVCS}}|^2 + |\mathcal{T}_{\text{BH}}|^2 + \mathcal{I}. \quad (2.40)$$

The interference term is

$$\mathcal{I} = \mathcal{T}_{\text{DVCS}}^* \mathcal{T}_{\text{BH}} + \mathcal{T}_{\text{DVCS}} \mathcal{T}_{\text{BH}}^*. \quad (2.41)$$

The cross section depends on 5 variables, because there are three particles in the final state which have 5 degrees of freedom. Some of these variables were introduced before, namely the opposite of the square four-momentum of the virtual photon  $Q^2 = -q_1^2$ , which now does not correspond to the momentum transfer to the hadron, and the Bjorken  $x$  defined as in (2.16). The square of the four-momentum transfer to the hadron is given as

$$t = \Delta^2 = (P_2 - P_1)^2. \quad (2.42)$$

We also introduce the symmetric combinations of momenta

$$q = \frac{1}{2}(q_1 + q_2), \quad P = P_1 + P_2. \quad (2.43)$$

In order to describe the photon-proton scattering, we need three independent variables. We can

choose from the following Lorentz scalars

$$Q^2 = -q^2, \quad \xi_B = \frac{Q^2}{P \cdot q}, \quad \xi = -\frac{\Delta \cdot q}{P \cdot q}. \quad (2.44)$$

Note the different font between  $Q^2$  and  $\overline{Q^2}$ .  $\xi_B$  is called the generalized Bjorken variable, and  $\xi$  is called the skewness. Skewness tells us how much the process is off-forward, meaning how much the struck parton momentum changes in the scattering. If the skewness is zero, we retrieve the forward Compton amplitude, and  $\xi_B$  coincides with  $x_B$ . If additionally  $\Delta = 0$ , we recover deep inelastic scattering. We can also use the variables defined in DIS

$$x_B = \frac{Q^2}{2P_1 \cdot q_1}, \quad W^2 = (P_1 + q_1)^2. \quad (2.45)$$

In order to perturbatively approach this process, we employ the Bjorken limit, which is given as

$$s = (P_1 + q_1)^2 \sim q_1^2 \rightarrow \infty, \quad -\Delta^2 \ll s, \quad x_B = \text{fixed}, \quad (2.46)$$

and for both DVCS and DVMP  $\xi_B \simeq \xi$ . In this limit we have

$$Q^2 \simeq 2\overline{Q^2}, \quad \xi \simeq \frac{x_B}{2 - x_B}, \quad s \simeq 2P \cdot q. \quad (2.47)$$

We also introduce the notation for the average fraction of the longitudinal momentum of the proton carried by the struck parton  $x$ , which will be more precisely defined in the next chapter.

The limits on the momentum transfer are given by

$$\Delta_{\min, \max}^2 = -\frac{Q^2}{4x_B(1-x_B) + \varepsilon^2} \left[ 2(1-x_B) + \varepsilon^2 \mp 2(1-x_B)\sqrt{1+\varepsilon^2} \right], \quad \varepsilon = 2x_B \frac{M}{Q^2}. \quad (2.48)$$

The remaining two variables are the two angles  $\phi$  and  $\varphi$ . In order to define them, we define the leptonic plane, which is subtended by the initial and final lepton 3-momenta, and the hadronic plane, which is subtended by the 3-momenta of the scattered nucleon and real photon. The angle  $\phi$  is the angle between the leptonic plane and the recoiled nucleon 3-momentum, and  $\varphi$  is the angle between the scattered nucleon 3-momentum and its transverse polarization in the case of a polarized target. This frame is called the BKM frame [23]. This frame of reference is depicted in figure 2.3 below.

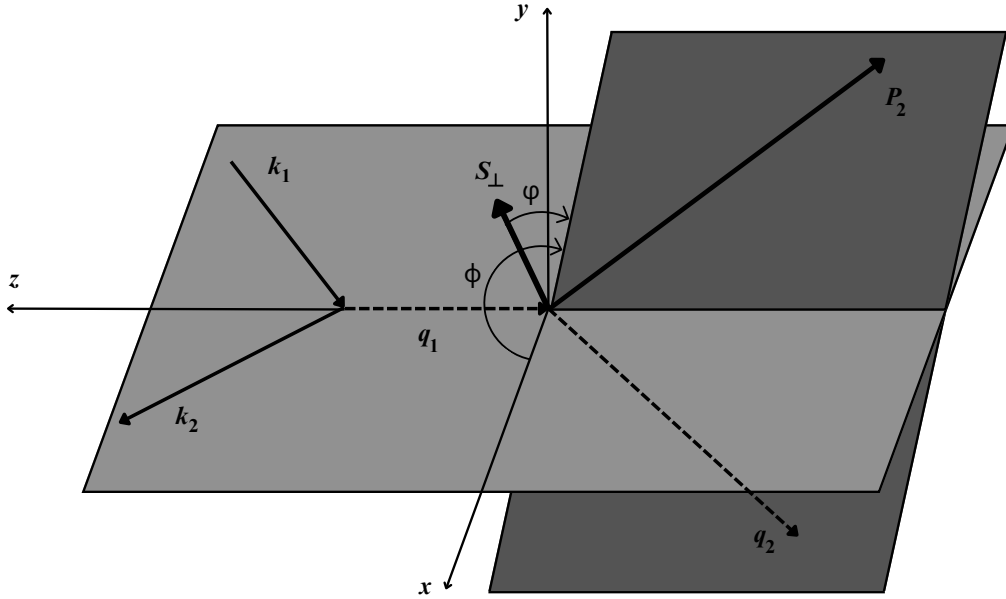


Figure 2.3: BKM reference frame. Adapted from [23].

In this frame the terms in the cross section (2.39) can be written as a decomposition into Fourier harmonics

$$|\mathcal{T}_{\text{BH}}|^2 = \frac{e^6}{x_{\text{B}}^2 y^2 (1 + \varepsilon^2)^2 \Delta^2 \mathcal{P}_1(\phi) \mathcal{P}_2(\phi)} \left\{ c_0^{\text{BH}} + \sum_{n=1}^2 c_n^{\text{BH}} \cos(n\phi) + s_1^{\text{BH}} \sin(\phi) \right\}, \quad (2.49)$$

$$|\mathcal{T}_{\text{DVCS}}|^2 = \frac{e^6}{y^2 Q^2} \left\{ c_0^{\text{DVCS}} + \sum_{n=1}^2 [c_n^{\text{DVCS}} \cos(n\phi) + s_n^{\text{DVCS}} \sin(n\phi)] \right\}, \quad (2.50)$$

$$\mathcal{I} = \frac{\pm e^6}{x_{\text{B}} y^3 \Delta^2 \mathcal{P}_1(\phi) \mathcal{P}_2(\phi)} \left\{ c_0^{\text{I}} + \sum_{n=1}^3 [c_n^{\text{I}} \cos(n\phi) + s_n^{\text{I}} \sin(n\phi)] \right\}, \quad (2.51)$$

where we only keep the first few harmonics. Higher harmonics are suppressed by factors of  $1/Q$ , and this expansion will be explained later. The sign ambiguity in the interference term comes from the charge sign of the lepton beam,  $+$  being for a negatively charged beam. The term  $1/\mathcal{P}_1(\phi)\mathcal{P}_2(\phi)$  in the interference term also has a  $\phi$  dependence coming from the lepton propagators, which makes the Fourier analysis of experimental data more complicated. The fact that the Bethe-Heitler process, which we can describe sufficiently well at the level of precision we have for DVCS, comes into the full  $\ell N \rightarrow \ell N \gamma$  cross section provides a unique opportunity to access GPDs linearly and quadratically. The problem is that we cannot access GPDs through DVCS directly, but rather their convolution with the hard-scattering part of the amplitude. These

convolutions are called *Compton form factors* (CFFs). This is not dissimilar to the extraction of PDFs in DIS, where experiments probe structure functions, which are convolutions of PDFs and the hard-scattering part as we move away from the naive parton model where gluon radiation and transverse momentum of partons are ignored.

At leading order DVCS is described through the so-called hand-bag diagrams, which are depicted in 2.4 below. In this part we observe only the hadronic part of the process, where at leading order we have the scattering of a virtual photon off a quark (or equivalently antiquark), which then emits a real photon and is absorbed back into the nucleon. Therefore, the initial and final nucleon have to be the same. Alternatively, this process could also be thought of as an emission of a quark-antiquark pair from the nucleon, which absorbs the virtual photon and then annihilates into the final photon. If we accept the former interpretation, then we draw the  $s$ - and  $u$ -channels, where the fermion propagator in the hard subprocess carries the  $s$  and  $u$  four-momentum squared, respectively.

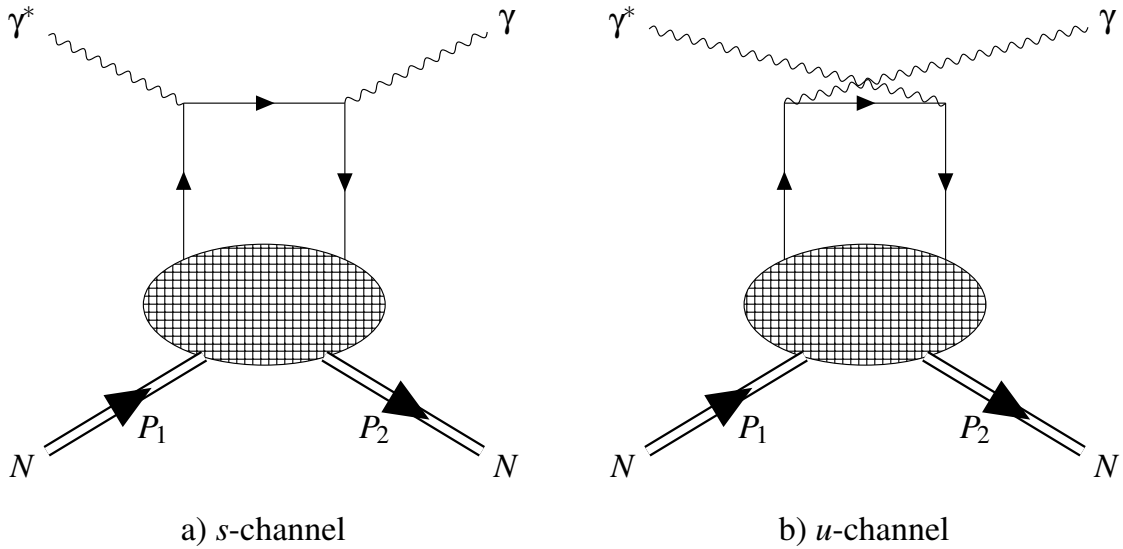


Figure 2.4: Deeply virtual Compton scattering at leading order of perturbation theory.

Starting from the Compton tensor (note that this is not the case of forward scattering)

$$T_{\mu\nu}(q, P, \Delta) = i \int d^4z d^4w e^{-iq_1z + iq_2w} \langle P_2 | j_\mu(z) j_\nu(w) | P_1 \rangle, \quad (2.52)$$

we can obtain the differential cross section for this process, where the scattering amplitude is

$$|\mathcal{T}_{\text{DVCS}}|^2 = \frac{2(2-2y+y^2)}{y^2 Q^2 (2-x_B)^2} \left[ 4(1-x_B) \left( |\mathcal{H}|^2 + |\tilde{\mathcal{H}}|^2 \right) - \left( x_B^2 + (2-x_B)^2 \frac{\Delta^2}{4M^2} \right) |\mathcal{E}|^2 \right. \\ \left. - x_B^2 \left( \mathcal{H}\mathcal{E}^* + \mathcal{E}\mathcal{H}^* + \tilde{\mathcal{H}}\tilde{\mathcal{E}}^* + \tilde{\mathcal{E}}\tilde{\mathcal{H}}^* \right) - x_B^2 \frac{\Delta^2}{4M^2} |\tilde{\mathcal{E}}|^2 \right], \quad y = \frac{Q^2}{xs}. \quad (2.53)$$

The differential cross section is expressed in terms of several CFFs. Symbolically, we can write CFFs as

$$\mathcal{F}^A(\xi, \Delta^2, Q^2) = {}^A T \left( \frac{\xi+x-i\epsilon}{2(\xi-i\epsilon)}, \xi \middle| \alpha_s(\mu_R), \frac{Q^2}{\mu_F^2} \right) \otimes F^A(x, \xi, \Delta^2, \mu_F^2), \quad (2.54)$$

where we introduce the notation for convolution

$$f(x) \otimes g(x) = \int_{-1}^1 \frac{dx}{2\xi} f(x)g(x). \quad (2.55)$$

The index  $A$  denotes all parton contributions, so  $A \in \{u, d, s, \dots G\}$ . We have four types of CFFs, corresponding to the four GPDs that enter the amplitude at LO, which are  $F \in \{H, E, \tilde{H}, \tilde{E}\}$ .

The CFFs in the cross section are summed over all partons,

$$\mathcal{F} = \sum_A Q_A^2 \mathcal{F}^A, \quad Q_G^2 = \frac{1}{N_f} \sum_q Q_q^2. \quad (2.56)$$

The fact that we can write CFFs as a convolution of GPDs, which describe the soft part of the process, and the hard-scattering amplitudes is a reflection of factorization, which was proven in [24] for transversally polarized virtual photons. The definitions of GPDs and CFFs, as well as their properties will be given in later chapters.

## 2.4 Deeply virtual meson production

Deeply virtual meson production (DVMP) is another hard exclusive process that gives access to GPDs, and it is symbolically written as

$$\ell(k_1) + N(P_1) \rightarrow \ell(k_2) + N'(P_2) + M(q_2). \quad (2.57)$$

In the final state we now have a meson instead of a photon like in DVCS, and depending on the meson, the final state hadron does not have to be the same as the initial hadron. The process is

depicted in figure 2.5 below.

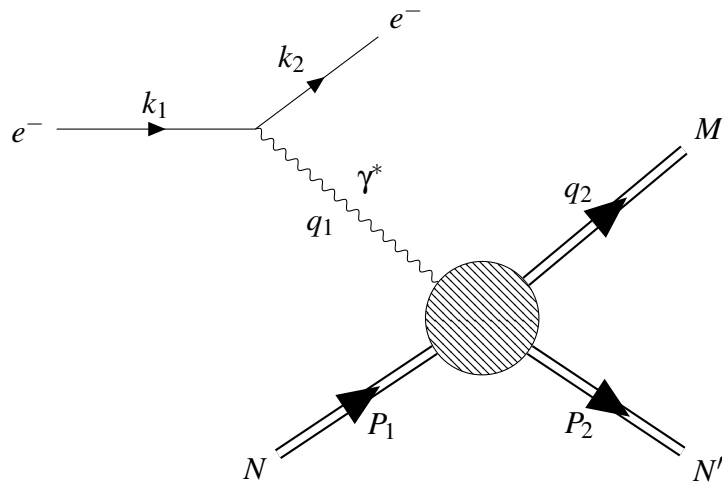


Figure 2.5: Deeply virtual meson production.

We again rely on factorization, which was proven for light pseudoscalar mesons and longitudinally polarized vector mesons in [25]. At LO, many channels have been studied [26, 27, 28, 29, 30, 31, 32, 33]. Some of these studies have been extended to NLO accuracy [34, 35, 36, 37, 38].

At leading order, we observe two types of diagrams, depicted in figure 2.6 below.

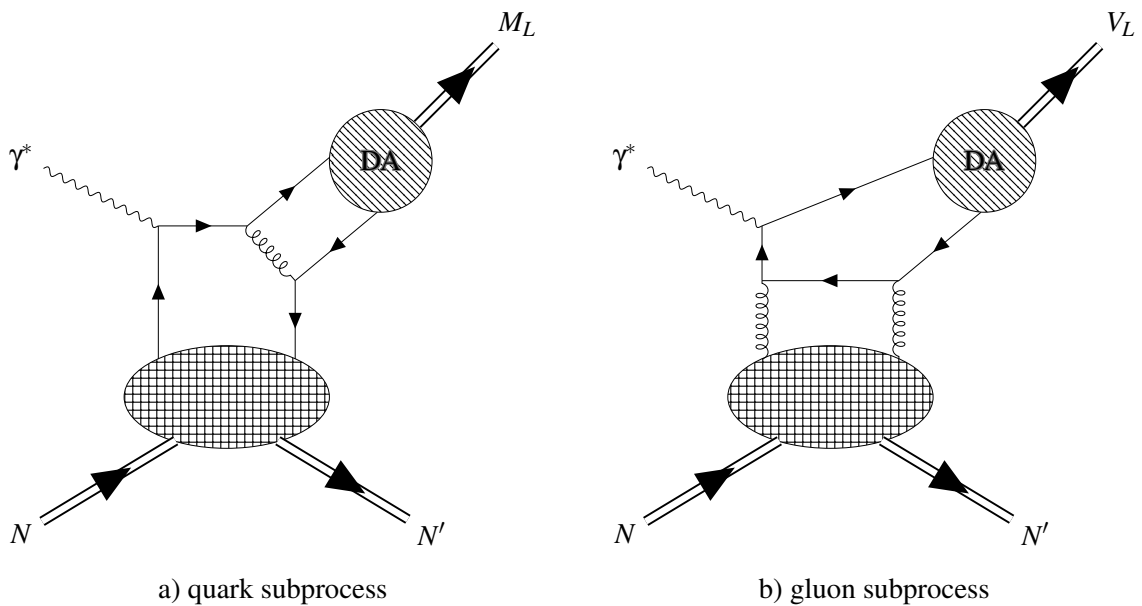


Figure 2.6: Deeply virtual meson production at leading order of perturbation theory.

Note that at LO DVMP has one less QED vertex in comparison to DVCS, because there is no final-state photon. The DVMP cross section is therefore larger than the DVCS cross section. Also, gluons enter DVMP at leading order, but for DVCS they appear in next-to-leading order corrections. In the case of the quark subprocess, we need a gluon in order to bind a quark and antiquark into the final meson state. This diagram can be observed in two ways. We can look at it as a quark emitted from the nucleon, which absorbs the virtual photon and emits a gluon, which then breaks up into a quark and antiquark. This quark is absorbed into the nucleon, and the original quark binds to the antiquark emitted from the gluon into the final-state meson. Alternatively, a quark-antiquark pair are emitted from the nucleon, they absorb the virtual photon and bind into the final-state meson by exchanging a gluon. Both of these processes can also be produced in the  $u$ -channel.

Due to charge parity conservation, only neutral vector mesons can be produced in the gluon subprocess. This is because photons have charge parity  $-1$ , charge parity of the quark-antiquark state is  $-1$ , and  $+1$  for the double gluon-gluon state. Since the subprocesses are  $\gamma^* q\bar{q} \rightarrow M$  and  $\gamma^* gg \rightarrow M$ , the charge parity conservation gives

$$C_\gamma C_q C_{\bar{q}} = +1 = C_M, \quad C_\gamma C_G C_G = -1 = C_M. \quad (2.58)$$

Neutral pseudoscalar mesons have charge parity  $+1$ , and neutral vector mesons have charge parity  $-1$ , which explains why there can be no pseudoscalar mesons produced this way.

Since we only have one QED vertex, the amplitude is described by the transition amplitude

$$A_\mu = \int d^4z e^{-iq_1 z} \langle q_2 P_2 | j_\mu(z) | P_1 \rangle, \quad (2.59)$$

which we use to calculate the cross section. This time the cross section, which is given as

$$\frac{d^2\sigma_{\text{L}}^{\gamma^* \rightarrow MN'}}{d\Delta^2 d\phi} = \frac{\alpha_{\text{em}} x_{\text{B}}^2 y^2}{32\pi Q^2 \sqrt{1+\epsilon^2}} \frac{1}{1-y} |\mathcal{T}^{\text{DVMP}}|^2, \quad (2.60)$$

with

$$|\mathcal{T}^{\text{VL}}|^2 = 16 \frac{1-y}{y^2 (2-x_{\text{B}})^2} \left[ 4(1-x_{\text{B}}) |\mathcal{H}|^2 - x_{\text{B}}^2 (\mathcal{H}\mathcal{E}^* + \mathcal{E}\mathcal{H}^*) - \left( x_{\text{B}}^2 + (2-x_{\text{B}})^2 \frac{\Delta^2}{4M^2} \right) |\mathcal{E}|^2 \right] \quad (2.61)$$

$$|\mathcal{T}^{\text{PS}}|^2 = 16 \frac{1-y}{y^2 (2-x_{\text{B}})^2} \left[ 4(1-x_{\text{B}}) |\tilde{\mathcal{H}}|^2 - x_{\text{B}}^2 (\tilde{\mathcal{H}}\tilde{\mathcal{E}}^* + \tilde{\mathcal{E}}\tilde{\mathcal{H}}^*) - x_{\text{B}}^2 \frac{\Delta^2}{4M^2} |\tilde{\mathcal{E}}|^2 \right] \quad (2.62)$$

is given in terms of *transition form factors* (TFFs). Symbolically, we can write them as

$$\mathcal{F}^A(\xi, \Delta^2, Q^2) = \frac{fC_F}{QN_c} \phi(v) \otimes^v A T \left( \frac{\xi + x - i\epsilon}{2(\xi - i\epsilon)}, v, \xi \middle| \alpha_s(\mu_R), \frac{Q^2}{\mu_F^2}, \frac{Q^2}{\mu_\phi^2}, \frac{Q^2}{\mu_R^2} \right) \otimes^x F^A(x, \xi, \Delta^2). \quad (2.63)$$

The  $x$  integral is defined in (2.55), and the  $v$  integral is given as

$$f(v) \otimes^v g(v) = \int_0^1 dv f(v) g(v). \quad (2.64)$$

TFFs are factorized into three parts, one being the standard hard-scale amplitude  $T$ , another being the soft-scale GPDs  $F$ , and the last one being the soft-scale distribution amplitude (DA)  $\phi(v)$ . The distribution amplitude describes the transition from vacuum to the final-state meson. The variable  $v$  is now the fraction of the longitudinal momentum of the meson. The distribution amplitude represents another soft-scale component of the process which we cannot access from first principles. The formal definition for TFFs and DAs will be given in later chapters.

Due to an intricate flavor structure of the final-state mesons, we can access several flavor combinations of GPDs through various DVMP measurements. We expect these GPDs to be universal for all DVCS and DVMP variations, as well as other processes that probe GPDs (or more precisely, their convolutions).

Other exclusive processes that probe GPDs are for example time-like Compton scattering (TCS) [39] and double DVCS (DDVCS) [40, 41, 42]. In TCS the incoming photon is real, and the outgoing photon is virtual. This process has a similar hard-scale amplitude as DVCS and its analysis could also offer a test for GPD universality. In DDVCS both the incoming and outgoing photons are virtual, so DVCS and TCS are limiting cases of this process. Aside from accessing different GPDs, these processes also offer access to different kinematic regions.

# Chapter 3

## Generalized parton distributions

We have so far given an overview of the experimental approach to studying the structure of nucleons. We have come across several soft-scale functions which describe the distribution of charge and momentum inside the nucleon. The first encounter with the properties of the proton was through form factors, but these do not probe the inner structure of the proton. The simplest description of the inner structure of the proton comes in the form of PDFs, which give us the distribution of the longitudinal momentum of the proton into its constituents. PDFs allow us to calculate structure functions, which give access to the 2D charge and magnetic momentum distributions of the proton. Ideally, we would want a full 3D picture of the proton, as well as how its spin and angular momentum are distributed among its constituents. One of the ways we can uncover this is through GPDs. Before we give the formal definition of GPDs and all of their relevant properties, we formalize the concept of factorization on the example of DIS, as well as explain the expansion in terms of powers of  $1/Q$ , called the *operator product expansion*.

### 3.1 Operator product expansion

A common mathematical structure in field theory is the product of operators that are spatially separated, which we have seen in the amplitudes of DIS and DVCS, where a product of two currents appears. This product is ill-defined as the separation between operators tends to zero. But there is a systematic way of writing such a product of operators as a series of local operators, where the coefficients of expansion depend on the distance between the operators and absorb all the singularities of the product. Useful references on this matter are [19, 43, 44, 45].

Say that we have two operators separated by a distance  $x$ . Their product can be written as

$$\mathcal{O}_1(z)\mathcal{O}_2(0) \rightarrow \sum_n C_{12}^n(z)\mathcal{O}_n(0), \quad (3.1)$$

where the coefficients  $C_{12}^n(z)$ , also called Wilson coefficients, are generally complex functions that satisfy renormalization group equations. This is called the *operator product expansion* (OPE) and it was originally proposed by Wilson [43].

We can apply OPE to the forward Compton tensor from DIS

$$T_{\mu\nu}(P, q) = i \int d^4z e^{iq \cdot z} \langle \mathbf{P} | T \{ j_\mu(z) j_\nu(0) \} | \mathbf{P} \rangle, \quad (3.2)$$

which contains a product of two currents with separation  $z$ . The OPE of the product of currents is given as

$$iT \{ j_\mu(z) j_\nu(0) \} = \sum_{\tau=2}^{\infty} \sum_{n=0}^{\infty} C_{\tau, n, \mu\nu}(z, \mu_F^2) z^{\mu_1} \dots z^{\mu_n} \mathcal{O}_{\mu_1 \dots \mu_n}^\tau(\mu_F^2), \quad (3.3)$$

where  $n$  is the spin of the local operator, and  $\mu_F^2$  is the renormalization scale. The Wilson coefficients scale as

$$C_{\tau, n}(z) \approx \left( \frac{1}{|z|} \right)^{d_{C_\tau}}, \quad (3.4)$$

where the scaling power is given as

$$d_{C_\tau} = n - d_{\mathcal{O}} + 2d_J = -\tau + 2d_J. \quad (3.5)$$

Here we denote  $d_J$  as the mass dimension of the current,  $d_{\mathcal{O}}$  as the mass dimension of the local operator, and  $\tau$  is the so-called *twist* of the local operator. Twist is given by the dimension of the local operator and its spin, and it governs the strength of the singularity of a term in OPE. The lower the twist, the larger the singularity, which allows us to categorize the operators in the expansion by the size of their contribution. We can also consider the expansion in terms of powers of  $1/Q^2$ . The higher the momentum transfer in the process, the larger the suppression of higher twist terms in the OPE.

We can now write the forward Compton tensor as

$$T_{\mu\nu}(P, q) = \sum_{\tau, n} \tilde{C}_{\tau, n}(Q^2, \mu_F^2) \tilde{\mathcal{O}}_{n\mu\nu}^\tau(\mu_F^2) \left( \frac{1}{x_B} \right)^n \left( \frac{1}{Q^2} \right)^{\tau/2-1}. \quad (3.6)$$

By writing the cross section in terms of structure functions, we can connect them to the OPE through the Compton tensor as

$$\int_{-1}^1 dx x^{n-1} F_1(x, Q^2) = \tilde{C}_{\tau=2, n}(Q^2, \mu_F^2) \tilde{\mathcal{O}}_n^{\tau=2}(\mu_F^2) + \mathcal{O}\left(\frac{1}{Q^4}\right), \quad (3.7)$$

where we only keep the leading twist. If we transform the previous expression to obtain the

structure function, and introduce

$$\int dy y^{n-1} f(y, \mu_F^2) = \tilde{O}_n^{\tau=2}(\mu_F^2), \quad (3.8)$$

$$\int dz z^{n-1} \sigma(z, Q^2, \mu_F^2) = \tilde{C}_{\tau,n}(Q^2, \mu_F^2), \quad (3.9)$$

we can write

$$F_1(x, Q^2) = \int_x^1 \frac{dy}{y} f(y, \mu_F^2) \sigma\left(\frac{x}{y}, Q^2, \mu_F^2\right). \quad (3.10)$$

Here we see that the Wilson coefficients give the hard-scale part of the process, i.e. the cross section that describes the photon-parton scattering, and that the local operators give the soft-scale part, which are PDFs in this case, denoted as  $f(y, \mu_F^2)$ . We can see that in general structure functions are convolutions of PDFs and the hard-scattering amplitude. Only at the leading order of perturbation theory, where we ignore interactions between partons, can we deconvolute expression (3.10).

OPE is useful because it naturally incorporates factorization at leading twist by connecting Wilson coefficients to the short range part of the process, which is perturbative, and the local operators to the long-range part, which are the PDFs and GPDs we are trying to uncover.

In our analysis of the three processes in this work, we only consider operators up to twist-2, which in both DVCS and DVMP includes four GPDs,  $H$ ,  $E$ ,  $\tilde{H}$  and  $\tilde{E}$ .

One more comment is in order. So far we have not discussed the fact that PDFs and GPDs, as well as the hard-scattering coefficients depend on several energy scales, and the one that is relevant to this discussion is the factorization scale  $\mu_F$ . Several times we have mentioned the factorization of the hard and soft part of a process, but it is not always clear where the cut-off between these two scales is. The factorization scale is somewhat arbitrary and therefore the structure function, which is an observable, should not depend on it. It can however make calculations easier if we chose a suitable factorization scale. This scale corresponds to the renormalization scale of the bilocal operator present in cross section calculations, in the sense that it represents the IR cut-off for the Wilson coefficients, and a UV cut-off for the distributions. It represents our ability to probe the structure of the proton because as it becomes higher, we can resolve more virtual partons that are then included in the distributions. We typically choose the renormalization scale to be close to the momentum transfer in the process, so that the logarithmic corrections, which will be of the form  $\ln(\mu_F^2/Q^2)^n$ , are not too large and do not cause problems in the resummation. These large logarithms would appear due to the mismatch of the scale at which the process is probed and the scale at which it is described.

## 3.2 Formal definition

In this section we list all GPD properties relevant for this study. Reviews on GPD properties are [46, 47].

In order to define GPDs, it is suitable to introduce light-cone coordinates. Using the standard spacetime coordinates  $z^\mu = (z^0, z^1, z^2, z^3)$  and the Minkowski metric signature  $(+, -, -, -)$ , we can define

$$z^\pm = \frac{1}{\sqrt{2}}(z^0 \pm z^3), \quad z_\perp^\mu = (0, z^1, z^2, 0). \quad (3.11)$$

We can then decompose any 4-vector as

$$z^\mu = z^+ n^\mu + z^- \tilde{n}^\mu + z_\perp^\mu, \quad (3.12)$$

where  $n$  and  $\tilde{n}$  are lightlike vectors which satisfy

$$n^2 = \tilde{n}^2 = 0, \quad n \cdot \tilde{n} = 1. \quad (3.13)$$

We saw that in the calculation of cross sections for the aforementioned processes we have bilocal operators, i.e. currents that flow from one spacetime point to another. At twist-2, the relevant bilocal operators are

$$\mathcal{O}^{qq}(z_1^-, z_2^-) = \bar{\Psi}(z_1^-) \gamma^+ \Psi(z_2^-), \quad (3.14)$$

$$\tilde{\mathcal{O}}^{qq}(z_1^-, z_2^-) = \bar{\Psi}(z_1^-) \gamma^+ \gamma^5 \Psi(z_2^-), \quad (3.15)$$

$$\mathcal{O}^{gg}(z_1^-, z_2^-) = F_a^{+\mu}(z_1^-) g_{\mu\nu} F_b^{\nu+}(z_2^-), \quad (3.16)$$

$$\tilde{\mathcal{O}}^{gg}(z_1^-, z_2^-) = F_a^{+\mu}(z_1^-) i\epsilon_{\mu\nu}^\perp F_a^{\nu+}(z_2^-), \quad (3.17)$$

where we introduced the transverse tensor

$$\epsilon_T^{\alpha\beta} = \epsilon^{\alpha\beta\gamma\delta} \tilde{n}_\gamma n_\delta, \quad (3.18)$$

whose nonvanishing components are  $\epsilon_T^{12} = -\epsilon_T^{21} = 1$ , with the convention  $\epsilon_{0123} = 1$ . The first two operators describe quark subprocesses, and the second two gluon subprocesses. The first and third operators are vector operators, and the second and last one are axial-vector operators. In order to ensure gauge invariance, bilocal operators should include a Wilson line, but we will mostly be working in the light-cone gauge, where the Wilson line is equal to unity.

We also introduce a basis for spinor bilinears

$$h^\mu, \quad e^\mu = \frac{t^{\nu\mu}\Delta_\nu}{M_{H_1} + M_{H_2}}, \quad \tilde{h}^\mu, \quad \tilde{e}^\mu = -\frac{\Delta^\mu \tilde{b}}{M_{H_1} + M_{H_2}}, \quad (3.19)$$

where

$$\begin{aligned} b &= \bar{U}(P_2) U(P_1), & \tilde{b} &= \bar{U}(P_2) \gamma^5 U(P_1), \\ h^\mu &= \bar{U}(P_2) \gamma^\mu U(P_1), & \tilde{h}^\mu &= \bar{U}(P_2) \gamma^\mu \gamma^5 U(P_1), \\ t^{\mu\nu} &= \bar{U}(P_2) i\sigma^{\mu\nu} U(P_1), & \tilde{t}^{\mu\nu} &= \bar{U}(P_2) i\sigma^{\mu\nu} \gamma^5 U(P_1). \end{aligned} \quad (3.20)$$

Capitalized  $U$  denotes the hadron spinor, and  $M_{H_{1,2}}$  denotes the mass of the incoming/outgoing hadron.

We can now finally define twist-2 GPDs [21] in the quark sector

$$\langle P_2 | \mathcal{O}^{qq}(-z^-, z^-) | P_1 \rangle = \int_{-1}^1 dx e^{-ixP^+z^-} [h^+ H^q(x, \xi, \Delta^2) + e^+ E^q(x, \xi, \Delta^2)], \quad (3.21)$$

$$\langle P_2 | \tilde{\mathcal{O}}^{qq}(-z^-, z^-) | P_1 \rangle = \int_{-1}^1 dx e^{-ixP^+z^-} [\tilde{h}^+ \tilde{H}^q(x, \xi, \Delta^2) + \tilde{e}^+ \tilde{E}^q(x, \xi, \Delta^2)], \quad (3.22)$$

and in the gluon sector

$$\langle P_2 | \mathcal{O}^{gg}(-z^-, z^-) | P_1 \rangle = \frac{1}{4} P^+ \int_{-1}^1 dx e^{-ixP^+z^-} [h^+ H^G(x, \xi, \Delta^2) + e^+ E^G(x, \xi, \Delta^2)], \quad (3.23)$$

$$\langle P_2 | \tilde{\mathcal{O}}^{gg}(-z^-, z^-) | P_1 \rangle = \frac{1}{4} P^+ \int_{-1}^1 dx e^{-ixP^+z^-} [\tilde{h}^+ \tilde{H}^G(x, \xi, \Delta^2) + \tilde{e}^+ \tilde{E}^G(x, \xi, \Delta^2)]. \quad (3.24)$$

It should be noted that these are not the only twist-2 GPDs that exist, but are the only ones that appear in DVCS and DVMP at the precision we will be studying them. All of the GPDs defined in (3.21-3.24) are chiral-even, meaning that they describe processes where the helicity of the struck parton does not change. There are also chiral-odd twist-2 GPDs, called transversity GPDs, but we will not discuss them here and the reader is referred to [48].

We can introduce a target-independent, boost invariant form of GPDs. In the parity-even sector we have

$$\langle P_2 | \mathcal{O}^{qq}(-z^-, z^-) | P_1 \rangle = P^+ \int_{-1}^1 dx e^{-ixP^+z^-} F^q(x, \xi, \Delta^2), \quad (3.25)$$

$$\langle P_2 | \mathcal{O}^{gg}(-z^-, z^-) | P_1 \rangle = \frac{1}{4} (P^+)^2 \int_{-1}^1 dx e^{-ixP^+z^-} F^g(x, \xi, \Delta^2), \quad (3.26)$$

where we introduce

$$F^A(x, \xi, \Delta^2) = \frac{h^+}{P^+} H^A(x, \xi, \Delta^2) + \frac{e^+}{P^+} E^A(x, \xi, \Delta^2), \quad A \in \{q, G\}. \quad (3.27)$$

and in the parity odd-sector

$$\langle P_2 | \tilde{\mathcal{O}}^{qq}(-z^-, z^-) | P_1 \rangle = P^+ \int_{-1}^1 dx e^{-ixP^+z} F^q(x, \xi, \Delta^2), \quad (3.28)$$

$$\langle P_2 | \tilde{\mathcal{O}}^{gg}(-z^-, z^-) | P_1 \rangle = \frac{1}{4} (P^+)^2 \int_{-1}^1 dx e^{-ixP^+z} F^g(x, \xi, \Delta^2), \quad (3.29)$$

where we similarly introduce

$$F^A(x, \xi, \Delta^2) = \frac{\tilde{h}^+}{P^+} \tilde{H}^A(x, \xi, \Delta^2) + \frac{\tilde{e}^+}{P^+} \tilde{E}^A(x, \xi, \Delta^2), \quad A \in \{q, G\}. \quad (3.30)$$

These GPDs can be written as Fourier transforms of matrix elements that describe the transition of the hadron from the initial state to the final state through the quark or gluon channels

$$F^q(x, \xi, \Delta^2) = \int \frac{dz^-}{2\pi} e^{ixP^+z^-} \langle P_2 | \mathcal{O}^{qq}(-z, z) | P_1 \rangle, \quad (3.31)$$

$$F^G(x, \xi, \Delta^2) = \frac{4}{P^+} \int \frac{dz^-}{2\pi} e^{ixP^+z^-} \langle P_2 | \mathcal{O}^{gg}(-z, z) | P_1 \rangle. \quad (3.32)$$

We can write analogous definitions for the parity-odd sector.

### 3.3 Partonic interpretation

We have seen in the previous chapter that GPDs appear in the description of the soft part of some exclusive processes, but we did not clarify how they actually describe the structure of the proton.

GPDs are functions of three variables, which we chose to be the Bjorken  $x$ , the skewness  $\xi$  and the Mandelstam variable  $\Delta^2 = t$ . In light-cone coordinates, we have

$$x = \frac{k_1^+ + k_2^+}{P^+} \quad (3.33)$$

$$\xi = -\frac{\Delta^+}{P^+}, \quad (3.34)$$

where  $k_{1,2}$  are the struck parton momenta before and after the scattering. In the frame where the hadron moves at near light-speed, its plus momentum component becomes very large and

proportional to the energy, whereas the minus component tends to zero. We therefore typically denote the plus component of the momentum as the forward or longitudinal, since it roughly coincides with the 3-momentum. This means that we can express the forward momenta of the struck parton as

$$k_{1,2}^+ = \frac{x \pm \xi}{2} P^+. \quad (3.35)$$

For DVCS and DVMP, the variable  $x$  takes values from  $-1$  to  $1$  in order to account for anti-quarks, for which  $x < 0$ . This means that GPDs are defined for  $(x, \xi) \in [-1, 1]^2$  [49]. Therefore, the forward momenta of the struck parton can be either positive or negative, and we generally recognize three regions:

- if  $x \geq |\xi|$ , then  $x \pm \xi$  are positive, which means that the struck parton is a quark;
- if  $x \leq -|\xi|$ , then  $x \pm \xi$  are negative, which means that the struck parton is an antiquark;
- if  $-|\xi| \leq x \leq |\xi|$ , then  $x + \xi$  is positive and  $x - \xi$  is negative, which means that the parton carrying the forward momentum  $x + \xi$  is a quark, and the parton carrying the forward momentum  $x - \xi$  is an antiquark, and this process can be interpreted as an emission of a quark-antiquark pair which annihilates into a photon or binds into a meson.

The first two regions are called DGLAP (Dokshitzer-Gribov-Lipatov-Altarelli-Parisi) regions [50, 51, 52, 53], and the last region is called the ERBL (Efremov-Radyushkin-Brodsky-Lepage) region [54, 55]. These regions are governed by different QCD evolution equations for GPDs. An example of these regions is given in figure 3.1 below.

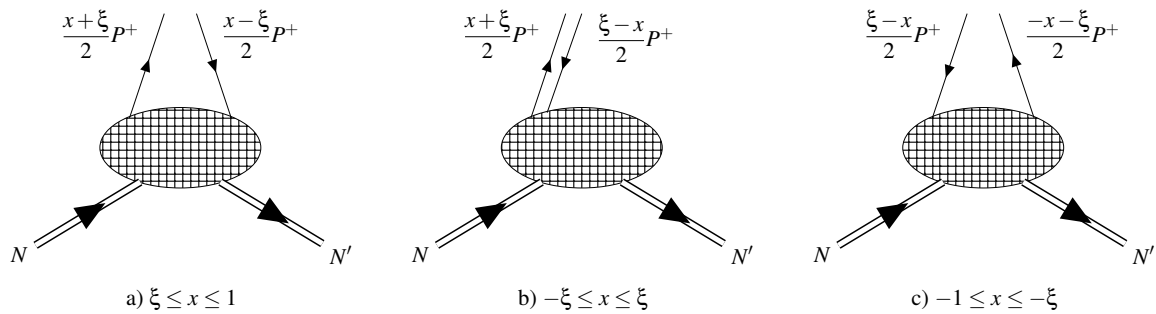


Figure 3.1: Partonic definition of GPDs for various values of  $x$  and  $\xi \geq 0$ . In a) the struck parton is a quark which is emitted and reabsorbed by the hadron. In b) a quark-antiquark pair are emitted. In c) the struck parton is an antiquark which is also emitted and reabsorbed by the hadron.

In the DGLAP region, GPDs are related to PDFs because they also depict a parton being struck by a virtual photon, the only difference being that this parton is reabsorbed by the hadron. There is no clear connection between GPDs and PDFs in the ERBL region.

Since the momenta of the struck parton and hadron before and after scattering are not the same, we cannot interpret GPDs as a probability distribution in the same way we can PDFs. GPDs represent the interference between amplitudes that describe different states of a nucleon, which is evident in the light-cone wave function representation of GPDs [56].

The point  $x = \pm\xi$ , called the *crossover line*, warrants special consideration. This is the point where the DGLAP and ERBL regions meet and where one of the partons, either in the initial or the final hadron, has vanishing plus-momentum. This offers a unique insight into partons with small momentum, which is different than the PDF description at small  $x$ . At LO in  $\alpha_S$ , imaginary parts of both DVCS and DVMP amplitudes probe GPDs at  $x = \pm\xi$ . Care must be taken that at such a configuration the factorization theorems still hold, for which purpose we need continuous GPDs. It was shown in [24] that GPDs can be decomposed into a part that is analytic at  $x = \pm\xi$ , and a part that is not analytic, but zero at  $x = \pm\xi$ . There has been some studies that have found discontinuous first derivatives of GPDs, such as [57].

## 3.4 Basic properties

### 3.4.1 Symmetry properties

In this section we discuss symmetry properties in the  $x$  and  $\xi$  variables.

Since  $x < 0$  is introduced to incorporate antiparticle partons, and since gluons are their own antiparticles, we expect  $H^G$  and  $E^G$  to be even in  $x$ , and  $\tilde{H}^G$  and  $\tilde{E}^G$  to be odd in  $x$ .

We cannot say the same for quarks, so we introduce charge even and odd functions

$$F^{q(\pm)}(x, \xi, \Delta^2) \equiv F^q(x, \xi, \Delta^2) \mp F^q(-x, \xi, \Delta^2), \quad F \in \{H, E\}, \quad (3.36)$$

$$F^{q(\pm)}(x, \xi, \Delta^2) \equiv F^q(x, \xi, \Delta^2) \pm F^q(-x, \xi, \Delta^2), \quad F \in \{\tilde{H}, \tilde{E}\}, \quad (3.37)$$

which satisfy

$$F^{q(\pm)}(-x, \xi, \Delta^2) = \mp F^{q(+)}(x, \xi, \Delta^2), \quad F \in \{H, E\}, \quad (3.38)$$

$$F^{q(\pm)}(-x, \xi, \Delta^2) = \pm F^{q(+)}(x, \xi, \Delta^2), \quad F \in \{\tilde{H}, \tilde{E}\}. \quad (3.39)$$

The charge-even GPDs correspond to an exchange of charge conjugation  $C = +1$  in the  $t$ -channel, and are sometimes referred to as singlet combinations. These GPDs appear in DVCS

and vector meson DVMP. The charge-odd GPDs correspond to an exchange of charge conjugation  $C = -1$  in the  $t$ -channel, and are sometimes referred to as non-singlet or valence combinations. They appear in the production of pseudoscalar mesons.

Since GPDs are defined through matrix elements that describe the transition from the initial to a final hadron state, they should be time-reversal invariant and hermitic. Time reversal gives

$$F^A(x, -\xi, t) = F^A(x, \xi, t), \quad A \in \{q, G\}, F \in \{H, E, \tilde{H}, \tilde{E}\}, \quad (3.40)$$

and hermiticity gives

$$[F^A(x, -\xi, t)]^* = F^A(x, \xi, t), \quad A \in \{q, G\}, F \in \{H, E, \tilde{H}, \tilde{E}\}. \quad (3.41)$$

These two properties imply that all GPDs should be real-valued functions. Skewness symmetry can be explained by noting that time reversal exchanges the initial and final states, which changes the sign of the skewness because it changes the sign of the vector  $\Delta$ .

### 3.4.2 Forward limit

In the case where  $P_1 = P_2$ , we have  $t = 0$  and  $\xi = 0$ , which is called the forward limit. In this limit, GPDs reduce to PDFs. Formally, only GPDs  $H$  and  $\tilde{H}$  survive in this limit, because  $E$  and  $\tilde{E}$  are multiplied by  $\Delta$  in their definition. This means that these two types of GPDs cannot be accessed in processes where the cross section is calculated utilizing the optical theorem, only from processes where there is a momentum transfer onto the target, i.e. where  $\Delta \neq 0$ .

We have for the quark sector

$$H^q(x, \xi = 0, \Delta^2 = 0) = f^q(x) = q(x)\theta(x) - \bar{q}(-x)\theta(-x), \quad (3.42)$$

$$\tilde{H}^q(x, \xi = 0, \Delta^2 = 0) = \Delta f^q(x) = \Delta q(x)\theta(x) + \Delta \bar{q}(-x)\theta(-x), \quad (3.43)$$

where  $\Delta f$  denotes polarized PDFs. For example, polarized quark distributions are defined as

$$\Delta q(x) = q^\uparrow(x) - q^\downarrow(x), \quad (3.44)$$

which represents the difference between quarks whose helicity is parallel to that of the nucleon, and quarks whose helicity is anti-parallel to that of the nucleon.

For gluon GPDs we have in the forward limit

$$H^G(x, \xi = 0, \Delta^2 = 0) = f^G(x) = xg(x)\theta(x) - xg(-x)\theta(-x), \quad (3.45)$$

$$\tilde{H}^G(x, \xi = 0, \Delta^2 = 0) = \Delta f^G(x) = x\Delta g(x)\theta(x) + x\Delta g(-x)\theta(-x). \quad (3.46)$$

Gluon PDFs inherit the  $x$  symmetry from gluon GPDs. Quark PDFs, like their corresponding GPDs, do not have definite parity so we define

$$H^{q(\pm)}(x, 0, 0) = f^{q(\pm)}(x) = f^q(x) \mp f^q(-x), \quad f^{q(\pm)}(-x) = \mp f^{q(\pm)}(x), \quad (3.47)$$

$$\tilde{H}^{q(\pm)}(x, 0, 0) = \Delta f^{q(\pm)}(x) = \Delta f^q(x) \pm \Delta f^q(-x), \quad \Delta f^{q(\pm)}(-x) = \pm \Delta f^{q(\pm)}(x). \quad (3.48)$$

Another useful decomposition is into the valence and sea quark contributions. This is more intuitively done in the case of PDFs, which then easily generalize for GPDs. We have

$$f^q(x) = f_{\text{val}}^q(x) + f_{\text{sea}}^q(x), \quad \Delta f^q(x) = \Delta f_{\text{val}}^q(x) + \Delta f_{\text{sea}}^q(x), \quad (3.49)$$

where the valence and sea quark contributions are defined as

$$f_{\text{val}}^q(x) = [q(x) - \bar{q}(x)]\theta(x), \quad \Delta f_{\text{val}}^q(x) = [\Delta q(x) - \Delta \bar{q}(x)]\theta(x), \quad (3.50)$$

$$f_{\text{sea}}^q(x) = \bar{q}(x)\theta(x) - \bar{q}(-x)\theta(-x), \quad \Delta f_{\text{sea}}^q(x) = \Delta \bar{q}(x)\theta(x) + \Delta \bar{q}(-x)\theta(-x). \quad (3.51)$$

Since all of the sea quarks are created in quark-antiquark pairs, the difference between the total quark and antiquark distributions cancels out all sea quarks, if we assume that  $q_{\text{sea}} = \bar{q}_{\text{sea}}$ . All antiquarks in nucleons are from the sea, so we can use them to define the distribution for sea quarks  $x > 0$  or antiquarks  $x < 0$ . In the context of charge definite PDFs, we can write

$$f^{q(+)}(x) = f_{\text{val}}^q(x) + 2f_{\text{sea}}^q(x), \quad \Delta f^{q(+)}(x) = \Delta f_{\text{val}}^q(x) + 2\Delta f_{\text{sea}}^q(x), \quad (3.52)$$

$$f^{q(-)}(x) = f_{\text{val}}^q(x), \quad \Delta f^{q(-)}(x) = \Delta f_{\text{val}}^q(x). \quad (3.53)$$

This is why we said that the charge odd distribution is called the valence distribution.

### 3.4.3 Link to elastic form factors

We have given the definition of elastic form factors in (2.4). We can define EFFs for each quark flavor as

$$\langle p_2 | \bar{\psi}^q(z) \gamma^\mu \psi^q(z) | p_1 \rangle = \bar{U}(P_2) \left[ F_1^q(t) \gamma^\mu + F_2^q(t) \frac{i\sigma^{\mu\nu} \Delta_\nu}{2M} \right] U(P_1), \quad (3.54)$$

where the Pauli and Dirac form factors  $F_1(t)$  and  $F_2(t)$  are given as

$$F_1(t) = \sum_q e_q F_1^q(t), \quad F_2(t) = \sum_q e_q F_2^q(t). \quad (3.55)$$

In order to connect the EFFs to GPDs, we start from the definition of GPDs (3.31), and integrate it over  $x$

$$\begin{aligned} & \int_{-\infty}^{\infty} dx \frac{1}{P^+} \bar{U}(P_2) \left( H^q(x, \xi, \Delta^2) \gamma^+ + \frac{e^+}{P^+} E^q(x, \xi, \Delta^2) \frac{i\sigma^{+\mu} \Delta_\mu}{2M} \right) U(P_1) \\ &= \int_{-\infty}^{\infty} dx \int \frac{dz^-}{2\pi} e^{ixP^+z^-} \langle P_2 | \bar{\psi}(-z) \gamma^+ \psi(z) | P_1 \rangle \\ &= \int \frac{dz^-}{2\pi} \underbrace{\left( \int_{-\infty}^{\infty} dx e^{ixP^+z^-} \right)}_{2\pi\delta(P^+z^-)} \langle P_2 | \bar{\psi}(-z) \gamma^+ \psi(z) | P_1 \rangle \\ &= \int \frac{dz^-}{2\pi} \frac{2\pi}{P^+} \delta(z^-) \langle P_2 | \bar{\psi}(-z) \gamma^+ \psi(z) | P_1 \rangle \\ &= \frac{1}{P^+} \langle P_2 | \bar{\psi}(0) \gamma^+ \psi(0) | P_1 \rangle. \end{aligned} \quad (3.56)$$

We used the definition of the Dirac delta distribution  $\delta$ , as well as the fact that GPDs are only non-zero for  $|x| \leq 1$ , so we can integrate over  $x \in \mathbb{R}$ . We have also implicitly assumed that  $P^+$  is positive, which is always the case for on-shell particles. We have obtained a local operator on the RHS, like in the definition of EFFs, so we can make the identification

$$\int_{-1}^1 dx H^q(x, \xi, t) = F_1^q(t), \quad \int_{-1}^1 dx E^q(x, \xi, t) = F_2^q(t). \quad (3.57)$$

The previous result is  $\xi$  independent, which is due to Lorentz invariance. Integration over  $x$  removes any dependence on the light-cone direction in which the hadron is moving, and this direction defines  $\xi$ .

### 3.4.4 Domain and positivity bounds

The variables  $x$  and  $\xi$  both have the support  $[-1, 1]$ . But since  $\xi$  is connected to  $\Delta$ , the specific kinematics of a process limit the value of  $\xi$ . Skewness is bound by the value of  $t$  as

$$|\xi| \leq \frac{\sqrt{-t}}{\sqrt{-t} + 4M^2}. \quad (3.58)$$

As we will see in further chapters, GPDs are connected to PDFs, and this connection sets an upper bound on GPDs, which stems from the norm on the Hilbert space because we expect some sort of probabilistic behavior. Without going into detail, we quote the bound for parity even quark GPDs from [58]

$$\left| \sqrt{1-\xi^2} \left( H^q - \frac{\xi^2}{1-\xi^2} E^q \right) \right| \leq \frac{1}{2} \left( \sqrt{(q+\Delta q)_{\text{in}} (q+\Delta q)_{\text{out}}} + \sqrt{(q-\Delta q)_{\text{in}} (q-\Delta q)_{\text{out}}} \right), \quad (3.59)$$

$$\left| \frac{\sqrt{t_0-t}}{2m} E^q \right| \leq \frac{1}{2} \left( \sqrt{(q+\Delta q)_{\text{in}} (q-\Delta q)_{\text{out}}} + \sqrt{(q-\Delta q)_{\text{in}} (q+\Delta q)_{\text{out}}} \right), \quad (3.60)$$

where we used the notation  $(q+\Delta q)_{\text{in}} = q(x_{\text{in}}) + \Delta q(x_{\text{in}})$  and

$$x^{\text{in}} = \frac{x+\xi}{1+\xi}, \quad (3.61)$$

$$x^{\text{out}} = \frac{x-\xi}{1-\xi}. \quad (3.62)$$

Here the maximum value of  $t$  at a given  $\xi$  is defined as

$$t_0 = -\frac{4\xi^2 m^2}{1-\xi^2}. \quad (3.63)$$

### 3.4.5 Distribution amplitudes

Distribution amplitudes (DAs) describe the transition from vacuum to a hadron and vice versa. If we set either the initial or the final momentum in GPDs to zero, we obtain DAs [59]

$$\langle P | \bar{\psi}(z_1^-) \gamma^+ \psi(z_2^-) | 0 \rangle = -iP^+ f_M \int_0^1 dv e^{iP^+(vz_1^- + \bar{v}z_2^-)} \phi(v). \quad (3.64)$$

Since we will be dealing with vector mesons, their DAs are given as

$$P^+ f_{\rho^+} \int_0^1 dv e^{iP \cdot (vz_1^- + \bar{v}z_2^-)} \Phi_{\rho^+}(v) = \langle \rho_L^+(P) | \bar{u}(z_1^-) \gamma^+ d(z_2^-) | 0 \rangle, \quad (3.65)$$

$$P^+ f_{\rho^0} \int_0^1 dv e^{iP \cdot (vz_1^- + \bar{v}z_2^-)} \Phi_{\rho^0}(v) = \left\langle \rho_L^0(P) \left| \frac{1}{\sqrt{2}} [\bar{u}(z_1^-) \gamma^+ u(z_2^-) - \bar{d}(z_1^-) \gamma^+ d(z_2^-)] \right| 0 \right\rangle, \quad (3.66)$$

$$P^+ f_{\omega^0} \int_0^1 dv e^{iP \cdot (vz_1^- + \bar{v}z_2^-)} \Phi_{\omega^0}(v) = \left\langle \omega_L^0(P) \left| \frac{1}{\sqrt{2}} [\bar{u}(z_1^-) \gamma^+ u(z_2^-) + \bar{d}(z_1^-) \gamma^+ d(z_2^-)] \right| 0 \right\rangle, \quad (3.67)$$

$$P^+ f_{\phi} \int_0^1 dv e^{iP \cdot (vz_1^- + \bar{v}z_2^-)} \Phi_{\phi}(v) = \langle \phi_L(P) | \bar{s}(z_1^-) \gamma^+ s(z_2^-) | 0 \rangle. \quad (3.68)$$

The evolution of DAs is given by the same ERBL evolution equations of GPDs.

### 3.4.6 Polynomiality

In this part we are interested in the polynomiality of GPDs in the skewness parameter  $\xi$ . We will study the operators that enter at the twist-2 level, as well as the Mellin moment of GPDs. Mellin moments are generally defined as

$$F_j = \int_{-1}^1 dx x^j F(x). \quad (3.69)$$

We have seen an example of this with EFFs, which are given as first moments of GPDs.

We start with writing the bi-local operators that appear in the definitions of GPDs in terms of OPE

$$\mathcal{O}_q^{\mu\mu_1 \dots \mu_n} = \mathbf{S} \bar{q} \gamma^\mu i \overleftrightarrow{D}^{\mu_1} \dots i \overleftrightarrow{D}^{\mu_n} q, \quad (3.70)$$

$$\tilde{\mathcal{O}}_q^{\mu\mu_1 \dots \mu_n} = \mathbf{S} \bar{q} \gamma^\mu \gamma_5 i \overleftrightarrow{D}^{\mu_1} \dots i \overleftrightarrow{D}^{\mu_n} q, \quad (3.71)$$

$$\mathcal{O}_G^{\mu\mu_1 \dots \mu_n \nu} = \mathbf{S} F^{\mu\alpha} i \overleftrightarrow{D}^{\mu_1} \dots i \overleftrightarrow{D}^{\mu_n} F_\alpha^\nu, \quad (3.72)$$

$$\tilde{\mathcal{O}}_G^{\mu\mu_1 \dots \mu_n \nu} = \mathbf{S} (-i) F^{\mu\alpha} i \overleftrightarrow{D}^{\mu_1} \dots i \overleftrightarrow{D}^{\mu_n} \tilde{F}_\alpha^\nu, \quad (3.73)$$

where  $\mathbf{S}$  denotes the symmetrization of all Lorentz indices and subtraction of trace terms. The covariant left-right derivative is defined as  $\overleftrightarrow{D} = \overrightarrow{D} - \overleftarrow{D}$ . To see how this is connected to the Mellin moments of GPDs, we perform a similar calculation as with the connection between GPDs and

EFFs, we just multiply the GPDs with  $x^n$  and then take the integral over  $x$

$$\begin{aligned}
& \int_{-\infty}^{\infty} dx x^n \bar{U}(P_2) \left( H^q(x, \xi, \Delta^2) \gamma^+ + \frac{e^+}{P^+} E^q(x, \xi, \Delta^2) \frac{i\sigma^{+\mu} \Delta_\mu}{2M} \right) U(P_1) \\
&= (P^+)^{n+1} \int_{-\infty}^{\infty} dx x^n \int \frac{dz^-}{2\pi} e^{ixP^+z^-} \langle P_2 | \bar{\Psi}(-z) \gamma^+ \Psi(z) | P_1 \rangle \\
&= P^+ \int \frac{dz^-}{2\pi} \int_{-\infty}^{\infty} dx \left( i \frac{d}{dz^-} \right)^n e^{ixP^+z^-} \langle P_2 | \bar{\Psi}(-z) \gamma^+ \Psi(z) | P_1 \rangle \\
&= \left\langle P_2 \left| \bar{\Psi}(0) \gamma^+ \left( i \overset{\leftrightarrow}{\partial}^+ \right)^n \Psi(0) \right| P_1 \right\rangle. \tag{3.74}
\end{aligned}$$

Since we are working in the light-cone gauge and there is no Wilson line, we obtained a regular derivative in the previous expression. For a regular gauge, we need to replace the partial derivative with a covariant derivative.

The matrix element of the quark parity-even twist-2 operators can be written in terms of form factors

$$\begin{aligned}
\langle P_2 | \mathcal{O}_q^{\mu\mu_1 \dots \mu_n}(0) | P_1 \rangle &= \mathbf{S} \bar{U}(P_2) \gamma^\mu U(P_1) \sum_{\substack{i=0 \\ \text{even}}}^n A_{n+1,i}^q(t) \Delta^{\mu_1} \dots \Delta^{\mu_i} P^{\mu_{i+1}} \dots P^{\mu_n} \\
&+ \mathbf{S} \bar{U}(P_2) \frac{i\sigma^{\mu\alpha} \Delta_\alpha}{2M} U(P_1) \sum_{\substack{i=0 \\ \text{even}}}^n B_{n+1,i}^q(t) \Delta^{\mu_1} \dots \Delta^{\mu_i} P^{\mu_{i+1}} \dots P^{\mu_n} \\
&+ \mathbf{S} \frac{\Delta^\mu}{M} \bar{U}(P_2) U(P_1) \text{mod}(n, 2) C_{n+1}^q(t) \Delta^{\mu_1} \dots \Delta^{\mu_n}, \tag{3.75}
\end{aligned}$$

where  $\text{mod}(n, 2)$  is 1 for odd  $n$  and zero for even  $n$ . This was originally proposed in [60], but we use the conventions from [46]. The last term can be written in terms of bilinears that enter the definition of GPDs using Gordon's identity. We connect these form factors to Mellin momenta of GPDs as

$$\int_{-1}^{+1} dx x^n H^q(x, \xi, t) = \sum_{i=0, \text{even}}^n \xi^i A_{n+1,i}^q(t) + \text{mod}(n, 2) \xi^{n+1} C_{n+1}^q(t), \tag{3.76}$$

$$\int_{-1}^{+1} dx x^n E^q(x, \xi, t) = \sum_{i=0, \text{even}}^n \xi^i B_{n+1,i}^q(t) - \text{mod}(n, 2) \xi^{n+1} C_{n+1}^q(t). \tag{3.77}$$

We can see that the  $n$ -th momentum of quark GPDs is given as a polynomial in  $\xi$  of order  $n+1$  if  $n$  is odd, or order  $n$  if  $n$  is even. A similar definition can be written for gluon GPDs, with the only difference being in the fact that the  $n-1$  momentum is a polynomial in  $\xi$  of order  $n+1$ . This is again a consequence of Lorentz invariance. We can perform a similar decomposition for

gluon GPDs and all parity-odd GPDs. This shows that the  $n - 1$  gluon moment is the same as the  $n$ -th quark moment, which means that quark and gluon operators mix under evolution.

Expressions for the other twist-2 GPDs can be obtained analogously, and can be found in [46, 47].

### 3.5 Energy-momentum tensor

A remarkable feature of GPDs is that they are directly connected to the QCD energy-momentum tensor (EMT). In order to see this, we can observe the quark contribution to the Belinfante EMT

$$T_q^{\mu\nu} = \bar{q}\gamma^{(\mu}i\overleftrightarrow{D}^{\nu)}q. \quad (3.78)$$

Here  $t^{(\mu\nu)} = (t^{\mu\nu} + t^{\nu\mu})/2$  denotes symmetrization of tensors. This expression is the leading-twist operator in the non-local matrix element, as seen in (3.70). It can be shown [61, 62, 63] that the EMT can be decomposed using the same form factors as the ones that enter the Mellin moments of GPDs

$$\begin{aligned} \langle P_2 | T_a^{\mu\nu}(0) | P_1 \rangle = & \bar{U}(P_2) \left\{ \frac{P^\mu P^\nu}{M} A^a(t) + \frac{\Delta^\mu \Delta^\nu - \xi^{\mu\nu} \Delta^2}{M} C^a(t) + M \xi^{\mu\nu} \bar{C}^a(t) \right. \\ & \left. + \frac{P^{[\mu} i \sigma^{\nu]\rho} \Delta_\rho}{2M} [A^a(t) + B^a(t)] + \frac{P^{[\mu} i \sigma^{\nu]\rho} \Delta_\rho}{2M} D_{GFF}^a(t) \right\} U(P_1), \quad a \in \{q, G\}, \end{aligned} \quad (3.79)$$

where  $t^{[\mu\nu]} = (t^{\mu\nu} - t^{\nu\mu})/2$  denotes antisymmetrization of tensors. Here  $A$ ,  $B$  and  $C$  coincide with the form factors  $A_{2,0}$ ,  $B_{2,0}$  and  $C_2$  given in (3.76) and (3.77). These form factors are called *gravitational form factors* (GFFs) and they are given in terms of moments of GPDs as [47]

$$\int_{-1}^1 dx x H^q(x, \xi, t) = A^q(t) + \xi^2 C^q(t), \quad (3.80)$$

$$\int_{-1}^1 dx x E^q(x, \xi, t) = B^q(t) - \xi^2 C^q(t), \quad (3.81)$$

$$\sum_q \int_{-1}^1 dx \tilde{H}^q(x, \xi, t) = - \sum_q D_{GFF}^q(t), \quad (3.82)$$

$$\int_{-1}^1 dx H^G(x, \xi, t) = A^G(t) + 4\xi^2 C^G(t), \quad (3.83)$$

$$\int_{-1}^1 dx E^G(x, \xi, t) = B^G(t) - 4\xi^2 C^G(t), \quad (3.84)$$

$$D_{GFF}^G(t) = 0. \quad (3.85)$$

We cannot access  $\bar{C}$  in terms of twist-2 GPDs [62, 64, 65].

### 3.5.1 Sum rules and the spin puzzle

Sum rules refer to various integrals of distributions which can give us additional insight into their properties. We can intuitively understand sum rules for PDFs, since we understand them as number densities for partons inside the nucleon. We know that the proton has 2 up valence quarks and one down, so the sum rules for valence PDFs give

$$\int_0^1 dx u_{\text{val}}^p(x) = 2, \quad \int_0^1 dx d_{\text{val}}^p(x) = 1. \quad (3.86)$$

Structure functions also satisfy certain sum rules, which experimentally showed that only 20% of the spin of the proton comes from quark spin. PDFs and structure functions cannot tell us how the spin is distributed among the spins and orbital angular momenta of its constituents, which motivates us to study more complex distributions, such as GPDs.

Another sum rule is the statement that all fractions of momenta of all partons inside the nucleon have to add up to one

$$1 = \sum_{a=q,\bar{q},G} \int_0^1 dx x a(x). \quad (3.87)$$

If we observe the highest contribution in terms of the power of  $\xi$  in the Mellin moments of GPDs  $H$  and  $E$ , we can see that they are the same up to a sign. Therefore, the sum of  $n$ -th moments of these two GPDs is a polynomial of degree  $n$ . The addition of their second moments gives

$$A^q(t) + B^q(t) = \int_{-1}^1 dx x [H^q(x, \xi, t) + E^q(x, \xi, t)], \quad (3.88)$$

$$A^G(t) + B^G(t) = \int_0^1 dx [H^G(x, \xi, t) + E^G(x, \xi, t)] \quad (3.89)$$

The reason we observe this is because we can connect these moments with the spin of the nucleon.

The angular momentum density operator can be written in terms of the EMT as

$$M^{\alpha\mu\nu} = T^{\alpha\nu} x^\mu - T^{\alpha\mu} x^\nu, \quad (3.90)$$

where the angular momentum operator in the  $z$  direction is given as

$$\int d^3x M^{012}(x). \quad (3.91)$$

Given that the angular momentum can be expressed through the EMT, which in turn is connected to Mellin moments of GPDs, we can connect GPDs to the spin of the nucleon through *Ji's sum rule* [66]

$$\langle J_3^q \rangle = \frac{1}{2} [A^q(0) + B^q(0)], \quad \langle J_3^G \rangle = \frac{1}{2} [A^G(0) + B^G(0)]. \quad (3.92)$$

This sum rule is similar to the sum rule for PDFs (3.87). The decomposition between quark and gluon spin and orbital angular momentum is renormalization scale and scheme dependent. Different decompositions have been proposed by Ji, as well as Jaffe and Manohar in collaboration [67, 68, 60].

### 3.5.2 Hadron tomography

Due to the off-forward nature of processes which feature GPDs, we cannot interpret GPDs as probability distributions in the same way we can interpret PDFs. But there is a way to obtain a probabilistic representation in the case where  $\xi = 0$ . If skewness is zero, then  $t = -\Delta_\perp^2$ . If we perform a Fourier transform with respect to  $\Delta_\perp$ , we obtain the so-called impact parameter distribution (IPD) [69, 70]

$$q(x, \mathbf{b}_\perp) = \int \frac{d^2\Delta_\perp}{(2\pi)^2} e^{-i\mathbf{b}_\perp \cdot \Delta_\perp} H^q(x, 0, t = -\Delta_\perp^2), \quad (3.93)$$

where  $\mathbf{b}_\perp$  is the impact parameter and is the Fourier conjugate variable to  $\Delta_\perp$ . Since  $\xi = 0$ , the IPD can be interpreted as the number density of quarks of any helicity with a longitudinal momentum fraction  $x$  and the transverse distance  $\mathbf{b}_\perp$  from the center of plus-momentum of the hadron. This means that GPDs allow for a 3D picture of the hadron in a hybrid space, one component being the longitudinal momentum and the other two being the position in the plane transversal to the direction of motion of the hadron. These distributions can be difficult to access from experiments because we cannot access a large range of  $|t|$  values, since for higher values of  $|t|$  in comparison to  $Q^2$ , the twist-2 approximation tends to fall apart.

### 3.5.3 Evolution of GPDs

As we have mentioned in our discussion of PDFs, they depend on the momentum transfer that the virtual photon carries, which is a reflection of the fact that our ability to probe the structure of a hadron depends on the wavefunction of our probe. The higher the energy of the virtual photon, the higher the resolution, which means that at some point the hadron stops looking like a collection of valence quarks. Instead, we start to see more and more processes that occur between the valence quarks, such as emission of gluons, which then in turn radiate additional gluons or quark-antiquark pairs. This results in a sea of quarks, antiquarks and gluons inside a hadron. Luckily, we know how this dependence on the momentum transfer behaves through evolution equations, which we are able to calculate perturbatively.

We can take again the example of PDFs. At leading order, we can have a struck quark that emits a gluon, a struck gluon that emits a quark-antiquark pair, or a struck gluon that splits into two gluons. Then we can write the DGLAP evolution equations for PDFs

$$\frac{d}{d \ln \mu^2} g(x, \mu^2) = \frac{\alpha_S(\mu^2)}{2\pi} \int_x^1 \frac{dz}{z} \left\{ P_{g \leftarrow q}(z) \sum_q \left[ q\left(\frac{x}{z}, \mu^2\right) + \bar{q}\left(\frac{x}{z}, \mu^2\right) \right] \right. \quad (3.94)$$

$$\left. + P_{g \leftarrow g}(z) g\left(\frac{x}{z}, \mu^2\right) \right\}, \quad (3.95)$$

$$\frac{d}{d \ln \mu^2} q(x, \mu^2) = \frac{\alpha_S(\mu^2)}{2\pi} \int_x^1 \frac{dz}{z} \left\{ P_{q \leftarrow q}(z) q\left(\frac{x}{z}, \mu^2\right) + P_{q \leftarrow g}(z) g\left(\frac{x}{z}, \mu^2\right) \right\}, \quad (3.96)$$

$$\frac{d}{d \ln \mu^2} \bar{q}(x, \mu^2) = \frac{\alpha_S(\mu^2)}{2\pi} \int_x^1 \frac{dz}{z} \left\{ P_{\bar{q} \leftarrow q}(z) \bar{q}\left(\frac{x}{z}, \mu^2\right) + P_{\bar{q} \leftarrow g}(z) g\left(\frac{x}{z}, \mu^2\right) \right\}. \quad (3.97)$$

Here the functions  $P$  are the splitting functions and they represent the probability that a parton would emit another parton. They are labeled so that  $P_{f \leftarrow i}$  describes a parton  $i$  which emits a parton  $f$ .

For GPDs, we can generalize these evolution equations to obtain at LO

$$\frac{1}{x^{p_a}} \frac{\partial H^a(x, \xi, t, \mu^2)}{\partial \log(\mu^2)} = \alpha_S(\mu^2) \sum_{b \in \{q, G\}} \int_x^1 \frac{dz}{\xi} K^{ab, (0)}\left(\frac{z}{\xi}, \frac{\xi}{x}\right) \frac{H^b(z, \xi, t, \mu^2)}{z^{p_b}}, \quad a \in \{q, G\}, \quad (3.98)$$

where  $p_q = 0$  and  $p_G = 1$ . We can see that, just like for PDFs, there is a case of mixing of different parton GPDs in the evolution equations. In the limit  $\xi = 0$  the equation (3.98) reduces to the DGLAP evolution equations of PDFs, whereas in the limit  $\xi \rightarrow 1$  it reduces to ERBL evolution equations.

In order to avoid this, we introduce the evolution basis as irreducible multiplets of  $SU(N_f)$

group, where  $N_f$  is the number of flavors we take into consideration, which is four in our case. This basis consists of flavor non-singlet multiplets ( $F^3, F^8, \dots, F^{N_f-1}$ ), and a flavor singlet multiplet  $F^0$ . These are connected to the quark GPDs as

$$F^0 = F^u + F^d + F^s + F^c, \quad (3.99)$$

$$F^3 = F^u - F^d, \quad (3.100)$$

$$F^8 = F^u + F^d - 2F^s, \quad (3.101)$$

$$F^{15} = F^u + F^d + F^s - 3F^c. \quad (3.102)$$

An arbitrary GPD can be decomposed into these two bases as

$$F = \hat{c}^u F^u + \hat{c}^d F^d + \hat{c}^s F^s + \hat{c}^c F^c \quad (3.103)$$

$$= \hat{c}^0 F^0 + \hat{c}^3 F^3 + \hat{c}^8 F^8 + \hat{c}^{15} F^{15}, \quad (3.104)$$

where the coefficients are connected as

$$\hat{c}^0 = \frac{1}{4} (\hat{c}^u + \hat{c}^d + \hat{c}^s + \hat{c}^c), \quad (3.105)$$

$$\hat{c}^3 = \frac{1}{2} (\hat{c}^u - \hat{c}^d), \quad (3.106)$$

$$\hat{c}^8 = \frac{1}{6} (\hat{c}^u + \hat{c}^d - 2\hat{c}^s), \quad (3.107)$$

$$\hat{c}^{15} = \frac{1}{12} (\hat{c}^u + \hat{c}^d + \hat{c}^s - 3\hat{c}^c). \quad (3.108)$$

This decomposition is the same for charge even and charge odd combinations of GPDs. When we introduced charge even and odd GPDs in chapter (3.4.1), we referred to them as non-singlet and singlet combinations. We can shed light onto this by connecting the evolution basis to the partonic basis, which we can write as a vector

$$\begin{pmatrix} F^{u_{\text{val}}} & F^{d_{\text{val}}} & F^{\text{sea}} & F^{\text{G}} \end{pmatrix}. \quad (3.109)$$

We expect the sea quark and anti-quark contributions to be the same for each flavor, and we only consider DVCS and DVMP off a proton or neutron, so we only need up and down valence contributions. The charge-positive singlet GPD is defined as

$$F^{0(+)} = \sum_q F^{q(+)} = F^{u_{\text{val}}} + F^{d_{\text{val}}} + F^{\text{sea}}. \quad (3.110)$$

This component together with the gluon GPD forms a singlet GPD vector

$$\mathbf{F}^\Sigma = \begin{pmatrix} F^{0(+)} \\ F^G \end{pmatrix}. \quad (3.111)$$

The charge-odd component does not have sea quark contributions, so we can write it as

$$F^{q^{(-)}} = F^{q_{\text{val}}}, \quad (3.112)$$

and it does not mix with gluon GPDs, since gluons are charge even.

It is worth noting that any dependence on the renormalization/factorization scale  $\mu$  should cancel between the hard-scattering amplitudes and GPDs, since their convolutions make up physical observables that cannot depend on any arbitrary scales. Evolution equations for PDFs and GPDs can be understood as renormalization group equations for the corresponding light-cone operators.

### 3.5.4 Other parton distributions

The goal of studying various parton distributions is to gain insight into the phase space of the quarks and gluons inside hadrons. The study of the proton started with elastic scattering and finding its total charge. But to uncover its internal structure, the first step was in the form of PDFs, which allow us to calculate structure functions and two-dimensional charge and magnetic momentum distributions. The next functions that we studied are the GPDs, which depend on three variables, and reduce to PDFs when  $\Delta = 0$  or form factors when integrated over  $x$ . By Fourier transforming GPDs with respect to  $\Delta_\perp$ , we obtain impact parameter distributions, which give the probability of finding a parton with longitudinal momentum fraction  $x$  and distance from the center of plus-momentum  $\mathbf{b}_\perp$ . We could equivalently be interested in the distribution of partons with respect to their longitudinal momentum fraction  $x$  and perpendicular momentum  $\mathbf{k}_\perp$ . This is what is given by transverse momentum dependent distribution functions (TMDs) [71, 72], which, unlike GPDs, are probability distributions and do not need to be further transformed. They reduce into PDFs when integrated over  $\mathbf{k}_\perp^2$  and they can give insight into the orbital angular momentum of partons, as well as spin-orbit correlations. When integrated over  $x$ , they give transverse-momentum dependent spin densities (TMSDs). TMSDs and form factors give the total charge of the nucleon by integrating over  $\mathbf{k}_\perp$  (TMSDs) or in the forward limit (FFs). A comprehensive review on TMDs can be found here [73].

GPDs and TMDs both yield 3D probability distributions for partons inside nucleons. But in order to obtain the full picture of the structure of a nucleon, we need to go a step further, to

the quantum mechanical Wigner quasiprobability distribution [74, 75, 47]. It is a semi-classical probability in the sense that it is not positive definite for states that do not have a classical interpretation [76]. Of course, the standard quantum mechanical Wigner distribution needs a field theory treatment. For asymmetric initial and final nucleon states we can define

$$\hat{W}_{\Lambda,\Lambda'}^{\Gamma}(\mathbf{b}_{\perp}, \mathbf{k}_{\perp}, x) = \frac{1}{2} \int \frac{d^4z}{(2\pi)^4} e^{ik \cdot z} \left\langle P_2, \Lambda_2 \left| \bar{\psi} \left( -\frac{1}{2}z \right) \Gamma \mathcal{W} \left( -\frac{1}{2}z, \frac{1}{2}z \right) \psi \left( \frac{1}{2}z \right) \right| P_1, \Lambda_1 \right\rangle, \quad (3.113)$$

where  $\Lambda_{1,2}$  are the initial and final helicities of the nucleon, and  $\Gamma$  is an operator from the standard basis  $\{\mathbb{1}, \gamma_5, \gamma^{\mu}, \gamma^{\nu}, \sigma^{\mu\nu}, \sigma^{\mu\nu} \gamma_5\}$ . This generalized parton correlation function depicts a quark created at  $-z/2$  and annihilated at  $z/2$ . This means that it propagates a finite distance before rehadronizing, which allows us to access its momentum.  $\mathcal{W}$  is the Wilson line between these two light-cone points and it ensures color gauge invariance.

The functions that reduce into GPDs and TMDs are Fourier transforms of (3.113)

$$W_{\Lambda,\Lambda'}^{\Gamma}(\Delta_{\perp}, \mathbf{k}_{\perp}, x) = \int d^2\mathbf{b}_{\perp} e^{-i\Delta_{\perp} \cdot \mathbf{b}_{\perp}} \hat{W}_{\Lambda,\Lambda'}^{\Gamma}(\mathbf{b}_{\perp}, \mathbf{k}_{\perp}, x) \quad (3.114)$$

and are called generalized transverse momentum dependent parton distributions (GTMDs) [77, 78, 79, 80, 81]. The connections between all of these distributions are given in figure (3.2) below.

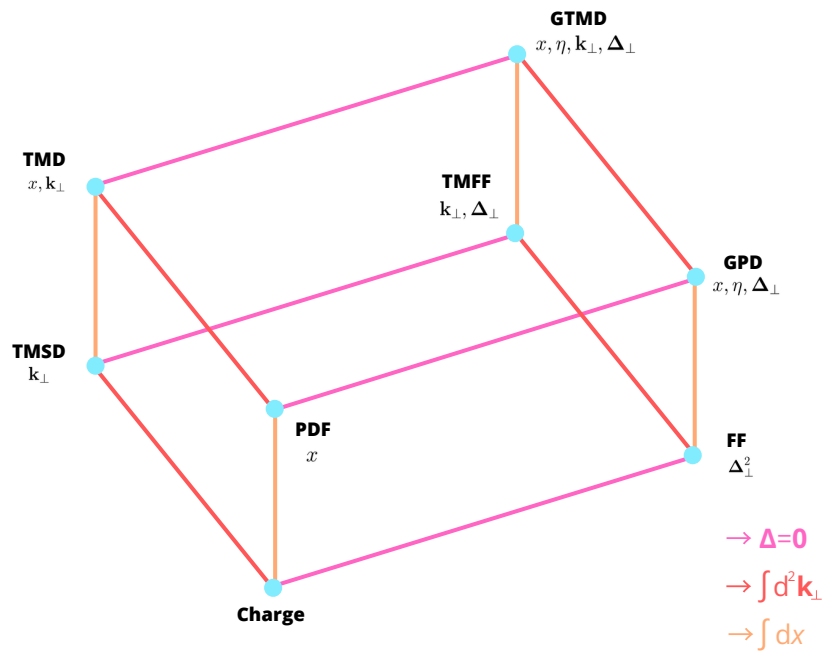


Figure 3.2: Hierarchy of parton distributions. Inspired by [82].

The kinematic dependences of the aforementioned distributions are depicted schematically in figure 3.3 below.

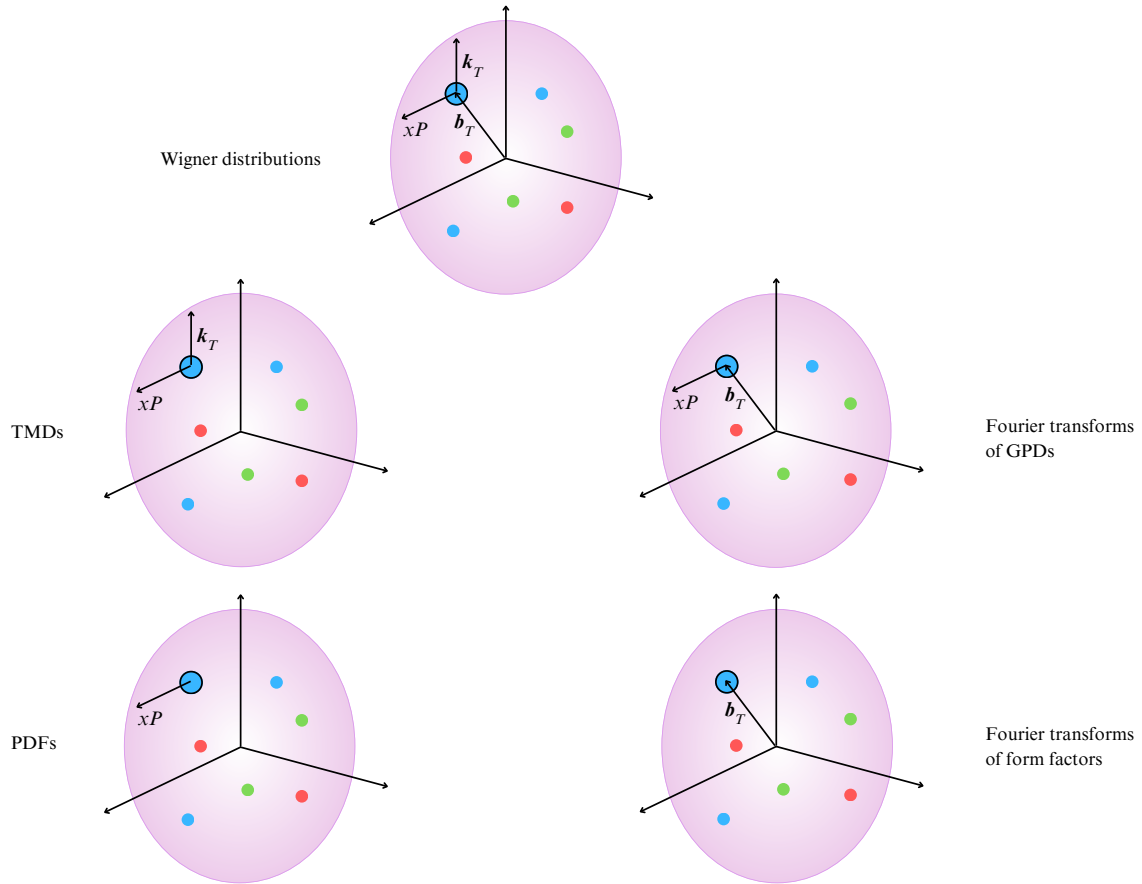


Figure 3.3: Depiction of kinematic dependences of various distributions.

### 3.5.5 Dispersion relations

Dispersion relations come from analyticity and causality considerations of Compton form factors and they relate their real and imaginary part [83, 84]. We give an example for the CFF  $\mathcal{H}$

$$\Re\mathcal{H}(\xi, t, Q^2) = \frac{1}{\pi} \text{P.V.} \int_0^1 d\xi' \Im\mathcal{H}(\xi', t, Q^2) \left( \frac{1}{\xi - \xi'} - \frac{1}{\xi + \xi'} \right) + \Delta_{\mathcal{H}}(t, Q^2), \quad (3.115)$$

where  $\Delta_{\mathcal{H}}(t, Q^2)$  is a subtraction constant that does not depend on the skewness. Expression (3.115) is formally a dispersion relation with one subtraction, referring to the subtraction constant  $\Delta$ , which does not depend on the skewness. This subtraction constant is necessary to cancel out divergences at the point  $\xi = 0$  and  $x = 0$  that occur in CFFs. It is worth noting that the integral over  $\xi'$  goes from 0 to 1, but skewness is bounded by (3.58) and for most exper-

imental setups this means that the integral (3.115) will go out of the physical domain where CFFs are defined. Therefore, analytic continuation is necessary in order to extract knowledge on the subtraction constant.

### 3.6 Status of experiments

The first experiments that probed the inner structure of the proton were performed at SLAC in collaboration with MIT [14] in 1969, which unequivocally showed that the proton has an underlying structure. Since then, many experiments have been conducted at SLAC, CERN and FNAL, using electron, muon and neutrino beams and a fixed target. Through technological advances, higher beam energies, higher  $Q^2$  and lower  $x$  were accomplished. Low  $x$  and diffraction studies have been conducted at HERA by the H1 and ZEUS collaborations. Even though DIS is not the focus of this work, some DIS measurements are still used for our analysis, such as the H1 and ZEUS measurements of the structure function  $F_2$ , because GPDs reduce to PDFs in the forward limit.

First DVCS experiments were conducted at HERA and JLab. H1 and ZEUS collaborations used a collider setup, and just like for DIS, they led studies into the low- $x$  and high- $Q^2$  regions. They were able to accomplish  $x \approx 10^{-4}$  and  $Q^2 \approx 100 \text{ GeV}^2$  kinematics, but unfortunately with low statistics. DVMP was also studied by these two collaborations at similar kinematics. The HERMES collaboration at HERA measured DVCS at intermediate kinematics in a fixed-target setup, with  $x$  ranging between 0.04 and 0.1 and  $Q^2$  going up to  $7 \text{ GeV}^2$ . HERA, the only electron-proton collider to date, was shut down in 2007.

The COMPASS collaboration at CERN uses a fixed-target setup with positively and negatively charged muons, and offers a kinematic coverage between that of HERMES and H1/ZEUS collaborations.

At JLab, CLAS and Hall A collaborations also use a fixed-target setup, and their measurements are taken at higher  $x$  and lower  $Q^2$ , namely their  $x$  ranges between 0.1 and 0.5, and their  $Q^2$  goes up to  $4 \text{ GeV}^2$ . They are currently at the stage of a new 12 GeV beam upgrade and new measurements with increased precision are being published.

The importance of studying the structure of the proton prompted several new experimental programs, such as the future electron-ion collider (EIC), which will offer a higher luminosity than currently existing experiments, in the region of small  $x$  and large  $Q^2$ , similarly to the HERA collider [85, 86]. Other projects are the Chinese electron-ion collider (EIC) [87, 88] and the hadron-electron collider (LHeC) [89].

Most of the current DVCS measurements are depicted in figure 3.4 below, as well as the

promised EIC kinematics.

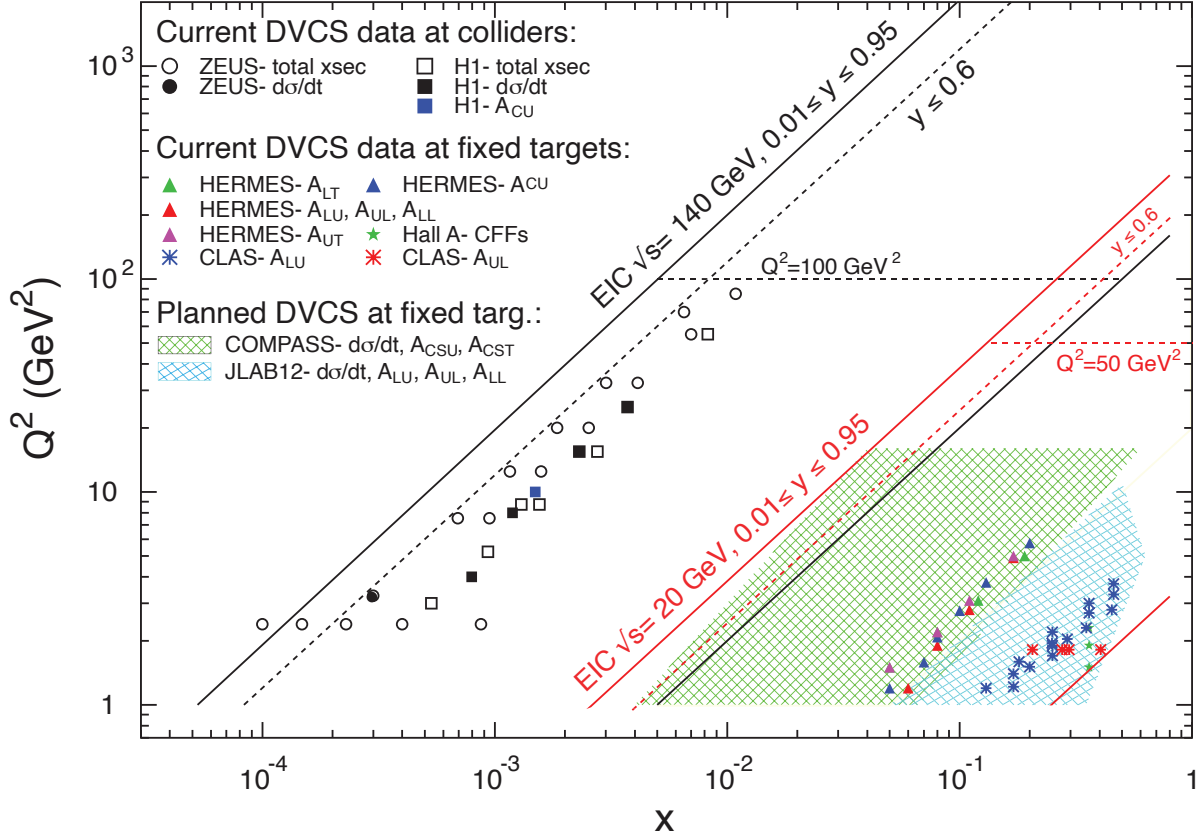


Figure 3.4: Kinematic coverage of DVCS measurements. Taken from [86].

Similar programs were conducted for DVMP measurements. Again, more or less in the same kinematics as DVCS, H1, ZEUS, HERMES, COMPASS and CLAS collaborations measured the production of various vector mesons, namely  $\rho^0$ ,  $\phi$ ,  $\omega$  and  $J/\psi$ . HERMES, CLAS and Hall C measured also the production of pseudoscalar mesons  $\pi^0$  and  $\pi^+$  [90, 91, 92, 93].

### 3.6.1 Observables

Using the experimental data for the differential cross section, total cross section and various asymmetries for proton and neutron DVCS, we access the twist-two Compton form factors,  $\mathcal{H}$ ,  $\mathcal{E}$ ,  $\tilde{\mathcal{H}}$ ,  $\tilde{\mathcal{E}}$ . The asymmetries are generally denoted as  $A_{BT}$ , where the first letter denotes the polarization of the beam, and the second the polarization of the target, and they can have values U for unpolarized, L for longitudinally polarized and T for transversally polarized.

One of these observables is the beam spin asymmetry, denoted BSA or  $A_{LU}$ , where the beam

is longitudinally polarized, and the target is unpolarized. It is defined as

$$A_{\text{LU}}(\phi) = \frac{d\sigma^\uparrow(\phi) - d\sigma^\downarrow(\phi)}{d\sigma^\uparrow(\phi) + d\sigma^\downarrow(\phi)} \propto \frac{\alpha' \sin \phi}{1 + \gamma \cos \phi}, \quad (3.116)$$

where

$$\alpha' = \frac{x_{\text{B}}}{y} (1 + \varepsilon^2)^2 \frac{s_1^{\mathcal{I}}}{c_0^{\text{BH}}}, \quad \gamma = \frac{y c_1^{\text{BH}} + x_{\text{B}} (1 + \varepsilon^2)^2 c_1^{\mathcal{I}}}{y c_0^{\text{BH}}}. \quad (3.117)$$

Here  $\sigma^\uparrow$  denotes the cross section where the beam is polarized in the direction of the flow of leptons, and  $\sigma^\downarrow$  denotes the cross section where the beam is polarized in the opposite direction to the flow of leptons. For typical kinematics the first sine harmonic is dominant, so we have

$$A_{\text{LU}} \propto \Im \left\{ F_1 \mathcal{H} + \xi (F_1 + F_2) \tilde{\mathcal{H}} - \frac{\Delta^2}{4M^2} F_2 \mathcal{E} \right\} \sin(\phi). \quad (3.118)$$

This is why we usually perform a Fourier transform and just observe the amplitude of the BSA. This quantity is particularly sensitive to the imaginary part of the CFF  $\mathcal{H}$ .

Another set of data that is used is for longitudinal target spin asymmetry, denoted as TSA or  $A_{\text{UL}}$ , which is given as

$$A_{\text{UL}}(\phi) = \frac{d\sigma^{\Rightarrow}(\phi) - d\sigma^{\Leftarrow}(\phi)}{d\sigma^{\Rightarrow}(\phi) + d\sigma^{\Leftarrow}(\phi)} \sim \frac{s_1^{\mathcal{I}, \text{LP}}}{c_0^{\text{BH}, \text{unp}}} \sin(\phi) \propto \Im \left[ F_1 \tilde{\mathcal{H}} + \xi (F_1 + F_2) \left( \mathcal{H} + \frac{x_{\text{B}}}{2} \mathcal{E} \right) - \xi \left( \frac{x_{\text{B}}}{2} F_1 + \frac{t}{4M^2} F_2 \right) \tilde{\mathcal{E}} \right] \sin(\phi), \quad (3.119)$$

where  $\sigma^{\Rightarrow}$  denotes the cross section where the target is polarized in the direction of the flow of leptons, and  $\sigma^{\Leftarrow}$  denotes the cross section where the target is polarized in the opposite direction to the flow of leptons. This quantity is sensitive to the imaginary parts of  $\mathcal{H}$  and  $\tilde{\mathcal{H}}$ .

The double spin asymmetry, denoted as BTSA or  $A_{LL}$ , which is given as

$$\begin{aligned}
A_{LL}(\phi) &= \frac{d\sigma^{\uparrow\uparrow}(\phi) - d\sigma^{\downarrow\uparrow}(\phi) - d\sigma^{\uparrow\downarrow}(\phi) + d\sigma^{\downarrow\downarrow}(\phi)}{d\sigma^{\uparrow\uparrow}(\phi) + d\sigma^{\downarrow\uparrow}(\phi) + d\sigma^{\uparrow\downarrow}(\phi) + d\sigma^{\downarrow\downarrow}(\phi)} \\
&\sim \frac{c_{0,LP}^{BH} + c_{0,LP}^{\mathcal{I}} + \left(c_{1,LP}^{BH} + c_{1,LP}^{\mathcal{I}}\right) \cos\phi}{c_{0,unp}^{BH}} \\
&\propto \Re \left[ F_1 \tilde{\mathcal{H}} + \xi (F_1 + F_2) \left( \mathcal{H} + \frac{x_B}{2} \mathcal{E} \right) - \xi \left( \frac{x_B}{2} F_1 + \frac{t}{4M^2} F_2 \right) \tilde{\mathcal{E}} \right] \cos\phi + BH, \quad (3.120)
\end{aligned}$$

is also used in the analysis. Here the arrow  $\uparrow$  denotes that the spin of the leptons is polarized in the direction of the beam, and  $\downarrow$  means that it is polarized in the opposite direction. The same is valid for the spin of the target, denoted with the double arrow. This quantity is sensitive to the Bethe-Heitler and interference contributions, but at certain kinematics it can be sensitive to real parts of  $\mathcal{H}$  and  $\tilde{\mathcal{H}}$ .

Other quantities that were used in our analysis are the beam spin sum BSS, which is unpolarized, and the beam spin difference BSD, which is helicity-dependent. They are given as

$$\begin{aligned}
d^4\sigma &= \frac{1}{2} \left[ \frac{d^4\sigma(\lambda = +1)}{dQ^2 dx_B dt d\phi} + \frac{d^4\sigma(\lambda = -1)}{dQ^2 dx_B dt d\phi} \right] \\
\Delta^4\sigma &= \frac{1}{2} \left[ \frac{d^4\sigma(\lambda = +1)}{dQ^2 dx_B dt d\phi} - \frac{d^4\sigma(\lambda = -1)}{dQ^2 dx_B dt d\phi} \right].
\end{aligned}$$

The helicity-independent cross section depends mostly on the real part of the same coefficient as the BSA, and the helicity-dependent cross section depends mostly on the imaginary part of that coefficient.

For a set of kinematic variables given in Table 3.1 below, we can obtain the contributions of CFFs to various observables, given in Table 3.2.

Experiment	Kinematics		
	$x_B$	$Q^2$ [GeV <sup>2</sup> ]	$t$ [GeV <sup>2</sup> ]
HERMES	0.09	2.50	-0.12
CLAS	0.19	1.25	-0.19
HALL A	0.36	2.30	-0.23
HERA	0.001	8.00	-0.30

Table 3.1: Typical kinematics used for experiments. Taken from [1].

Experiment	Observable	Normalized CFF dependence
HERMES	$A_C^{\cos 0\phi}$	$\text{Re } \mathcal{H} + 0.06 \text{Re } \mathcal{E} + 0.24 \text{Re } \tilde{\mathcal{H}}$
	$A_C^{\cos \phi}$	$\text{Re } \mathcal{H} + 0.05 \text{Re } \mathcal{E} + 0.15 \text{Re } \tilde{\mathcal{H}}$
	$A_{LU,I}^{\sin \phi}$	$\text{Im } \mathcal{H} + 0.05 \text{Im } \mathcal{E} + 0.12 \text{Im } \tilde{\mathcal{H}}$
	$A_{UL}^{+, \sin \phi}$	$\text{Im } \tilde{\mathcal{H}} + 0.10 \text{Im } \mathcal{H} + 0.01 \text{Im } \mathcal{E}$
	$A_{UL}^{+, \sin 2\phi}$	$\text{Im } \tilde{\mathcal{H}} - 0.97 \text{Im } \mathcal{H} + 0.49 \text{Im } \mathcal{E} - 0.03 \text{Im } \tilde{\mathcal{E}}$
	$A_{LL}^{+, \cos 0\phi}$	$1 + 0.05 \text{Re } \tilde{\mathcal{H}} + 0.01 \text{Re } \mathcal{H}$
	$A_{LL}^{+, \cos \phi}$	$1 + 0.79 \text{Re } \tilde{\mathcal{H}} + 0.11 \text{Im } \mathcal{H}$
	$A_{UT, DVCS}^{\sin(\phi - \phi_S)}$	$\text{Im } \mathcal{H} \text{Re } \mathcal{E} - \text{Im } \mathcal{E} \text{Re } \mathcal{H}$
	$A_{UT, I}^{\sin(\phi - \phi_S) \cos \phi}$	$\text{Im } \mathcal{H} - 0.56 \text{Im } \mathcal{E} - 0.12 \text{Im } \tilde{\mathcal{H}}$
CLAS	$A_{LU}^{-, \sin \phi}$	$\text{Im } \mathcal{H} + 0.06 \text{Im } \mathcal{E} + 0.21 \text{Im } \tilde{\mathcal{H}}$
	$A_{UL}^{-, \sin \phi}$	$\text{Im } \tilde{\mathcal{H}} + 0.12 \text{Im } \mathcal{H} + 0.04 \text{Im } \mathcal{E}$
	$A_{UL}^{-, \sin 2\phi}$	$\text{Im } \tilde{\mathcal{H}} - 0.79 \text{Im } \mathcal{H} + 0.30 \text{Im } \mathcal{E} - 0.05 \text{Im } \tilde{\mathcal{E}}$
HALL A	$\Delta \sigma^{\sin \phi}$	$\text{Im } \mathcal{H} + 0.07 \text{Im } \mathcal{E} + 0.47 \text{Im } \tilde{\mathcal{H}}$
	$\sigma^{\cos 0\phi}$	$1 + 0.05 \text{Re } \mathcal{H} + 0.007 \mathcal{H} \mathcal{H}^*$
	$\sigma^{\cos \phi}$	$1 + 0.12 \text{Re } \mathcal{H} + 0.05 \text{Re } \tilde{\mathcal{H}}$
HERA	$\sigma_{DVCS}$	$\mathcal{H} \mathcal{H}^* + 0.09 \mathcal{E} \mathcal{E}^* + \tilde{\mathcal{H}} \tilde{\mathcal{H}}^*$

Table 3.2: Dependence of observables on CFFs, normalized to the highest coefficient. The coefficients are evaluated at the kinematics from Table 3.1. Coefficients smaller than 1% are not kept, except for the Hall A cross section. Taken from [1].

# Chapter 4

## Conformal symmetry and conformal moments

Conformal symmetry has had many uses in various fields of physics over the years. It is a maximal extension of the Poincaré group that leaves the light-cone invariant. It is also a symmetry of QCD when the  $\beta$  function vanishes, i.e. for a free theory, which in our case takes the form of a naive parton model. This is of course not always applicable and has therefore limited uses in QCD. Nevertheless, there are certain advantages in implementing conformal symmetry in QCD, one of which is the simplification of evolution equations (3.98). Evolution kernels and anomalous dimension have been calculated up to NLO in [94, 95] and NNLO in [96], and the operator product expansion for DVCS has been formalized in the conformal space in [97, 98].

We give a brief outline of the material presented in review [99] in order to introduce the conformal group and its collinear subgroup. Here we show that the conformal operators corresponding to the bilocal operators in the definition of GPDs form irreducible representations of the collinear subgroup. We obtain the conformal operator product expansion of a product of two local conformal operators

Finally, we outline the conformal partial wave expansion of GPDs. We use the Mellin-Barnes representation in order to achieve convergence of the expansion [100]. This is then extended to the Mellin-Barnes representation of CFFs and TFFs [101, 37].

### 4.1 Conformal group and conformal towers

The conformal group is formed by operations that transform the metric by rescaling it

$$g'_{\mu\nu}(x') = \Omega^2 g_{\mu\nu}(x). \quad (4.1)$$

These transformations do not change angles and therefore conserve the light-cone. The Poincaré transformations also belong in the group of conformal transformations since they do not change the metric at all, so formally  $\Omega = 1$ . Aside from transformations of the Poincaré group, the conformal group also contains dilatations

$$D: x^\mu \rightarrow x'^\mu = \lambda x^\mu, \quad \lambda \in \mathbb{R}, \quad (4.2)$$

and special conformal transformations

$$K^\mu: x^\mu \rightarrow x'^\mu = \frac{x^\mu + a^\mu x^2}{1 + 2a \cdot x + a^2 x^2}. \quad (4.3)$$

Typically we observe the processes in this work in the regime where partons are collinear to the nucleon, and they move close to the light-cone. This is why we use light-cone coordinates, which naturally separate motion on the light-cone to the motion transversal to it. We consider a special conformal transformation, a translation and a dilatation by a lightlike vector  $a^\mu = an^\mu$

$$z_- \rightarrow z'_- = \frac{z_-}{1 + 2az_-}, \quad z^- \rightarrow z^- + a^-, \quad z^- \rightarrow az^-. \quad (4.4)$$

These transformations form the collinear subgroup of the conformal group, which is denoted as  $SL(2, \mathbb{R})$ . We will use the notation for fields that denote particles on the light-line

$$\Phi(z) \rightarrow \Phi(\alpha n) \equiv \Phi(\alpha). \quad (4.5)$$

The fields  $\Phi$  are typically called primary fields in this context.

We can write the algebra of the collinear subgroup as

$$[L_0, L_\pm] = \pm L_\pm, \quad [L_-, L_+] = -2L_0. \quad (4.6)$$

We want to construct a basis of operators that are eigenstates of the spin operator with a fixed spin projection onto the plus-direction. It can be shown that a primary field at  $\alpha = 0$  satisfies

$$[L_-, \Phi(0)] = 0, \quad [L_0, \Phi(0)] = j\Phi(0). \quad (4.7)$$

This state is a state with the highest weight and we use it to construct all other states of the

representation as

$$\mathcal{O}_0 = \Phi(0) \quad (4.8)$$

$$\mathcal{O}_1 = [L_+, \Phi(0)] = -\partial_+ \Phi(\alpha)|_{\alpha=0}, \quad (4.9)$$

$\vdots$

$$\mathcal{O}_k = [L_+, \dots, [L_+, [L_+, \Phi(0)]]] = (-\partial_+)^k \Phi(\alpha)|_{\alpha=0}. \quad (4.10)$$

We see that the operators  $L_-$  and  $L_+$  play the role of lowering and raising operator, similarly to standard raising and lowering operators for spin states of the  $SU(2)$  group. From the commutation relations one can deduce the action of  $L_0$  on the operator  $\mathcal{O}_0$

$$[L_0, \mathcal{O}_0] = j\mathcal{O}_0, \quad [L_0, \mathcal{O}_1] = (j+1)\mathcal{O}_1, \quad [L_0, \mathcal{O}_{k+1}] = (j+k)\mathcal{O}_k, \quad (4.11)$$

and the action of raising and lowering operators on the operators  $\mathcal{O}_k$

$$[L_+, \mathcal{O}_k] = \mathcal{O}_{k+1}, \quad [L_-, \mathcal{O}_k] = -k(2j+k-1)\mathcal{O}_{k-1}. \quad (4.12)$$

The primary field defined at an arbitrary coordinate  $\alpha$  can be expanded in a Taylor series over local conformal operators

$$\Phi(\alpha) = \sum_{k=0}^{\infty} \frac{(-\alpha)^k}{k!} \left( -\partial_+^k \right) \Phi(\alpha) \Big|_{\alpha=0} = \sum_{k=0}^{\infty} \frac{(-\alpha)^k}{k!} \mathcal{O}_k. \quad (4.13)$$

This construction represents a conformal tower. The lowest operator in a conformal tower is the highest weight vector in the space of representations, and higher operators are obtained by adding total derivatives, each of which adds one unit to the conformal spin projection on the zero light-cone axis.

Our goal is to build conformal towers for operators that appear in cross sections of processes of interest to us. At twist-2 we often encounter the non-local operator built of a quark and antiquark field at lightlike separation

$$Q_\mu(\alpha_1, \alpha_2) = \bar{\Psi}(\alpha_1) \gamma_\mu[\alpha_1, \alpha_2] \Psi(\alpha_2), \quad (4.14)$$

where the Wilson line is given as

$$[\alpha_1, \alpha_2] = \text{P exp} \left[ ig \int_{\alpha_2}^{\alpha_1} dt A_+(t) \right]. \quad (4.15)$$

Expanding this operator at small distances gives rise to local operators of the form

$$\bar{\Psi}(0) \left( \overleftarrow{D}_+ \right)^{n_1} \gamma_\mu \left( \overrightarrow{D}_+ \right)^{n_2} \Psi(0), \quad (4.16)$$

and our task is to find their conformal counterparts.

Since quark and antiquark spinors do not have a definite spin projection, we define projection operators  $\Psi_\pm$  with spin  $\pm 1/2$ , where  $\Psi = \Psi_+ + \Psi_-$ . Considering that the canonical dimension of the spinor is  $3/2$ , the conformal spin for  $\Psi_\pm$  is  $j_+ = 1$  and  $j_- = 1/2$ , and the conformal twist is  $t_+ = 1$  and  $t_- = 2$ . Different Lorentz components of the operator  $Q_\mu(\alpha_1, \alpha_2)$  therefore include different spinor components and they have different properties under conformal transformations

$$\text{twist-2: } Q_+ = \bar{\Psi}_+ \gamma_+ \Psi_+ \equiv Q^{1,1}, \quad (4.17)$$

$$\text{twist-3: } Q_\perp = \bar{\Psi}_+ \gamma_\perp \Psi_- + \bar{\Psi}_- \gamma_\perp \Psi_+ \equiv Q^{1,1/2} + Q^{1/2,1}, \quad (4.18)$$

$$\text{twist-4: } Q_- = \bar{\Psi}_- \gamma_- \Psi_- \equiv Q^{1/2,1/2}. \quad (4.19)$$

The superscripts on  $Q$  denote the conformal spin of the quark and antiquark, respectively. The corresponding local operators are given as

$$\mathbb{Q}_n^{1,1}(x) = (i\partial_+)^n \left[ \bar{\Psi}(x) \gamma_+ C_n^{3/2} \left( \overleftrightarrow{D} / \partial_+ \right) \Psi(x) \right], \quad (4.20)$$

$$\mathbb{Q}_n^{1,1/2}(x) = (i\partial_+)^n \left[ \bar{\Psi}(x) \gamma_+ \gamma_\perp \gamma_- P_n^{(1,0)} \left( \overleftrightarrow{D} / \partial_+ \right) \Psi(x) \right], \quad (4.21)$$

$$\mathbb{Q}_n^{1/2,1/2}(x) = (i\partial_+)^n \left[ \bar{\Psi}(x) \gamma_- C_n^{1/2} \left( \overleftrightarrow{D} / \partial_+ \right) \Psi(x) \right], \quad (4.22)$$

where  $\overleftrightarrow{D}_+ = \overrightarrow{D}_+ - \overleftarrow{D}_+$ ,  $\partial_+ = \overrightarrow{\partial}_+ + \overleftarrow{\partial}_+$ . Jacobi polynomials enter these expressions with the same indices, so we introduce Gegenbauer polynomials which are given as  $P_n^{(1,1)} \sim C_n^{3/2}$ ,  $P_n^{(0,0)} \sim C_n^{1/2}$ . Gegenbauer polynomials are orthogonal polynomials which form a complete basis in the interval  $[-1, 1]$  and are the only solution to the differential equation

$$\frac{d^2}{dx^2} (1-x^2) C_n^{3/2}(x) = -(n+1)(n+2) C_n^{3/2}(x), \quad (4.23)$$

which is finite at the singular points  $x = \pm 1$ .

The same procedure can be applied for gluons, where the leading twist operator built from two gluon fields is given as

$$\mathbb{G}_n^{3/2,3/2}(x) = (i\partial_+)^n \left[ G_{+\perp}^a(x) C_n^{5/2} \left( \overleftrightarrow{D}_+ / \partial_+ \right) G_{+\perp}^a(x) \right]. \quad (4.24)$$

## 4.2 Conformal operator product expansion

Conformal operator product expansion (COPE) was shown to provide powerful constraints on the Wilson coefficients appearing in operator product expansion we used for amplitudes of DIS, DVCS and DVMP. In this section we present the COPE of a product of two local conformal operators following [102, 103, 104, 105].

We observe the product  $A(z)B(0)$  where operators  $A$  and  $B$  have conformal twist  $t_A$  and  $t_B$ , and the spin projection onto the plus direction  $s_A$  and  $s_B$ , respectively. We expand this product in the lightcone limit  $z_+, z_\perp \rightarrow 0$ ,  $z_-$  fixed, or equivalently  $z^2 = 0$ , over a conformal tower of operators and their derivatives, which we denote as  $\mathbb{O}_{n,n+k}^{j_1, j_2}$  and which we assume to be a complete basis. We ignore contributions of the unity operator and up to leading twist we have

$$A(z)B(0) = \sum_{n=0}^{\infty} \left( \frac{1}{z^2} \right)^{\frac{t_A+t_B-t_n}{2}} \sum_{k=0}^{\infty} C_{n,k} z_-^{n+k+\Delta} \mathbb{O}_{n,n+k}^{j_1, j_2}(0). \quad (4.25)$$

Here  $C_{n,k}$  are the Wilson coefficients, and  $\Delta = s_1 + s_2 - s_A - s_B$ , where  $s_{1,2}$  are the spin projections of the constituents field of the operator  $\mathbb{O}_{n,n+k}^{j_1, j_2}$ . The singularity of the local operators is determined by the twist  $t_A + t_B - t_n$ , where  $t_n = \ell_n - n - s_1 - s_2 = \ell_1 + \ell_2 - s_1 - s_2$  is the twist of the conformal operators  $\mathbb{O}_{n,n+k}^{j_1, j_2}$ .

We can use conformal symmetry to obtain Wilson coefficients  $C_{n,k}$ , with  $k = 1, 2, \dots$ , which correspond to operators with total derivatives, by using the coefficient of the highest weight operator  $C_n \equiv C_{n,k=0}$ , which contains no total derivatives. We apply the lowering operator on both sides of the equation (4.25). Using (4.12), we have

$$\left[ L_-, \mathbb{O}_{n,n+k}^{j_1, j_2}(0) \right] = -k(k + 2j_n - 1) \mathbb{O}_{n,n+k-1}^{j_1, j_2}(0), \quad j_n = j_1 + j_2 + n, \quad (4.26)$$

so the right-hand side becomes

$$\sum_{n=0}^{\infty} \left( \frac{1}{z^2} \right)^{\frac{t_A+t_B-t_n}{2}} \sum_{k=0}^{\infty} (j_A - j_B + j_n + k) C_{n,k} (z_-)^{n+k+\Delta+1} \mathbb{O}_{n,n+k}^{j_1, j_2}(0), \quad (4.27)$$

and the left-hand side becomes

$$\left[ L_-, A(z)B(0) \right] = \left\{ z_- (2j_A + z \cdot \partial_z) A(z) - \frac{1}{2} z_-^2 \tilde{n} \cdot \partial_z A(z) \right\} B(0) + \dots, \quad (4.28)$$

where the ellipsis denotes the higher-twist contributions. Comparing the previous two equa-

tions, we obtain a solution for the Wilson coefficients

$$C_{n,k} = (-1)^k \frac{(j_A - j_B + j_n)_k}{k! (2j_n)_k} C_n, \quad C_n \equiv C_{n,0}. \quad (4.29)$$

Here we used the Pochhammer symbol

$$(a)_k = \frac{\Gamma(a+k)}{\Gamma(a)}. \quad (4.30)$$

The sum over  $k$  gives a hypergeometric function

$$\sum_{k=0}^{\infty} (-1)^k \frac{(j_A - j_B + j_n)_k}{k! (2j_n)_k} (-z \cdot \partial)^k = {}_1F_1 \left( \begin{matrix} j_A - j_B + j_n \\ 2j_n \end{matrix} \middle| z \cdot \partial \right). \quad (4.31)$$

Using the integral representation for the hypergeometric function, we can write the twist-two COPE

$$\begin{aligned} A(z)B(0) &= \sum_{n=0}^{\infty} C_n \left( \frac{1}{z^2} \right)^{\frac{t_A + t_B - t_n}{2}} \frac{(z^-)^{n+\Delta}}{\mathbf{B}(j_A - j_B + j_n, j_B - j_A + j_n)} \\ &\times \int_0^1 du u^{j_A - j_B + j_n - 1} \bar{u}^{j_B - j_A + j_n - 1} \mathbb{Q}_n^{j_1, j_2}(u z^-), \end{aligned} \quad (4.32)$$

with the Euler Beta function

$$B(a, b) = \frac{\Gamma(a)\Gamma(b)}{\Gamma(a+b)}. \quad (4.33)$$

As promised, we apply this procedure to the product of two currents found in the Compton tensor

$$T(P, q, \Delta) = i \int d^4 z e^{iqz - i\frac{\Delta}{2}z} \langle \mathbf{P}_1 | T \{ j_{\perp}(z) j_{\perp}(0) \} | \mathbf{P}_2 \rangle, \quad (4.34)$$

where at the tree level we only need transverse components of the currents, whose spin projection is zero. The currents have dimension 3 and consequently conformal twist 3. The operator basis consists of quark operators  $\mathbb{Q}_{n, n+k}^{1,1}$  with twist  $t_n = 2$  and conformal spin  $j_n = 2 + n$ . We also have  $\Delta = 1$ . Conformal symmetry provides Wilson coefficients for DVCS using Wilson coefficients for DIS [97, 98]. Plugging all of the parameters into the COPE (4.32) gives the Compton tensor

$$T(P, q, \Delta) = i \int d^4 z e^{iqz - i\frac{\Delta}{2}z} \sum_{n=0}^{\infty} C_n \left( \frac{1}{z^2} \right)^{\frac{6-t_n}{2}} \frac{(-iz^-)^{n+1}}{\mathbf{B}(j_n, j_n)} \int_0^1 du (u\bar{u})^{j_n-1} \langle \mathbf{P}_2 | \mathbb{Q}_n^{1,1}(u z^-) | \mathbf{P}_1 \rangle. \quad (4.35)$$

In an interacting theory the canonical dimension has to be replaced by the anomalous dimension  $\gamma_n$ , so the conformal twist of the local operators is given as  $t_n = 2 + \gamma_n$ .

It can be shown that the previous equation can be written as

$$T(P, q, \Delta) = \sum_{n=0}^{\infty} \tilde{c}_n \left( \frac{\mu^2}{Q^2} \right)^{\gamma_n/2} \xi^{-n-1} \frac{2^{n+1+\gamma_n/2} \Gamma(n+5/2+\gamma_n/2)}{\Gamma(3/2) \Gamma(n+3+\gamma_n/2)} \langle\langle \mathbb{Q}_n(0) \rangle\rangle (\xi, \Delta^2, \mu^2), \quad (4.36)$$

where we have introduced the notation

$$\langle P_2 | \mathbb{Q}_n^{1,1}(uz^-) | P_1 \rangle = e^{iu\xi P_+ z} P_+^{n+1} \langle\langle \mathbb{Q}_n^{1,1}(0) \rangle\rangle (\xi, \Delta^2, \mu^2). \quad (4.37)$$

The matrix elements in the Compton tensor are parametrized using GPDs, and our next step is to derive the conformal moments of GPDs in the so-called momentum fraction representation. This procedure is analogous to calculating inverse Mellin moments of PDFs.

### 4.3 Conformal partial wave expansion

In this work we approach GPD modeling in the space of conformal moments, and the goal of this section is to derive a representation of GPDs in the conformal space. Analogous steps were taken in modeling PDFs, where an expansion in terms of Mellin moments was used

$$f_j^q = \int_{-1}^1 dx x^j f^q(x), \quad f_j^G = \int_{-1}^1 dx x^{j-1} f^G(x). \quad (4.38)$$

The inverse Mellin transform reads

$$f^q(x) = \frac{1}{2\pi i} \int_{c-i\infty}^{c+i\infty} dj x^{-j-1} f_j^q, \quad f^G(x) = \frac{1}{2\pi i} \int_{c-i\infty}^{c+i\infty} dj x^{-j} f_j^G, \quad (4.39)$$

where the integration contour is chosen to lie to the right of all singularities of the PDF moments.

For details refer to [4] and references therein.

#### 4.3.1 Generalized parton distributions

The goal of this section is to find the conformal moments of GPDs and to calculate the inverse transformation in order to recover GPDs in the  $x$  space. We follow the derivation in [100].

The conformal moments of quark and gluons are given by

$$F_n^q(\xi, \Delta^2) = \int_{-1}^1 dx c_n^{3/2}(x, \xi) F^q(x, \xi, \Delta^2), \quad (4.40)$$

$$F_n^G(\xi, \Delta^2) = \int_{-1}^1 dx c_{n-1}^{5/2}(x, \xi) F^G(x, \xi, \Delta^2), \quad (4.41)$$

where the coefficients  $c_n^\lambda$  contain Gegenbauer polynomials and normalization factors which recover the Mellin moments of PDFs in the forward limit. The coefficients for quarks and gluons are given as

$$c_n^{3/2}(x, \xi) = \xi^n \frac{\Gamma(3/2)\Gamma(n+1)}{2^n \Gamma(n+3/2)} C_n^{3/2}\left(\frac{x}{\xi}\right), \quad (4.42)$$

$$c_{n-1}^{5/2}(x, \xi) = \xi^{n-1} \frac{\Gamma(3/2)\Gamma(n+1)}{2^n \Gamma(n+3/2)} \frac{3}{n} C_{n-1}^{5/2}\left(\frac{x}{\xi}\right), \quad (4.43)$$

which we combine into a single expression

$$c_n^\lambda(x, \xi) = \xi^n \frac{\Gamma(\lambda)\Gamma(n+1)}{2^n \Gamma(n+\lambda)} C_n^\lambda\left(\frac{x}{\xi}\right), \quad \lim_{\xi \rightarrow 0} c_n^\lambda(x, \xi) = x^n. \quad (4.44)$$

For the vector sector, gluon GPDs are even under  $x \rightarrow -x$ , so the corresponding Gegenbauer polynomial is odd in  $n$ . For the axial-vector sector the gluon GPDs are odd under  $x \rightarrow -x$ , and the corresponding Gegenbauer polynomial is even in  $n$ . In order to analyze quark GPDs, which do not have a definite  $x$  parity, we use quark GPDs with definite charge parity  $F^{q(\pm)}$ , as defined in (3.36) and (3.37). The degree of the Gegenbauer polynomials in  $n$  is even for charge odd quark GPDs, and odd for charge even quark GPDs. Since the quark singlet GPD  $F^{0(+)}$  mixes with the gluon GPD under evolution, we have to shift the gluon polynomial degree by one unit in order to match the indices  $n$ .

To study quarks and gluons simultaneously, we utilize the notation

$$F_n^A(\xi, \Delta^2) = \int_{-1}^1 dx c_n^\lambda(x, \xi) F^A(x, \xi, \Delta^2), \quad (4.45)$$

where  $A \in \{q, G\}$  and  $\lambda \in \{3/2, 5/2\}$ . In order to match quark and gluon polynomial degrees, we perform a shift  $n \rightarrow n-1$  for gluons. We decompose quark GPDs into quark and antiquark distributions

$$F^{q(C)}(x, \xi, \Delta^2) = q(x, \xi, \Delta^2) - \sigma \bar{q}(-x, \xi, \Delta^2), \quad \sigma \in \{-1, 1\}, \quad (4.46)$$

where  $-\xi \leq x \leq 1$  for the first term, and  $-1 \leq x \leq \xi$  for the second term. For the vector sector we have  $C = \pm 1$  and  $\sigma = \pm 1$ , and for the axial-vector sector  $C = \pm 1$  and  $\sigma = \mp 1$ .

For the gluon GPDs, which have definite  $x$  parity, we simply write

$$F^G(x, \xi, \Delta^2) = g(x, \xi, \Delta^2) + \sigma g(-x, \xi, \Delta^2). \quad (4.47)$$

We can again treat both of these cases simultaneously by using

$$F^A(x, \xi, \Delta^2) = f^A(x, \xi, \Delta^2) - \sigma \bar{f}^A(-x, \xi, \Delta^2), \quad (4.48)$$

where

$$f^q \rightarrow q, \quad \bar{f}^q \rightarrow \bar{q}, \quad f^G \rightarrow g, \quad \bar{f}^G \rightarrow -g. \quad (4.49)$$

The conformal moments for the distributions  $f^A$  and  $\bar{f}^A$  are

$$f_n^A(\xi, \Delta^2) = \int_{-\xi}^1 dx c_n^\lambda(x, \xi) f^A(x, \xi, \Delta^2), \quad (4.50)$$

$$\bar{f}_n^A(\xi, \Delta^2) = \int_{-\xi}^1 dx c_n^\lambda(x, \xi) \bar{f}^A(x, \xi, \Delta^2). \quad (4.51)$$

In order to reconstruct GPDs from their conformal moments, we use the fact that the Gegenbauer polynomials are orthogonal in the central region  $[-\xi, \xi]$  with the weight function  $(1-x^2)^{\lambda-1/2}$ . We introduce polynomials  $p_n^\lambda$ , which contain the weight and normalization, in order to define the orthogonality relation

$$\int_{-\xi}^{\xi} dx c_n^\lambda(x, \xi) p_m^\lambda(x, \xi) = (-1)^n \delta_{mn}, \quad (4.52)$$

where the polynomials explicitly read

$$p_n^\lambda(x, \xi) = \frac{1}{\xi^{n+1}} \frac{2^{n-2\lambda} \Gamma(n+\lambda)}{\Gamma(\lambda) \Gamma(n+1)} \frac{1}{N_k^\lambda} C_n^\lambda\left(-\frac{x}{\xi}\right) \left[1 - \left(\frac{x}{\xi}\right)^2\right]^{\lambda-\frac{1}{2}}. \quad (4.53)$$

The definition of these polynomials allows us to expand GPDs in terms of Gegenbauer polynomials as

$$f^A(x, \xi, \Delta^2) = \sum_{n=0}^{\infty} (-1)^n p_n^\lambda(x, \xi) f_n^A(\xi, \Delta^2), \quad (4.54)$$

which is evident from (4.50). Note that this expansion is defined in the central region only, which means that it diverges for  $|\xi| < 1$  when  $n \rightarrow \infty$  due to the factor  $\xi^{-n-1}$ . This means that

terms for high  $n$  can have a high contribution to the GPD and the series cannot be truncated. The issue is solved by performing a Sommerfeld-Watson transformation, which replaces the infinite sum with a contour integral in the complex plane that includes the positive real axis. We consider the unphysical region  $\xi > 1$  and replace the integer indices  $n$  with the continuous complex variable  $j$ , which yields

$$f^A(x, \xi, \Delta^2) = \frac{1}{2i} \oint_{(0)}^{(\infty)} dj \frac{1}{\sin(\pi j)} p_j^\lambda(x, \xi) f_j^A(\xi, \Delta^2). \quad (4.55)$$

Using Cauchy's residue theorem and the fact that the function  $1/\sin(\pi j)$  has poles at  $j \in \mathbb{N}_0$  with residues  $(-1)^j/\pi$ , we can easily show that (4.55) coincides with (4.54) if there are no other singularities inside the contour of the integral. The task now lies in finding the appropriate analytic continuation of the functions  $p_j^\lambda$  and  $f_j^A$  in order to obtain the resummation in the unphysical region as well.

The polynomials  $p_j$  can be written using the Schläfli integral

$$p_j^\lambda(x, \xi) = (-1)^{\lambda-\frac{1}{2}} \frac{\Gamma(j+\lambda+1)}{\Gamma(1/2)\Gamma(j+\lambda+1/2)} \cdot \frac{1}{2\pi i} \oint_{(-1+\varepsilon)}^{(1-\varepsilon)} du \frac{(u^2-1)^{j+\lambda-\frac{1}{2}}}{(x+u\xi)^{j+1}}, \quad (4.56)$$

where the integration contour is a unit circle with points  $\pm 1$  included. We fix  $\xi$  to be positive and observe two cases. When  $x \leq -\xi$  and  $-x/\xi \geq 1$ , the pole lies outside the integration contour and the integral vanishes. In the case when  $x \geq -\xi$  and  $-x/\xi \leq 1$ , the pole lies inside the integration contour. In this case, for  $|x| \leq \xi$  the pole is inside the interval  $[-x/\xi, 1]$  and we can restrict the integration contour, which is not possible for  $|x| \geq \xi$ . We separate the previous expression into the two non-vanishing cases

$$p_j^\lambda(x, \xi) = (-1)^{\lambda+\frac{1}{2}} \frac{\Gamma(j+\lambda+1)}{\Gamma(1/2)\Gamma(j+\lambda+1/2)} \frac{\sin[\pi(j+\lambda-1/2)]}{\pi} \times \left[ \theta(\xi - |x|) \int_{-x/\xi}^1 du \frac{(1-u^2)^{j+\lambda-\frac{1}{2}}}{(x+u\xi)^{j+1}} + \theta(x-\xi) \int_{-1}^1 du \frac{(1-u^2)^{j+\lambda-\frac{1}{2}}}{(x+u\xi)^{j+1}} \right], \quad (4.57)$$

which can be solved in terms of the hypergeometric function  ${}_2F_1$  as

$$p_j^\lambda(x, \xi) = \theta(\xi - |x|) \xi^{-j-1} \mathcal{P}_j^\lambda\left(\frac{x}{\xi}\right) + \theta(x-\xi) \xi^{-j-1} \mathcal{Q}_j^\lambda\left(\frac{x}{\xi}\right), \quad (4.58)$$

where

$$\mathcal{P}_j^\lambda(y) = \frac{2^{j+\lambda-1/2}\Gamma(j+\lambda+1)}{\Gamma(1/2)\Gamma(j+1)\Gamma(\lambda+1/2)}(1+y)^{\lambda-1/2} {}_2F_1\left(\begin{matrix} -j-\lambda+1/2 & j+\lambda+1/2 \\ \lambda+1/2 \end{matrix} \middle| \frac{1+y}{2}\right), \quad (4.59)$$

$$\mathcal{Q}_j^\lambda(y) = -\frac{\sin(\pi j)}{\pi} y^{-j-1} {}_2F_1\left(\begin{matrix} (j+1)/2 & (j+2)/2 \\ j+\lambda+1 \end{matrix} \middle| \frac{1}{y^2}\right). \quad (4.60)$$

On the crossover line these polynomials reduce to

$$p_j^\lambda(x, \xi = x) = (-1)^{\lambda+1/2} 2^{j+2\lambda-1} x^{-j-1} \frac{\Gamma(\lambda-1/2)\Gamma(j+\lambda+1)}{\Gamma(1/2)\Gamma(j+2\lambda)} \frac{\sin[\pi(j+\lambda-1/2)]}{\pi}, \quad (4.61)$$

and for zero skewness to

$$p_j^\lambda(x, \xi = 0) = (-1)^{\lambda+1/2} x^{-j-1} \frac{\sin[\pi(j+\lambda-1/2)]}{\pi}. \quad (4.62)$$

Up to a few prefactors, this is the integral kernel for the inverse Mellin moments, which should be the case because in the forward limit we need to recover PDFs.

The next step is to deform the contour in the Sommerfeld-Watson integral in order to follow a straight vertical line in the complex plane, the choice of which depends on the poles of the GPD moments. The idea is to have all of the poles coming from the GPD moments on the left side of the vertical line so that they are not included in the contour. The contour is depicted in figure 4.1 below.

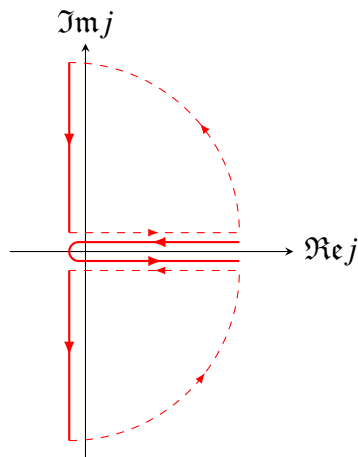


Figure 4.1: Integral contour of the Mellin-Barnes representation of the GPD.

We can write the Mellin-Barnes integral representation of GPDs

$$f^A(x, \xi, \Delta^2) = \frac{i}{2} \int_{c-i\infty}^{c+i\infty} dj \frac{1}{\sin \pi j} p_j^\lambda(x, \xi) f_j^A(\xi, \Delta^2), \quad (4.63)$$

where the value of the constant  $c$  determines the position of the vertical line in the contour. This contour includes two quarter circles whose contribution to the integral vanishes.

Let us derive the Mellin-Barnes representation for GPDs on the cross-over line  $x = \xi$ . We first write the GPD representations for quarks and gluons

$$F^{q(\pm)}(x, \xi = x, \Delta^2) = \frac{1}{2\pi i} \int_{c-i\infty}^{c+i\infty} dj \frac{2^{j+1} \Gamma(j+5/2)}{\Gamma(3/2) \Gamma(j+3)} x^{-j-1} F_j^{q(\pm)}(\xi, \Delta^2), \quad (4.64)$$

$$F^G(x, \xi = x, \Delta^2) = \frac{1}{2\pi i} \int_{c-i\infty}^{c+i\infty} dj \frac{2^{j+2} \Gamma(j+5/2)}{\Gamma(3/2) \Gamma(j+4)} x^{-j} F_j^G(\xi, \Delta^2). \quad (4.65)$$

For ease of presentation we introduce the shorthand notation

$$\Gamma_j^{3/2} = \frac{2^{j+1} \Gamma(j+5/2)}{\Gamma(3/2) \Gamma(j+3)}, \quad \Gamma_j^{5/2} = \frac{2^{j+2} \Gamma(j+5/2)}{\Gamma(3/2) \Gamma(j+4)}. \quad (4.66)$$

The GPDs in the integral include the evolution operator, and for ease of calculation we use the evolution basis defined in chapter 2. In that case, at NLO, the non-singlet contribution evolves without mixing of quarks and gluons, and separately from the singlet contribution, where quarks and gluons do mix. For the singlet quark and gluon GPD moments we introduce the vector

$$\mathbf{F}_j(\xi, \Delta^2) = \begin{pmatrix} F_j^{0(+)} \\ F_j^G \end{pmatrix}(\xi, \Delta^2). \quad (4.67)$$

In this work we evolve GPDs in the  $\overline{\text{MS}}$  scheme, where we write the GPD evolution from the input scale  $\mu_0$  to the factorization scale  $\mu_F$  for non-singlet GPDs as

$$F_j^A(\xi, \Delta^2, \mu_F^2) = \sum_{k=0}^j \frac{1 - \sigma(-1)^k}{2} \sigma E_{jk}(\mu_F, \mu_0; \xi) F_k^A(\xi, \Delta^2, \mu_0^2), \quad (4.68)$$

where  $A \in \{q(-), 3(+), 8(+), 15(+)\}$  and the factor  $\sigma$  is the same factor that we introduced in the definition of charge even and odd GPDs. Notice that the evolution operator also has a  $\sigma$  index, which signifies the need to replace all ambiguous factors  $(-1)^j$  in the anomalous

dimension with  $-\sigma$ . For the singlet GPD 4.67 the evolution is given as

$$F_j(\xi, \Delta^2, \mu_F^2) = \sum_{k=0}^j \frac{1 \mp (-1)^k}{2} E_{jk}(\mu_F, \mu_0; \xi) F_k(\xi, \Delta^2, \mu_0^2), \quad (4.69)$$

where the evolution operator is a matrix. The detailed form of the evolution operator will be given in Section 6.2.

For the non-singlet GPD we can write

$$F^A(x, \xi = x, \Delta^2, \mu_F^2) = \frac{1}{2\pi i} \int_{c-i\infty}^{c+i\infty} dj x^{-j-1} \sigma \Gamma_j^{3/2}(\mu_F, \mu_0) F_j^A(\xi = x, \Delta^2, \mu_0^2), \quad (4.70)$$

where we have combined the polynomials and the evolution operator as

$$\sigma \Gamma_j^{3/2}(\mu_F, \mu_0) = \Gamma_j^{3/2\sigma} E_{j,j}(\mu_F, \mu_0; 1) - \frac{1}{4i} \int_{d-i\infty}^{d+i\infty} dm \cot\left(\frac{\pi m}{2}\right) \Gamma_{j+m+2}^{3/2} \sigma E_{j+m+2,j}(\mu_F, \mu_0; 1). \quad (4.71)$$

The evolution and conformal prefactors are written in the form of a Mellin-Barnes integral, where due to the poles of  $\cot(\pi m/2)$  at even integer values of  $m$ , we choose  $-2 < d < 0$  [101].

For the singlet sector we write

$$F(x, \xi = x, \Delta^2, \mu_F^2) = \frac{1}{2\pi i} \int_{c-i\infty}^{c+i\infty} dj x^{-j-1} \begin{pmatrix} 1 & 0 \\ 0 & x \end{pmatrix} \sigma \Gamma_j(\mu_F, \mu_0) F_j(\xi = x, \Delta^2, \mu_0^2), \quad (4.72)$$

where the mixing of quarks and gluons is given in terms of the evolution matrix

$$\sigma \Gamma_j(\mu_F, \mu_0) = \sum_{\substack{m=0 \\ \text{even}}}^{\infty} \begin{pmatrix} \Gamma_{j+m}^{3/2} & 0 \\ 0 & \Gamma_{j+m}^{5/2} \end{pmatrix} \sigma E_{j+m,j}(\mu_F, \mu_0; \xi = 1). \quad (4.73)$$

In order to control the convergence of the integrand and simplify numerical integration, the integration contour can be deformed by introducing

$$j = c + ye^{i\phi}, \quad (4.74)$$

where  $y$  is now the integration variable. We do this in order to dampen the integrand for large values of  $y$  due to the factor  $x^{-y \exp(i\phi)}$ , which can be accomplished by choosing  $\phi > \pi/2$ . The original contour is recovered for  $\phi = \pi/2$ . The deformed contour is represented in figure 4.2 below.

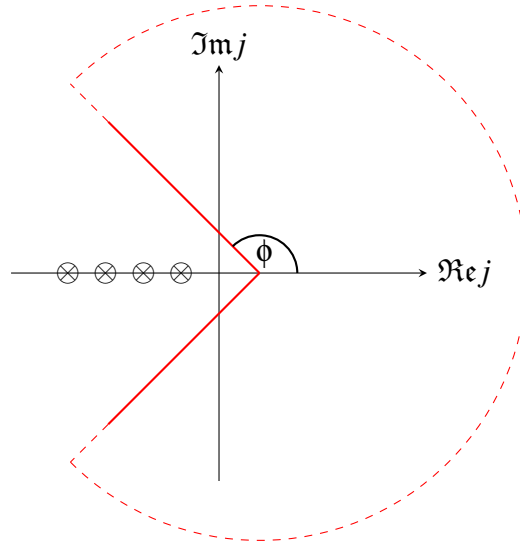


Figure 4.2: Deformed integral contour of the Mellin-Barnes integral.

The choice of  $\phi$  and  $c$  should not change the final result, but care must be taken to avoid any poles coming from GPD moments or the evolution operator, which are depicted in Figure 4.2 with  $\otimes$  symbols.

Finally, the Schwarz reflection principle can be used to integrate only over one of the legs in the deformed contour. This gives us GPDs at the crossover line in the Mellin-Barnes representation

$$F^{q(\pm)}(x, \xi = x, \Delta^2) = \frac{1}{\pi} \Im m e^{i\phi} \int_0^\infty dy \frac{2^{j+1} \Gamma(j+5/2)}{\Gamma(3/2) \Gamma(j+3)} x^{-j-1} F_j^{q(\pm)}(\xi = x, \Delta^2) \Big|_{j=c+ye^{i\phi}}, \quad (4.75)$$

$$F^G(x, \xi = x, \Delta^2) = \frac{1}{\pi} \Im m e^{i\phi} \int_0^\infty dy \frac{2^{j+2} \Gamma(j+5/2)}{\Gamma(3/2) \Gamma(j+4)} x^{-j} F_j^G(\xi = x, \Delta^2) \Big|_{j=c+ye^{i\phi}}. \quad (4.76)$$

A similar procedure can be applied for GPDs evaluated at any  $\xi$ , but since we will only be using GPDs at the crossover line, we just write the general Mellin-Barnes representation of GPDs

$$F^{q(\pm)}(x, \xi, \Delta^2) = \frac{1}{2\pi i} \int_{c-i\infty}^{c+i\infty} dj \frac{p_j^{3/2}(x, \xi)}{\sin(\pi j)} F_j^{q(\pm)}(\xi, \Delta^2), \quad (4.77)$$

$$F^G(x, \xi, \Delta^2) = \frac{1}{2\pi i} \int_{c-i\infty}^{c+i\infty} dj \frac{p_{j-1}^{5/2}(x, \xi)}{\sin(\pi j)} F_j^G(\xi, \Delta^2), \quad (4.78)$$

where the polynomials are given in (4.58).

We have managed to reconstruct the GPDs in the  $x$ -space from conformal moments using analytic continuation. The study of GPDs in the conformal space can be useful because the evolution is simpler, it is multiplicative as opposed to it being a convolution, which is numerically easier to treat.

## 4.4 Mellin-Barnes representation of scattering amplitudes

In this section we study the scattering amplitudes of DVCS and DVMP, which contain convolutions of GPDs with the corresponding hard scattering part of the amplitude. The Mellin-Barnes representation of GPDs can be used to directly calculate CFFs and TFFs without having to first obtain GPDs in the  $x$ -space. As a primer, we observe structure functions which are also written as convolutions of PDFs and the hard scattering part of the amplitude in the forward limit.

### 4.4.1 Structure functions

We have seen in (2.37) that at LO the structure functions are proportional to PDFs, but at NLO the structure functions are convolutions of the hard and soft parts of the DIS, similarly to CFFs in DVCS and TFFs in DVMP. We introduce the notation

$$F_\ell(x_B, Q^2) = \sum_q Q_q^2 F_\ell^{q(+)}(x_B, Q^2) + Q_G^2 F_\ell^G(x_B, Q^2), \quad (4.79)$$

with  $Q_G$  defined in (2.56), and  $\ell \in \{1, 2\}$ . The structure functions are defined as

$$F_\ell^{q(+)}(x_B, Q^2) = \int_{-1}^1 \frac{dx}{x} {}^q T_\ell^V \left( \frac{x_B}{x} \middle| \alpha_s(\mu_R), \frac{Q^2}{\mu_F^2} \right) f^{q(+)}(x, \mu_F^2), \quad (4.80)$$

$$F_\ell^G(x_B, Q^2) = \int_{-1}^1 \frac{dx}{x} {}^G T_\ell^V \left( \frac{x_B}{x} \middle| \alpha_s(\mu_R), \frac{Q^2}{\mu_F^2} \right) f^G(x, \mu_F^2). \quad (4.81)$$

At LO the hard-scattering amplitudes are

$${}^q T_\ell^{V(0)} \left( \frac{x_B}{x} \right) = \frac{1}{\pi} \Im \frac{1}{\frac{x_B}{x} - 1 - i\epsilon} = \delta \left( \frac{x_B}{x} - 1 \right), \quad {}^G T_\ell^{V(0)} \left( \frac{x_B}{x} \right) = 0, \quad (4.82)$$

which reflects the fact that at LO we observe DIS as a scattering of a virtual photon off a point particle which is one of the quarks inside the proton.

Writing the PDFs in terms of Mellin moments gives

$$F_l^{q(+)}(x_B, Q^2) = \frac{1}{2\pi i} \int_c dj x_B^{-j} q_{\tilde{c}_{l,j}}^{\mathcal{V}} \left( \alpha_s(\mu_R), \frac{Q^2}{\mu_F^2} \right) f_j^{q(+)}(\mu_F^2), \quad (4.83)$$

$$F_l^G(x_B, Q^2) = \frac{1}{2\pi i} \int_c dj x_B^{-j} G_{\tilde{c}_{l,j}}^{\mathcal{V}} \left( \alpha_s(\mu_R), \frac{Q^2}{\mu_F^2} \right) f_j^G(\mu_F^2). \quad (4.84)$$

We denote the Mellin moments of the hard-scattering amplitude as  $\tilde{c}$ . At LO they are

$$q_{\tilde{c}_{1,j}}^{\mathcal{V}(0)} = q_{\tilde{c}_{2,j}}^{\mathcal{V}(0)} = 1, \quad G_{\tilde{c}_{1,j}}^{\mathcal{V}(0)} = G_{\tilde{c}_{2,j}}^{\mathcal{V}(0)} = 0. \quad (4.85)$$

Structure functions also mix under evolution, so we introduce the same evolution basis as for CFFs and TFFs. The structure functions in this basis are given as

$$F_l(x_B) = \sum_A \hat{c}_\gamma^A F_l^A(x_B), \quad A \in \{0(+), 3(+), 8(+), 15(+), G\}, \quad (4.86)$$

with the same coefficients as for CFFs. For the non-singlet sector the Mellin-Barnes representation of the structure function yields

$$F_l^A(x_B) = \frac{1}{2\pi i} \int_c dj x_B^{-j} \tilde{q}_{l,j}^{\mathcal{V}} \left( \alpha_s(\mu_R), \frac{Q^2}{\mu_F^2} \right) f_j^A(\mu_F), \quad A \in \{3(+), 8(+), 15(+)\}. \quad (4.87)$$

The evolution is given as

$$F_l^A(x_B) = \frac{1}{2\pi i} \int_c dj x_B^{-j} \tilde{c}_{l,j}^{\mathcal{V}}(Q^2, Q_0^2) f_j^A(Q_0^2), \quad (4.88)$$

where the hard-scattering coefficients and the evolution operator are written succinctly as

$$q_{\tilde{c}_{l,j}}^{\mathcal{V}}(Q^2, Q_0^2) = q_{\tilde{c}_{l,j}}^{\mathcal{V}} \left( \alpha_s(\mu_R), \frac{Q^2}{\mu_F^2} \right) \sigma E_{j,j}(\mu_F, Q_0; 0). \quad (4.89)$$

In the singlet sector we introduce the same vector as we did for GPDs

$$\mathbf{f}_j = \begin{pmatrix} f_j^{0(+)} \\ f_j^G \end{pmatrix} \quad (4.90)$$

so that the Mellin-Barnes representation can be written as

$$F_l^S(x_B, Q^2) = \frac{1}{2\pi i} \int_c dj x_B^{-j} \tilde{c}_{l,j}^{\mathcal{V}} \left( \alpha_s(\mu_R), \frac{Q^2}{\mu_F^2} \right) \cdot \mathbf{f}_j(\mu_F^2), \quad (4.91)$$

with the hard-scattering amplitude vector

$$\tilde{\mathbf{c}}_{l,j}^{\mathbf{V}} = \begin{pmatrix} q \tilde{c}_{l,j}^{\mathbf{V}} & G \tilde{c}_{l,j}^{\mathbf{V}} \end{pmatrix}. \quad (4.92)$$

The evolution in the Mellin-Barnes representation is incorporated as

$$F_l^{\mathbf{S}}(x_{\mathbf{B}}, Q^2) = \frac{1}{2\pi i} \int_c dj x_{\mathbf{B}}^{-j} \tilde{\mathbf{c}}_{l,j}^{\mathbf{V}}(Q^2, \mu_0^2) \cdot \mathbf{f}_j(\mu_{\mathbf{F}}^2), \quad (4.93)$$

with the hard scattering vector and evolution operator written succinctly as

$$\tilde{\mathbf{c}}_{l,j}^{\mathbf{V}}(Q^2, \mu_0^2) = \tilde{\mathbf{c}}_{l,j}^{\mathbf{V}} \left( \alpha_s(\mu_{\mathbf{R}}), \frac{Q^2}{\mu_{\mathbf{F}}^2} \right) E_{j,j}(\mu_{\mathbf{F}}, Q_0; 0). \quad (4.94)$$

#### 4.4.2 Compton form factors

Compton form factors appear in the DVCS amplitude and due to the factorization theorem, can be written as a convolution of the hard and soft scattering parts. The soft parts are GPDs, and in this chapter we use their Mellin-Barnes representation in order to expand the CFFs in conformal partial waves. The uniqueness of the analytic continuation  $n \rightarrow j$  is guaranteed by Carlson's theorem [106].

We start with the quark CFFs at LO

$$\mathcal{F}^q(\xi, \Delta^2, Q^2) = \int_{-1}^1 dx \left[ \frac{1}{\xi - x - i\epsilon} \mp \frac{1}{\xi - x - i\epsilon} \right] F^q(x, \xi, \Delta^2, Q^2), \quad (4.95)$$

where the minus sign corresponds to the vector CFFs, and the plus sign corresponds to axial-vector CFFs. Writing the GPDs in terms of quark and antiquark distributions and using the Mellin-Barnes representation, we can integrate out the  $x$  dependence and write [100]

$$\mathcal{F}^q(\xi, \Delta^2, Q^2) = \frac{1}{2i} \int_{c-i\infty}^{c+i\infty} dj \xi^{-j-1} \frac{2^{j+1} \Gamma(j+5/2)}{\Gamma(3/2) \Gamma(j+3)} \left[ i \pm \left\{ \begin{matrix} \tan \\ \cot \end{matrix} \right\} \left( \frac{\pi j}{2} \right) \right] F_j^q(\xi, \Delta^2, Q^2). \quad (4.96)$$

This can easily be expanded to include higher orders in perturbation theory, so we can write

$$\mathcal{F}^q(\xi, \Delta^2, Q^2) = \frac{1}{2i} \int_{c-i\infty}^{c+i\infty} dj \xi^{-j-1} \frac{2^{j+1} \Gamma(j+5/2)}{\Gamma(3/2) \Gamma(j+3)} \left[ i \pm \left\{ \begin{matrix} \tan \\ \cot \end{matrix} \right\} \left( \frac{\pi j}{2} \right) \right] {}^q c_j^{\mathbf{I}F_j^q}(\xi, \Delta^2, Q^2). \quad (4.97)$$

We adopt the convention for expansion of the hard-scattering coefficients in terms of the strong

coupling constant

$${}^q c_j^I \left( \alpha_s(\mu_R), \frac{Q^2}{\mu_F^2} \right) = {}^q c_j^{I(0)} + \frac{\alpha_s^2(\mu_R)}{2\pi} {}^q c_j^{I(1)} \left( \alpha_s(\mu_R), \frac{Q^2}{\mu_F^2} \right) + \mathcal{O}(\alpha_s^4). \quad (4.98)$$

For the purposes of easier evolution, we work with quark GPDs with definite charge symmetry. For example, the GPD  $F^{q(+)}$  is antisymmetric for vector GPDs and symmetric for axial-vector GPDs, which in turn means that their conformal moments are odd and even, respectively. Under charge parity the conformal moments obtain a factor  $(-1)^n$ , which cannot be analytically continued in an unambiguous way when we make the transition  $n \rightarrow j$ . This is why we introduce a replacement  $(-1)^n \rightarrow -\sigma$  for the non-singlet CFFs, where  $\sigma = +1$  for the vector sector, and  $\sigma = -1$  for the axial-vector sector. We already encountered this in the definition of GPD evolution operators. The signature for all GPDs is given in Table 4.1 below.

GPD	$C$	$\sigma$	moments	MBR
$H^{q(C)}, E^{q(C)}$	+	+	odd	tan
	-	-	even	cot
$H^G, E^G$	+	+	odd	tan
$\tilde{H}^{q(C)}, \tilde{E}^{q(C)}$	+	-	even	cot
	-	+	even	tan
$\tilde{H}^G, \tilde{E}^G$	-	-	odd	cot

Table 4.1: Charge parity, signature, conformal momenta and Mellin-Barnes representation factors for all GPDs occurring in CFFs and TFFs.

We define the conformal moments with a definite signature

$$\sigma_{T_j} = \frac{1 - \sigma(-1)^j}{2} q_{T_j}, \quad (4.99)$$

which allows for the same Mellin-Barnes representation of CFFs for any choice of the hard-scattering amplitude.

In order to implement the evolution, we observe the quantities that make up the CFFs, namely the hard-scattering amplitudes, the evolution operators and the GPDs, we reshuffle the

summation indices in order to obtain

$$\mathbf{T}_j(\dots Q^2/\mu^2 \dots) \otimes^j \mathbf{E}_{jl}(\mu, \mu_0; \xi) \otimes^l \mathbf{H}_l(\dots \mu_0^2) = \mathbf{T}_l(\dots Q^2/\mu^2 \dots) \otimes^l \mathbf{E}_{lj}(\mu, \mu_0; \xi) \otimes^j \mathbf{H}_j(\dots \mu_0^2). \quad (4.100)$$

This formality switches the evolution operator from GPDs to the hard-scattering coefficients, allowing us to store the "evolved" hard-scattering coefficients into computer memory and to call them up during fitting of GPDs to data. By using the same procedure as for writing the Mellin-Barnes representation of GPDs, we can transform the summation over  $l$  into an integral, so that the expression (4.100) is written as

$$\mathbf{T}_j(\dots Q^2/\mu^2 \dots) \otimes^j \mathbf{H}_j(\dots \mu^2) = \bar{\mathbf{T}}_j(\dots Q^2/\mu^2 \dots; \{\mu, \mu_0\}) \otimes^j \mathbf{H}_j(\dots \mu_0^2), \quad (4.101)$$

where we introduced

$$\begin{aligned} \bar{\mathbf{T}}_j\left(\dots \frac{Q^2}{\mu^2} \dots; \{\mu, \mu_0\}\right) &= \mathbf{T}_j(\dots Q^2/\mu^2 \dots) E_{jj}(\mu, \mu_0; 1) \\ &\quad - \frac{1}{4i} \int_{c'-i\infty}^{c'+i\infty} dl \cot\left(\frac{\pi l}{2}\right) \mathbf{T}_{j+l+2}(\dots Q^2/\mu^2 \dots) E_{j+l+2,j}(\mu, \mu_0; 1), \end{aligned} \quad (4.102)$$

similar to (4.71), and  $\otimes^j$

$$\mathbf{T}_j(\dots) \otimes^j \mathbf{H}_j(\dots) \equiv \frac{1}{2i} \int_{c-i\infty}^{c+i\infty} dj \xi^{-j-1} \left[ i + \tan\left(\frac{\pi j}{2}\right) \right] \mathbf{T}_j(\dots) \mathbf{H}_j(\dots). \quad (4.103)$$

In this work we will use  $c' = -0.25$ . This form is applicable to both the vector and axial-vector GPDs. By writing the hard-scattering amplitude in this way, we can access the gluon contribution already at LO. This way we can also assess the contributions of quarks and gluons at the input scale since they are all written under one expression, and not separated into hard-scattering coefficients and evolution.

Without going into detail, we write the final form of the Mellin-Barnes representation of non-singlet and singlet CFFs in the evolution basis

$$\mathcal{F}^A(\xi, \Delta^2, Q^2) = \frac{1}{2i} \int_{c-i\infty}^{c+i\infty} dj \xi^{-j-1} \begin{bmatrix} \tan \\ \cot \end{bmatrix} \sigma \bar{\mathbf{T}}_j^I(Q^2, \mu_0^2) F_j^A(\xi, \Delta^2, \mu_0^2), \quad (4.104)$$

$$\mathcal{F}^S(\xi, \Delta^2, Q^2) = \frac{1}{2i} \int_{c-i\infty}^{c+i\infty} dj \xi^{-j-1} \begin{bmatrix} \tan \\ \cot \end{bmatrix} \bar{\mathbf{T}}_j^I(Q^2, \mu_0^2) F_j^S(\xi, \Delta^2, \mu_0^2), \quad (4.105)$$

where the singlet hard-scattering amplitude is given as a row vector

$$\mathbf{T}_j^I = \frac{2^{n+1}\Gamma(n+5/2)}{\Gamma(3/2)\Gamma(n+3)} \left( {}^q c_j^I \quad \frac{2}{j+3} G_{c_j^I} \right), \quad (4.106)$$

with the index I denoting the order of perturbation, and where we introduce the short-hand notation

$$\left[ i \pm \left\{ \begin{array}{c} \tan \\ \cot \end{array} \right\} \left( \frac{\pi j}{2} \right) \right] = \left[ \begin{array}{c} \tan \\ \cot \end{array} \right]. \quad (4.107)$$

The tan factor corresponds to the vector GPDs, and the cot factor to the axial-vector GPDs. Here we again wrote the hard scattering part together with the evolution operator.

### 4.4.3 Transition form factors

We now apply the same procedure for the Mellin-Barnes representation of transition form factors, which appear in the cross section of DVMP. Here we have an additional complication because of the presence of distribution amplitudes. We have shown the expansion of DAs and GPDs in terms of conformal moments, so we write the TFFs as an infinite sum over the conformal moments

$$\mathcal{F}^{q(\pm)}(\xi, \Delta^2, Q^2) = \frac{f C_F}{Q N_c} \sum_{n,k=0}^{\infty} \xi^{-n-1} \varphi_k(\mu_\phi^2) {}^q T_{nk}^I \left( \frac{Q^2}{\mu_F^2}, \frac{Q^2}{\mu_\phi^2}, \frac{Q^2}{\mu_R^2} \right) F_n^{q(\pm)}(\xi, \Delta^2, \mu_F^2), \quad (4.108)$$

$$\mathcal{F}^G(\xi, \Delta^2, Q^2) = \frac{f}{Q N_c} \sum_{n,k=0}^{\infty} \xi^{-n-1} \varphi_k(\mu_\phi^2) G T_{nk}^I \left( \frac{Q^2}{\mu_F^2}, \frac{Q^2}{\mu_\phi^2}, \frac{Q^2}{\mu_R^2} \right) F_n^G(\xi, \Delta^2, \mu_F^2). \quad (4.109)$$

Note that we now have a dependence on the factorization scale of the DA, so we denote the factorization scales for GPDs ( $\mu_F$ ) and DAs ( $\mu_\phi$ ) differently.

We again need to introduce the signature for non-singlet quark hard-scattering coefficients

$${}^q T_{nk} \rightarrow {}^\sigma T_{nk}. \quad (4.110)$$

We observe the TFFs in the same evolution basis as we did the CFFs, and we observe the non-singlet and singlet sectors separately. This time we also need to include the evolution of DAs

$$\varphi_k(\mu_\phi^2) = \sum_{l=0}^k E_{kl}(\mu_\phi, \mu_0) \varphi_l(\mu_0^2), \quad (4.111)$$

which are evolved by the non-singlet evolution operator. The hard-scattering coefficients can

be written as a row vector

$$\mathbf{T}_{jk}^{\text{I}} = \frac{2^{n+1}\Gamma(n+5/2)}{\Gamma(3/2)\Gamma(n+3)} \cdot 3 \cdot \left( \frac{1}{N_f} + c_{jk}^{\text{I}} + {}^{\text{pS}}c_{jk}^{\text{I}} \quad \frac{1}{C_F} \frac{2}{j+3} {}^{\text{G}}c_{jk}^{\text{I}} \right). \quad (4.112)$$

Here we have the factor coming from the color structure

$$C_F = \frac{N_c^2 - 1}{2N_c}. \quad (4.113)$$

In the case of TFFs, as opposed to CFFs, we have an addition of DAs and their evolution. By expanding the DA in terms of conformal moments, often only a finite number of effective conformal moments is taken into consideration, so at LO in evolution we have a finite sum. At NLO, there is a mixing between DA moments, which introduces another infinite sum. Since higher conformal moments are suppressed, this sum is in practice truncated. We can then employ the same procedure as for CFFs and calculate both evolution operators together with the hard-scattering amplitude

$$\bar{\mathbf{T}}_{jk} \left( \dots, \frac{Q^2}{\mu_F^2}, \frac{Q^2}{\mu_\Phi^2}; \{\mu_F, \mu_0\}, \{\mu_\Phi, \mu'_0\} \right) = \left[ \mathbf{T}_{lm} \left( \dots, \frac{Q^2}{\mu_F^2}, \frac{Q^2}{\mu_\Phi^2} \right) \otimes^m E_{mk}(\mu_\Phi, \mu'_0) \right] \otimes^l E_{lj}(\mu_F, \mu_0; \xi). \quad (4.114)$$

Here the first evolution operator is the DA one, which is evident in the lack of skewness dependence. In practice one often takes  $\mu_0 = \mu'_0$ .

The non-singlet TFF is therefore

$$\mathcal{F}_{\text{PS}}^A(\xi, \Delta^2, Q^2) = \frac{f_{\text{CF}}}{QN_c} \frac{1}{2i} \int_c dj \xi^{-j-1} \left[ \frac{\tan}{\cot} \right] \varphi_k(\mu_0^2) \bigoplus_{\text{even}}^k \sigma \bar{\mathbf{T}}_{jk}^{\text{I}}(Q^2, \mu_0^2) F_j^A(\xi, \Delta^2, \mu_0^2), \quad (4.115)$$

where  $\bigoplus^k$  denotes the summation over the index  $k$ . In the singlet sector we have similarly

$$\mathcal{F}_{\text{V}}^S(\xi, \Delta^2, Q^2) = \frac{C_F f_{\text{V}0}}{N_c Q} \frac{1}{2i} \int_c dj \xi^{-j-1} \left[ \frac{\tan}{\cot} \right] \varphi_k(\mu_0^2) \bigoplus_{\text{even}}^k \bar{\mathbf{T}}_{jk}^{\text{I}}(Q^2, \mu_0^2) F_j(\xi, \Delta^2, \mu_0^2). \quad (4.116)$$

It is worth noting that the expressions for CFFs and TFFs derived in this chapter incorporate the dispersion relation (3.115) without the subtraction constant.

# Chapter 5

## Machine learning methods

Artificial intelligence (AI) encompasses a vast set of computer techniques that seek to replicate what is currently considered to be the most sophisticated form of natural intelligence - the human brain. Humans process vast amounts of data every second, categorize, make decisions and are able to learn how to solve problems without having prior programming to do so. Learning is one of the key elements that AI tries to tackle in replicating the human behavior. One of the subsets of AI is machine learning (ML), which uses statistical methods in order to train a computer algorithm how to perform tasks and self-improve by processing a large set of data.

We currently know that the human brain contains a multitude of neurons, which process sensory data from our surroundings in a parallel manner and send it to one another. This behavior is sought to be replicated by artificial neural networks, or simply neural nets (NN), which fall under the category of machine learning.

There are currently many resources regarding this topic. The reader is referred to [107, 108] for more details.

### 5.1 Artificial neuron

The first attempt in simulating the actions of a biological neuron came in the form of an algorithm called a perceptron [109, 110], which was used for binary classification.

The perceptron mimics human biology in the sense that it takes an input, which we label as  $x_i$ , the same way a neuron takes inputs through its dendrites. It then produces an output signal which is sent through the axon. While being sent to other neurons, the signal is multiplied by a weight  $w_{k,i}$  at the synapse, which mimics the strength of the connection between neurons. Here the index  $i$  denotes the signal, and the index  $k$  denotes the perceptron/neuron. These synaptic strengths, or weights, are the learnable part of machine learning and they tell the perceptron

how important each signal is. All of the input signals multiplied by their weights are summed in the cell body. This part is called a linear combiner. If this sum exceeds a certain threshold, the neuron fires the signal through the axon. For computational purposes we implement an activation function at this point, which squashes the amplitude of the output. Often times we chose this function to give us an output in the range  $[0, 1]$  or  $[-1, 1]$ . At this point we can also add a bias  $b_k$  to the linear combiner in order to shift the weighted sum to include a broader spectrum of possible outputs.

Mathematically, a perceptron  $k$  can be described by the equation of the linear combiner

$$u_k = \sum_{i=1}^m w_{k,i} x_i, \quad (5.1)$$

and the output

$$y_k = f(u_k + b_k), \quad (5.2)$$

where  $x_i$  are the inputs in the perceptron,  $w_{k,i}$  are the weights of each input,  $u_k$  is the linear combiner output,  $f$  is the activation function,  $b_k$  is the bias on this perceptron, and  $y_k$  is the output of this perceptron. We see that the bias applies an affine transformation to the output. The input and output are related linearly in this model.

The original perceptron was used for binary classification, therefore it utilized a threshold activation function, i.e. a Heaviside step function. This model of the perceptron is depicted in figure 5.1 below.

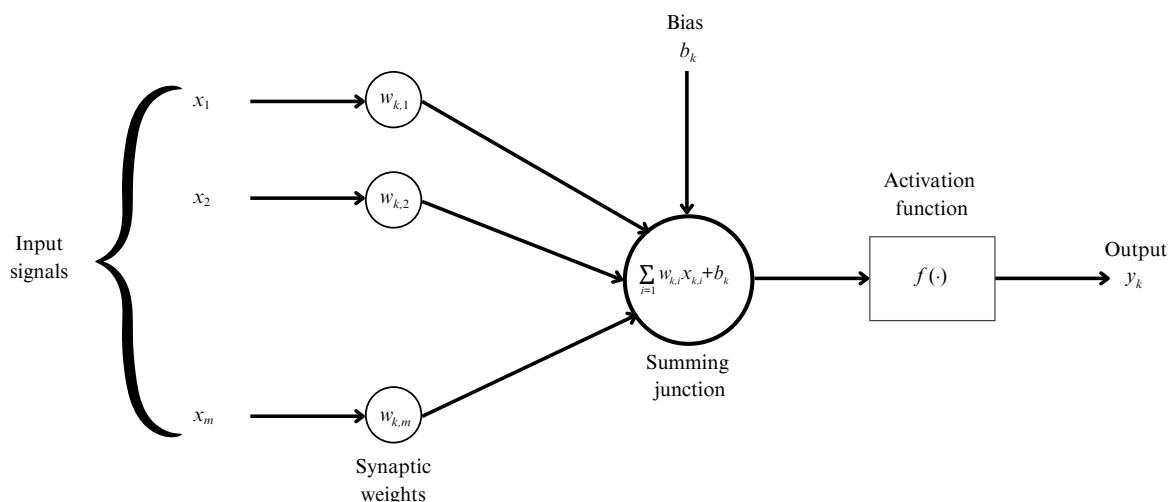


Figure 5.1: Model of a perceptron.

## 5.2 Neural networks

Neural networks used in this work can be thought of as multilayered perceptrons, with the exception that the activation function is typically non-linear. There are several types of activation functions. In modern applications we often see a sigmoid function, more specifically a logistic sigmoid function with saturating properties for large and small values of  $x$

$$f(x) = \frac{1}{1 + e^{-x}}, \quad (5.3)$$

which is the one we will be using in this work. It is depicted in figure 5.2 below.

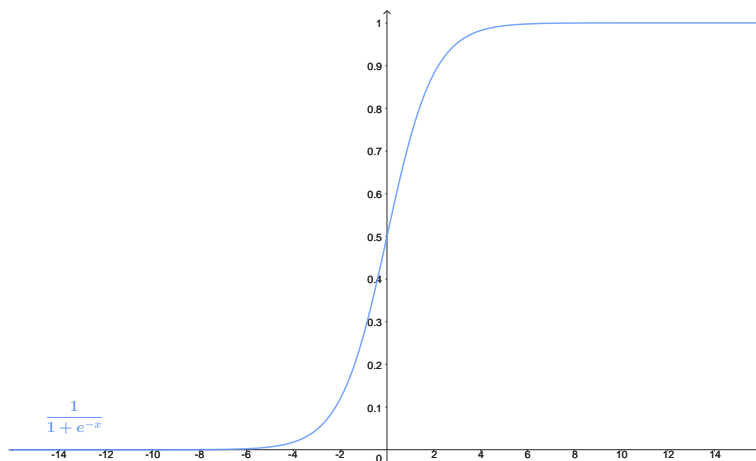


Figure 5.2: Sigmoid activation function.

Neural network models can be depicted by signal-flow graphs, which are networks of directed links or branches that are interconnected at various points called nodes. An example of that is depicted in figure 5.1. These graphs depict the layout of the neural network, which is commonly referred to as an architecture.

There are many types of neural network architectures, depending on the type of problem they are trying to solve. One of them is a multilayer feedforward network, in which neurons are organized into layers. We can consider the simplest perceptron as having an input and output layer, where the flow of information is from the input to the output, and not vice versa. This is a feedforward or acyclic type of network. Multilayer networks have additional layers between the input and output layer, called hidden layers. This yields a more complex model which is able to achieve higher order statistics. The outputs of the previous layer represent inputs for the next layer, and typically the input comes only from the preceding layer. In figure 5.3 below we have an example of a multilayer feedforward perceptron network with two hidden layers. This

architecture is sometimes denoted as 3-4-4-1, which symbolizes three source neurons or nodes, four neurons in the first hidden layer, four neurons in the second hidden layer, and one neuron in the output. This type of network is also completely connected, meaning that each neuron is connected to all neurons from the preceding and following layer.

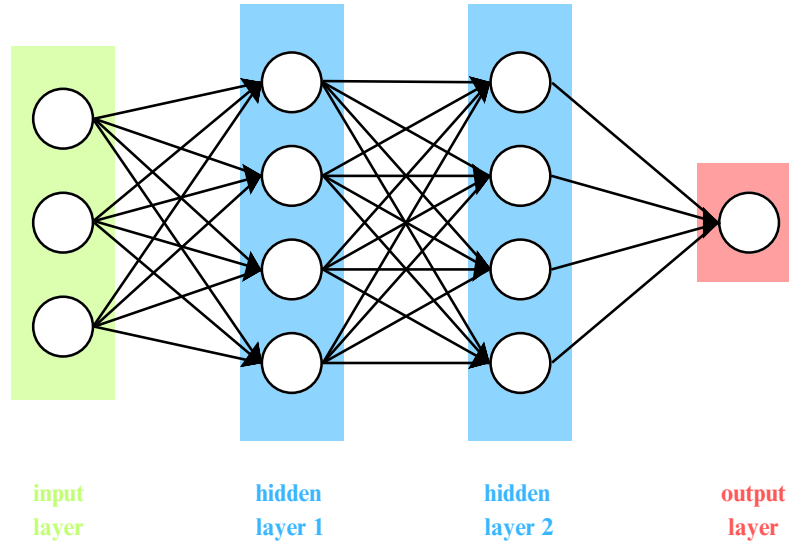


Figure 5.3: Example of a neural network architecture.

Say that we have a neural network with  $m$  layers, not including the input layer, and the number of nodes in layer  $l$  is denoted as  $N_l$ , with  $l = 1, 2, \dots, m$ . The inputs can be written as a vector  $\mathbf{x} = (x_1, x_2, \dots, x_n)^T$ . In the first hidden layer, each neuron acts on the inputs with weights  $w_{k,1}, w_{k,2}, \dots, w_{k,n}$ , where  $k$  denotes the neuron in the first hidden layer. After the action of the activation function in the first layer, we denote the outputs as  $h_{k,1}$ , where  $k$  again denotes the neuron in the first layer. Since the first layer has  $N_1$  nodes, we have  $N_1$  equations for the outputs of each neuron

$$h_{k,1} = f \left( \sum_{i=1}^n w_{k,i} x_i + b_{k,1} \right). \quad (5.4)$$

We can introduce the notation

$$\mathbf{h}_1 = f(\mathbf{W}_1 \mathbf{x} + \mathbf{b}_1), \quad (5.5)$$

where we assume the convention that the activation function acts elementwise on each component of the input vector. The first output vector is  $\mathbf{h}_1 = (h_{1,1}, h_{2,1}, \dots, h_{N_1,1})^T$  and the bias vector

is  $\mathbf{b}_1 = (b_{1,1}, b_{2,1}, \dots, b_{N_1,1})$ . The weight matrix for the first layer is

$$W_1 = \begin{pmatrix} w_{1,1} & w_{1,2} & \dots & w_{1,n} \\ w_{2,1} & w_{2,2} & \dots & w_{2,n} \\ \vdots & & \ddots & \\ w_{N_1,1} & w_{N_1,2} & \dots & w_{N_1,n} \end{pmatrix}. \quad (5.6)$$

We see that the first layer introduces  $N_1 \times n$  weights and  $N_1$  biases, which is  $(n + 1)N_1$  free parameters.

The outputs of the second layer can now be compactly written as

$$\mathbf{h}_2 = f(W_2 \mathbf{h}_1 + \mathbf{b}_2), \quad (5.7)$$

using the same conventions as for the first layer. The vectors  $\mathbf{h}_2$  and  $\mathbf{b}_2$  have dimension  $N_2$ , and the matrix  $W_2$  has dimension  $N_2 \times N_1$ . This layer has  $(N_1 + 1)N_2$  free parameters.

We write the rest of the hidden layers in the same manner, until we reach the output layer, which is the  $m$ -th layer. We denote the outputs as  $\hat{\mathbf{y}} = (\hat{y}_1, \hat{y}_2, \dots, \hat{y}_{N_m})$ . The dimension of the output vector is determined by the dimension of the function we are trying to replicate. The equation for the output layer is

$$\hat{\mathbf{y}} = f(W_m \mathbf{h}_{m-1} + \mathbf{b}_m). \quad (5.8)$$

This network has

$$(n + 1)N_1 + (N_1 + 1)N_2 + \dots + (N_{m-1} + 1)N_m \quad (5.9)$$

free parameters in total. The architecture from figure 5.3 has  $(3 + 1)4 + (4 + 1)4 + (4 + 1)1 = 41$  free parameters.

Such a neural network can have several applications, such as classification of input data into groups, or regression, i.e. modeling of functions. The latter is the application we are interested in.

### 5.2.1 Backpropagation

We have mentioned so far the free parameters that one finds in a typical architecture, namely the weights and biases. These are the parts of a network that constitute learning, and since a typical network has many parameters, it is important to develop an efficient algorithm for their learning. These algorithms typically utilize backpropagation, wherein a loss function is

calculated, which tells us the difference between the predicted and expected value, its gradient is obtained in dependence to all the parameters, and then each parameter is corrected in a way that reduces the gradient, since a negative gradient means that the loss function is decreasing. This method relies on the chain rule for derivations to recognize which parameter, i.e. which neuron is responsible for the value of the loss function. In this way we work from the loss function backward through the layers, hence the name backpropagation. This is an example of a gradient descent.

There are several ways we can implement a gradient descent: a full-batch gradient descent, where we update the parameter every time the whole input dataset passes through the network and back; a mini-batch gradient descent, where we pass a subset of data through the net and back and then update the parameters after each batch; a stochastic gradient descent, where the parameters are updated after each datapoint passes through the network and back. This method increases our chances of escaping a local minimum or saddle point of the loss function. Note that for a multidimensional space, the probability of encountering a saddle point is much higher than for a local minimum.

The batch gradient descent calculates the actual gradient, but it is the slowest, whereas the stochastic gradient descent calculates an approximate value of the gradient, but it is the fastest. The mini-batch gradient descent is a compromise between these two options. An example of how a full-batch gradient descent method finds a minimum in comparison to a stochastic gradient descent is given in figure 5.4 below.

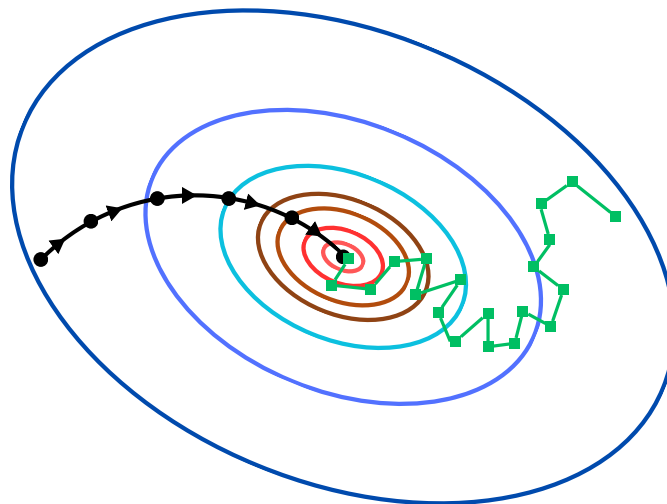


Figure 5.4: Black line represents the full-batch gradient descent, and the green line represents the stochastic gradient descent.

Let us demonstrate how the backpropagation algorithm adjusts the weights in the last layer. Say that the loss function is denoted as  $L$ . The weights in the last layer are  $w_{m,i,j}$ , where  $m$  is the index of the last layer,  $i$  is the index of the  $i$ -th output neuron, i.e. it corresponds to the output  $\hat{y}_i$ , and  $j$  is the index of the  $j$ -th neuron in the second to last layer, i.e. it is the  $j$ -th input into the last layer  $h_{m-1,j}$ . We will additionally denote  $o_i = W_i \mathbf{h}_{i-1} + \mathbf{b}_i$  and  $f_{i,j} = f(o_{i,j})$ , where  $f_{i,j}$  is the  $j$ -th component of the activation function vector  $f_i$ ,  $i$  is the index of the network layer, and  $j$  denotes the  $j$ -th component of the vector  $o_i$ . For the hidden layers we have  $f_i = \mathbf{h}_i$ , and for the last layer  $f_m = \hat{\mathbf{y}}$ .

The change in the weight can be written using the chain rule of derivatives as

$$\Delta w_{m,i,j} = \frac{\partial L}{\partial w_{m,i,j}} = \frac{\partial L}{\partial f_{m,i}} \frac{\partial f_{m,i}}{\partial o_{m,i}} \frac{\partial o_{m,i}}{\partial w_{m,i,j}}. \quad (5.10)$$

Using the definition of  $o$  and  $f$ , we can write the last term as

$$\frac{\partial o_{k,i}}{\partial w_{k,i,j}} = \frac{\partial}{\partial w_{k,i,j}} \left( \sum_l w_{k,i,l} f_{k-1,l} + b_{k,i} \right) = f_{k-1,j}. \quad (5.11)$$

The change in the weight is therefore

$$\Delta w_{m,i,j} = \frac{\partial L}{\partial f_{m,i}} \frac{\partial f_{m,i}}{\partial o_{m,i}} f_{m-1,j} = L'(f_{m,i}) f'(o_{m,i}) f_{m-1,j}. \quad (5.12)$$

Both of the derivatives in the last expression are known since we are the ones choosing the activation and loss functions.

For the weights in the inner hidden layers, it is more difficult to determine the derivative of the loss function because it depends on all the neurons that take input from the layer in question, i.e. the derivative in layer  $k$  is given as

$$\frac{\partial L}{\partial f_{k,i}} = \sum_{l=1}^{N_{k+1}} \frac{\partial L}{\partial f_{k+1,l}} \frac{\partial f_{k+1,l}}{\partial f_{k,i}}. \quad (5.13)$$

If we introduce the notation

$$\delta_{k,i} = \frac{\partial L}{\partial f_{k,i}} \frac{\partial f_{k,i}}{\partial o_{k,i}} = f'(o_{k,i}) \times \begin{cases} \sum_{l=1}^{N_{k+1}} w_{k+1,li} \delta_{k+1,l} & \text{inner neuron} \\ L'(f_{k,i}) & \text{output neuron} \end{cases}, \quad (5.14)$$

we can write the change in the weights as

$$\Delta w_{k,ij} = \delta_{k,i} f'_{k-1,j}. \quad (5.15)$$

We can see from the recursive equation (5.14) that by determining the derivatives in one layer, the calculations for the layer preceding it is greatly simplified. This procedure can be repeated for the biases, or we can add the biases to the output of each neuron and treat it as a  $(k + 1)$ -th weight.

### 5.2.2 Network training

While training a neural network on data, we need a way to produce a model that gives predictions on data it has never seen, while still predicting the data it is trained on. We do not want a model which performs artificially well on the data it learned from, only to have it fail on new data.

The way a neural network is trained is by dividing the data set into three sets, the training set, validation set and testing set. The model is first trained on the training set, which determines some values for the weights and biases. This model is then validated on the validation set, which helps us determine the so-called hyperparameters, which are the number of layers and neurons in each layer. By validating the model, we determine whether or not we need to change the hyperparameters and retrain our net. But by doing this several times, we cause an information leak from the validation set into the training set. Even though the net is not directly trained on the validation set, it still knows information about it which can result in overfitting onto the validation set, i.e. the network becomes tailored to the validation set and can have limited predicting power on a broader dataset. This model then needs to be tested against a whole new set, called the test set. The network should not have any prior knowledge of the test set. This procedure is called cross-validation.

In the case of underfitting, as we make more passes, also called epochs, through the training and validation sets, the loss function decreases on both the sets, so the generalizing ability of the model is probably very low. This occurs when the model is too simple and does not have enough parameters to adjust to the data, especially data it has not seen, so it becomes too biased to the training and validation sets.

On the other hand, overfitting occurs when the model is too complex and starts learning the noise in the data. In this instance the loss function constantly decreases on the training set, but on the validation set it decreases up until a certain point, and then starts to increase. This model has a large variance and is not specific enough to the problem we are trying to solve.

Examples of overfitting, underfitting and achieving a good fit are given in figure 5.5 below.

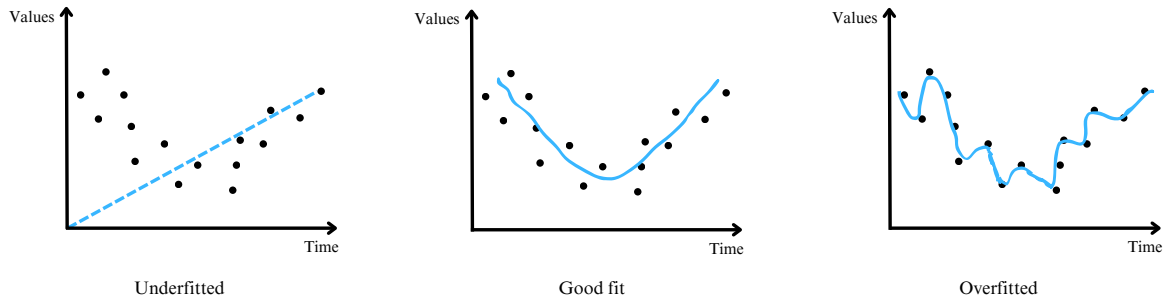


Figure 5.5: Example of an underfitted network, a good fit and an overfitted network.

An optimal model is the one between these two cases, which strikes a balance between a large bias and a large variance, called the bias-variance trade-off. One way we can determine when our model performs optimally is to use a model with a lot of parameters and determine after how many epochs the loss function on the validation set starts to increase. This is when we stop training the network. The loss function on the training and validation sets is depicted in figure 5.6 below.

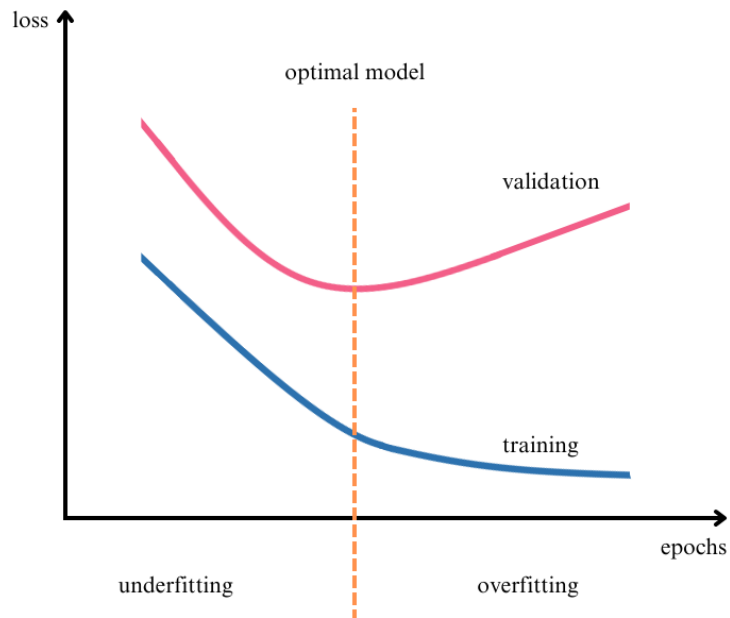


Figure 5.6: Example of loss function for an overfitted model.

The methods described in this chapter are going to be used to predict Compton form factors. We can rely on these methods and their predictive power due to the universal approximation theorem [111, 112] which states that a feedforward neural network with one hidden layer and a finite number of neurons can approximate any continuous function on a compact subset of  $\mathbb{R}^n$  with arbitrary precision. So in theory we can extract reliable CFFs, but in practice we need to find a suitable number of parameters not to overfit to the data, and we need to make sure that our model does not end up in a local minimum.

## **Part II**

### **Global fits**

## Chapter 6

# Conformal partial wave parametrization

In chapter 4 we introduced the conformal moments of GPDs and the Mellin-Barnes representation of CFFs and TFFs. Now we will write full expressions for evolution, hard-scattering amplitudes and GPD moments that we use in our numerical analysis at low  $x$ . In the case of DVMP, we will only observe neutral vector mesons, so we will only give expressions for those mesons here.

So far we have calculated the Mellin-Barnes representation of CFFs and TFFs. In our analysis of small- $x$  data we will only model the sea quarks and gluons in the conformal space, which make up the singlet sector. We therefore repeat expressions for the singlet CFF (4.105)

$$\mathcal{F}^S(\xi, \Delta^2, Q^2) = \frac{1}{2i} \int_{c-i\infty}^{c+i\infty} dj \xi^{-j-1} \begin{bmatrix} \tan \\ \cot \end{bmatrix} \bar{T}_j^I(Q^2, \mu_0^2) F_j(\xi, \Delta^2, \mu_0^2), \quad (6.1)$$

and the singlet TFF (4.116)

$$\mathcal{F}_{\text{VL}}^S(\xi, \Delta^2, Q^2) = \frac{C_{\text{F}} f_{\text{V}0}}{N_c Q} \frac{1}{2i} \int_c dj \xi^{-j-1} \begin{bmatrix} \tan \\ \cot \end{bmatrix} \Phi_k(\mu_0^2) \bigoplus_{\text{even}}^k \bar{T}_{jk}^I(Q^2, \mu_0^2) F_j(\xi, \Delta^2, \mu_0^2). \quad (6.2)$$

The index  $S$  denotes the quark singlet and gluon sectors combined.

We assume that the sea quarks are symmetric since they are created in quark-antiquark pairs, and we ignore the fact that more massive quarks have a somewhat smaller presence, as well as any mass corrections necessary for describing heavier quarks. We therefore write

$$H^{\text{sea}}(x, \dots) \approx H^\Sigma(x, \dots) \equiv \sum_{q=\text{u,d,s},\dots} H^q(x, \dots) - H^q(-x, \dots). \quad (6.3)$$

The  $t$ -dependent differential cross sections for DVCS ( $\gamma^* p \rightarrow \gamma p$ ) and DVMP ( $\gamma^* p \rightarrow \text{V}_L p$ ) at

twist-2 are given as

$$\frac{d\sigma_\gamma}{dt} = \pi\alpha_{\text{em}}^2 \frac{x_B^2}{Q^4} \left\{ |\mathcal{H}(\xi, t, Q^2)|^2 - \frac{t}{4M^2} |\mathcal{E}(\xi, t, Q^2)|^2 + |\tilde{\mathcal{H}}(\xi, t, Q^2)|^2 \right\}, \quad (6.4)$$

$$\frac{d\sigma_{\text{VL}}}{dt} = 4\pi^2\alpha_{\text{em}} \frac{x_B^2}{Q^4} \left\{ |\mathcal{H}_{\text{VL}}(\xi, t, Q^2)|^2 - \frac{t}{4M^2} |\mathcal{E}_{\text{VL}}(\xi, t, Q^2)|^2 \right\}, \quad (6.5)$$

where we have ignored contributions proportional to  $x_B^2$  from (2.53) and (2.61). We can introduce further simplifications by using arguments from Regge theory, which suggest the small- $x$  behavior  $H \sim 1/x$  and  $\tilde{H} \sim 1/\sqrt{x}$ , which in turn implies the same behavior of CFFs.  $\tilde{H}$  therefore rises slower at low  $x$  and we can ignore the  $\tilde{\mathcal{H}}$  contribution to the DVCS cross section (6.4). We can see that in both cross section the CFF/TFF  $\mathcal{E}$  contributes with the prefactor  $t/4M^2$ . For the kinematics we are studying, this prefactor is of the order  $10^{-2}$ , which allows us to ignore  $\mathcal{E}$  as well. Therefore, the cross sections for both processes depend only on the CFF/TFF  $\mathcal{H}$  and we have

$$\frac{d\sigma_\gamma}{dt} = \pi\alpha_{\text{em}}^2 \frac{x_B^2}{Q^4} |\mathcal{H}(\xi, t, Q^2)|^2, \quad (6.6)$$

$$\frac{d\sigma_{\text{VL}}}{dt} = 4\pi^2\alpha_{\text{em}} \frac{x_B^2}{Q^4} |\mathcal{H}_{\text{VL}}(\xi, t, Q^2)|^2, \quad (6.7)$$

where  $\alpha_{\text{em}}$  is the electromagnetic fine structure constant. Note that for DVCS and DVMP at low  $x$  we have  $x \approx \xi \approx x_B/2$ .

The CFFs and TFFs are given in terms of the singlet and non-singlet contributions as

$$\mathcal{H} = Q_{\text{NS}}^2 \mathcal{H}^{\text{NS}} + Q_{\text{S}}^2 \mathcal{H}^{\text{S}} = Q_{\text{NS}}^2 \mathcal{H}^{\text{NS}} + Q_{\text{S}}^2 (\mathcal{H}^\Sigma + \mathcal{H}^{\text{G}}), \quad (6.8)$$

$$\mathcal{H}_{\text{VL}}^0 = \mathcal{H}_{\text{VL}}^{\text{NS}} + Q_{\text{VL}}^0 \mathcal{H}_{\text{VL}}^{\text{S}} = \mathcal{H}_{\text{VL}}^{\text{NS}} + Q_{\text{VL}}^0 (\mathcal{H}_{\text{VL}}^\Sigma + \mathcal{H}_{\text{VL}}^{\text{G}}), \quad (6.9)$$

where for four active flavors we have

$$Q_{\text{NS}}^2 = \frac{1}{6}, \quad Q_{\text{S}}^2 = \frac{5}{18}. \quad (6.10)$$

$Q_{\text{VL}}^0$  depends on the produced meson, and we have

$$Q_{\rho^0} = \frac{1}{\sqrt{2}}, \quad Q_\phi = -\frac{1}{3}. \quad (6.11)$$

As we already mentioned, we will only be observing the singlet sector.

Our analysis of low- $x$  DVCS and DVMP data will be extended up to NLO in the strong

coupling constant. The beta function, which dictates the scale dependence of the coupling constant is itself expanded up to NLO. The scale dependence of  $\alpha_S$  is given with the equation

$$\frac{da_s}{d\ln\mu^2} = \beta_0 a_s^2 + \beta_1 a_s^3, \quad (6.12)$$

where  $a_s = \alpha_S/4\pi$ , and

$$\beta_0 = \frac{2}{3}N_f - \frac{11}{3}C_A, \quad \beta_1 = \frac{10}{3}C_A N_f + 2C_F N_f - \frac{34}{3}C_A^2. \quad (6.13)$$

For the value of  $\alpha_S$  at LO we use the analytically obtained value  $\alpha_S(\mu_0)/2\pi = 0.0606$ , and at NLO we utilize the numerical fourth-order Runge-Kutta integration to obtain  $\alpha_S(\mu_0)/2\pi = 0.0518$ , where the input scale is  $\mu_0^2 = 2.5 \text{ GeV}^2$ , and we take the number of active flavors to be  $N_f = 4$ .

## 6.1 Hard-scattering amplitudes

In this section we give the conformal hard-scattering amplitude for DVCS and DVMP in the  $\overline{\text{MS}}$  scheme up to NLO.

### 6.1.1 DVCS

The DVCS hard-scattering amplitude up to NLO in perturbation theory for the singlet parity even sector in the  $\overline{\text{MS}}$  scheme can be written as [101, 113]

$$\mathbf{T}_j^{\text{DVCS}} \left( \alpha_s(\mu_R), \frac{Q^2}{\mu_R^2}, \frac{Q^2}{\mu_F^2} \right) = \frac{2^{j+1}\Gamma(j+5/2)}{\Gamma(3/2)\Gamma(j+3)} \left[ \mathbf{c}_j^{(0)} + \frac{\alpha_s(\mu_R)}{2\pi} \mathbf{c}_j^{(1)} \left( Q^2/\mu_F^2 \right) + \mathcal{O}(\alpha_s^2) \right]. \quad (6.14)$$

At LO, the coefficients are given as

$$\Sigma c_j^{(0)} = 1, \quad \mathbf{G} c_j^{(0)} = 0, \quad (6.15)$$

and at NLO

$$\Sigma c_j^{(1)} \left( Q^2/\mu_F^2 \right) = C_F \left[ 2S_1^2(1+j) - \frac{9}{2} + \frac{5-4S_1(j+1)}{2(j+1)_2} + \frac{1}{[(j+1)_2]^2} \right] - \frac{\Sigma \Sigma \gamma_j^{(0)}}{2} \ln \frac{Q^2}{\mu_F^2} \quad (6.16)$$

$$\mathbf{G} c_j^{(1)} \left( Q^2/\mu_F^2 \right) = -N_f \frac{(4+3j+j^2)[S_1(j)+S_1(j+2)]+2+3j+j^2}{(1+j)_3} - \frac{\Sigma \mathbf{G} \gamma_j^{(0)}}{2} \ln \frac{Q^2}{\mu_F^2}. \quad (6.17)$$

Here  $(j)_n$  is the Pochhammer symbol

$$(j)_n = \frac{\Gamma(j+n)}{\Gamma(j)} = \prod_{k=0}^{n-1} (j+k), \quad (6.18)$$

and  $S_1(j)$  is the harmonic number

$$S_1(j) = \frac{d}{dj} \ln \Gamma(j+1) + \gamma_E, \quad (6.19)$$

with the Euler-Mascheroni constant  $\gamma_E = 0.57721566$ . We have elements of the LO anomalous dimension matrix, namely  ${}^{\Sigma G} \gamma_j^{(0)}$  and  ${}^{\Sigma \Sigma} \gamma_j^{(0)}$ , which will be defined in Section 6.2.

Up to NLO, the hard-scattering amplitude for the non-singlet sector is identical to the singlet quark one. Similarly, the amplitude for the CFF  $\mathcal{E}$  is also the same as the one listed here. Note that the strong coupling constant  $\alpha_s$  comes into the expression at NLO, since at LO the gluons contribute only through the evolution.

### 6.1.2 DVMP

Here we list the contributions to the singlet hard-scattering amplitude up to NLO of perturbation theory for the production of neutral vector mesons in the parity even sector

$$\begin{aligned} \mathbf{T}_{jk}^{\text{DVVP}^0\text{LP}} \left( \alpha_s(\mu_R), \frac{Q^2}{\mu_R^2}, \frac{Q^2}{\mu_F^2}, \frac{Q^2}{\mu_\Phi^2} \right) \\ = 3 \frac{2^{j+1} \Gamma(j+5/2)}{\Gamma(3/2) \Gamma(j+3)} \left[ \alpha_s(\mu_R) c_{jk}^{(0)} + \frac{\alpha_s^2(\mu_R)}{2\pi} c_{jk}^{(1)} \left( \frac{Q^2}{\mu_R^2}, \frac{Q^2}{\mu_F^2}, \frac{Q^2}{\mu_\Phi^2} \right) + \mathcal{O}(\alpha_s^3) \right], \end{aligned} \quad (6.20)$$

where the factor 3 comes from the normalization of the DA. At LO we have

$${}^{\Sigma} c_{jk}^{(0)} = \frac{1}{N_f}, \quad {}^G c_{jk}^{(0)} = \frac{2}{C_F(j+3)}. \quad (6.21)$$

At NLO we have a slightly different anatomy of the coefficients

$$\mathbf{c}_{jk}^{(1)}(\dots) = \left( \frac{1}{N_f} {}^q c_{jk}^{(1)} \left( \frac{Q^2}{\mu_R^2}, \frac{Q^2}{\mu_F^2}, \frac{Q^2}{\mu_\Phi^2} \right) + {}^{\text{PS}} c_{jk}^{(1)} \left( \frac{Q^2}{\mu_F^2} \right), \frac{2}{C_F(j+3)} {}^G c_{jk}^{(1)} \left( \frac{Q^2}{\mu_R^2}, \frac{Q^2}{\mu_F^2}, \frac{Q^2}{\mu_\Phi^2} \right) \right), \quad (6.22)$$

where we now have a combination of the non-singlet contribution  ${}^q c_{jk}$  and the pure singlet contribution  ${}^{\text{PS}} c_{jk}$ , which does not appear in DVCS at this order in perturbation theory. Typically

the contributions are separated in terms of color

$$q_{jk}^{(1)}(\dots) = C_F c_{jk}^{(1, F)} \left( \frac{Q^2}{\mu_F^2}, \frac{Q^2}{\mu_{DA}^2} \right) + \beta_0 c_{jk}^{(1, \beta)} \left( \frac{Q^2}{\mu_R^2} \right) + C_G c_{jk}^{(1, G)}, \quad (6.23)$$

$${}^{\text{pS}}c_{jk}^{(1)}(\dots) = {}^{\text{pS}}c_{jk}^{(1)} \left( \frac{Q^2}{\mu_F^2} \right), \quad (6.24)$$

$${}^{\text{G}}c_{jk}^{(1)}(\dots) = C_F {}^{\text{G}}c_{jk}^{(1, F)} \left( \frac{Q^2}{\mu_F^2}, \frac{Q^2}{\mu_{DA}^2} \right) + C_A {}^{\text{G}}c_{jk}^{(1, A)} \left( \frac{Q^2}{\mu_F^2} \right) + \frac{\beta_0}{2} \ln \frac{\mu_R^2}{\mu_F^2}, \quad (6.25)$$

where

$$C_F = \frac{4}{3}, \quad C_A = 3, \quad C_G = C_F - \frac{C_A}{2} = -\frac{1}{6}, \quad (6.26)$$

and  $\beta_0$  is given in (6.13). Here the non-singlet contributions  $c_{jk}^{(1, F)}$ ,  $c_{jk}^{(1, \beta)}$  and  $c_{jk}^{(1, G)}$ , the pure singlet contribution  ${}^{\text{pS}}c_{jk}$  and the gluon contributions  ${}^{\text{G}}c_{jk}^{(1, F)}$  and  ${}^{\text{G}}c_{jk}^{(1, A)}$  are given in [37]. As it was shown in [38], the factorization of the gluon contributions used in [37] was not the same for DVMP as it was for DVCS and DIS, and corrections were necessary to the pure singlet and gluon contributions. The two corrected expressions from [38] are

$$\begin{aligned} {}^{\text{pS}}c_{jk}^{(1)}(\dots) &= \left[ -\ln \frac{Q^2}{\mu_F^2} - 1 + 2S_1(j+1) + 2S_1(k+1) - 1 \right] \frac{\Sigma \gamma_j^{(0)}}{C_F(j+3)} \\ &\quad - \left[ \frac{1}{2} + \frac{1}{(j+1)_2} + \frac{1}{(k+1)_2} \right] \frac{2}{(j+1)_2} + {}^{\text{pS}}\Delta c_{jk}^{(1)}, \end{aligned} \quad (6.27)$$

and

$$\begin{aligned} {}^{\text{G}}c_{jk}^{(1, F)}(\dots) &= \left[ -\ln \frac{Q^2}{\mu_F^2} + S_1(j+1) + S_1(k+1) - \frac{3}{4} - \frac{1}{2(k+1)_2} - \frac{1}{(j+1)_2} \right] \frac{\Sigma \Sigma \gamma_k^{(0)}}{2C_F} \\ &\quad + \left[ -\ln \frac{Q^2}{\mu_F^2} + 1 + 3S_1(j+1) - \frac{1}{2} + \frac{2S_1(j+1) - 1}{(k+1)_2} - \frac{1}{(j+1)_2} \right] \frac{j+3}{2} \frac{\Sigma \text{G} \gamma_j^{(0)}/N_f}{2} \\ &\quad - \left[ 35 - [(k+1)_2 + 2] \Delta S_2 \left( \frac{k+1}{2} \right) + \frac{4}{[(k+1)_2]^2} \right] \frac{1}{8} \\ &\quad + \left[ \frac{[(k+1)_2 + 2] S_1(j+1)}{(k+1)_2} + 1 \right] \frac{1}{(j+1)_2} + {}^{\text{G}}\Delta c_{jk}^{(1, F)}. \end{aligned} \quad (6.28)$$

Here  $\Delta S_2$  is the difference of second order harmonic sums

$$\Delta S_2 \left( \frac{n+1}{2} \right) \equiv S_2 \left( \frac{n+1}{2} \right) - S_2 \left( \frac{n}{2} \right), \quad (6.29)$$

defined as

$$S_2(n) = \sum_{i=1}^n \frac{1}{i^2}. \quad (6.30)$$

The rest of the coefficients are listed in [37], and are the same for the TFF  $\mathcal{E}_{V_{L0}}$ . For the parity odd sector, the coefficients are given in [38].

We can see that the strong coupling constant is present at LO in the hard-scattering coefficients, and that the gluon coefficient is non-zero at LO, in contrast to DVCS where there are no gluons at LO. We can also notice that the gluon contribution to DVCS at NLO (6.17) is negative, where the dominant contribution to the amplitude is

$$-N_f \frac{S_1(j+2)}{(1+j)_3}, \quad (6.31)$$

which in the  $x$ -space corresponds to the most singular part of the amplitude

$$\frac{\ln^2(x-\xi)}{x-\xi}. \quad (6.32)$$

This means that the gluon contribution can suppress the quark contribution, which is positive. This will be tested by our analysis.

## 6.2 Evolution of GPDs and DAs

In this section we give the evolution operator mentioned in chapter 4. One of the main reasons we model CFFs and TFFs in the conformal space is to avoid the convolution (3.98) that enters these functions once we introduce QCD evolution. A code for LO evolution in the  $x$ -space has existed for a long time [114]. New advances in the  $x$ -space evolution have been made in [115] and are being implemented in the PARTONS framework [116]. Likewise, there is a code for NLO  $x$ -space evolution implemented in [117].

In the conformal partial wave expansion, the evolution at LO is diagonal and there is no mixing between conformal moments. At NLO, there is mixing in the singlet sector, and mixing of different conformal moments, but nevertheless, evolution is multiplicative and closed analytic expressions exist for all components up to NLO. For DVCS, there have been results that extend this framework up to NNLO in the conformal scheme [118, 101, 37], and in the  $\overline{\text{MS}}$  scheme [119, 120, 96, 121].

We again present the singlet case, where the evolution of the previously introduced singlet

GPD vector is given as

$$\begin{pmatrix} H_j^\Sigma(\xi, t, \mu^2) \\ H_j^G(\xi, t, \mu^2) \end{pmatrix} = E_{jl}(\mu, \mu_0; \xi) \begin{pmatrix} H_l^\Sigma(\xi, t, \mu_0^2) \\ H_l^G(\xi, t, \mu_0^2) \end{pmatrix}, \quad (6.33)$$

with the evolution operator

$$E_{jl}(\mu, \mu_0; \xi) = \sum_{a,b=\pm} \left[ \delta_{ab} P_j^a \delta_{jl} + \frac{\alpha_S(\mu)}{2\pi} \left( \mathcal{A}_j^{(1)ab}(\mu, \mu_0) \delta_{jl} + \mathcal{B}_{jl}^{(1)ab}(\mu, \mu_0) \xi^{j-l} \right) + O(\alpha_S^2) \right] \left[ \frac{\alpha_S(\mu)}{\alpha_S(\mu_0)} \right]^{-\frac{\lambda_j^b}{\beta_0}}. \quad (6.34)$$

The evolution operator up to NLO accuracy in the  $\overline{\text{MS}}$  scheme lives in the two-dimensional flavor space  $(\Sigma, G)$ , and the infinitely dimensional conformal space, and it is non-diagonal in both of them. The summation in the definition of the evolution operator goes over the eigenstates  $a, b \in \{+, -\}$  of the LO evolution operator in the  $(\Sigma, G)$  space, where the projectors onto the eigenvalue states  $P_j^\pm$  are

$$P_j^\pm = \frac{\pm 1}{\lambda_j^+ - \lambda_j^-} \left( \gamma_j^{(0)} - \lambda_j^\mp \mathbf{1} \right). \quad (6.35)$$

We can see that the first term in (6.34), which is the LO contribution, is diagonal by design in both spaces due to the two Kronecker symbols. The NLO contribution, which is proportional to  $\alpha_S$ , has a term diagonal in the conformal moments, and a non-diagonal term. Both of them are non-diagonal in the  $(\Sigma, G)$  space.

The anomalous dimensions are organized into a  $2 \times 2$  matrix  $\gamma_j^{(0)}$ , and in the parity even sector we have [122, 123]

$$\Sigma\Sigma\gamma_j^{(0)} = -C_F \left( 3 + \frac{2}{(j+1)(j+2)} - 4S_1(j+1) \right), \quad (6.36)$$

$$\Sigma G\gamma_j^{(0)} = -4N_f T_F \frac{4 + 3j + j^2}{(j+1)(j+2)(j+3)}, \quad (6.37)$$

$$G\Sigma\gamma_j^{(0)} = -2C_F \frac{4 + 3j + j^2}{j(j+1)(j+2)}, \quad (6.38)$$

$$GG\gamma_j^{(0)} = -C_A \left( -\frac{4}{(j+1)(j+2)} + \frac{12}{j(j+3)} - 4S_1(j+1) \right) + \beta_0, \quad (6.39)$$

where  $T_F = 1/2$  and the eigenvalues are

$$\lambda_j^\pm = \frac{1}{2} \left( \Sigma\Sigma\gamma_j^{(0)} + \text{GG}\gamma_j^{(0)} \mp \left( \Sigma\Sigma\gamma_j^{(0)} - \text{GG}\gamma_j^{(0)} \right) \sqrt{1 + \frac{4\Sigma\text{G}\gamma_j^{(0)}\text{G}\Sigma\gamma_j^{(0)}}{\left( \Sigma\Sigma\gamma_j^{(0)} - \text{GG}\gamma_j^{(0)} \right)^2}} \right). \quad (6.40)$$

The diagonal term in the NLO part of the evolution operator is given as

$$\mathcal{A}_j^{(1)ab} = R_{jj}^{ab}(\mu, \mu_0) \mathbf{P}_j^a \left[ \frac{\beta_1}{2\beta_0} \gamma_j^{(0)} - \gamma_j^{(1)} \right] \mathbf{P}_j^b, \quad (6.41)$$

with

$$R_{jl}^{ab}(\mu, \mu_0) = \frac{1}{\beta_0 + \lambda_j^a - \lambda_l^b} \left[ 1 - \left( \frac{\alpha_s(\mu_0)}{\alpha_s(\mu)} \right)^{\frac{\beta_0 + \lambda_j^a - \lambda_l^b}{\beta_0}} \right]. \quad (6.42)$$

Here  $\beta_0$  and  $\beta_1$  are given in (6.13), and the NLO anomalous dimension is given in [124]. The part of the NLO evolution operator that introduces mixing between conformal moments is given as

$$\mathcal{B}_{jl}^{(1)ab}(\mu, \mu_0) = -R_{jl}^{ab}(\mu, \mu_0) \left( \lambda_j^a - \lambda_l^b \right) \left[ \left( \beta_0 - \lambda_l^b \right) \mathbf{P}_j^a d_{jl} \mathbf{P}_l^b + \mathbf{P}_j^a g_{jl} \mathbf{P}_l^b \right], \quad (6.43)$$

with matrices [125]

$$d_{jk} = -\frac{2^k \Gamma(j+1) \Gamma(k+3/2)}{2^j \Gamma(k+1) \Gamma(j+3/2)} \frac{2k+3}{(j-k)(j+k+3)} \begin{pmatrix} 1 & 0 \\ 0 & k/j \end{pmatrix} \quad (6.44)$$

$$g_{jk} = \frac{2^k \Gamma(j+1) \Gamma(k+3/2)}{2^j \Gamma(k+1) \Gamma(j+3/2)} \begin{pmatrix} \Sigma\Sigma g_{jk} & k/6^{\Sigma\text{G}} g_{jk} \\ 6/j^{\text{G}\Sigma} g_{jk} & k/j^{\text{G}\text{G}} g_{jk} \end{pmatrix}. \quad (6.45)$$

The matrix elements in (6.45) are

$$\begin{aligned} \Sigma\Sigma g_{jk} = & -C_F \frac{4(2k+3)}{(j-k)(j+k+3)} \left\{ - \left( 1 + \frac{(j-k)(j+k+3)}{(k+1)(k+2)} \right) S_1(j+1) \right. \\ & \left. + \left( 1 + \frac{(j-k)(j+k+3)}{2(k+1)(k+2)} \right) \left[ S_1 \left( \frac{j+k+2}{2} \right) + S_1 \left( \frac{j-k-1}{2} \right) + \ln(4) \right] \right\}, \end{aligned} \quad (6.46)$$

$$\Sigma G g_{jk} = 0, \quad (6.47)$$

$$G\Sigma g_{jk} = -C_F \frac{(3+2k)}{3(k+1)(k+2)}, \quad (6.48)$$

$$\begin{aligned} G G g_{jk} = & -C_A \frac{4(2k+3)}{(j-k)(j+k+3)} \left\{ - \frac{(j)_4}{(k)_4} S_1(j+1) + \frac{(j-k)(j+k+3)}{(k)_4} \right. \\ & \left. + \frac{1}{2} \left( 1 + \frac{(j)_4}{(k)_4} \right) \left[ S_1 \left( \frac{j+k+2}{2} \right) + S_1 \left( \frac{j-k-1}{2} \right) + \ln(4) \right] \right\}. \end{aligned} \quad (6.49)$$

The non-singlet evolution operator is obtained from previously written quantities by reducing the matrix-valued quantities to scalar ones associated with quark components  $\Sigma\Sigma$ , i.e.

$$\begin{aligned} \gamma_j & \rightarrow {}^{\text{NS}}\gamma_j, & {}^a\lambda_j & \rightarrow {}^{\text{NS}}\gamma_j^{(0)} = \Sigma\Sigma\gamma_j^{(0)}, & {}^a\mathbf{P}_j & \rightarrow 1, \\ \gamma_{jk} & \rightarrow {}^{\text{NS}}\gamma_{jk} = \Sigma\Sigma\gamma_{jk}, & \mathbf{g}_{jk} & \rightarrow {}^{\text{NS}}\mathbf{g}_{jk} = \Sigma\Sigma\mathbf{g}_{jk}, & \mathbf{d}_{jk} & \rightarrow {}^{\text{NS}}\mathbf{d}_{jk} = \Sigma\Sigma\mathbf{d}_{jk}. \end{aligned} \quad (6.50)$$

See [101] for details. The non-singlet anomalous dimension up to NLO accuracy used here is equal to the quark-quark anomalous dimension.

The evolution operator of DAs is given by the non-singlet evolution operator for GPDs evaluated at  $\xi = 1$ , i.e.

$$\Phi_k(\mu^2) = E_{km}(\mu, \mu_0) \Phi_m(\mu_0^2), \quad (6.51)$$

with

$$\gamma_k = {}^{\text{NS}}\gamma_k, \quad E_{km}(\mu, \mu_0) = E_{km}(\mu, \mu_0; 1). \quad (6.52)$$

The DA can be written in terms of conformal moments as [54, 55]

$$\Phi(u) = 6u\bar{u} \sum_{n=0}^{\infty} C_n^{3/2} (2u-1) \Phi_n, \quad (6.53)$$

where the normalization condition gives  $\Phi_0 = 1$ . Since DAs are relatively poorly known, in our study we choose their asymptotic form

$$\Phi_{\text{V.L.},0} = 1, \quad \Phi_{\text{V.L.},k>0} = 0, \quad (6.54)$$

with the evolution operator components

$$E_{0,0}^{(0)}(\mu_\varphi, \mu_0) = 1, \quad E_{0,0}^{(1)}(\mu_\varphi, \mu_0) = \frac{1}{\beta_0} \left[ \frac{\beta_{1\text{NS}}}{\beta_0} \gamma_0^{(0)} - \text{NS} \gamma_0^{(1)} \right]. \quad (6.55)$$

We do not include the NLO evolution component since it would be a pretty small contribution to the numerical values of TFFs. For this reason our analysis is not technically fully at NLO, but for the asymptotic form of DAs that we use here, we do not expect big effect from the evolution. This effectively means that we include no contributions from the DA and its evolution, so the TFFs take on the same form as CFFs, just with different hard-scattering coefficients.

### 6.3 Modeling GPDs

In this chapter we will present our approach to modeling GPDs in the conformal space, which will be utilized in simultaneous global fits to DIS, DVCS and DVMP at low  $x$  in this chapter, and for proton and neutron DVCS fits in the next. Much of our assumptions will rely on conclusions drawn from Regge theory and studies performed on PDFs.

We have seen that GPDs depend on three variables, which we choose to be  $x$ ,  $\xi$  and  $t$ . When we expand the  $x$ -space GPDs in the conformal space, the GPD conformal moments depend on  $\xi$  and  $t$ . We adopt the approach where the skewness dependence is expanded via  $t$ -channel SO(3) partial waves, meaning that our GPDs have a double partial wave (PW) expansion. Formally we have

$$F_j^a(\xi, t) = \sum_{\substack{J=j+1 \\ \text{even}}}^{j+1} F_{j,J}^a(t) \xi^{j+1-J} \hat{d}_{\alpha,\beta}^J(\xi), \quad J = j+1, j-1, j-3, \dots, \quad a \in \{q, G\}, \quad (6.56)$$

where  $J$  is the angular momentum in the  $t$ -channel, and  $\hat{d}_{\alpha,\beta}^J(\xi)$  are the crossed version of Wigner's reduced rotation matrices. The reason we call this a  $t$ -channel expansion is that it comes about naturally in the process which is the crossed process of DVCS. If we write DVCS symbolically as a virtual photon scattering off a hadron in the  $s$ -channel

$$\gamma^*(q) + h(p) \rightarrow \gamma(q') + h(p'), \quad (6.57)$$

its  $t$ -channel counterpart is the process

$$\gamma^*(q) + \gamma(-q') \rightarrow h(p') + \bar{h}(-p). \quad (6.58)$$

Here the scattering amplitude is given by meson GPDs, which can be expanded into irreducible SO(3) representations labeled by the orbital angular momentum quantum number. By crossing this expansion back onto DVCS, we need to introduce the substitution

$$\cos \theta_t \rightarrow -\frac{1}{\xi} + \mathcal{O}(1/Q^2), \quad (6.59)$$

where  $\theta_t$  is the  $t$ -channel center-of-mass scattering angle. We can therefore describe a process in the  $s$ -channel by an exchange in the  $t$ -channel.

The partial wave amplitude  $F_{j,j+1}$  is the Mellin moment of the zero-skewness GPD, and the subleading amplitudes, with  $J$  smaller than  $j+1$ , are suppressed by the factor  $\xi^{j+1-J}$ . By considering helicities and spins of the involved particles, one can conclude that two Wigner matrices contribute to the expansion (6.56), which are  $\hat{d}_{0,0}^J$  and  $\hat{d}_{0,1}^J$ , which are given in terms of the Gegenbauer polynomials with indices  $1/2$  and  $3/2$ , respectively. Equivalently, they can also be expressed in terms of the hypergeometric function  ${}_2F_1$

$$\hat{d}_{0,0}^J(\xi) = \frac{\Gamma(1/2)\Gamma(J+1)}{2^J\Gamma(J+1/2)} \xi^J C_J^{1/2}\left(\frac{1}{\xi}\right) = \frac{\Gamma(1/2)\Gamma(J+1)}{2^J\Gamma(J+1/2)} \xi^J {}_2F_1\left(\begin{matrix} -J & J+1 \\ 1 \end{matrix} \middle| \frac{\xi-1}{2\xi}\right), \quad (6.60)$$

$$\hat{d}_{0,1}^J(\xi) = \frac{\Gamma(1/2)\Gamma(J)}{2^J\Gamma(J+1/2)} \xi^{J-1} C_{J-1}^{3/2}\left(\frac{1}{\xi}\right) = \frac{\Gamma(3/2)\Gamma(J+1)}{2^J\Gamma(J+1/2)} \xi^{J-1} {}_2F_1\left(\begin{matrix} -J+1 & J+2 \\ 2 \end{matrix} \middle| \frac{\xi-1}{2\xi}\right). \quad (6.61)$$

We can find a basis where the amplitudes do not mix, which are linear combinations of GPDs  $H_j$  and  $E_j$ . The  $t$ -channel helicity conserving, or "electric" combination [46]

$$H_j^a + \frac{t}{4M^2} E_j^a, \quad a \in \{q, \mathbf{G}\} \quad (6.62)$$

is given in terms of  $\hat{d}_{0,0}^J$ , and the  $t$ -channel helicity flip, or "magnetic" combination

$$H_j^a + E_j^a, \quad a \in \{q, \mathbf{G}\} \quad (6.63)$$

is given in terms of  $\hat{d}_{0,1}^J$ .

For more details see [101, 126] and references therein. It was shown in [101] that for the kinematics we are interested in, roughly  $\xi \leq 0.3$ , which corresponds to  $x \leq 0.46$ , we can ap-

proximate the coefficients in the expansion (6.56) as

$$\hat{d}_{\alpha,\beta}^J(\xi) \approx 1. \quad (6.64)$$

In the forward limit  $\xi = 0$ , the leading amplitude in the PW expansion should reduce to the Mellin moment of the corresponding PDF

$$F_{j,j+1}^a(0) = f_j^a = \int_0^1 dx x^j f^a(x). \quad (6.65)$$

This prompts us to use the known PDF ansatz to model the leading amplitude in the PW expansion. But in this approach we do not use state-of-the-art results for PDFs obtained from experiment, since current methods for modeling PDFs are more sophisticated than our approach and could lead to inconsistencies. Instead, we use a well-known ansatz for PDFs

$$f^a(x) = \frac{N_a}{B(2 - \alpha_0^a, \beta^a + 1)} x^{-\alpha_0^a} (1-x)^{\beta^a}, \quad (6.66)$$

which in the conformal space corresponds to

$$f_j^a = N_a \frac{B(1 - \alpha_0^a + j, \beta^a + 1)}{B(2 - \alpha_0^a, \beta^a + 1)}. \quad (6.67)$$

The  $1-x$  part of the PDF describes its high  $x$  behavior, which we cannot access in our analysis. We therefore rely on counting results to fix  $\beta^{\text{sea}} = 8$  and  $\beta^{\text{G}} = 6$ . In (6.66) and (6.67) the normalization is chosen so that  $N_a$  corresponds to the average longitudinal momentum fraction of parton  $a$ . All of these factors need to sum up to 1, i.e.

$$N_{\text{sea}} + N_{\text{val}} + N_{\text{G}} = 1. \quad (6.68)$$

In order to introduce the  $t$  dependence, which factorizes from the  $x$  dependence at low  $x$  [127], we take note from Regge phenomenology to complete the Regge trajectory

$$\alpha_0^a \rightarrow \alpha^a(t) = \alpha_0^a + \alpha'^a t. \quad (6.69)$$

We use this trajectory to decorate the forward GPDs with a factor

$$\frac{1}{1 - \frac{t}{(m_j^a)^2}}, \quad (m_j^a)^2 = \frac{1 + j - \alpha_0^a}{\alpha'^a}. \quad (6.70)$$

Regge theory tells us that at high energies the scattering amplitude behaves as  $\Gamma(-\alpha(t))s^{\alpha(t)}$ , where  $\alpha(t)$  is a trajectory in the complex  $j$  space which contains all particles in the  $t$ -channel exchange, and for each of these particles  $\alpha(t) = j + 1$ , where  $j$  is a non-negative integer. The exchange of these particles induces poles in the amplitude and these poles are here modeled as a monopole factor (6.70). We then add a residual  $t$ -dependence in the form of a dipole impact factor

$$\beta(t) = \left(1 - \frac{t}{m_a^2}\right)^{-2}, \quad (6.71)$$

where we ignore all  $j$  dependence of the mass parameter  $m_a^2$  since this dependence cannot be discerned at low  $x$ .

The final GPD form is therefore

$$F_{j,j+1}^a(t) \equiv f_j^a(t) = f_j^a \frac{1 + j - \alpha_0^a}{1 + j - \alpha_0^a - \alpha'^a t} \left(1 - \frac{t}{m_a^2}\right)^{-2}, \quad (6.72)$$

with  $f_j^a$  given in (6.67). Another possibility for the residual  $t$ -dependence is an exponential function

$$\beta(t) = e^{Bt}, \quad (6.73)$$

but it is unlikely that such a  $t$ -dependence would come about naturally from a field theoretical standpoint. However, for low values of  $x$  both of the residual functions similarly reproduce data.

Using previous analyses, it was shown that the data we will be working with does not distinguish between the  $t$  dependencies of the different partial waves, and that the description works sufficiently well by truncating (6.56) after the second subleading PW [128]. Our full model is therefore

$$F_j^a(\xi, t) = (1 + s_2^a \xi^2 + s_4^a \xi^4) f_j^a(t), \quad (6.74)$$

where the parameters  $s_2$  and  $s_4$  are determined in fits. In the Mellin-Barnes representation we can shift the terms in the subleading partial waves by  $j \rightarrow j - 2$  and  $j \rightarrow j - 4$  so that we can write the CFFs/TFFs as

$$\mathcal{H} = \frac{1}{2i} \int_{c-i\infty}^{c+i\infty} dj \xi^{-j-1} \left[ i + \tan\left(\frac{\pi j}{2}\right) \right] \left[ \bar{T}_j^I + s_2 \bar{T}_{j+2}^I + s_4 \bar{T}_{j+4}^I \right] H_j. \quad (6.75)$$

In the former expression the subtraction constant is set to zero, since for such a small range of kinematic variable values we cannot extract its form.

A similar model has already been used in [3], with the difference of having more parameters due to not taking the subleading partial waves to be proportional to the leading one, but having different parameters for each partial wave. In this model, the normalization for DVMP cross

sections was also considered as a free parameter in fits. A model with more parameters offers more flexibility, but our model has proven sufficiently flexible for the low- $x$  analysis presented here.

All of the expressions listed here and many more are implemented into the Python software Gepard, which will be detailed in Section [7.2.4](#).

# Chapter 7

## Multichannel fits

In this chapter we present the application of the model described in chapter 6 onto low- $x$  data. Similar analyses in terms of simultaneous fits were conducted at LO in [1], where a fit to DVMP data reasonably reproduces DVCS observables, specifically HERA data, and at NLO in [2, 3, 4], where a simultaneous fit to DVCS and DVMP was obtained with HERA data. In the latter case, the analyses did not include correct hard-scattering expressions, as explained in Chapter 6.1.2, and their model had more parameters, as mentioned in the previous section.

For this analysis we use H1 and ZEUS measurements obtained with the HERA collider since they have measured these processes at the lowest  $x$  and highest photon virtuality  $Q^2$ . The data we will be using is:

- H1 measurements of the DIS structure function  $F_2(x, Q^2)$  from [129];
- H1 and ZEUS measurements of the DVCS photoproduction cross section  $\sigma(\gamma^* p \rightarrow \gamma p)$  from [130, 131, 132, 133];
- H1 and ZEUS measurements of the DVMP photoproduction cross section for the production of the  $\rho^0$  meson  $\sigma(\gamma^* p \rightarrow \rho^0 p)$  from [134, 135].

In order to be certain that the twist-2 and low- $x$  approximations we introduce reproduce the data reliably, we make cuts on the kinematics. Namely, we make a cut at  $Q^2 > 5 \text{ GeV}^2$  for DVCS and at  $Q^2 > 10 \text{ GeV}^2$  for DVMP. Because our model takes only sea quark and gluon contributions into consideration, it can easily be generalized to the production of other mesons, such as the  $\phi$  meson. We just replace the meson specific prefactors that come into the definition of TFFs to obtain

$$\sigma(\gamma^* p \rightarrow \phi p) = \left( \frac{\sqrt{2} f_\phi}{3 f_{\rho^0}} \right)^2 \sigma(\gamma^* p \rightarrow \rho^0 p), \quad (7.1)$$

where the meson decay constants are  $f_{\rho^0} = 0.209$  GeV and  $f_{\phi} = 0.221$  GeV. As we will see later, this relation does not represent the data accurately, because if we multiply the  $\phi$  production measurements with the same prefactor as in (7.1), we obtain values that are consistently smaller than the  $\rho^0$  measurements. We therefore omit the  $\phi$  production measurements from fits, and keep only the measurements for  $\rho^0$  production with good statistics.

For the sake of simplicity, we set the renormalization and factorization scales to be equal to the photon virtuality

$$\mu_F = \mu_R = \mu_\phi = Q, \quad (7.2)$$

and the initial evolution scale to  $Q_0 = 2$  GeV.

## 7.1 L/T separation

The goal of this study is to assess the validity of a collinear twist-2 approach to describe the longitudinal meson production, because the factorization theorem was proven for this case. Unlike DVCS, where the twist-2 approximation is dominant, it is known that DVMP has a substantial higher-twist contribution from the exchange of transversally polarized photons [136, 137]. In order to assess the accuracy of our model, we need to work with the longitudinal cross section, which we denote as  $\sigma_L^{\rho^0} = \sigma(\gamma_L^* p \rightarrow \rho_L^0 p)$ . It is impossible to determine the polarization of the virtual photon experimentally, so in practice the polarization of the out-going meson is measured, and is equated to the polarization of the virtual photon under the  $s$ -channel helicity conservation (SCHC) assumption. Under this assumption we have  $\sigma_L^{\rho^0} \approx \sigma^{\rho^0} = \sigma(\gamma^* p \rightarrow \rho_L^0 p)$  and ignore transitions where the helicity changes. The SCHC assumption has been discussed in [134] and references therein.

The SCHC assumption is experimentally tested by measuring the spin density matrix elements (SDMEs) [138], which are used to calculate the ratio of the longitudinal and transverse cross section

$$R \equiv \frac{\sigma_L^{\rho^0}}{\sigma_T^{\rho^0}}. \quad (7.3)$$

Both H1 and ZEUS collaborations have studied this ratio and its kinematic dependencies. The H1 results from [134] have shown that  $R$  depends on  $Q^2$ , that it has some dependence on  $t$  at higher values of  $Q^2$ , and that it has no clear dependence on  $W$  within uncertainties.

In [134] the values for  $\sigma_L^{\rho^0}$  and  $\sigma_T^{\rho^0}$  have been measured, but they were binned only in  $Q^2$ . Since we are modeling GPDs, which depend on three variables, we need the values of the cross section in terms of three variables, such as  $W$  and  $t$ , in addition to the  $Q^2$  dependence. To extract

the values for  $\sigma_L^{\rho^0}$ , we use the measurements for  $R$  and the total cross section  $\sigma_L^{\rho^0}$ , which is given as

$$\sigma_L^{\rho^0} = \sigma_T^{\rho^0} + \varepsilon \sigma_L^{\rho^0}, \quad (7.4)$$

with the flux ratio of longitudinal to transverse photons  $\varepsilon(y)$

$$\varepsilon \approx \frac{1-y}{1-y+\frac{1}{2}y^2}, \quad y = \frac{W^2 + Q^2 - M^2}{s - M^2}. \quad (7.5)$$

An issue we run into is that the measurements for  $R$  and  $\sigma_L^{\rho^0}$  were not taken at the same kinematic points, so we need to model  $R$  in terms of all kinematic variables and interpolate its values for the same kinematic points that  $\sigma_L^{\rho^0}$  is measured at.

Some analysis of  $R$  has been previously made in [2], where any  $W$  and  $t$  dependence is ignored and the following model is proposed

$$R(Q^2) = \frac{Q^2}{m_{\rho^0}^2} \left( 1 + a \frac{Q^2}{m_{\rho^0}^2} \right)^{-p}, \quad (7.6)$$

where  $a$  and  $p$  are fitting parameters, and  $m_{\rho^0} = 0.776$  GeV is the mass of the  $\rho^0$  meson. This is a modification to the expectation that  $\sigma_L^{\rho^0} \propto 1/Q^6$  and  $\sigma_T^{\rho^0} \propto 1/Q^8$  [139].

In [2, 4, 3] the model (7.6) was tested against H1 and ZEUS data and the parameters  $a$  and  $p$  were obtained. As we have mentioned, we observe kinematics with large  $Q^2$ , where the uncertainties of  $R$  measurements are larger and it is unclear whether there is a  $W$  dependence. This is illustrated in Fig. 39 in [134].

In this work, we added a  $W$  dependence to  $R$  to obtain

$$R(W, Q^2) = \frac{Q^2}{m_{\rho^0}^2} \left( 1 + a \frac{Q^2}{m_{\rho^0}^2} \right)^{-p} \left( 1 + b \frac{Q^2}{W} \right), \quad (7.7)$$

where  $b$  is an additional parameter to be obtained in fits. A similar argument could be made for the  $t$  dependence, which is also evident at higher  $Q^2$  values, as shown in measurements of light vector meson production at slightly higher  $x_B$  made by the COMPASS collaboration, specifically measurements depicted in Fig. 11b in [140]. Since the HERA measurements of  $R(t)$  were taken at  $Q^2 < 10$  GeV<sup>2</sup>, which is the cut-off we are working with, we cannot determine the  $t$  dependence and therefore choose not to work with  $d\sigma_L^{\rho^0}/dt$ , but only with DVMP cross section measurements integrated over  $t$ .

It is evident that H1 and ZEUS measurements show some disagreement in  $R$  for higher values of  $Q^2$ , so we fit the function  $R$  separately to H1 and ZEUS data. The parameters we obtain are

$$\text{H1:} \quad a = 3 \pm 29 \quad p = 1.0 \pm 0.6 \quad b = -82 \pm 780 \text{ GeV}^{-1}, \quad (7.8)$$

$$\text{ZEUS:} \quad a = 2 \pm 4 \quad p = 0.44 \pm 0.26 \quad b = 0.3 \pm 1.1 \text{ GeV}^{-1}. \quad (7.9)$$

Notice that the parameter  $b$  is not dimensionless, which is a choice purely for the sake of avoiding  $W^2$  in the denominator for numerical efficiency. The functions  $R(W, Q^2)_{\text{H1}}$  and  $R(W, Q^2)_{\text{ZEUS}}$ , as well as the functions  $R(Q^2)$  obtained in [3], are given in figure 7.1 below.

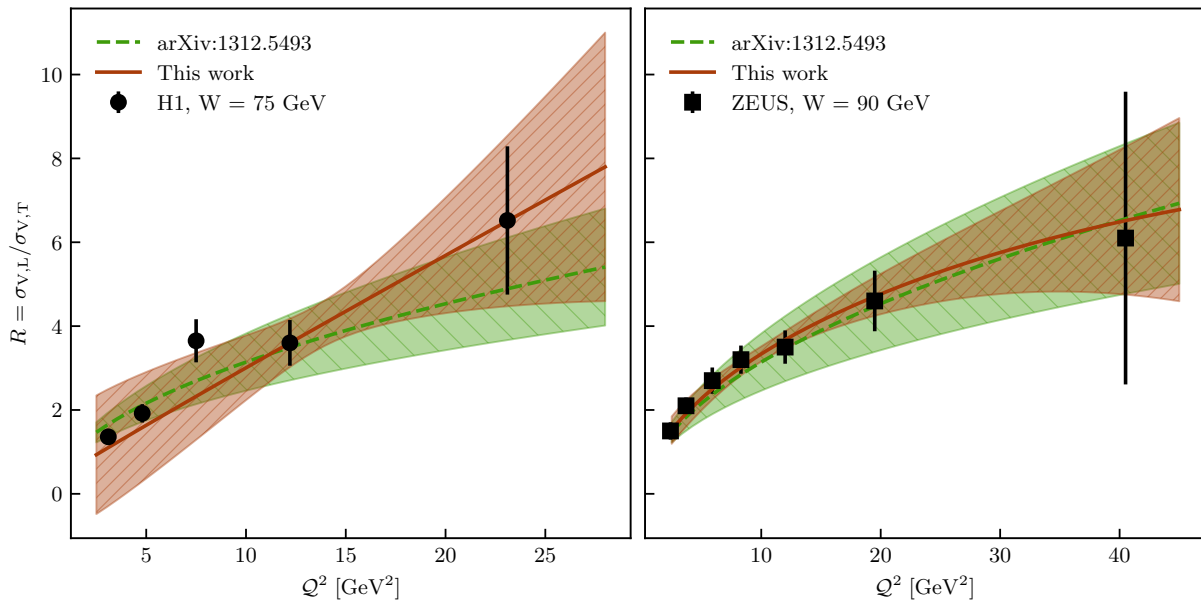


Figure 7.1: Comparison of  $R(W, Q^2)_{\text{H1}}$  to measurements from [134] (left) and  $R(W, Q^2)_{\text{ZEUS}}$  to measurements in [135] (right). Both measurements are compared to the function  $R(Q^2)$  from [2], which is plotted in green.

## 7.2 Results

### 7.2.1 Fits and parameters

As previously mentioned, the goal of this study is to assess the NLO corrections to the processes we are analyzing, as well as verifying the universality of the GPD description of DVCS and DVMP. For this purpose we perform six different fits. We perform three fits at LO accuracy,

and three fits at NLO accuracy. For the LO and NLO fits we perform a fit to all DIS, DVCS and DVMP data mentioned at the beginning of this discussion, a fit to DIS and DVCS data, and a fit to DIS and DVMP data. Since all fits contain DIS data, in the labeling of these fits we will omit the DIS label, so the fits will be labeled as (N) LO-DVCS-DVMP, (N) LO-DVCS and (N) LO-DVMP. All of the models and the data they have been fitted to are listed in Table 7.1 below.

model name	order	DIS	DVCS	DVMP
LO-DVCS	LO	✓	✓	
LO-DVMP	LO	✓		✓
LO-DVCS-DVMP	LO	✓	✓	✓
NLO-DVCS	NLO	✓	✓	
NLO-DVMP	NLO	✓		✓
NLO-DVCS-DVMP	NLO	✓	✓	✓

Table 7.1: List of models used in this work, order of perturbation theory, and datasets to which the model was fitted. References to used DIS, DVCS and DVMP experimental data are given in Table 7.2.

We perform the fits to all data by first fitting to DIS  $F_2$  data and fixing the parameters relevant to PDFs, i.e. relevant in the forward limit of GPDs

$$\{N_{\text{sea}}, \alpha_0^{\text{sea}}, \alpha_0^{\text{G}}\}. \quad (7.10)$$

Using the results of DIS analysis, we set  $N_{\text{val}} = 0.4$ , which was mentioned in (6.68). We do this because we expect that valence quarks have a negligible contribution, so the data will not be sensitive to the valence sector parameters. From (6.68) it follows that only one normalization parameter is free, and we choose  $N_{\text{sea}}$ , which fixes  $N_{\text{G}}$ . With the parameters (7.10) fixed, the models are fitted to the rest of the datasets, either DVCS, DVMP, or both, releasing the parameters

$$\{\alpha'_{\text{sea}}, \alpha'_{\text{G}}, m_{\text{sea}}^2, m_{\text{G}}^2, s_2^{\text{sea}}, s_2^{\text{G}}, s_4^{\text{sea}}, s_4^{\text{G}}\}. \quad (7.11)$$

At some point in the analysis the fitting was done in three steps in case of the (N) LO-DVCS-DVMP models, where the last fitting was performed to all three datasets, but the difference in the results was negligible. For the fitting we used the least square fitting routine MINUIT [141, 142].

The way we assess the quality of the fits is by using the  $\chi^2$  goodness of fit test. It is a way of comparing the model predictions to observed data by calculating the  $\chi^2$  value of the model as

$$\chi^2 = \sum_i \frac{(o_i - e_i)^2}{\Delta o_i^2}, \quad (7.12)$$

where  $o_i$  are the observed values, which are in our case the measurements, and  $e_i$  are the expected values, which are our model predictions of the measurements. The  $\chi^2$  itself does not assess the quality of the fit since it depends on the number of datapoints we are comparing the model to, so we usually calculate  $\chi^2/N_{\text{d.o.f.}}$ , where  $N_{\text{d.o.f.}}$  is the number of degrees of freedom. Ideally, we would want this number to be as small as possible, but realistically if this number is close to 1, we consider the fit to be sufficiently accurate in representing the data. The degrees of freedom are in some cases taken to be as the number of datapoints, and in others this number is decreased by the number of free parameters in the fits. It is sometimes not clear how to determine the degrees of freedom in a dataset, such as in the fits to DIS+DVCS or DIS+DVMP, since the 9 parameters that are released in the second step of the fitting procedure (7.11) come from GPDs which are present in both DVCS and DVMP. We can obtain the degrees of freedom in the case of the fits to the total dataset by subtracting the parameters from the total number of datapoints, so we give  $\chi^2/N_{\text{d.o.f.}}$

$$\chi^2/N_{\text{d.o.f.}}(\text{LO-DVCS-DVMP}) = 1.5, \quad \chi^2/N_{\text{d.o.f.}}(\text{NLO-DVCS-DVMP}) = 1.2. \quad (7.13)$$

The values of  $\chi^2/n_{\text{pts}}$  for all six of the models tested on all four sets of datapoints, DIS, DIS+DVCS, DIS+DVMP and DIS+DVCS+DVMP are given in Table 7.2 below.

Dataset	Refs.	$N_{\text{pts}}$	LO-			NLO-		
			DVCS	DVMP	DVCS-DVMP	DVCS	DVMP	DVCS-DVMP
DIS	[129]	85	0.6	0.6	0.6	0.8	0.8	0.8
DVCS	[130, 131, 132, 133]	27	0.4	$\gg 1$	0.6	0.6	$\gg 1$	0.8
DVMP	[134, 135]	45	$\gg 1$	3.1	3.3	$\gg 1$	1.5	1.8
Total		157	$\gg 1$	$\gg 1$	1.4	3.7	$\gg 1$	1.1

Table 7.2: Values of  $\chi^2/N_{\text{pts}}$  for all of the six models described in this section (columns) tested against four different datasets (rows). The values denoted by  $\gg 1$  are greater than 10.

We can see that models that have not been fitted to a certain dataset exhibit  $\chi^2/N_{\text{pts}}$  larger than 10, as denoted by  $\gg 1$ . This is not unexpected, since with all of the intricacies of modeling these processes, it would be highly unlikely that a model accidentally describes data it has never seen accurately. Both the LO and NLO models to all datasets describe the data sufficiently well, especially the NLO model, which we deem to perform the best out of all six models. The LO fits to DIS and DVCS are satisfactory, but not so much to DVMP.

All of the fits were also performed by using a universal function  $R(W, Q^2)$  fitted together to the H1 and ZEUS data, and the value of  $\chi^2/n_{\text{d.o.f.}}(\text{NLO-DVCS-DVMP})$  changes from 1.2 to 1.3. All of the predictions made with this model are practically the same as with the model with two

different  $R(W, Q^2)$  functions.

The parameters of the best model are given in Table 7.3 below. The first row gives the initial values we used for the parameters. We set all of the subleading wave parameters to zero, except for  $s_2^{\text{sea}}$ , which was set to a negative value because this value was favoured by previous LO DVCS models [128]. Using the knowledge of Regge phenomenology, we set the intercepts  $\alpha_0^a$  to 1 and the slopes  $\alpha'_a$  to 0.15 for both sea quarks and gluons.

In order to achieve stable fits, we needed to restrict some parameters. For physical reasons, we limit the squares of masses  $m_a^2$  and Regge slopes  $\alpha'_a$  to positive values of order one. Negative values of  $\alpha'_a$  enable discontinuous values of the form factors as a function of  $t$ , which we want to avoid. We also want a natural hierarchy of the subleading partial wave normalizations in comparison to the leading one, i.e.  $1 \gg s_2^{\text{sea}} \gg s_4^{\text{sea}}$ . We would want the same for the gluon sector, but imposing such a strict limit does not yield satisfactory fits. As can be seen from Table 7.3, by leaving the gluon partial wave normalizations more flexible, they turn out relatively large. This has been the case in previous models [143] and it remains to be seen with more data whether the problem lies with this type of model.

The second row in Table 7.3 gives the values of the parameters of the best models, and the last row gives their uncertainties, also obtained by the MINUIT routine.

parameter	$N^{\text{sea}}$	$\alpha_0^{\text{sea}}$	$\alpha'_{\text{sea}}$	$m_{\text{sea}}^2$	$s_2^{\text{sea}}$	$s_4^{\text{sea}}$	$\alpha_0^G$	$\alpha'_G$	$m_G^2$	$s_2^G$	$s_4^G$
unit		1	$\text{GeV}^{-2}$	$\text{GeV}^2$	1	1	1	$\text{GeV}^{-2}$	$\text{GeV}^2$	1	1
initial	0.15	1.00	0.15	0.70	-0.20	0.00	1.00	0.15	0.70	0.00	0.00
limits			(0.0,1.0)	(0,3)	(-0.3,0.3)	(-0.1,0.1)		(0.0,1.0)	(0,3)	(-3.0,3.0)	(-1.0,1.0)
final	0.168	1.128	0.125	0.412	0.280	-0.044	1.099	0.000	0.145	2.958	-0.951
uncert.	0.002	0.011	0.043	0.056	0.037	0.012	0.011	0.011	0.008	0.032	0.023

Table 7.3: The initial values of the parameters and their limits are given in the first two rows. The final fitted values and their uncertainties (one standard deviation) of the best NLO-DVCS-DVMP model are given in the last two rows. The values of  $\chi^2/n_{\text{pts}}$  are given in the last column of Table 7.2.

We also observed the correlations between the parameters of the model. The parameters  $\alpha'_{\text{sea}}$  and  $m_{\text{sea}}^2$  have the highest correlation of 0.937, which indicates that the  $t$ -dependence coming from the Regge trajectory is indistinguishable from the residual  $t$ -dependence controlled by the parameter  $m_{\text{sea}}^2$ . Due to this high correlation we cannot observe the shrinkage effect, where for high  $x$  we observe a flattening of the proton in the transversal direction. This is to be expected since we are observing low- $x$  kinematics. The subleading partial wave normalizations show a strong anticorrelation, where  $s_2^{\text{sea}}$  and  $s_4^{\text{sea}}$  have an anticorrelation of -0.940, and  $s_2^G$  and  $s_4^G$  have an anticorrelation of -0.931, which suggests that we cannot distinguish between contributions

from the second and third  $SO(3)$  partial wave in neither the sea quark nor the gluon sector.

## 7.2.2 Data representation

In this section we depict graphically all of the predictions of the models described in the previous section. Note that we do not draw error bands for any of the model predictions, which is due to the fact that we currently have no way to assess the errors incurred by all of the specific choices made in modeling CFFs and TFFs, which are also called systematic errors. We could include the statistic errors propagated from the measurements, but we believe they would grossly underestimate the overall error of these models, so we omit the errors all together.

In all of our models we perform fits to DIS data, instead of matching the obtained GPDs to the previously known PDFs in the forward limit. Aside from the current methods of fitting PDFs being more sophisticated than our methods, it is also a good confirmation that the models can reproduce DIS data given all of the specific choices made. The first row of Table 7.2 shows that all models have a very good description of DIS, which is also evident in Figure 7.2 below.

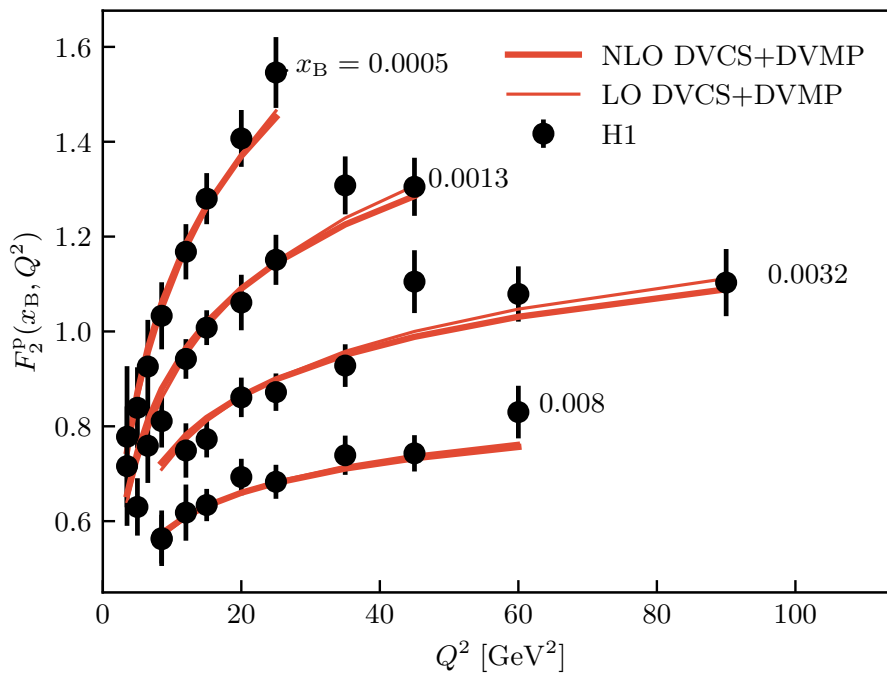


Figure 7.2: Description of H1 measurements [129] of the structure function  $F_2(x_B, Q^2)$  at LO (thin line) and NLO (thick line).

Figure 7.3 shows the description of H1 and ZEUS DVCS cross section data by (N) LO-DVCS and (N) LO-DVCS-DVMP models. Some difficulties are encountered at low  $Q^2$ , such as in the

upper right panel, but these kinematic points were excluded from fits so it is not unexpected that the models perform somewhat worse. These results are reflected in the second row in Table 7.2, which gives the  $\chi^2/n_{\text{pts}}$  values for all six models.

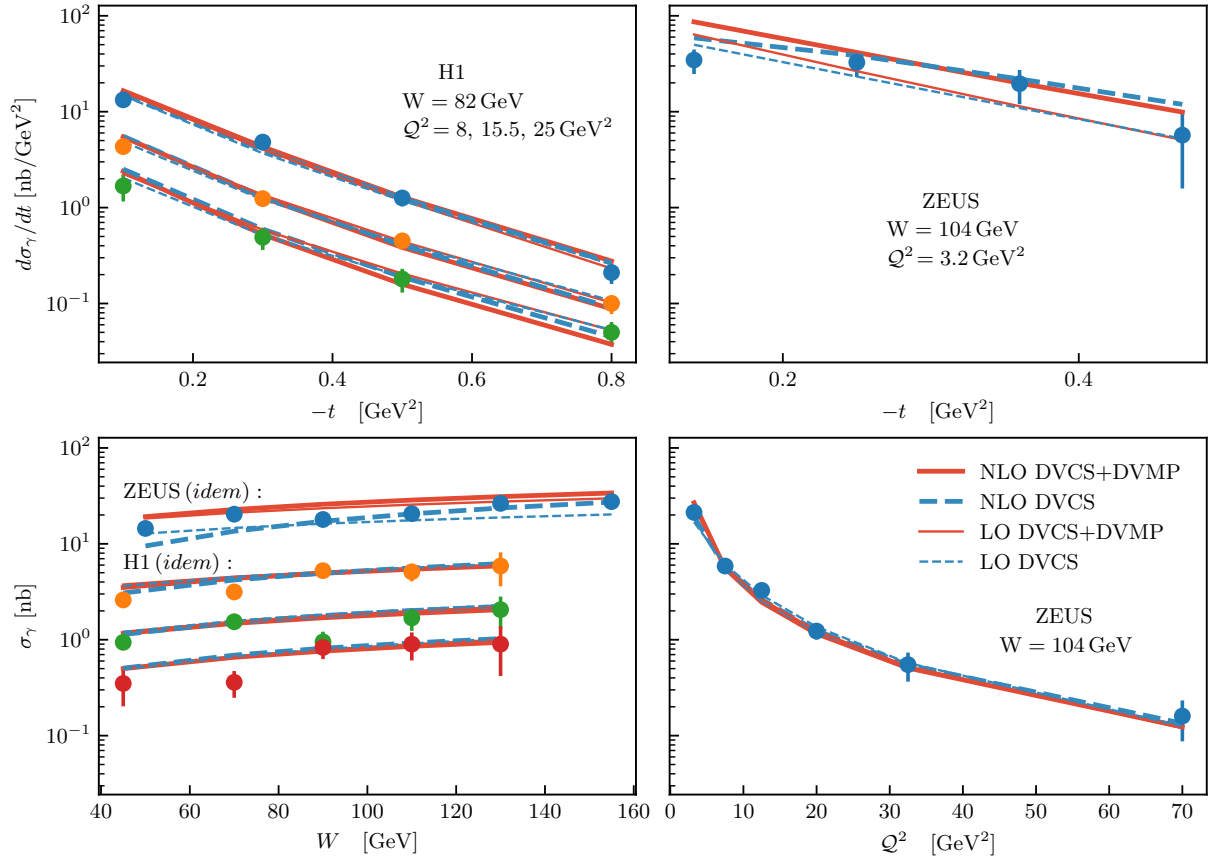


Figure 7.3: Description of H1 [130, 131] and ZEUS [132, 133] measurements of the cross section dependence on  $t$ ,  $W$  and  $Q^2$ . The LO (thin lines) and NLO (thick lines) models fitted to DIS+DVCS (blue dashed), and DIS+DVCS+DVMP (red solid) are compared to the data. The three H1 lines on the left panels correspond, from top to bottom, to  $Q^2 = 8, 15.5$  and  $25 \text{ GeV}^2$ , respectively.

Figures 7.4 and 7.5 depict the model predictions of H1 and ZEUS DVMP cross section measurements, respectively. Here we show the predictions made by models (N) LO-DVMP and (N) LO-DVCS-DVMP. We can see in the left panels of both figures that the LO description does not perform well for  $Q^2 > 30 \text{ GeV}^2$ , and from the right panels we see that it does not perform well in the description of the  $W$  dependence, especially for the ZEUS data. This is also reflected in the third row of Table 7.2. However, the NLO description improves significantly, specially in the left panels. The slope for the  $W$  dependent cross sections is somewhat too steep, but overall the description is satisfactory. This answers the questions we set out to answer, which is

whether or not it is possible to describe DVMP at the twist-2 collinear level.

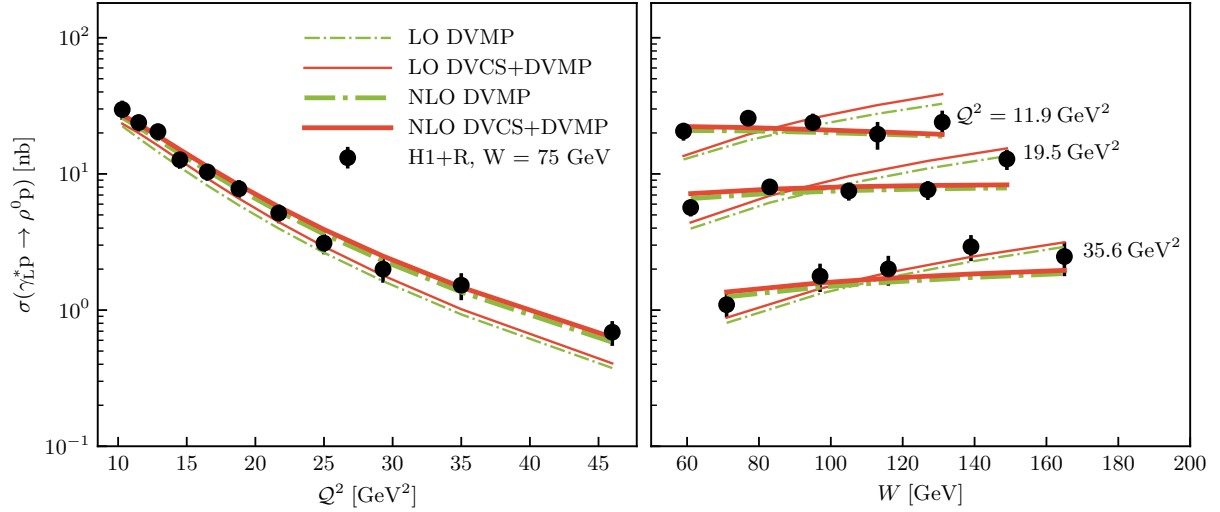


Figure 7.4: Description of H1 DVMP measurements [134] of the cross section dependence on  $Q^2$  and  $W$  by LO (thin lines) and NLO (thick lines) models fitted to H1 and ZEUS DVMP data (green dot-dashed), as well as DVCS data (red solid).

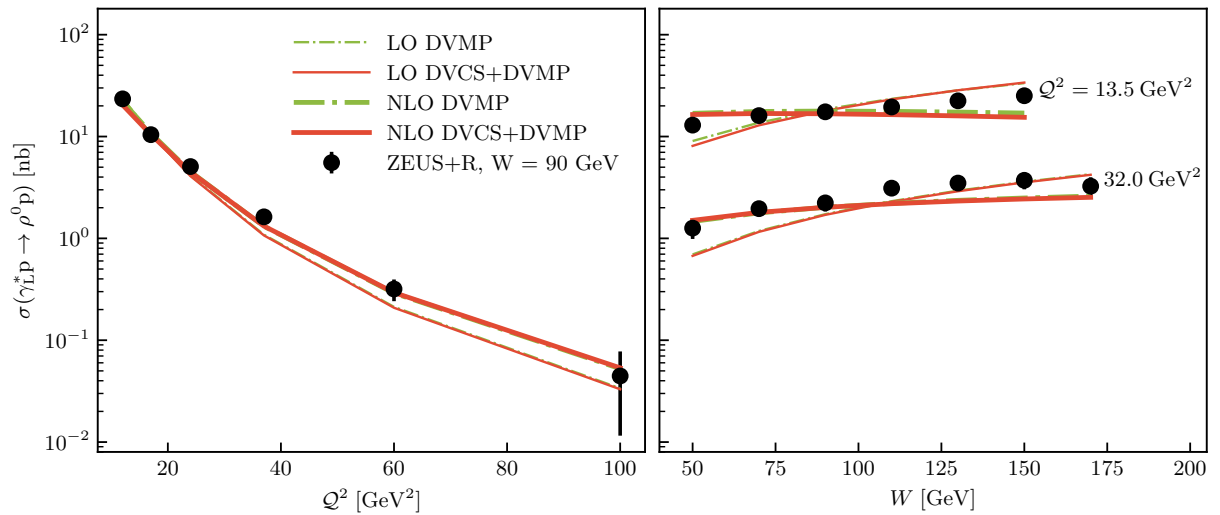


Figure 7.5: Description of ZEUS DVMP measurements [135] of the cross section dependence on  $Q^2$  and  $W$  by LO (thin lines) and NLO (thick lines) models fitted to H1 and ZEUS DVMP data (green dot-dashed), as well as DVCS data (red solid).

We also check if the models reproduce the  $\phi$  production H1 data [134], even though we did not fit to this data. The predictions of all four models fitted to DVMP data are given below in

Figure 7.6. The models are not too precise, which is to be expected because we did not fit to this data, but another reason could also be our choice of the DA, which does not discern between the final-state mesons.

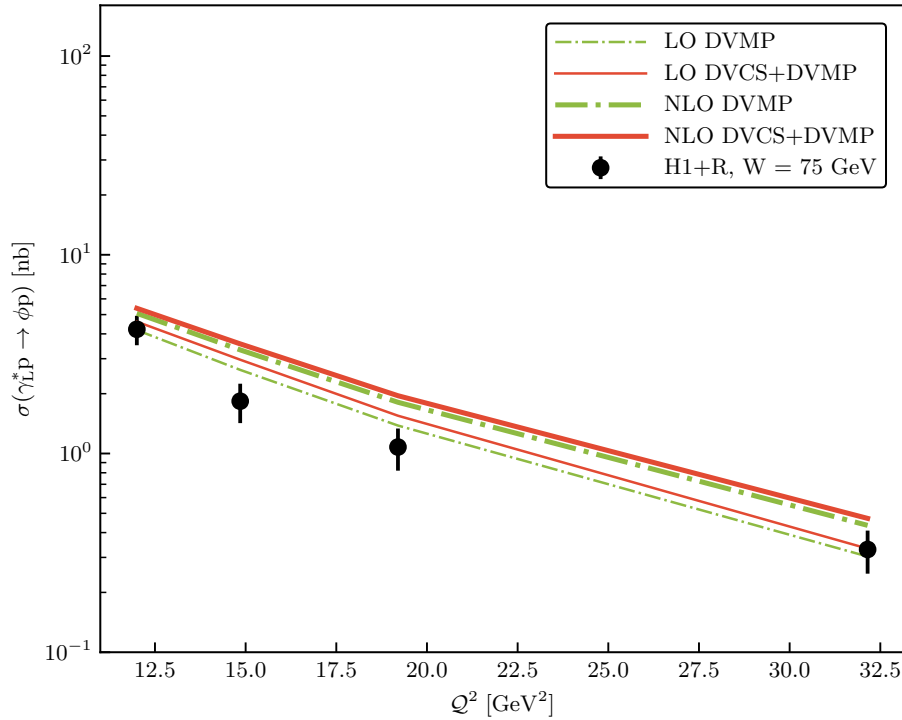


Figure 7.6: Description of H1 DVMP measurements of  $\phi$  production [134] of the cross section dependence on  $Q^2$  and  $W$  by LO (thin lines) and NLO (thick lines) models fitted to H1 and ZEUS DVMP data (green dot-dashed), as well as DVCS data (red solid).

Another point of interest is the  $Q^2$  scaling of the DVMP cross section. Theoretical expressions (6.2) and (6.5) suggest that the longitudinal cross section at fixed  $x$  scales as  $Q^{-6}$ , but experimental results for the total cross section suggest a scaling  $Q^{-4}$ . It is important to discern between the longitudinal and transversal contributions to the total cross section in this analysis. If we fit the data in the left panel of Figure 7.4, which has a fixed value of  $W$ , to the function  $\sigma_L^{\rho^0} \propto Q^{-w}$ , we reproduce the value

$$w = 5.1 \pm 0.1, \quad (7.14)$$

but if we fit the same function to the data that has a fixed value of  $x$ , we obtain

$$w = 3.8 \pm 0.2. \quad (7.15)$$

This result is quite different from  $w = 6$  predicted by the collinear twist-2 QCD approach, and it is a good test for our models.

By using the L/T separation function (7.7) and observing the prediction for the few H1 datapoints with fixed  $x$  that are available, we also reproduce the behavior  $\sigma_L^{\rho^0} \propto Q^{-4}$  in the experimental region. We can see in Figure 7.7 that both the LO-DVMP and NLO-DVMP models reproduce a  $Q^{-4}$  scaling within the experimental errors for the H1 measurements. At higher  $Q^2$  both models predict the expected  $Q^{-6}$  scaling.

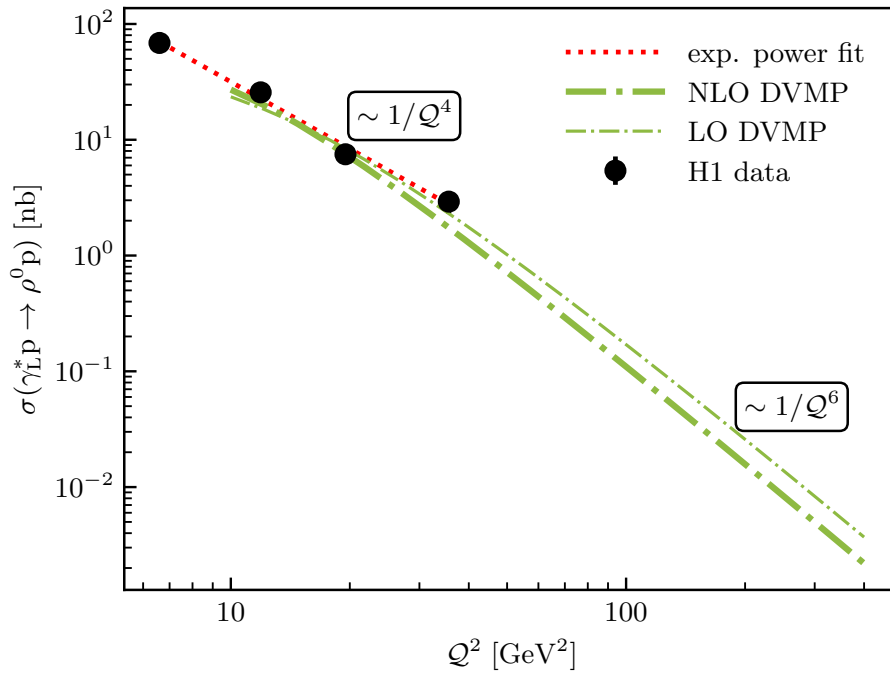


Figure 7.7: Prediction for the H1 longitudinal cross section from [134] at fixed  $x = 0.0018$  by LO-DVMP (thin) and NLO-DVMP (thick) models.

A more reliable assessment of the  $Q^2$  scaling can be done for the fixed- $W$  data, which we have more of. The fit to fixed- $W$  data (7.14) suggests a scaling  $Q^{-5}$ , so we depict  $Q^5 \sigma_L^{\rho^0}$  data for the production of  $\rho^0$  and  $\phi$  mesons in Figure 7.8, alongside the four fits to DVMP data. The prediction for the  $\phi$  production is obtained using (7.1), and the data for the  $\phi$  production has been rescaled using the same parameter. We can see that only the NLO fits can reproduce the correct scaling for large  $Q^2$ . We can also see that the predictions for  $\phi$  production are too large.

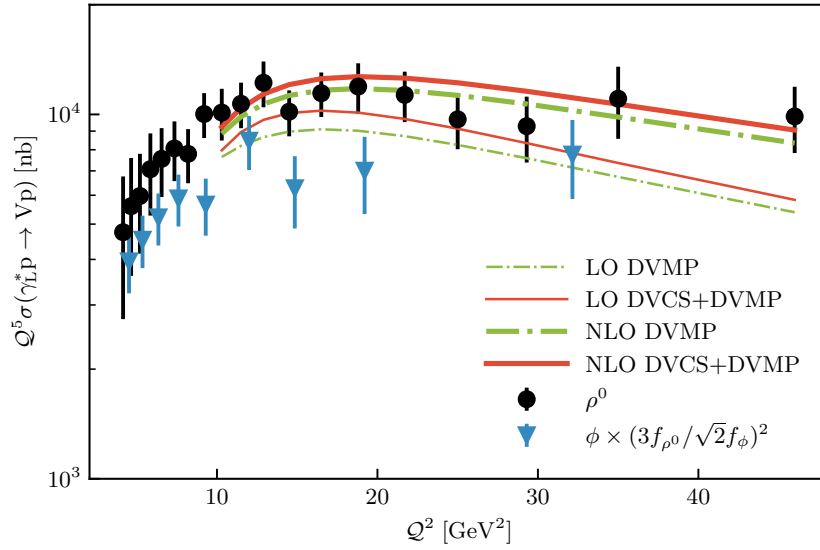


Figure 7.8: Prediction for the H1 longitudinal cross section from [134] at fixed  $W$  by LO (thin) and NLO (thick) models, specifically the models fit to DIS+DVMP data (green dot-dashed), and the models fit to all datapoints (red full). The data and the model predictions have been rescaled by the approximate  $Q^{-5}$  scaling, and the  $\phi$  production data and predictions have been rescaled by the factor from (7.1).

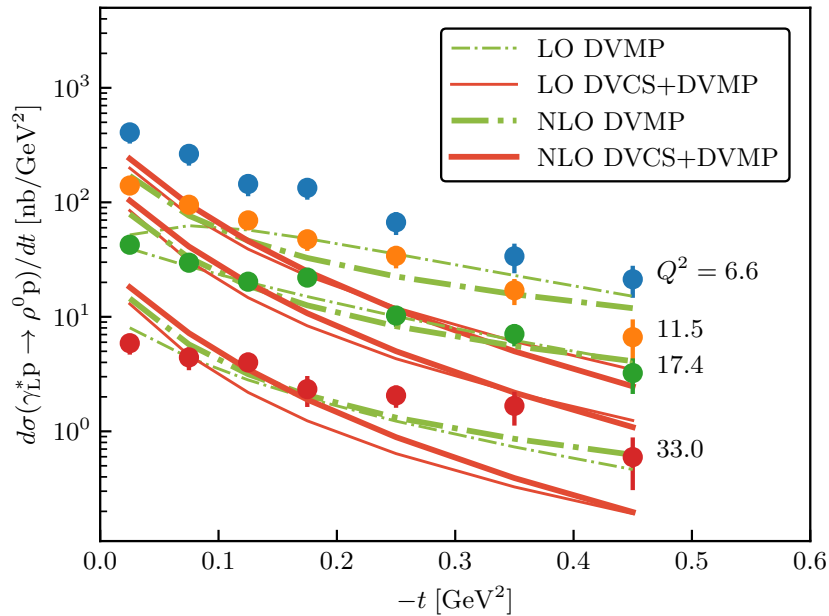


Figure 7.9: Depiction of the H1  $t$ -dependent cross section from [134] at fixed  $x$  for each line. The data are compared to LO (thin) and NLO (thick) models, specifically the models fit to DIS+DVMP data (green dot-dashed), and the models fit to all datapoints (red full).

For a final consistency check, we plot the  $t$ -dependent data, even though we do not fit to it nor do we consider it since there is no clarity on the  $t$ -dependent L/T separation. We depict the H1  $t$ -dependent data for the  $\rho^0$  meson production in Figure 7.9, and compare it to the four models fitted to DVMP data. The points with  $Q^2 = 6.6 \text{ GeV}^2$  have no lines running through them since they are below the kinematic cut-off. This plot serves as a check that there is no pathological behavior in the  $t$  variable. We can see that the only model that has a somewhat acceptable prediction is  $\text{NLO-DVMP}$ . Some previous iterations of this model with fewer constraints displayed unphysical behavior in the  $t$  variable.

### 7.2.3 Quark and gluon contributions

In the last section we explored the idea of describing DVMP at the twist-2 collinear level. If we accept the models obtained above as satisfactory, we can now observe the quark-gluon structure of the proton and how it changes in the transition from an LO to an NLO description. This is enabled because we have added DVMP to our analysis, which offers access to gluons at LO, and, unlike DIS and DVCS, offers access to a richer flavor structure due to the meson probe. This allows for a cleaner separation of different quark flavor and gluon GPDs. We can study the quark and gluon contributions more easily because we consider the hard-scattering amplitude as the one being evolved by the GPD evolution operator. In the figures below, we have studied the quark and gluon contributions to DIS, DVCS and DVMP both at LO and NLO.

In Figure 7.10 we can see the quark and gluon contributions to the structure function  $F_2$  for  $x = 0.001$  at LO, which is depicted in the left panel, and at NLO, which is depicted in the right panel. We can see that at the initial scale  $Q_0^2 = 4 \text{ GeV}^2$  there is no gluon contribution at LO, which is to be expected since at LO DIS is described in terms of the naive parton model where the virtual photon scatters off a quark. We expect that at LO gluons will only contribute through the QCD evolution, which is evident in the left panel. The contributions from quarks and gluons become equal at  $Q^2 \sim 50 \text{ GeV}^2$ . The figure remains fairly similar at NLO, aside from a small contribution of gluons at the input scale.

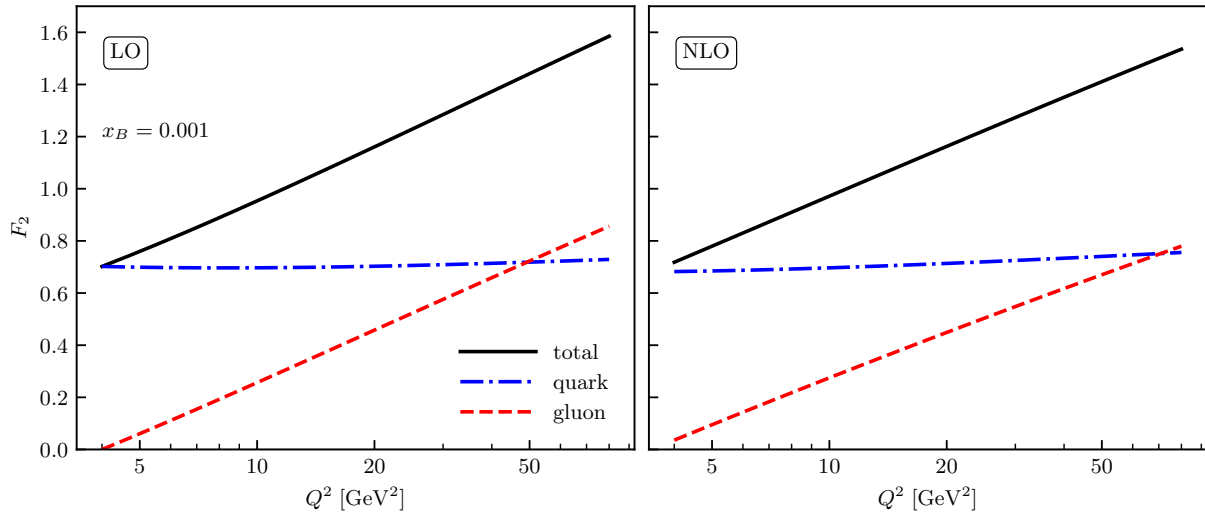


Figure 7.10: Separation of quark (blue dot-dashed) and gluon (red dashed) contributions to the DIS structure function  $F_2$  (black solid) at LO (left) and NLO (right) for  $x = 0.001$ .

In Figure 7.11 we depict the quark and gluon contributions to the CFF  $\mathcal{H}$  for  $x = 0.001$  and  $t = 0$  at LO, which is depicted in the left panel, and at NLO, which is depicted in the right panel. We separately observe the imaginary part, which is given in the top panels, and the real part, which is given in the bottom panels. We notice a similar configuration to DIS at LO, in the sense that the gluons only contribute through evolution and that they equal the quark contribution at  $Q^2 \sim 50 \text{ GeV}^2$ . For the imaginary part, which is what the experiments are more sensitive to, we see that the gluons have a significant and negative contribution at NLO immediately at the initial scale  $Q_0^2 = 4 \text{ GeV}^2$ , even though they are suppressed by  $\alpha_S/2\pi$ . Therefore, the quark contribution has to be twice as large as the LO contribution in order to reproduce the correct CFF. This has already been confirmed in [144, 145]. This behavior does not show up in the real component of the CFF  $\mathcal{H}$ , but it is difficult to draw conclusions for this component because the data are not sensitive to it as much as they are to the imaginary component.

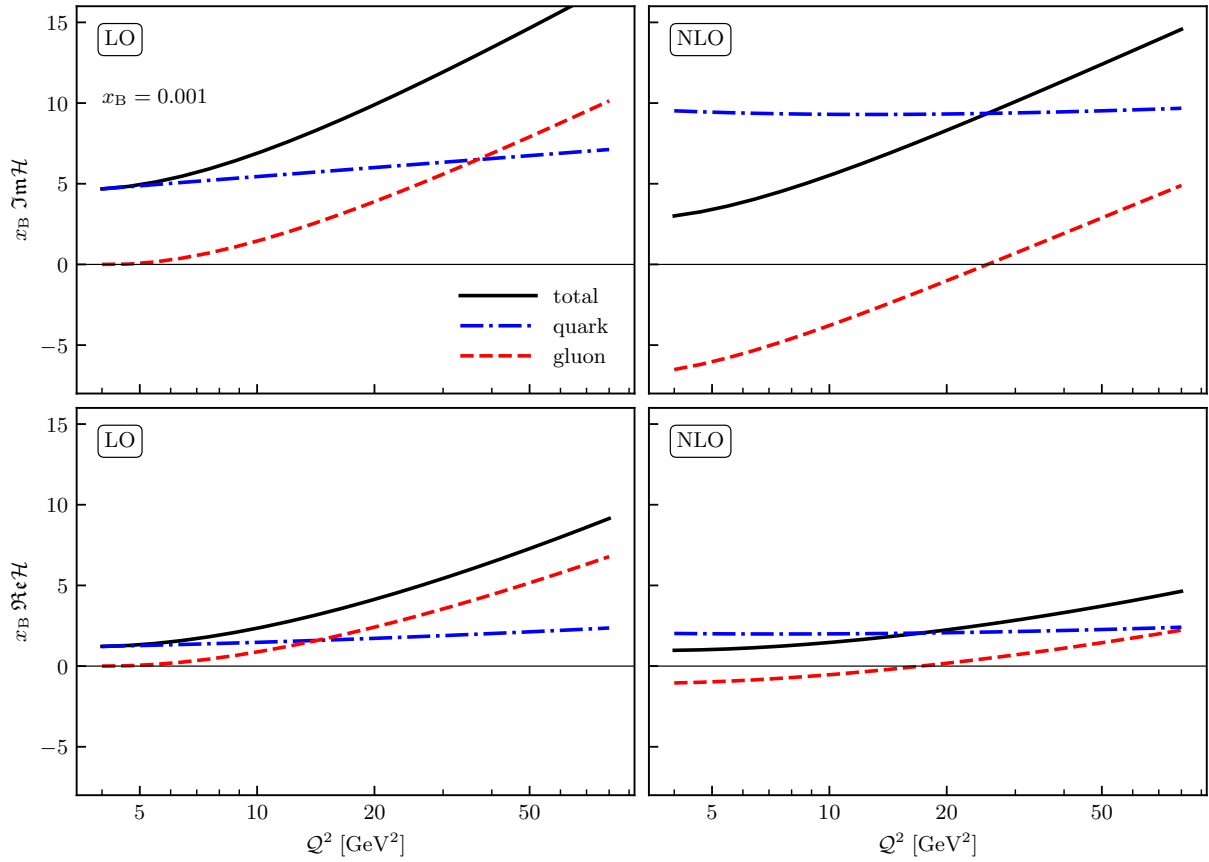


Figure 7.11: Separation of quark (blue dot-dashed) and gluon (red dashed) contributions to the real (top) and imaginary (bottom) CFF  $\mathcal{H}$  (black solid) with models LO-DVCS-DVMP (left) and NLO-DVCS-DVMP (right) for  $x = 0.001$  and  $t = 0$ .

In Figure 7.12 we depict the quark and gluon contributions to the TFF  $\mathcal{H}^p$  for  $x = 0.001$  and  $t = 0$  at LO, which is depicted in the left panel, and at NLO, which is depicted in the right panel. We separately observe the imaginary part, which is given in the top panels, and the real part, which is given in the bottom panels. We have a confirmation that gluons contribute to DVMP at LO, and quite strongly so. For the imaginary part the configuration does not change significantly when going to NLO, but we can notice a relative suppression of the real component when going to NLO. We can see in all four panels that the gluon contribution dominates the amplitude and would likely be sufficient to describe DVMP at high energies.

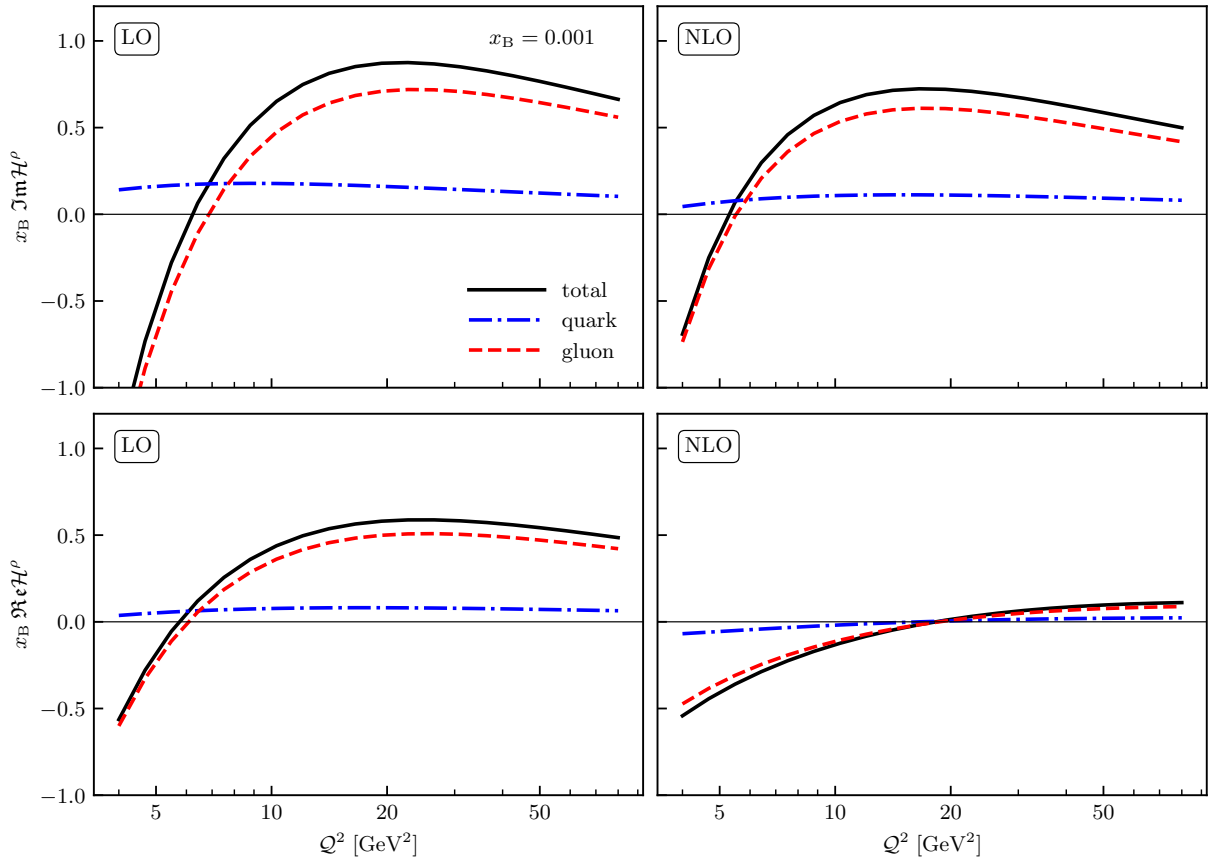


Figure 7.12: Separation of quark (blue dot-dashed) and gluon (red dashed) contributions to the real (top) and imaginary (bottom) TFF  $\mathcal{H}^p$  (black solid) with models LO-DVCS-DVMP (left) and NLO-DVCS-DVMP (right) for  $x = 0.001$  and  $t = 0$ .

These results can be reframed in the context of the so-called skewness ratio of GPDs at the crossover line and the corresponding PDFs

$$r^a(Q^2) = \frac{H^a(x, \xi = x, t = 0, Q^2)}{H^a(x, \xi = 0, t = 0, Q^2)}, \quad (7.16)$$

which for small values of  $x$  does not depend on  $x$ . According to [146, 147], for a fixed  $t$  this value should be completely determined by the value of the corresponding PDF and take on the values

$$r_{\text{con}}^{\Sigma} = \frac{2^{\lambda} \Gamma(3/2 + \lambda)}{\Gamma(3/2) \Gamma(2 + \lambda)}, \quad r_{\text{con}}^{\text{G}} = \frac{2^{1+\lambda} \Gamma(3/2 + \lambda)}{\Gamma(3/2) \Gamma(3 + \lambda)}. \quad (7.17)$$

We call it the conformal ratio because it is a Clebsch-Gordan coefficient occurring in the COPE of the product of two currents. It was obtained by taking a simple power-like ansatz for PDFs, performing a Shuvaev transform [148] and comparing to previously obtained global PDF fits to

obtain the parameter  $\lambda$ . It was concluded that the skewness ratios take on the fixed values

$$r^{\text{Quark}} \approx 1.65, \quad r^{\text{Gluon}} \approx 1.0. \quad (7.18)$$

A similar result was obtained by the popular Radyushkin's double distribution ansatz [149, 150]. These predictions were obtained using several assumptions and simplifications, so we do not expect them to hold exactly. We have seen from Figures 7.11 and 7.12 that the NLO description differs significantly from the LO description, which is not the case for DIS, and so we expect the skewness ratio to differ as well.

In Figure 7.13 we have plotted the skewness ratio at  $x = 0.001$  for quarks and gluons obtained by all six models. We can see that for both quarks, which are depicted in the left panel, and gluons, which are depicted in the right panel, the LO description is not consistent and varies greatly with the process. Once we go to NLO, the skewness ratio starts to agree much more between processes and comes relatively close to the values in (7.18). This is a confirmation that a universal GPD description of DVCS and DVMP emerges at NLO. We can see that the skewness ratios predicted by the NLO models are somewhat higher than the conformal ones. For quarks, all three lines sit right above the value 2, and for gluons they sit roughly above the value 1.5. For gluons we can also notice that the NLO fit to all datapoints and the NLO fit to DIS+DVMP give a similar value, while the NLO fit to DIS+DVCS somewhat disagrees with them, which could be due to the stronger presence of gluons in DVMP.

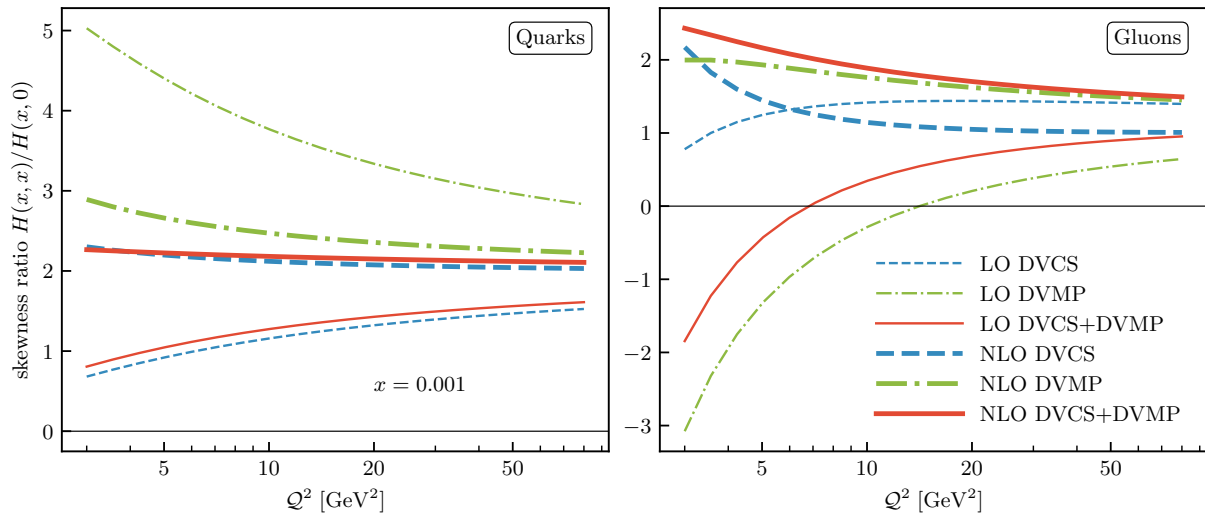


Figure 7.13: Depiction of skewness ratio at  $x = 0.001$  for quark (left) and gluon (right) GPD  $H$  for three LO (thin) and three NLO (thick) models from Table 7.1.

Through this analysis we conclude that at low  $x$  and  $Q^2 > 10 \text{ GeV}^2$  a collinear twist-2 description of DVMP is possible once NLO corrections are included. We have also shown that at NLO a simultaneous fit to DIS, DVCS and DVMP is possible, thus uncovering a universal GPD description of the proton structure.

### 7.2.4 Gepard

Gepard is a software used to perform all of the numerical calculations and to plot all of the graphs. The software was predominantly coded by prof. K. Kumerički, and parts of it were independently verified by various people. Specifically, the full DVMP cross section with evolution was coded and cross-checked with Gepard by the author of this thesis. Gepard is available publicly as a Python package that can be installed in the same way as any other. The detailed documentation and instructions on its use are given in the website <https://gepard.phy.hr/index.html>. On the website you can also find a GPD server which directly plots and generates GPD or CFF values for a given model.

We give here a short tutorial on how to use it. After installing it, you can import it as any other package. The first step for calculating anything is to choose a model and define the kinematics you are interested in. Say that we want to use an already defined model such as KM15, which is one of the more popular models. We define a datapoint in the JLab kinematics that can be used to calculate the DVCS cross section. The code for importing Gepard, the model KM15 and defining a datapoint is given bellow.

```
import gepard as g
from gepard.fits import th_KM15
pt = g.DataPoint(xB=0.348, t=-0.3, Q2=3., phi=0.3,
                 process='ep2epgamma', exptype='fixed target',
                 inlenergy=6., inlcharge=-1, inlpolarization=+1,
                 observable='XS', val=0.21, err=0.01)
```

If we want to calculate the observable defined in the datapoint, we simply write

```
th_KM15.predict(pt)
```

and if we want to calculate another observable given at the same kinematics, such as the charge asymmetry, we write

```
th_KM15.AC(pt)
```

We can calculate CFFs as

```
th_KM15.ImH(pt)
```

If we want to build our own theory by taking various analytical expressions for GPDs, CFFs/TFFs and observables, we can write

```
import gepard as g
class MyTheory(g.PWNormGPD, g.MellinBarnesCFF, g.DIS, g.BMK, g.DVCS,
g.MellinBarnesTFF, g.DVMP):
    pass
th = MyTheory()
```

For example, our two-step fit was performed as

```
f = g.MinuitFitter(DISpoints, th)
f.release_parameters('ns', 'al0s', 'al0g')
f.fit()
f.fix_parameters('ALL')
f = g.MinuitFitter(th.fitpoints, th)
f.release_parameters('ms2', 'alps', 'secs', 'this', 'mg2', 'alpg',
'secg', 'thig')
f.limit_parameters(pars_range)
f.fit()
```

where `th` denotes the six models described in this chapter. The datapoints and the parameter ranges were also defined in this chapter.

There are more aspects to Gepard, such as our neural network framework, which we explain in the next chapter.

## **Part III**

# **Neural network parametrization**

# Chapter 8

## Neural network extraction of CFFs

In this chapter we use the methods detailed in Chapter 5 to extract Compton form factors from DVCS data, and to obtain flavored contributions to CFFs. The results given here were published in [5].

### 8.1 Neural network framework

We are currently in the intermediate stage of studying DVCS through machine learning methods, meaning that we cannot yet deconvolute the GPDs inside of the CFFs, so we presently only extract CFFs from the data. We do this by utilizing neural network algorithms, where we input the kinematic points from the measurements and train the CFFs found in theoretical expressions for observables on the measurements. More formally, the steps in obtaining a neural network extraction of CFFs are:

- i) the values for  $x_B$  and  $t$  from the measurements are fed into input neurons with two layers, datapoint by datapoint;
- ii)  $(x_B, t)$  values are propagated through the network with certain weights and activation functions, where the weights in the first iteration are set to random values;
- iii) the net calculates the values of the real and imaginary CFF components as functions of  $x_B$  and  $t$ ;
- iv) the predicted values of CFFs are used to calculate observables, which are then compared to actual measurements using the squared error utilized in the calculation of  $\chi^2$ ;
- v) the error obtained in the previous step is weighted by the inverse uncertainty of the measurement, if possible, and then used to modify the network through backpropagation;

vi) the process is repeated through the entire training dataset.

This is called a training epoch, and an example of a neural net architecture used for extraction of CFFs is given in Figure 8.1 below.

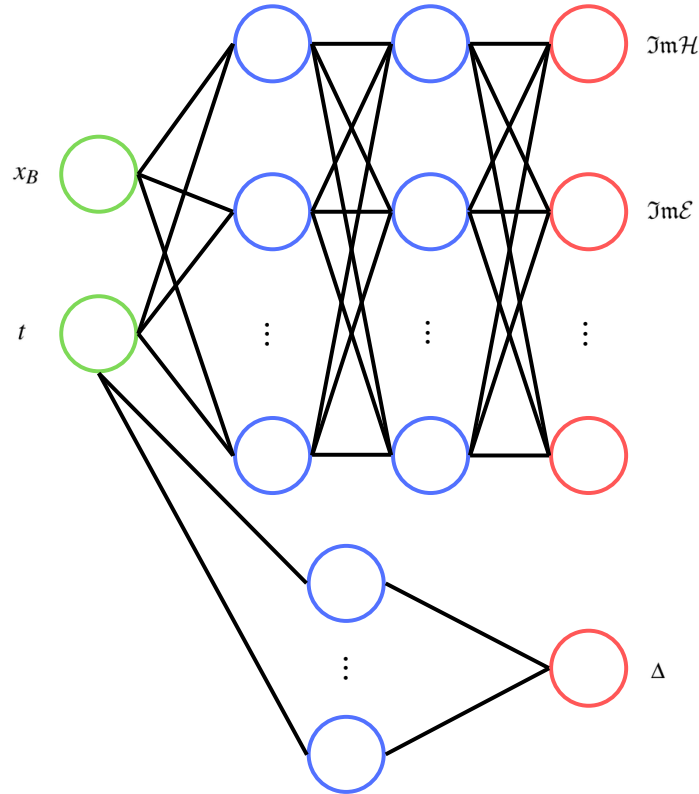


Figure 8.1: Example of a neural network architecture that parametrizes CFFs as functions of  $x_B$  and  $t$ .

The reason we only use  $x_B$  and  $t$  as input values, and not also the virtuality of the process, is because the analysis we perform is on a dataset with a very narrow span of  $Q^2$  values, so we do not expect that the  $Q^2$  dependence would have a significant impact. We therefore do not implement QCD evolution in this framework.

This procedure is equivalent to a least squares fit in the sense that a neural network is basically a non-linear multi-parameter function, and its training is equivalent to least-square fitting. There are several advantages to using a neural network framework. One is the fact that a neural network approach is unbiased because we do not suggest any functional form of the CFFs. Also, neural networks can arbitrarily accurately approximate any smooth function due to the universal approximation theorem, as mentioned before. This process is also algorithmically efficient

because the backpropagation of errors uses values and gradients of the activation function only from the immediate neighborhood of a given layer.

Another advantage of this method is the ease of propagating experimental uncertainties and their correlations into the final result using the Monte Carlo method [151, 152, 153]. The way this method is utilized in this approach is by interpolating a replica dataset. A random set of datapoints is generated using a Gaussian probability distribution with a width determined by the error bars of the measured data. We generate a large set of these replicas  $N_{\text{rep}}$ , where the family of the resulting neural nets  $\mathcal{F}^{(1)}, \dots, \mathcal{F}^{(N_{\text{rep}})}$  defines the probability distribution of CFFs  $\mathcal{F}(x_B, t)$  and their functionals  $F[\mathcal{F}]$ . The value of a functional of CFFs and its variance is given as

$$\langle F[\mathcal{F}] \rangle = \frac{1}{N_{\text{rep}}} \sum_{k=1}^{N_{\text{rep}}} F[\mathcal{F}^{(k)}], \quad (8.1)$$

$$(\Delta F[\mathcal{F}])^2 = \langle F[\mathcal{F}]^2 \rangle - \langle F[\mathcal{F}] \rangle^2. \quad (8.2)$$

The Monte Carlo method is a general method for propagating errors, and is not just applicable to neural network methods.

All of our numerical studies were done in the Python programming language, where the neural network parametrization was implemented using the PyBrain software library, which has shown great flexibility for our purposes. One of the extenuating circumstances when using preexisting neural network softwares for our analysis is that most readily available softwares compare the output of the net directly to data for error calculation, which is not applicable in our case, where the network predicts CFFs. The outputs have to be transformed into DVCS observables we are training on, which adds another step and we therefore needed to adapt the PyBrain library for our needs.

One aspect of a neural network algorithm is the correction of the network with respect to the error between the net predictions and data. Several types of error propagating networks are in use in this field of study, from a simple backpropagation algorithm described in Chapter 5, to genetic algorithms used by the NNPDF group [154, 152]. The algorithm used in our studies is the resilient backpropagation algorithm [155], which is a modification of the standard backpropagation algorithm in the sense that it only uses the signs of the derivatives of the error functions, and not their magnitude, in order to correct the weights in the network. Because it only uses the signs of the derivatives, it is fast and does not depend on the parameters of the network nor the learning process, but it is still very reliable. It would not be sophisticated enough if the relationship between the network output and observables were very non-linear, which would be the case if we tried to parametrize GPDs.

Another choice we have to make is the number of hidden layers and neurons in each layer. It was shown in several studies [128, 156] that CFFs, at least the ones that had been extracted at that point, are relatively well-behaved functions and there is no need for deep learning studies and many hidden layers with many neurons. Also, we do not work with a large number of datapoints. In the models described here we will use one to two hidden layers.

## 8.2 Extraction of CFFs

This study was prompted by the proton and neutron DVCS measurements made with the 6 GeV upgrade at JLab's Hall A Collaboration [157, 158]. Aside from a higher precision coming from the increased beam energy, these measurements enabled us to extract the  $u$  and  $d$  quark flavor contributions to CFFs. The first part of our study attempts to extract all 8 CFFs from the new proton DVCS data, and to add the constraint of dispersion relations (3.115) in order to reduce the uncertainties of the neural network predictions.

For the purpose of this study, we perform both neural network fits and standard model least-square fits described in Chapter 6.

### 8.2.1 Model fits

Since JLab data is not measured at low  $x$  and high  $Q^2$  like HERA data, we cannot make the same approximations as in the previous chapter. Specifically, in this study we cannot ignore the valence quark sector, nor the presence of CFFs other than  $\mathcal{H}$ . The model presented in this section was detailed in [128, 159, 160].

Given that our computer codes do not have the valence sector implemented in the conformal space, the model is a hybrid one. The valence sector is modeled in the  $x$ -space on the crossover line  $x = \eta$

$$H_q^{\text{val}}(x, x, t) = \frac{n_q r_q}{1+x} \left( \frac{2x}{1+x} \right)^{-\alpha_v(t)} \left( \frac{1-x}{1+x} \right)^{b_q} \frac{1}{1 - \frac{1-x}{1+x} \frac{t}{M_q^2}}, \quad q = u, d. \quad (8.3)$$

This model is based on the same arguments made for the conformal moments of GPDs in Section 6.3. Now the Regge trajectory is not a parameter, but is given by the Reggeon exchange

$$\alpha_v(t) = 0.43 + 0.85t/\text{GeV}^2. \quad (8.4)$$

The parameter  $n_q$  is the normalization known from PDF studies, and  $r^q$  parametrizes the skew-

ness ratio given in (7.16).

We argued the use of conformal moments in our description of GPDs due to easier implementation of evolution. Given the difficulties, we do not implement QCD evolution in the valence sector, and we also remain at the LO level, where the imaginary part of the valence CFF  $\mathcal{H}$  is given simply as

$$\Im\mathcal{H}^{\text{val}}(\xi, t) = \pi \sum_{q=u,d} Q_q^2 \left[ H_q^{\text{val}}(\xi, \xi, t) - H_q^{\text{val}}(-\xi, \xi, t) \right]. \quad (8.5)$$

For the analysis of proton data, a simple model was used  $F_u^{\text{val}} = 2F_d^{\text{val}}$ .

This model also includes dispersion relations, where we cannot ignore the subtraction constant. We model it separately as

$$\Delta_{\mathcal{F}}(t) = \frac{C}{\left(1 - \frac{t}{M_C^2}\right)^2}, \quad (8.6)$$

also ignoring its dependence on  $Q^2$ . The implementation of dispersion relations allows us to model only the imaginary parts of CFFs and one subtraction constant, since  $\Delta_{\mathcal{H}} = -\Delta_{\mathcal{E}}$  and  $\Delta_{\tilde{\mathcal{H}}} = \Delta_{\tilde{\mathcal{E}}} = 0$ . In principle, this reduces the number of functions to model from 8 to 5, and the subtraction constant depends only on one kinematic variable. The free parameters of this sector are therefore  $r_q, b_q, M_q, C$  and  $M_C$ .

The sea quark and gluon GPDs are modeled in the conformal space as explained in Chapter 6, also at LO to match the valence sector, with the QCD evolution implemented.

By observing Table 3.2, we can see that the influence of CFFs  $\mathcal{E}$  and  $\tilde{\mathcal{E}}$  is kinematically suppressed in most proton DVCS observables, therefore in our models we set  $\Im\mathcal{E}$  and  $\Im\tilde{\mathcal{E}}$  to zero. This is not to say that these CFF components are small, but rather that they are not accessible from the data we are observing. The real component of the CFF  $\mathcal{E}$  is given by the subtraction constant  $-\Delta_{\mathcal{H}}$ , but the CFF  $\tilde{\mathcal{E}}$  has an additional contribution from the pion pole, which yields a real contribution. This phenomenon occurs due to an exchange of a virtual pion inside the nucleon, which decays into the  $q\bar{q}$  pair probed by the photon in the ERBL region. For small  $|t|$ , the pion is only weakly off-shell, and for  $t = m_\pi^2$  we have an exchange of an on-shell particle, which results in a pole contribution because the pion propagator diverges. The pion

pole contribution is equal to [161]

$$\Re\tilde{\mathcal{E}} = \frac{1}{\xi} \frac{2g_A M^2 r_\pi}{m_\pi^2 - t} \frac{1}{\left(1 - \frac{t}{M_\pi^2}\right)^2}. \quad (8.7)$$

Here  $g_A \approx 1.26$  is the axial charge of the nucleon,  $M$  is the nucleon mass,  $m_\pi$  is the mass of the pion expressed in GeV, and  $M_\pi$  is a free parameter. In the case of the neutron, this contribution has an opposite sign. This model therefore parametrizes 3 CFF components and one subtraction constant.

This model is of the type usually denoted as KM, so we denote it as KM20. It was obtained by using the sea quark and gluon parameters from a previously obtained model KM15, which was fitted to H1, ZEUS, HERMES, and JLab data, and then releasing the valence parameters on the same dataset, with added 2017 Hall A [157] measurements. This model is the only one in this analysis that is truly global because it describes both the low- $x$  measurements from H1, ZEUS and HERMES, as well as the intermediate- $x$  data from JLab. The singlet quark and gluon sector parameters are set to

$$\begin{aligned} N^{\text{sea}} = 0.152, \quad \alpha_0^{\text{sea}} = 1.158, \quad \alpha'_{\text{sea}} = 0.15, \quad m_{\text{sea}}^2 = 0.482, \quad s_2^{\text{sea}} = 1.071, \quad s_4^{\text{sea}} = -0.366, \\ N^{\text{G}} = 0.5, \quad \alpha_0^{\text{G}} = 1.247, \quad \alpha'_{\text{G}} = 0.15, \quad m_{\text{G}}^2 = 0.7, \quad s_2^{\text{G}} = -2.990, \quad s_4^{\text{G}} = -0.905. \end{aligned} \quad (8.8)$$

In the KM15 model the parameters  $\alpha'_a$  and  $m_{\text{G}}^2$  were not released for fits, but kept fixed to their initial values obtained from previous studies, and the norm  $N_{\text{G}}$  is fixed by the summation rule (6.68). The valence parameters obtained by fitting are

$$\begin{aligned} r_v = 0.754, \quad b_v = 0.062, \quad C = 2.070, \quad M_v = 1.040, \\ \tilde{r}_v = 1.02, \quad \tilde{b}_v = 0.555, \quad \tilde{M}_v = 3.31, \quad r_\pi = 2.78, \quad M_\pi = 5.36. \end{aligned} \quad (8.9)$$

Note that we have taken the valence parameters to be flavor independent. The constants fixed by the forward limit are  $n^{\text{val}} = 1.35$  and  $\tilde{n}^{\text{val}} = 0.6$ . The parameters  $r_\pi$  and  $M_\pi$  describe the pion pole.

## 8.2.2 Neural network models

As for the neural network fits, the method was described in the first section of this chapter. One type of model was obtained by taking the values of  $x_{\text{B}}$  and  $t$  as inputs, and giving the values of 6 out of 8 leading twist-2 CFF components. The training and validation sets are separated

randomly, but we do not have enough data to also have a separate test set. When doing some preliminary studies with a reduced dataset, it was shown that  $\Re\tilde{\mathcal{H}}$  and  $\Re\tilde{\mathcal{E}}$  were consistent with zero and have negligible influence on the goodness of fit, as was shown in [162], meaning that the data are not sensitive to these components. In order to simplify the model and reduce variance, they were excluded from all fits to the whole dataset. This model will be denoted as NN20. The other type of the model is constrained by dispersion relations (DR), and we denote it as NNDR20. This model outputs 4 imaginary components of CFFs and one subtraction constant, while  $\Re\mathcal{H}$  and  $\Re\mathcal{E}$  are calculated from (3.115). By introducing DRs, this model is more constrained and so we expect narrower error bands, but it is also more biased. The architecture of this model is depicted in Figure 8.1.

The experimental errors are propagated using the Monte Carlo method explained in the first section of this chapter. For this study we had to determine how many replicas are necessary for reliable results, so we made preliminary studies to a reduced dataset with 10 replicas, as well as 80 replicas. By comparing the results, we found that they differ by less than 5%. We have therefore settled on 20 replicas for each model, partially motivated by the fact that the DR constrained models take a longer time to train because they have to evaluate the principal value of the integral in (3.115).

Similar preliminary studies showed that there is no need for deep learning methods with many layers and neurons. The architecture for the NN20 model is 2-13-6, and for NNDR20 it is 2-13-4, while for the calculation of the subtraction constant it is 1-5-1. So all of these models have just one hidden layer.

As mentioned at the beginning of this chapter, none of the neural network models implement QCD evolution.

### 8.2.3 Experimental data and results

In order to be safe from any QCD evolution aspects, we only fit the neural network models to JLab's CLAS and Hall A Collaboration data, which are measured in a narrow span of  $Q^2$  values. We compare these results to the KM20 model, which was fitted to HERA data as well, so only the comparison for higher values of  $x$  has merit. We used the data for the unpolarized cross section and various beam and target asymmetries

$$d\sigma_{\lambda,\Lambda} = d\sigma (1 + \lambda A_{LU} + \Lambda A_{UL} + \lambda \Lambda A_{LL}), \quad (8.10)$$

as well as the data for the helicity-dependent cross section

$$\Delta\sigma \equiv d\sigma_{A_{LU}}. \quad (8.11)$$

Here  $\lambda/2$  is the helicity of the electron, and  $\Lambda/2$  is the longitudinal spin of the nucleon.

As was detailed in Section 3.6.1, all of these observables can be expanded as a truncated Fourier series in the angle  $\phi$  at the twist-2 level. We have therefore Fourier transformed all of the data and kept only the first one or two harmonics, which we call the  $n$ -space. We then used this data for fits for several reasons, one being their efficiency. Another reason concerns the statistics of error propagation. Namely, we mentioned that the Fourier series of most observables is truncated at the level of the first or second harmonic, which is because higher harmonics are suppressed by  $Q^2$  factors. But current experimental setups are incapable of discerning any higher harmonics from the data, which means that it would be inconsistent to keep any higher harmonics in the theoretical expressions. We have propagated experimental uncertainties using the Monte Carlo method explained before, and have indeed verified that no harmonics higher than the second one are discernible from the data with any statistical significance. Since in most observables only the first harmonic is present, both theoretically and experimentally, the agreement between data and models regarding the phase and frequency of  $\phi$ -oscillations will be trivial. This can then skew  $\chi^2$  values because it can build up good description of datapoints in trivial points such as at sine or cosine zeros. Also, if some measurements are available in the  $\phi$ -space, and some in the  $n$ -space, there would be a mismatch in statistical weights because there are many more datapoints in the  $\phi$ -space. Therefore, for current purposes only the amplitude will carry any relevant information regarding GPD extraction.

In this study we again check the quality of the fit by calculating  $\chi^2/N_{\text{pts}}$  for each dataset and all of the data together. The results and all of the data used are given in Table 8.1 below. Even though we fit only to the harmonics, as explained above, calculating the  $\chi^2$  values on these data would lead to inaccurate interpretations of the quality of the fit. This is due to the difficulty of propagating systematic errors in fitting procedures because errors that are uncorrelated are treated differently than errors which correlate for different values of  $\phi$ . Uncorrelated systematic uncertainties are added in quadrature to the statistical ones, before a Fourier transform is performed, and correlated systematic uncertainties should in principle be added to systematic ones after the Fourier transform. In many analyses these uncertainties are combined into one uncertainty under the name "normalization uncertainty", which removes all possibility to assess which errors could be correlated. In order to avoid this problem, we assess the quality of fits by calculating  $\chi^2$  values in the  $\phi$ -space. For more details, see [163].

Observable	$N_{\text{pts}}$	KM20	NN20	NNDR20
# CFFs + $\Delta s$		3+1	6	4+1
Total (harmonics)	277	1.3	1.6	1.7
CLAS [164] $A_{\text{LU}}$	162	0.9	1.0	1.1
CLAS [164] $A_{\text{UL}}$	160	1.5	1.7	1.8
CLAS [164] $A_{\text{LL}}$	166	1.3	3.9	0.8
CLAS [165] $d\sigma$	1014	1.1	1.0	1.2
CLAS [165] $\Delta\sigma$	1012	0.9	0.9	1.0
Hall A [166] $d\sigma$	240	1.2	1.9	1.7
Hall A [166] $\Delta\sigma$	358	0.7	0.8	0.8
Hall A [157] $d\sigma$	450	1.5	1.6	1.7
Hall A [157] $\Delta\sigma$	360	1.6	2.2	2.2
Total ( $\phi$ -space)	4018	1.1	1.3	1.3

Table 8.1: Values of  $\chi^2/N_{\text{pts}}$  for presented models and for each set of JLab DVCS measurements used in this study ( $\phi$ -space). First row specifies the number of real independent CFFs plus the number of subtraction constants. Second row gives the total value for leading harmonics of Fourier-transformed data, to which we actually fit.

We can see that a few of the datasets are not well described, but the overall values of  $\chi^2/N_{\text{pts}} = 1.1 - 1.3$  are satisfactory and would indicate that the obtained CFFs are realistic. We can also see that we have a similar description between different models, which could imply some correlations between different CFFs. Of course, the real and imaginary parts of each CFF are correlated through dispersion relations, which we would consider as intrinsic correlations, but some correlations are brought on by the specifics of the current data and they might be broken with more upcoming measurements.

In Figure 8.2 below we depict the six extracted CFFs obtained by the standard neural network model NN20, a dispersion relations constrained neural network model NNDR20, and a standard hybrid model fit KM20. The CFFs are depicted in dependence to  $\xi$  at  $Q^2 = 4 \text{ GeV}^2$  and  $t = -0.2 \text{ GeV}^2$ .

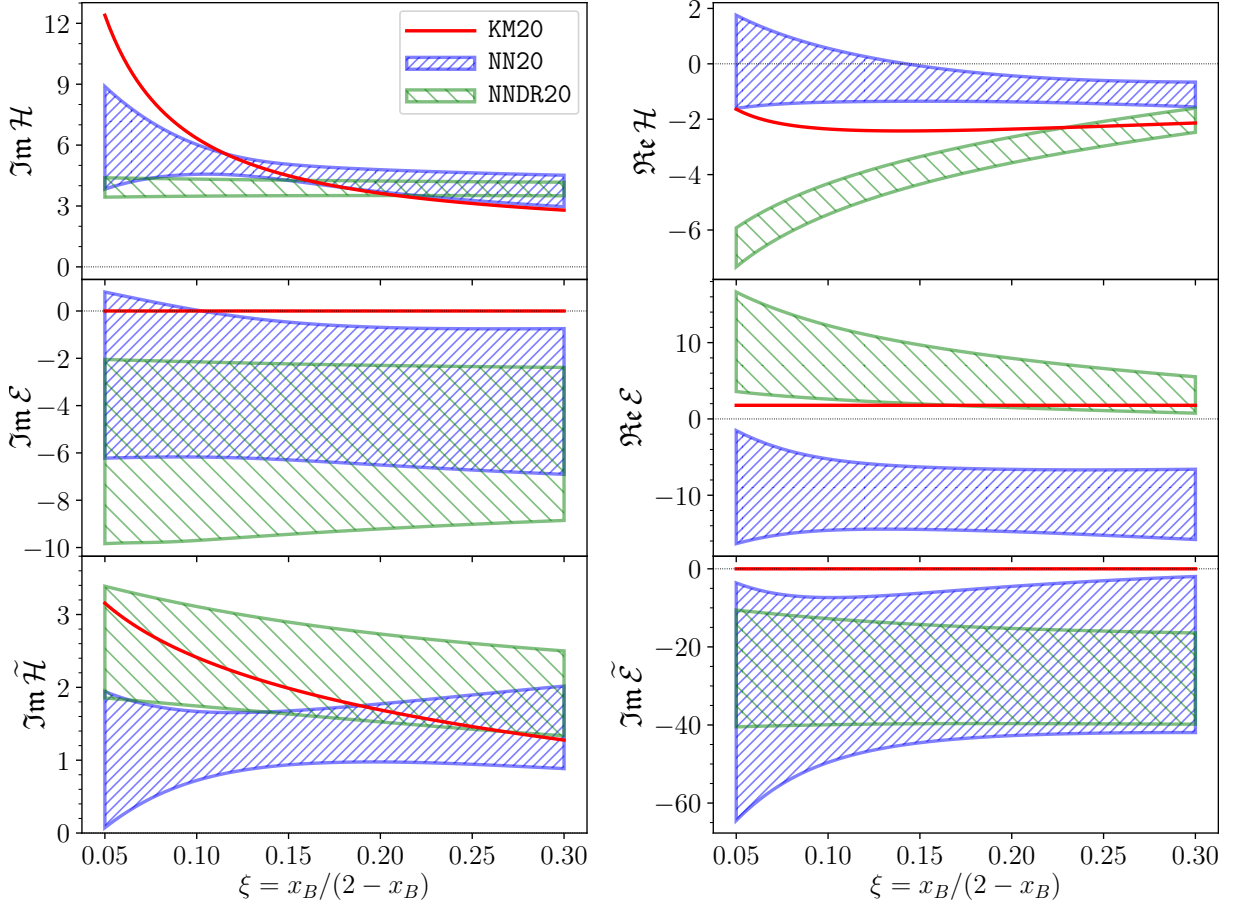


Figure 8.2: Extraction of CFFs at  $Q^2 = 4 \text{ GeV}^2$  and  $t = -0.2 \text{ GeV}^2$  by two neural network models fitted to JLab proton data, NN20 and NNDR20, as well as a standard model fit KM20 [5].

The reason we implemented dispersion relations into the neural network framework is the hope of reduced uncertainties, which is visible in  $\Im\mathcal{H}$ ,  $\Re\mathcal{H}$  and  $\Im\tilde{\mathcal{E}}$ . The mean values for  $\Re\mathcal{H}$  and  $\Re\mathcal{E}$  are shifted, even changing the sign of  $\Re\mathcal{E}$ . In model NNDR20, the value of  $\Re\mathcal{E}$  is positive, which is reproduced in [167], but the popular models Vanderhaeghen-Guichon-Guidal (VGG) [168] and Goloskokov-Kroll (GK) [169] give a negative sign, as is predicted by model NN20. The model NNDR20 is in a somewhat better agreement with KM20, since they are both constrained by dispersion relations. As mentioned before, the model KM20 was fit to low- $x$  data as well, so it is to be expected that its low- $x$  behavior differs from the neural net models, which have never seen low- $x$  data, and it is therefore unlikely for them to reproduce it.

The CFFs extracted using the model NNDR20 agree with the extraction obtained by a dispersion relation constrained model fit from [167], the only difference being the sign of  $\Im\mathcal{E}$ . This CFF has the largest uncertainties, so we hope that with more data this sign discrepancy will be

resolved. In [162], a global neural network extraction was performed, and it is in agreement with our extraction within uncertainties. The agreement is better with model NN20, because it is also not constrained by dispersion relations, so these models predict the same sign for  $\Re\mathcal{E}$ .

### 8.3 Flavor separation of CFFs

In this section we fit our models to the same data as in the previous chapter, but we add the neutron DVCS data from [158]. The goal of this study is to use the proton and neutron DVCS data to extract the flavor contributions to CFFs by using the isospin symmetry of GPDs

$$F_{u,\text{proton}} = F_{d,\text{neutron}} \equiv F_u. \quad (8.12)$$

For the model fit we implement the flavor separated GPDs by leaving the sea quark sector the same as in previous models, but separately parametrizing flavored valence GPDs  $F_u^{\text{val}}$  and  $F_d^{\text{val}}$  by using parameters  $r_u \neq r_d$ ,  $b_u \neq b_d$ , and  $M_u \neq M_d$ . Since our goal is flavor separation, and there are very few neutron datapoints in comparison to the whole dataset, we perform flavored fits only to JLab data. We denote this fit as fKM20. The total proton and neutron GPDs, and equivalently CFFs, are written in terms of flavored GPDs as

$$F^{p,n} = \frac{4}{9}F^{u,d} + \frac{1}{9}F^{d,u}. \quad (8.13)$$

This model parametrizes 5 CFF components,  $\Im\mathcal{H}^u$ ,  $\Im\mathcal{H}^d$ ,  $\Im\tilde{\mathcal{H}}^u$ ,  $\Im\tilde{\mathcal{H}}^d$  and  $\Re\mathcal{E}$ , which is the same for up and down quarks, up to a sign. We also parametrize 2 subtraction constants,  $\Delta^u$  and  $\Delta^d$ . Previous models, such as KM15, could treat neutron data by using a simple isospin rotation

$$\mathcal{F}_n^{\text{val}} = \frac{2Q_d^2 + Q_u^2}{2Q_u^2 + Q_d^2} \mathcal{F}_p^{\text{val}} = \frac{2}{3} \mathcal{F}_p^{\text{val}}, \quad \mathcal{F}_n^{\text{sea}} = \mathcal{F}_p^{\text{sea}}, \quad (8.14)$$

which did not prove to be complex enough to predict neutron DVCS data accurately.

Since the analysis of proton-only data revealed that the model NNDR20 is preferred, we only fit this type of model to proton and neutron data. Flavor separation is introduced by considering flavored CFFs as separate functions to be parametrized by the nets, i.e. our outputs are now  $\Im\mathcal{F}^u$  and  $\Im\mathcal{F}^d$  for all four types of twist-2 CFFs, and the proton and neutron CFFs are also given using (8.13). There are also two subtraction constants.

The results for  $\chi^2/N_{\text{pts}}$  for all datasets and models fKM20 and fNNDR20 are given in Table 8.2 below. We can see similar results as in Table 8.1, which could again be due to some correlations between CFFs. The new neutron data is also well described by both models.

Observable	$N_{\text{pts}}$	fKM20	fNNDR20
# CFFs + $\Delta\sigma$		5+2	8+2
Total (harmonics)	277	1.7	1.8
CLAS [164] $A_{\text{LU}}$	162	1.2	1.3
CLAS [164] $A_{\text{UL}}$	160	1.8	2.0
CLAS [164] $A_{\text{LL}}$	166	1.1	1.6
CLAS [165] $d\sigma$	1014	1.2	1.1
CLAS [165] $\Delta\sigma$	1012	0.9	1.1
Hall A [166] $d\sigma$	240	0.9	1.3
Hall A [166] $\Delta\sigma$	358	0.7	0.7
Hall A [157] $d\sigma$	450	1.9	2.0
Hall A [157] $\Delta\sigma$	360	1.9	1.7
Hall A [158] $d\sigma_n$	96	1.2	0.9
Total ( $\phi$ -space)	4018	1.2	1.3

Table 8.2: Values of  $\chi^2/N_{\text{pts}}$  for flavor separated models. See the caption of Table 8.1 for details.

The good  $\chi^2$  values are confirmed by Figure 8.3 below, where we compare the proton and neutron DVCS measurements from [158]. We plot the cross section, which is in the top panels, and its first cosine harmonic, which is on the bottom panels, at beam energies 4.45 GeV, which is on the left, and 5.55 GeV, which is on the right. We can see a somewhat worse model fit prediction for the first cosine harmonic in the proton DVCS at higher  $|t|$ , which has been a common problem with many KM models and is currently still unresolved.

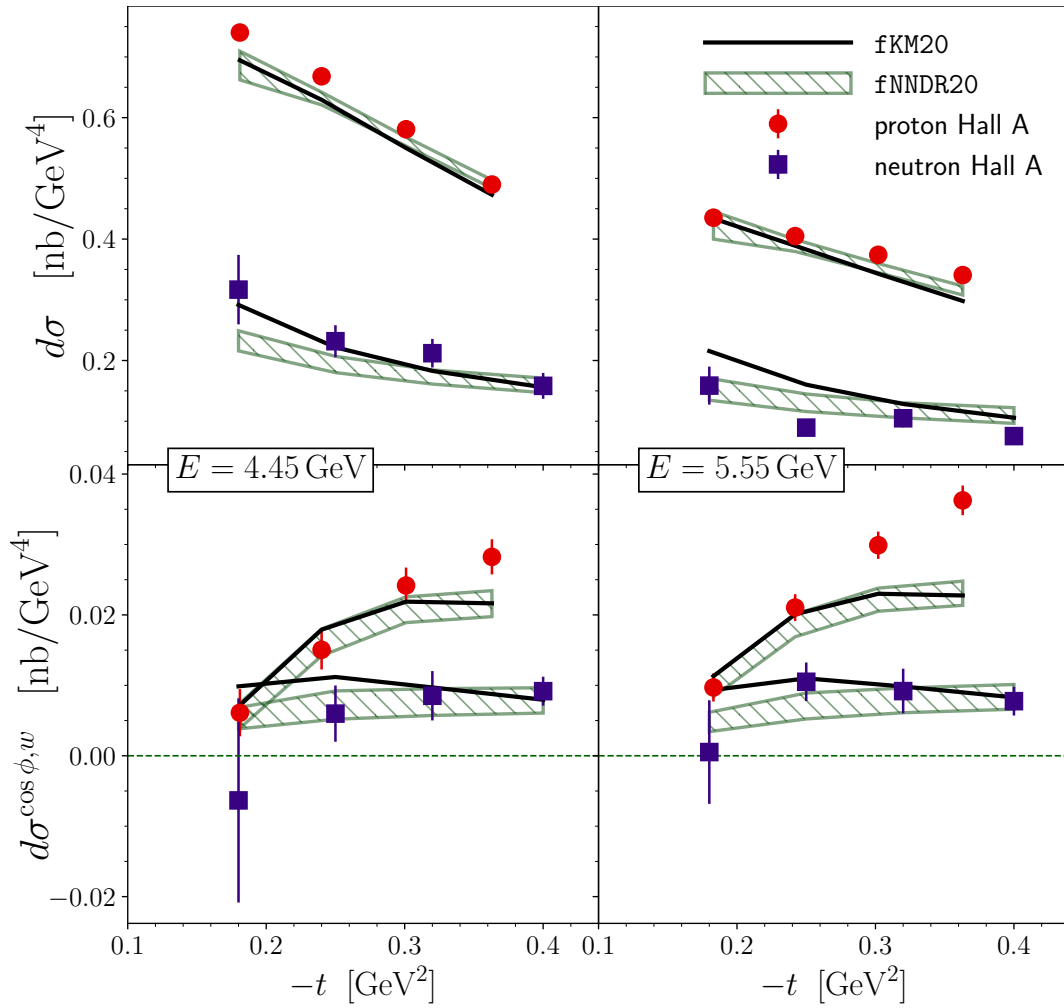


Figure 8.3: Predictions of Hall A proton (red) and neutron (blue) cross section (up) and its first cosine harmonic (down) by models  $f_{\text{KM20}}$  (black line) and  $f_{\text{NDR20}}$  (green band) at beam energies 4.45 GeV (left) and 5.55 GeV (right) [5].

We now observe flavor separated CFFs. In Figure 8.4 below, we plot the up and down components of the real and imaginary parts of the CFF  $\mathcal{H}$  at  $Q^2 = 4$  GeV<sup>2</sup> and  $x_B = 0.36$ . In the left panels we first compare the predictions of models  $f_{\text{KM20}}$  and  $f_{\text{NDR20}}$  for total CFFs. These models have now both been fitted to JLab data, so they are expectedly in better agreement across the whole measured kinematic range. In the right panels, we see a clear separation of the flavor components for both the real and imaginary part.

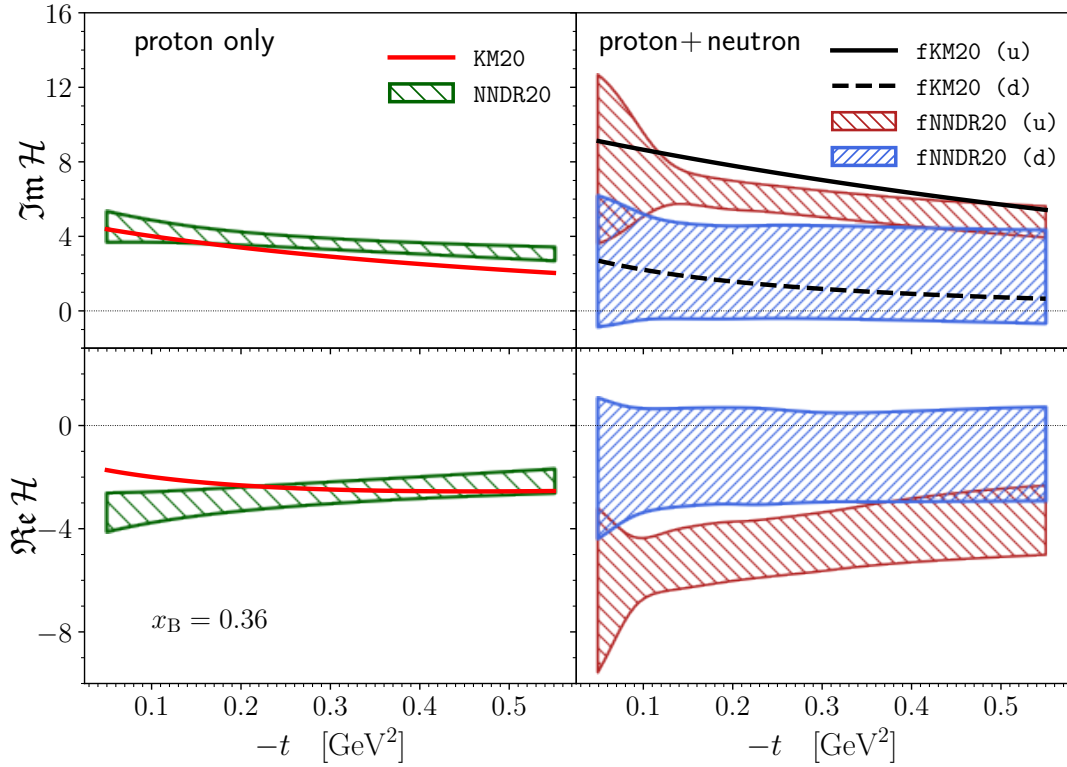


Figure 8.4: Extraction (left) and flavor separation (right) of the real and imaginary components of the CFF  $\mathcal{H}$  predicted by the flavored models  $f_{\text{KM20}}$  and  $f_{\text{NNDR20}}$  [5].

For the purpose of comparison, we plot the predictions of  $f_{\text{KM20}}$  for flavored contributions to  $\Im\mathcal{H}$  and we see a decent agreement. In magnitude, the up quark contribution in both real and imaginary components is roughly twice as large as the down quark contribution.

The flavor separation of the CFF  $\mathcal{E}$  is depicted in Figure 8.5 below. We can see that flavor separation of neither the real nor the imaginary part is possible, which is also the case for the other two CFFs.

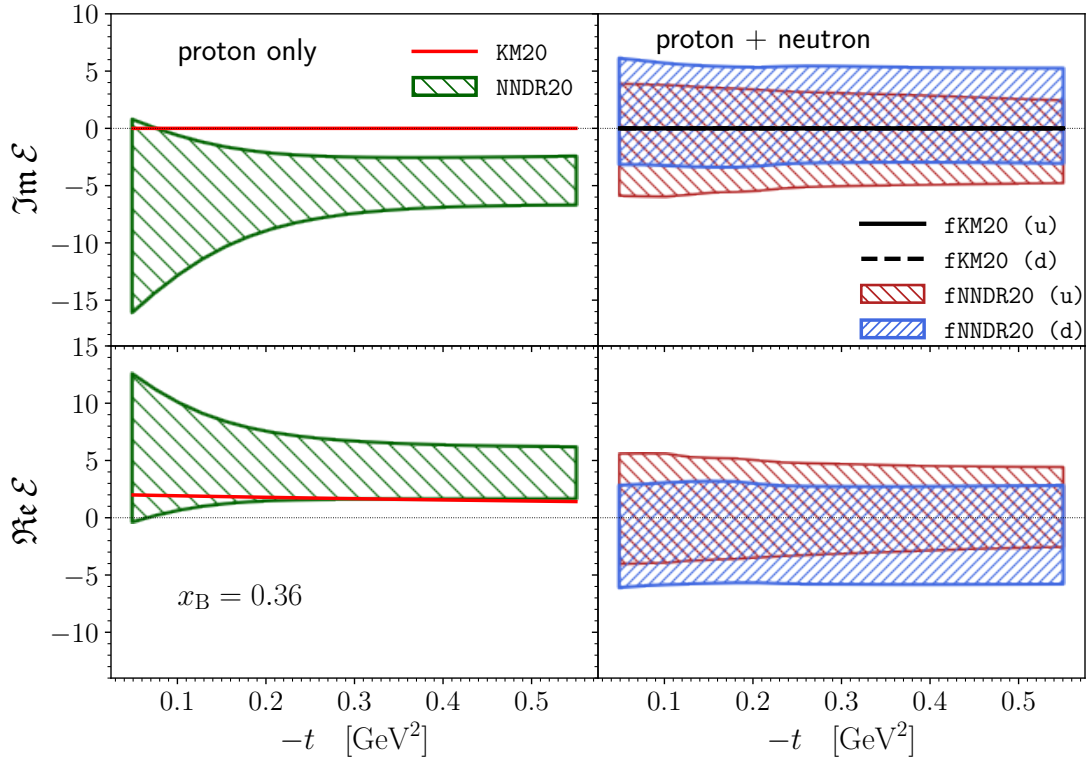


Figure 8.5: Extraction (left) and flavor separation (right) of the real and imaginary components of the CFF  $\mathcal{E}$  predicted by the flavored models  $f_{\text{KM20}}$  and  $f_{\text{NNDR20}}$ .

For both flavor separated CFFs the uncertainties are much larger than for the total CFF. It is also unclear if the flavored components have a different  $t$ -slope, which is connected to the spatial distribution of quarks, so we cannot say if the up and down quarks have a different spatial distribution.

Overall, we have managed to extract 6 out of the 8 twist-2 CFF components, and to obtain a clear flavor separation of the real and imaginary parts of the CFF  $\mathcal{H}$ . Hopefully further data will allow us to separate other CFFs, as well as to extract all 8 CFF components.

We note that the models obtained here are not available in Gepard at this point.

# Chapter 9

## Closure tests

We have so far detailed the extraction of CFFs using neural network methods. We have also mentioned that there are several undergoing experimental efforts to obtain more precise data, both currently, with various JLab updates, and in the long run, such as at the EIC. As new measurements with higher precision come out, it is important to eliminate potential sources of uncertainty in our methodology, in order to obtain reliable error bands, and in general to obtain physical CFFs. In order to verify that our method can be applied to a broad range of data, we employ the so-called closure tests. These tests have long been implemented in the NNPDF framework [170], as well as the PARTONS framework, where they are called feasibility tests [162].

All of our NN type models were implemented using the PyBrain library, where it took each replica of the neural network between a few hours and a day of training on a single thread CPU of a 2.4 GHz Intel Xeon processor. The longer time was necessary for the DR-constrained models. In order to reduce this time, the whole neural network framework we use has been transferred into the PyTorch framework from the Torch library [171], which allowed us to reduce the training time significantly. This framework is now available in Gepard.

The potential steps where we can introduce errors are in the choice of the fitting function, which introduces a theoretical bias, leading to a systematic error, and in the propagation of errors from experiments, because these errors are not always Gaussian as we take them to be when generating replicas. There are of course many more theoretical biases we introduce that increase uncertainties, such as the order in perturbation theory, twist, choice of scales, etc., but since GPDs are functions of three variables, not including the scale dependence, and since they are not directly probed in measurements, the space of possible functions that reproduce the measured observables is very large, and this introduces a much more serious uncertainty that for example in PDFs.

The way we implement closure tests is the following:

1. take some GPD or CFF model as the ground truth;
2. generate simulated data by calculating observables in a certain kinematic range, which may coincide with actual measurements;
3. apply a fitting and extraction procedure to the simulated data;
4. check that the result of the fitting and extraction procedure is consistent with the ground truth.

## 9.1 Testing the extraction of CFFs

For this demonstration, we will take the model  $\text{KM15}$  as the ground truth. We will use this model to generate data which roughly coincides with CLAS6 (beam energy around 6 GeV) kinematics. The observables we will generate in this study are the helicity dependent and independent cross sections, which we denote as  $X_{\text{LU}}$  and  $X_{\text{UU}}$ , respectively, the beam spin asymmetry  $A_{\text{LU}}$ , the beam charge asymmetry  $A_{\text{C}}$ , which may be possible in the future, and the transversal target spin asymmetry  $A_{\text{UT}}$ . In Figure 9.1 below we can see the kinematics at which we randomly simulate data.

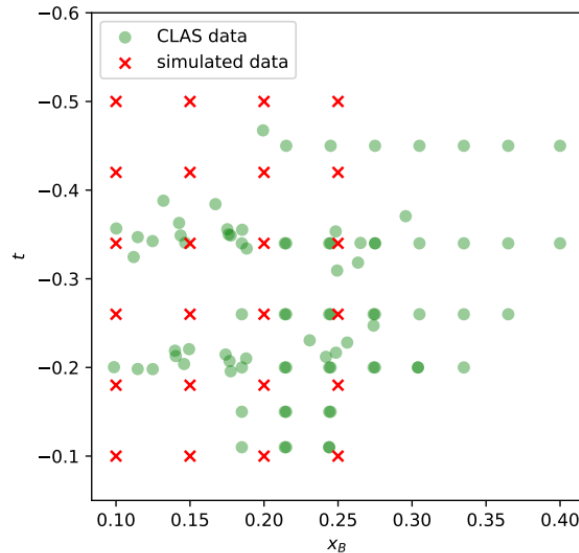


Figure 9.1: Kinematics of the simulated data in comparison to CLAS data kinematics.

We will start off simple by simulating only  $X_{\text{LU}}$  data and extracting  $\Im\mathcal{H}(x_{\text{B}} = 0.2, t)$ , where we fixed the value of  $x_{\text{B}}$  to 0.2. In Figure 9.2 below we depict the mock data, where the  $x$ -axis gives the ordinal number of the datapoint, and it represents the  $t$ -axis. We generated 20 datapoints for  $-t \in [0.1, 0.6]$ , where the errorbars were simulated symmetrically for each datapoint using the formula

$$\text{error} = 0.2 \cdot \text{value} + 0.0001. \quad (9.1)$$

In this model no noise was included, so the simulated data were given strictly by the KM15 model.

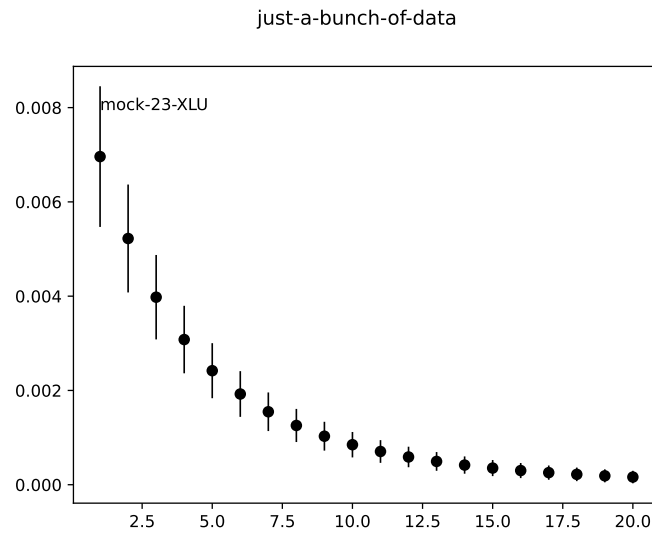


Figure 9.2: Simulated data for the helicity-dependent cross section  $X_{\text{LU}}$ .

We then trained a neural network model with 10 replicas on this data, where the replicas were trained between 20 and 35 epochs, and their output was  $\Im\mathcal{H}(t)$ . Their prediction of the simulated observable is given in Figure 9.3 below.

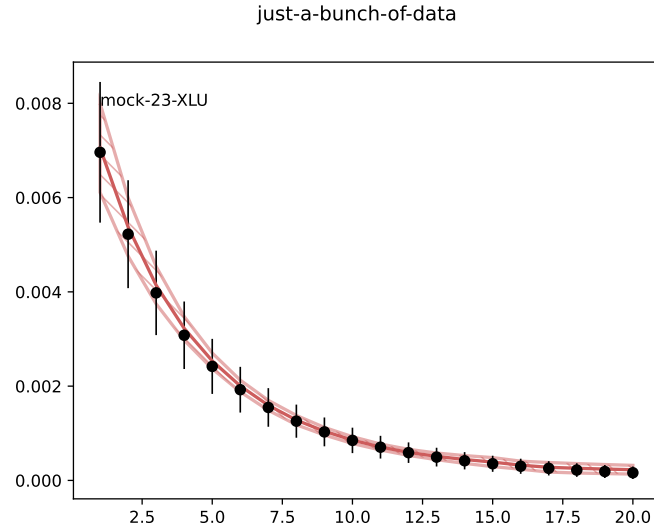


Figure 9.3: Prediction of simulated data for the helicity-dependent cross section  $X_{LU}$  by a neural net model, which is depicted as a red band.

We can see that the neural networks reproduce the data well. Now we must verify that the CFF they extracted is physical, which in this case means that it agrees with the one predicted by the KM15 model. This comparison is given in Figure 9.4 below for values  $x_B = 0.1$ , which is on the left, and 0.2, which is on the right, and  $Q^2 = 4 \text{ GeV}^2$ . For this purpose we draw the average value of the net predictions with a symmetric standard deviation instead of drawing each of the nets.

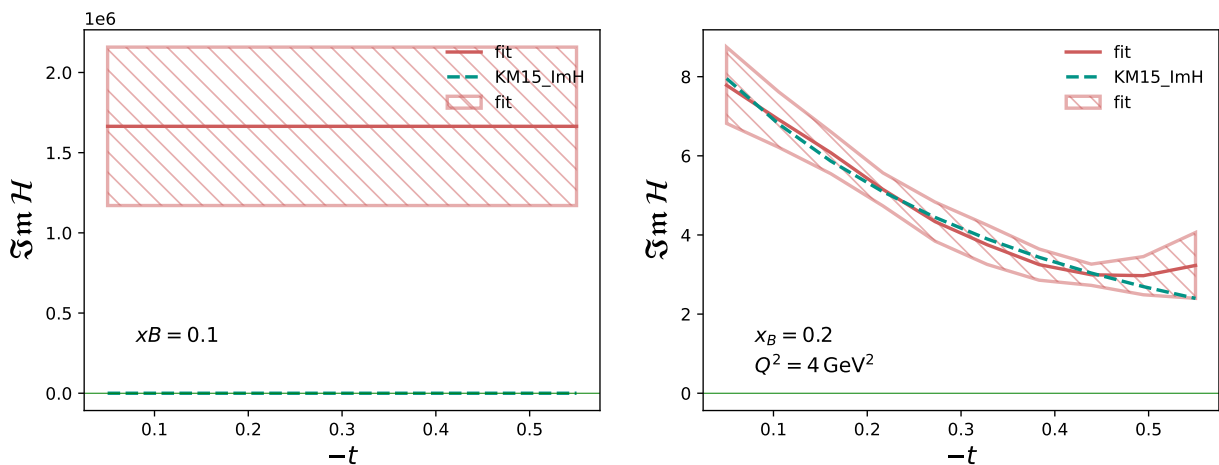


Figure 9.4: Comparison of  $\Im m \mathcal{H}(t)$  obtained by the KM15 model (green line) and the neural net model (red band) trained on simulated data at  $x_B = 0.1$  (left) and 0.2 (right), and  $Q^2 = 4 \text{ GeV}^2$ .

The nets do not contain the CFF at  $x_B = 0.1$ , which is to be expected since the nets were not trained at this value. At  $x_B = 0.2$ , where the nets were trained, the models coincide well.

We now test various more complicated scenarios. We can add noise to the simulated data using a Gaussian distribution. The error of the datapoints is given as

$$\text{error} = 0.1 \cdot \text{value} + 0.0002, \quad (9.2)$$

and the value of each datapoint is obtained by adding to its calculated value a value obtained randomly from a Gaussian distribution centered around zero with a standard deviation equal to the error of the datapoint. We then train a neural network model on this data with 5 nets for simplicity. The simulated data and the neural network prediction are given in Figure 9.5 below, where we again only model the  $t$  dependence at  $x_B = 0.2$ . We now generated 20 datapoints with  $-t$  between 0.1 and 0.5.

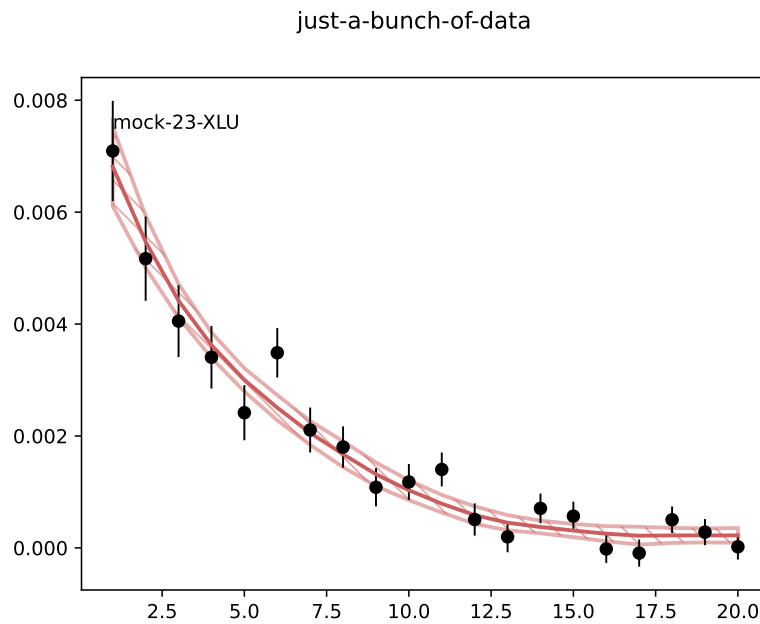


Figure 9.5: Prediction of simulated data for the helicity-dependent cross section  $X_{LU}$  with added noise by a neural net model.

This time around it is a bit more difficult to predict the data, as is the case in real life with real measurements. The extraction of  $\Im\mathcal{H}(t)$  is compared to the prediction by model KM15 in Figure 9.6 below.

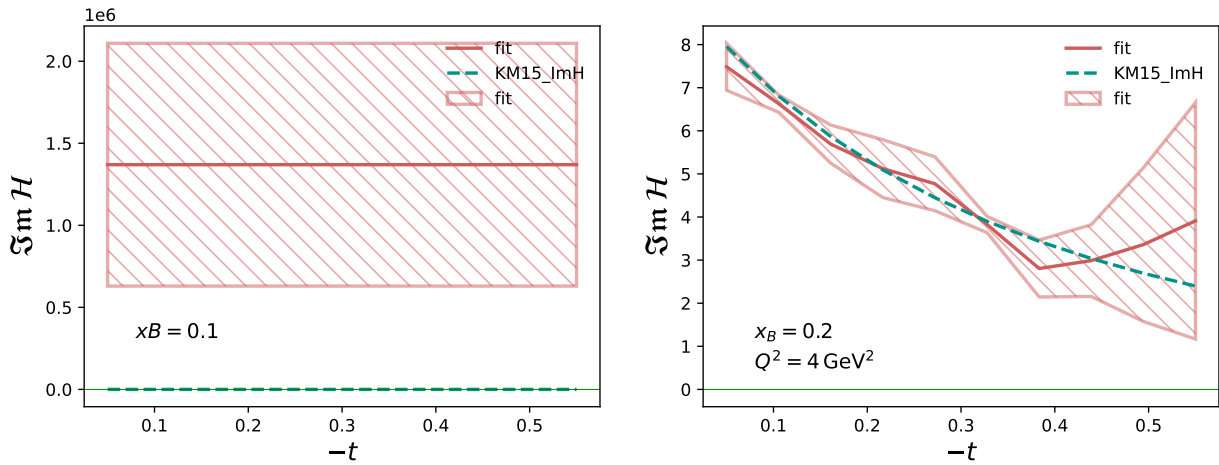


Figure 9.6: Comparison of  $\Im m \mathcal{H}(t)$  modeled by the KM15 model (green line) and extracted by the neural net model (red band) from simulated  $X_{LU}$  data with noise at  $x_B = 0.1$  (left) and  $0.2$  (right), and  $Q^2 = 4 \text{ GeV}^2$ .

We can see that the errorbands are now larger and the average value of the nets does not coincide with the ground truth CFF, but overall, the prediction is not too bad.

We can now add more CFF components, the  $x_B$  dependence to the CFFs, and more observables.

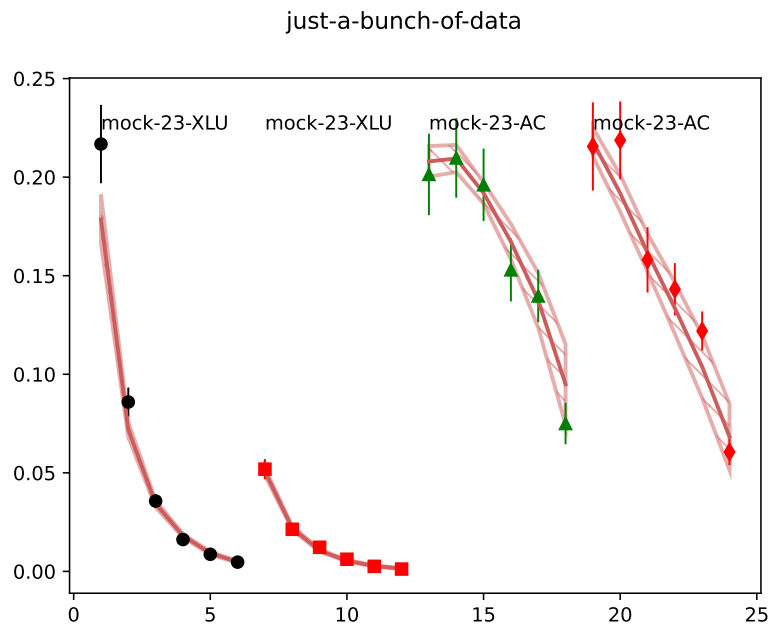


Figure 9.7: Comparison of simulated  $X_{LU}$  and  $A_C$  data and the neural network predictions.

In Figure 9.7 we added the  $x_B$  dependence and simulated data for  $X_{LU}$  and  $A_C$  by modeling

$\Im\mathcal{H}$  and  $\Re\mathcal{E}$ . We also added noise to this data in the same way as in the previous example. The data is generated for six values of  $t$  in the same interval as before, and for four  $x_B$  values between 0.1 and 0.25. The figure depicts simulated data and neural network predictions. For this purpose we generated 30 neural nets.

We compare the predictions of the neural network to the ground truth in Figure 9.8 below for two values of  $x_B$ . We can see that the neural network extraction mostly contains the CFFs calculated by the KM15 model. We can attempt to extrapolate the obtained CFFs to the entire  $\xi$  domain. The results for this extrapolation are depicted in Figure 9.9 below at  $t = -0.2 \text{ GeV}^2$ . We do not expect a good agreement between the KM15 model and the neural network model since the neural nets were not trained at very high and very low  $x_B$ . The agreement is closest at values of  $\xi$  where the nets were trained.

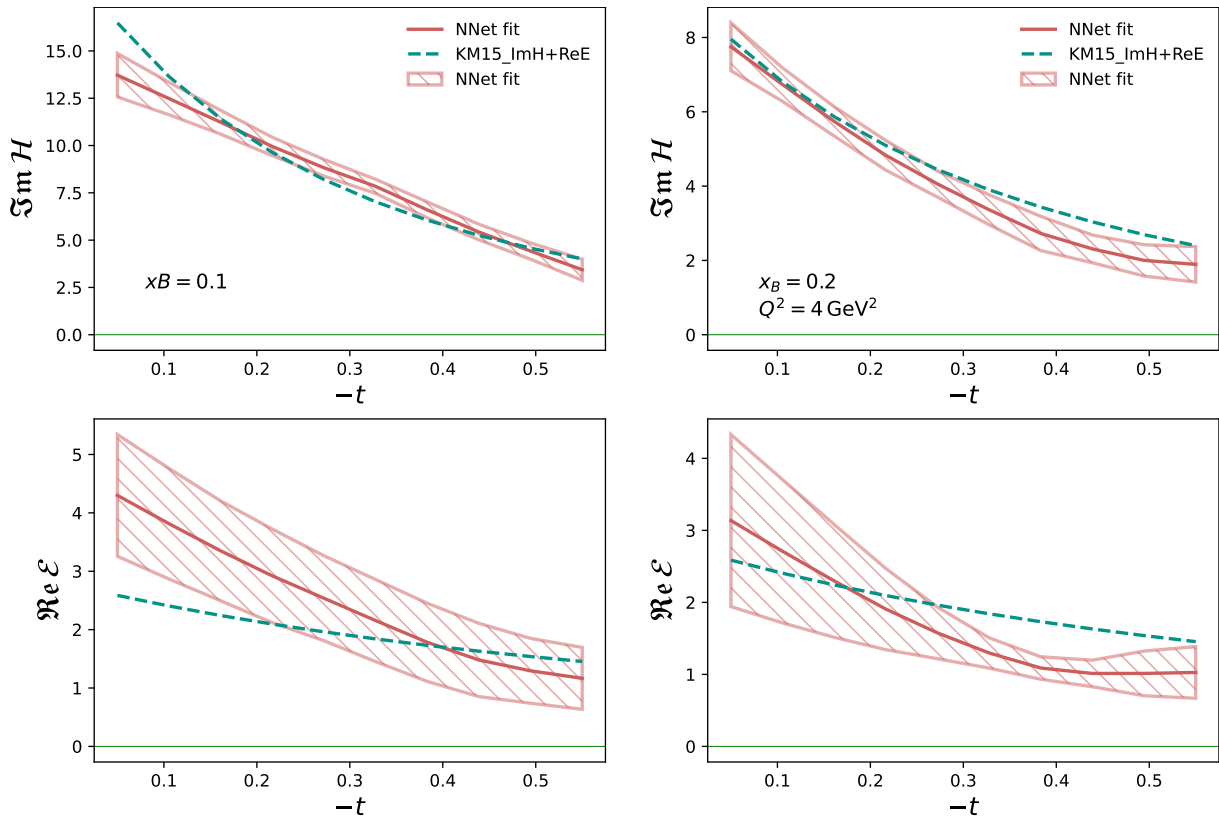


Figure 9.8: Comparison of  $\Im\mathcal{H}(x_B, t)$  and  $\Re\mathcal{E}(x_B, t)$  modeled by the KM15 model and extracted by the neural net model trained on simulated  $X_{LU}$  and  $A_C$  data with noise at  $Q^2 = 4 \text{ GeV}^2$  and  $x_B = 0.1$  (left) and  $x_B = 0.2$  (right).

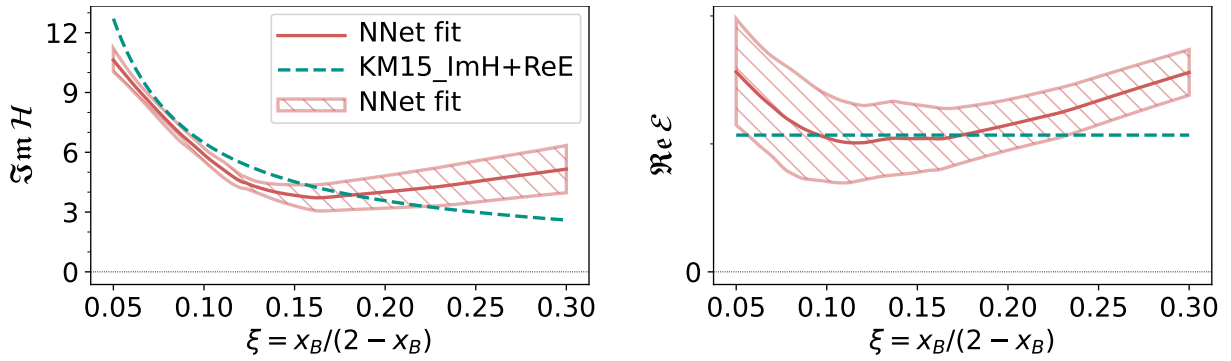


Figure 9.9: Extrapolation of CFFs extracted in Figure 9.8 to the entire domain of  $\xi$  at  $t = -0.2 \text{ GeV}^2$ .

The last example we will observe is simulating data for  $X_{UU}$ ,  $X_{LU}$ ,  $X_{UL}$ ,  $A_C$  and  $A_{UT}$  with CFFs  $\text{Im}\mathcal{H}$ ,  $\text{Re}\mathcal{H}$ ,  $\text{Im}\mathcal{E}$ ,  $\text{Re}\mathcal{E}$  and  $\text{Im}\tilde{\mathcal{H}}$ . The data is simulated at the same points as the previous example, with the same errorbars, and it has the same added noise. In Figure 9.10 below we depict the simulated data and the neural network predictions. We generated 20 neural nets in this instance.

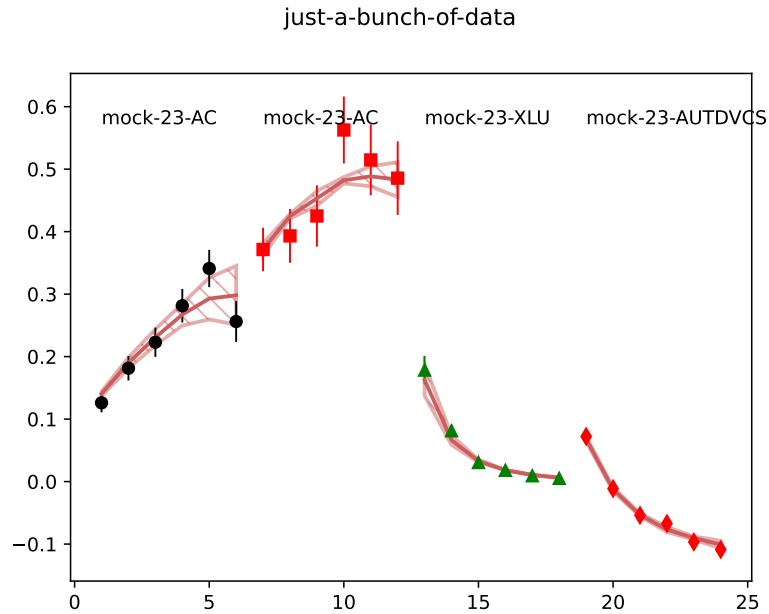


Figure 9.10: Comparison of simulated  $X_{LU}$ ,  $A_C$  and  $A_{UT}$  data and the neural network predictions.

The comparison of the CFFs extracted by the neural net model and the KM15 model are given in Figure 9.11 below for  $x_B = 0.1$  and  $x_B = 0.2$ .

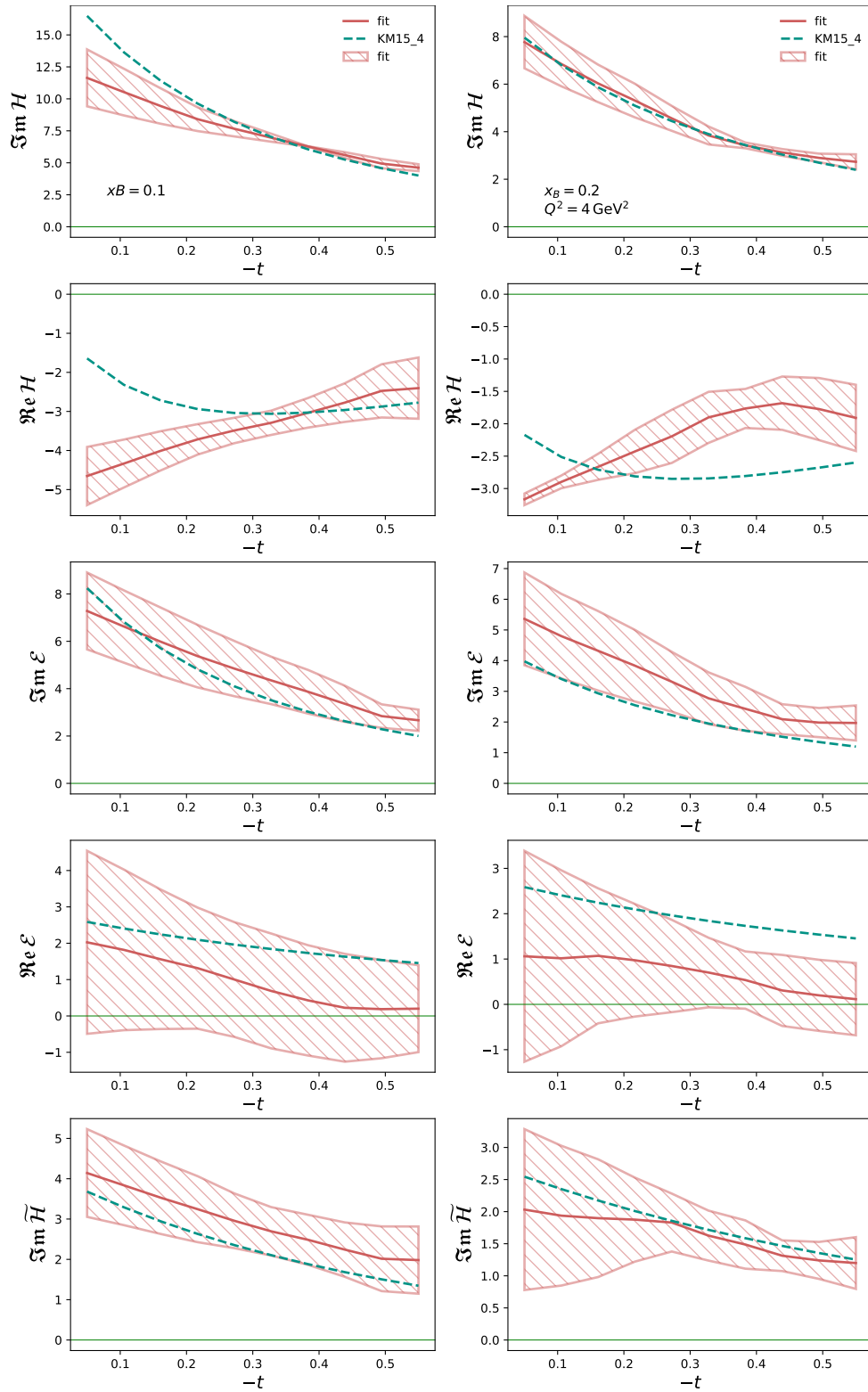


Figure 9.11: Comparison of  $\Im\mathcal{H}$ ,  $\Re\mathcal{H}$ ,  $\Im\mathcal{E}$ ,  $\Re\mathcal{E}$  modeled by the KM15 model (green line) and extracted by the neural net model (red band) trained on simulated  $X_{UU}$ ,  $X_{LU}$ ,  $X_{UL}$ ,  $A_C$  and  $A_{UT}$  data with noise at  $Q^2 = 4 \text{ GeV}^2$ , and  $x_B = 0.1$  (left) and  $x_B = 0.2$  (right).

We can see that the neural net extractions coincide with the  $\text{KM15}$  predictions well. The only disagreement is for the real and imaginary components of the CFF  $\mathcal{E}$  at  $x_B = 0.2$ . We have seen from the analysis in the previous chapter that  $\Im\mathcal{E}$  had the biggest uncertainties, and we had the biggest discrepancies between the  $\Re\mathcal{E}$  obtained by the DR-constrained and unconstrained model, so this CFF is difficult to model with data at this kinematics.

From this analysis we conclude that our methodology is reliable and robust enough to extract most of the CFFs from the presently available data.

## 9.2 Testing the flavor separation of CFFs

As a last test, we turn our attention to the flavor separation of CFFs performed in Section 8.3. For the first example, we simulate proton and neutron  $X_{UU}$  and  $X_{LU}$  data by modeling CFFs  $\Im\mathcal{H}_u$ ,  $\Im\mathcal{H}_d$ ,  $\Re\mathcal{H}_u$  and  $\Re\mathcal{H}_d$ . Since the model  $\text{KM15}$  treats neutron data using a simple isospin rotation of the proton CFFs, it does not predict neutron data reliably. We will use a random smooth single neural net trained on simulated proton and neutron data as the ground truth, because the model  $\text{fKM20}$  has some GPDs set to zero. We show an example with simulated  $A_{LU}$  and  $A_{UU}$ . In Figure 9.12 below we can see the agreement between the CFFs randomly extracted from real data and the neural network prediction of these CFFs. We again show the comparison at  $Q^2 = 4 \text{ GeV}^2$ , and  $x_B = 0.1$  and  $x_B = 0.2$ . The flavor separation of the CFF  $\Im\mathcal{H}$  seems to be successful for this kinematic regime, but it fails for  $\Re\mathcal{H}$ . We also attempted to extract flavored contributions of the imaginary part of the CFF  $\mathcal{E}$  alongside the imaginary part of the CFF  $\mathcal{H}$ , which was somewhat successful for smaller  $x_B$ . The flavor separation fails when only proton DVCS data is used, which is to be expected. Overall, this method confirms that it is indeed possible to reliably separate the CFF  $\mathcal{H}$  with presently available data.

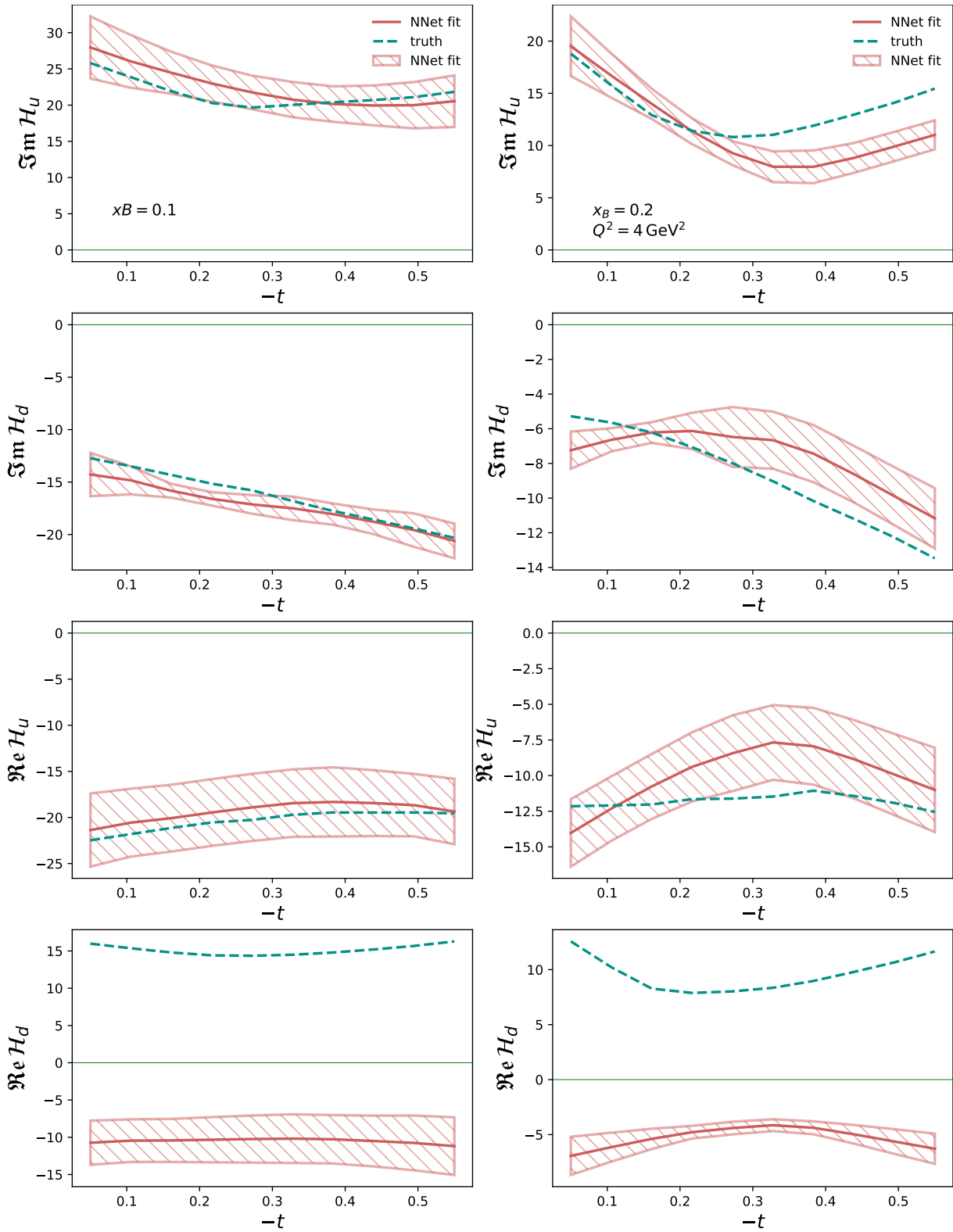


Figure 9.12: Comparison of the extraction of flavor separated imaginary and real components of the CFF  $\mathcal{H}$  obtained by a neural network fit (red band) and a random single net extraction (green line) at  $Q^2 = 4 \text{ GeV}^2$ , and  $x_B = 0.1$  (left) and  $x_B = 0.2$  (right).

# Chapter 10

## Thesis summary and outlook

In this thesis we presented two main approaches to GPD phenomenology, one being a model fit of GPDs in the conformal space, and the other being an extraction of CFFs using machine learning methods. Both of these approaches are used in complement. One is grounded in physics and offers a direct test of our physical assumptions, while the other is an unbiased approach which offers a more realistic way of obtaining uncertainties of extracted CFFs, and GPDs in the future. The experimental coverage of exclusive processes, which probe GPDs, is entering an unprecedented high-precision era, and therefore reducing as many sources of errors in our models is of great importance.

In the first part we have given an overview of the processes we study in this work, namely DIS, DVCS and DVMP, and their experimental coverage, as well as some of the properties of GPDs relevant for their understanding in the context of our analysis. We have also given a presentation of the procedure of obtaining a conformal moments representation of GPDs, CFFs and TFFs using Mellin-Barnes integration. Finally, we gave a brief overview of machine learning methods required for this analysis.

In the second part, we applied the conformal moment representation of GPDs in order to simultaneously describe DIS, DVCS and DVMP data at low  $x$ . This work is a continuation of the unpublished work presented in [3], which was based on the methods developed in [101, 37]. This analysis was extended to NLO of perturbation theory, allowing us to assess the NLO corrections, and to study the quark and gluon contributions and how they change when we transition from LO to NLO. The main goal of this analysis is to see whether or not we can obtain a simultaneous fit at the twist-2 collinear level. In this analysis we only described the production of the vector meson  $\rho^0$  using only the singlet sea quark and gluon GPDs, so the next step would be to add the non-singlet GPDs. Even though this analysis was performed only using the GPD  $H$ , the description is satisfactory and seems to stabilize at NLO, giving rise to a

universal GPD description of all three processes.

In the third part, we present our results for CFF extraction obtained using machine learning methods, specifically neural networks [5]. In this work we studied the proton and neutron DVCS data obtained with the JLab 6 GeV beam upgrade [157, 158]. We used this data, alongside previous proton DVCS data obtained at JLab to extract 6 out of the 8 twist-2 CFFs. The novelty in this analysis was the implementation of dispersion relation constraints, which so far have not been present in our neural network extraction of CFFs. These constraints allowed us to reduce the uncertainties for the CFFs to which the data are most sensitive, but they introduced a significant discrepancy in the prediction of  $\Re\epsilon\mathcal{E}$  between the DR-constrained and unconstrained model. This should be alleviated with more data. These results were compared to the standard model fit, which was trained to HERA and JLab data. The other purpose of this analysis was to obtain a flavor separation of CFFs by adding neutron data and using isospin symmetry. Both a flavored model fit and a neural network model were fitted to this data, and a flavor separation of the real and imaginary parts of the CFF  $\mathcal{H}$  has been achieved. The flavor separation fails for the other CFFs, which we hope to remedy with more data.

Given that one of our main concerns is the reliability of our predictions, especially their uncertainties, we have conducted closure tests of the type present in PDF analysis, as well as in the PARTONS framework for studying GPDs. These tests rely on the ability of neural network models to reproduce models which were used to generate simulated data used for training the neural nets. Most of our tests were successful, giving us hope that our methods give reliable results grounded in physics, and that these models will be able to work with the incoming data from JLab upgrades and the data that will come from the upcoming EIC.

The motivation to study GPDs lies in their potential to describe the three-dimensional structure of nucleons, and to tell us how the angular momentum of the nucleon is distributed amongst its constituents. We are currently quite far from solving this problem, because even if we set aside the fact that we cannot deconvolute the GPDs from the CFFs, the experimental data does not give access to the full domain of the kinematic variables that the GPDs depend on. For this purpose we need to study different processes, such as DDVCS, that probe GPDs away from the cross-over line. Some of the next steps we are going to take in this approach are de-hybridizing the  $\mathcal{KM}$ -type models and taking the whole analysis to NLO level. We also need to find a way of assessing the systematic errors introduced by various choices we make in modeling GPDs and CFFs.

# References

- [1] Kroll P., Moutarde H., Sabatie F., 2013, *Eur. Phys. J. C*, 73, 2278, *From hard exclusive meson electroproduction to deeply virtual Compton scattering*
- [2] Meskauskas M., Müller D., 2014, *Eur. Phys. J. C*, 74, 2719, *A Fresh Look at Exclusive Electroproduction of Light Vector Mesons*
- [3] Lautenschlager T., Muller D., Schaefer A., 2013, *Global analysis of generalized parton distributions – collider kinematics –*
- [4] Lautenschlager T., 2015, Phd thesis, University of Regensburg, [doi:10.5283/epub.32332](https://doi.org/10.5283/epub.32332)
- [5] Čuić M., Kumerički K., Schäfer A., 2020, *Phys. Rev. Lett.*, 125, 232005, *Separation of quark flavors using deeply virtual compton scattering data*
- [6] Thomson M., 2013, *Modern particle physics*. Cambridge University Press, [doi:10.1017/CBO9781139525367](https://doi.org/10.1017/CBO9781139525367)
- [7] Halzen F., Martin A. D., 1984, *Quarks and Leptons: An Introductory Course in Modern Particle Physics*
- [8] Hofstadter R., Fechter H. R., McIntyre J. A., 1953, *Phys. Rev.*, 92, 978, *High-energy electron scattering and nuclear structure determinations*
- [9] Hofstadter R., Fechter H. R., McIntyre J. A., 1953, *Phys. Rev.*, 91, 422, *Scattering of high-energy electrons and the method of nuclear recoil*
- [10] Hofstadter R., 1956, *Rev. Mod. Phys.*, 28, 214, *Electron scattering and nuclear structure*
- [11] Gao H., 2003, *International Journal of Modern Physics E*, 12, 1, *Nucleon electromagnetic form factors*
- [12] Hyde-Wright C. E., de Jager K., 2004, *Annual Review of Nuclear and Particle Science*, 54, 217, *Electromagnetic form factors of the nucleon and compton scattering*
- [13] Perdrisat C., Punjabi V., Vanderhaeghen M., 2007, *Progress in Particle and Nuclear Physics*, 59, 694, *Nucleon electromagnetic form factors*
- [14] Bloom E. D., et al., 1969, *Phys. Rev. Lett.*, 23, 930, *High-energy inelastic  $e - p$  scattering at  $6^\circ$  and  $10^\circ$*
- [15] Friedman J. I., 1991, *Rev. Mod. Phys.*, 63, 615, *Deep inelastic scattering: Comparisons with the quark model*
- [16] Kendall H. W., 1991, *Rev. Mod. Phys.*, 63, 597, *Deep inelastic scattering: Experiments on the proton and the observation of scaling*
- [17] Taylor R. E., 1991, *Rev. Mod. Phys.*, 63, 573, *Deep inelastic scattering: The early years*
- [18] Feynman R. P., 1969, *Phys. Rev. Lett.*, 23, 1415, *Very high-energy collisions of hadrons*
- [19] Roberts R. G., 1990, *The structure of the proton: Deep inelastic scattering*. Cambridge Monographs on Mathematical Physics, Cambridge University Press, [doi:10.1017/CBO9780511564062](https://doi.org/10.1017/CBO9780511564062)
- [20] Devenish R., Cooper-Sarkar A., 2004, *Deep inelastic scattering*, [doi:10.1093/acprof:oso/9780198506713.001.0001](https://doi.org/10.1093/acprof:oso/9780198506713.001.0001).
- [21] Ji X., 1997, *Phys. Rev. D*, 55, 7114, *Deeply virtual compton scattering*
- [22] Radyushkin A., 1996, *Physics Letters B*, 380, 417, *Scaling limit of deeply virtual compton scattering*
- [23] Belitsky A., Müller D., Kirchner A., 2002, *Nuclear Physics B*, 629, 323, *Theory of deeply virtual compton scattering on the nucleon*
- [24] Collins J. C., Freund A., 1999, *Phys. Rev. D*, 59, 074009, *Proof of factorization for deeply virtual compton scattering in  $qcd$*

- [25] Collins J. C., Frankfurt L., Strikman M., 1997, *Phys. Rev. D*, 56, 2982, *Factorization for hard exclusive electroproduction of mesons in qcd*
- [26] Frankfurt L., Koepf W., Strikman M., 1996, *Phys. Rev. D*, 54, 3194, *Hard diffractive electroproduction of vector mesons in qcd*
- [27] Frankfurt L., Koepf W., Strikman M., 1998, *Phys. Rev. D*, 57, 512, *Diffractive heavy quarkonium photoproduction and electroproduction in qcd*
- [28] Frankfurt L. L., Pobylitsa P. V., Polyakov M. V., Strikman M., 1999, *Phys. Rev. D*, 60, 014010, *Hard exclusive pseudoscalar meson electroproduction and spin structure of the nucleon*
- [29] Frankfurt L. L., Polyakov M. V., Strikman M., Vanderhaeghen M., 2000, *Phys. Rev. Lett.*, 84, 2589, *Hard exclusive electroproduction of decuplet baryons in the large  $N_c$  limit*
- [30] Mankiewicz L., Piller G., Radyushkin A., 1999, *Eur. Phys. J. C*, 10, 307, *Hard exclusive electroproduction of pions*
- [31] Mankiewicz L., Piller G., Weigl T., 1998, *Eur. Phys. J. C*, 5, 119, *Hard exclusive meson production and nonforward parton distributions*
- [32] Mankiewicz L., Piller G., Weigl T., 1998, *Phys. Rev. D*, 59, 017501, *Hard leptonproduction of charged vector mesons*
- [33] Radyushkin A., 1996, *Physics Letters B*, 385, 333, *Asymmetric gluon distributions and hard diffractive electroproduction*
- [34] Belitsky A., Müller D., 2001, *Physics Letters B*, 513, 349, *Hard exclusive meson production at next-to-leading order*
- [35] Diehl M., Kugler W., 2007, *Eur. Phys. J. C*, 52, 933, *Next-to-leading order corrections in exclusive meson production*
- [36] Ivanov D. Y., Szymanowski L., Krasnikov G., 2004, *JETP Lett.*, 80, 226, *Vector meson electroproduction at next-to-leading order*
- [37] Müller D., Lautenschlager T., Passek-Kumerički K., Schäfer A., 2014, *Nuclear Physics B*, 884, 438, *Towards a fitting procedure to deeply virtual meson production – the next-to-leading order case*
- [38] Duplančić G., Müller D., Passek-Kumerički K., 2017, *Physics Letters B*, 771, 603, *Next-to-leading order corrections to deeply virtual production of pseudoscalar mesons*
- [39] Berger E. R., Diehl M., Pire B., 2002, *Eur. Phys. J. C*, 23, 675, *Time - like Compton scattering: Exclusive photoproduction of lepton pairs*
- [40] Guidal M., Vanderhaeghen M., 2003, *Phys. Rev. Lett.*, 90, 012001, *Double deeply virtual compton scattering off the nucleon*
- [41] Belitsky A. V., Müller D., 2003, *Phys. Rev. Lett.*, 90, 022001, *Exclusive electroproduction of lepton pairs as a probe of nucleon structure*
- [42] Pire B., Szymanowski L., Wagner J., 2011, *Phys. Rev. D*, 83, 034009, *Next-to-leading order corrections to timelike, spacelike, and double deeply virtual compton scattering*
- [43] Wilson K. G., Zimmermann W., 1972, *Commun. Math. Phys.*, 2, 87, *Operator product expansions and composite field operators in the general framework of quantum field theory*
- [44] Peskin M. E., Schroeder D. V., 1995, *An Introduction to quantum field theory*. Addison-Wesley, Reading, USA
- [45] Collins J., 2013, *Foundations of perturbative qcd*. Vol. 32, Cambridge University Press, doi:10.1017/9781009401845
- [46] Diehl M., 2003, *Physics Reports*, 388, 41, *Generalized parton distributions*
- [47] Belitsky A., Radyushkin A., 2005, *Physics Reports*, 418, 1, *Unraveling hadron structure with generalized parton distributions*
- [48] Ivanov D., Pire B., Szymanowski L., Teryaev O., 2002, *Physics Letters B*, 550, 65, *Probing chiral-odd gpd's in diffractive electroproduction of two vector mesons*
- [49] Diehl M., Gousset T., 1998, *Physics Letters B*, 428, 359, *Time ordering in off-diagonal parton distributions*

- [50] Gribov V. N., Lipatov L. N., 1972, *Sov. J. Nucl. Phys.*, 15, 438, *Deep inelastic  $e p$  scattering in perturbation theory*
- [51] Lipatov L. N., 1974, *Yad. Fiz.*, 20, 181, *The parton model and perturbation theory*
- [52] Altarelli G., Parisi G., 1977, *Nuclear Physics B*, 126, 298, *Asymptotic freedom in parton language*
- [53] Dokshitzer Y. L., 1977, *Sov. Phys. JETP*, 46, 641, *Calculation of the Structure Functions for Deep Inelastic Scattering and  $e^+ e^-$  Annihilation by Perturbation Theory in Quantum Chromodynamics.*
- [54] Efremov A., Radyushkin A., 1980, *Physics Letters B*, 94, 245, *Factorization and asymptotic behaviour of pion form factor in  $qcd$*
- [55] Peter Lepage G., Brodsky S. J., 1979, *Physics Letters B*, 87, 359, *Exclusive processes in quantum chromodynamics: Evolution equations for hadronic wavefunctions and the form factors of mesons*
- [56] Diehl M., Feldmann T., Jakob R., Kroll P., 2001, *Nuclear Physics B*, 605, 647, *Erratum to: “the overlap representation of skewed quark and gluon distributions”*: [*nucl. phys. b* 596 (2001) 33–65]
- [57] Radyushkin A. V., 1997, *Phys. Rev. D*, 56, 5524, *Nonforward parton distributions*
- [58] Pobylitsa P. V., 2002, *Phys. Rev. D*, 65, 114015, *Disentangling positivity constraints for generalized parton distributions*
- [59] Lepage G. P., Brodsky S. J., 1980, *Phys. Rev. D*, 22, 2157, *Exclusive processes in perturbative quantum chromodynamics*
- [60] Ji X.-D., 1998, *J. Phys. G*, 24, 1181, *Off forward parton distributions*
- [61] Bakker B. L. G., Leader E., Trueman T. L., 2004, *Phys. Rev. D*, 70, 114001, *Critique of the angular momentum sum rules and a new angular momentum sum rule*
- [62] Leader E., Lorcé C., 2014, *Physics Reports*, 541, 163, *The angular momentum controversy: What’s it all about and does it matter?*
- [63] Lorcé C., 2015, *JHEP*, 08, 045, *The light-front gauge-invariant energy-momentum tensor*
- [64] Leader E., 2013, *Physics Letters B*, 720, 120, *A critical assessment of the angular momentum sum rules*
- [65] Tanaka K., 2018, *Phys. Rev. D*, 98, 034009, *Operator relations for gravitational form factors of a spin-0 hadron*
- [66] Ji X., 1998, *Phys. Rev. D*, 58, 056003, *Lorentz symmetry and the internal structure of the nucleon*
- [67] Jaffe R., Manohar A., 1990, *Nuclear Physics B*, 337, 509, *The  $g_1$  problem: Deep inelastic electron scattering and the spin of the proton*
- [68] Ji X., 1997, *Phys. Rev. Lett.*, 78, 610, *Gauge-invariant decomposition of nucleon spin*
- [69] Burkardt M., 2002, *Phys. Rev. D*, 66, 119903, *Erratum: Impact parameter dependent parton distributions and off-forward parton distributions for  $\vec{\zeta} = 0$*  [*phys. rev. d* 62, 071503(r) (2000)]
- [70] Diehl M., 2002, *Eur. Phys. J. C*, 25, 223, *Generalized parton distributions in impact parameter space*
- [71] Collins J. C., Soper D. E., 1981, *Nuclear Physics B*, 193, 381, *Back-to-back jets in  $qcd$*
- [72] Bacchetta A., Conti F., Radici M., 2008, *Phys. Rev. D*, 78, 074010, *Transverse-momentum distributions in a diquark spectator model*
- [73] Boussarie R., et al., 2023, *TMD Handbook*
- [74] Ji X., 2003, *Phys. Rev. Lett.*, 91, 062001, *Viewing the proton through “color” filters*
- [75] Belitsky A., Ji X., Yuan F., 2004, *Phys. Rev. D*, 69, 074014, *Quark imaging in the proton via quantum phase-space distributions*
- [76] Wigner E., 1932, *Phys. Rev.*, 40, 749, *On the quantum correction for thermodynamic equilibrium*
- [77] Meissner S., Metz A., Schlegel M., 2008, in 16th International Workshop on Deep Inelastic Scattering and Related Subjects. p. 99 ([arXiv:0807.1154](https://arxiv.org/abs/0807.1154)), [doi:10.3360/dis.2008.99](https://doi.org/10.3360/dis.2008.99)
- [78] Meissner S., Metz A., Schlegel M., Goeke K., 2008, *JHEP*, 08, 038, *Generalized parton correlation functions for a spin-0 hadron*
- [79] Meissner S., Metz A., Schlegel M., 2009, *JHEP*, 08, 056, *Generalized parton correlation functions for a spin-1/2 hadron*

- [80] Kanazawa K., Lorcé C., Metz A., Pasquini B., Schlegel M., 2014, *Phys. Rev. D*, 90, 014028, *Twist-2 generalized transverse-momentum dependent parton distributions and the spin/orbital structure of the nucleon*
- [81] Echevarria M. G., Idilbi A., Kanazawa K., Lorcé C., Metz A., Pasquini B., Schlegel M., 2016, *Physics Letters B*, 759, 336, *Proper definition and evolution of generalized transverse momentum dependent distributions*
- [82] Lorce C., Pasquini B., Vanderhaeghen M., 2011, *JHEP*, 05, 041, *Unified framework for generalized and transverse-momentum dependent parton distributions within a  $3Q$  light-cone picture of the nucleon*
- [83] Anikin I. V., Teryaev O. V., 2007, *Phys. Rev. D*, 76, 056007, *Dispersion relations and subtractions in hard exclusive processes*
- [84] Diehl M., Ivanov D. Y., 2007, *Eur. Phys. J. C*, 52, 919, *Dispersion representations for hard exclusive processes: beyond the Born approximation*
- [85] Accardi A., et al., 2016, *Eur. Phys. J. A*, 52, 268, *Electron Ion Collider: The Next QCD Frontier: Understanding the glue that binds us all*
- [86] Abdul Khalek R., et al., 2022, *Nuclear Physics A*, 1026, 122447, *Science requirements and detector concepts for the electron-ion collider: Eic yellow report*
- [87] Chen X., 2018, *PoS*, DIS2018, 170, *A Plan for Electron Ion Collider in China*
- [88] Anderle D. P., et al., 2021, *Front. Phys. (Beijing)*, 16, 64701, *Electron-ion collider in China*
- [89] Abelleira Fernandez J. L., et al., 2012, *J. Phys. G*, 39, 075001, *A Large Hadron Electron Collider at CERN: Report on the Physics and Design Concepts for Machine and Detector*
- [90] Capua M., 2012, in 3rd International Workshop on Multiple Partonic Interactions at the LHC. pp 137–143 ([arXiv:1202.2828](https://arxiv.org/abs/1202.2828)), [doi:10.3204/DESY-PROC-2012-03/58](https://doi.org/10.3204/DESY-PROC-2012-03/58)
- [91] Movsisyan, Aram 2015, *EPJ Web of Conferences*, 85, 02035, *Overview of hermes results on exclusive processes*
- [92] Kim, Andrey 2015, *EPJ Web of Conferences*, 85, 02034, *Exclusive processes at jlab at 6 gev*
- [93] Ferrero A., (on behalf of the COMPASS collaboration) 2011, *Journal of Physics: Conference Series*, 295, 012039, *Study of dvcs and dvmp processes at compass*
- [94] Belitsky A., Müller D., 1998, *Nuclear Physics B*, 527, 207, *Next-to-leading order evolution of twist-two conformal operators: The abelian case*
- [95] Belitsky A., Müller D., 1999, *Nuclear Physics B*, 537, 397, *Broken conformal invariance and spectrum of anomalous dimensions in qcd*
- [96] Braun V. M., Manashov A. N., Moch S., Strohmaier M., 2017, *JHEP*, 06, 037, *Three-loop evolution equation for flavor-nonsinglet operators in off-forward kinematics*
- [97] Müller D., 1998, *Phys. Rev. D*, 58, 054005, *Restricted conformal invariance in qcd and its predictive power for virtual two-photon processes*
- [98] Belitsky A., Müller D., 1998, *Physics Letters B*, 417, 129, *Predictions from conformal algebra for the deeply virtual compton scattering*
- [99] Braun V., Korchemsky G., Müller D., 2003, *Progress in Particle and Nuclear Physics*, 51, 311, *The uses of conformal symmetry in qcd*
- [100] Müller D., Schäfer A., 2006, *Nuclear Physics B*, 739, 1, *Complex conformal spin partial wave expansion of generalized parton distributions and distribution amplitudes*
- [101] Kumerički K., Müller D., Passek-Kumerički K., 2008, *Nuclear Physics B*, 794, 244, *Towards a fitting procedure for deeply virtual compton scattering at next-to-leading order and beyond*
- [102] Ferrara S., Gatto R., Grillo A., 1971, *Nuclear Physics B*, 34, 349, *Conformal invariance on the light cone and canonical dimensions*
- [103] Ferrara S., Grillo A., Gatto R., 1971, *Physics Letters B*, 36, 124, *Improved light-cone expansion*
- [104] Ferrara S., Grillo A. F., Gatto R., 1972, *Phys. Rev. D*, 5, 3102, *Manifestly conformal-covariant expansion on the light cone*
- [105] Craigie N., Dobrev V., Todorov I., 1985, *Annals of Physics*, 159, 411, *Conformally covariant composite operators in quantum chromodynamics*

- [106] Carlson F., 1914, Phd thesis, Uppsala University
- [107] Haykin S., 1999, *Neural networks: A comprehensive foundation*. International edition, Prentice Hall, <https://books.google.hr/books?id=bX4pQAAMAAJ>
- [108] Chollet F., 2017, *Deep learning with python*. Manning
- [109] McCulloch W., Pitts W., 1943, *Bulletin of Mathematical Biophysics*, 5, 127, *A logical calculus of ideas immanent in nervous activity*
- [110] Rosenblatt F., 1957, *The perceptron, a perceiving and recognizing automaton project para*. Report: Cornell Aeronautical Laboratory, Cornell Aeronautical Laboratory, [https://books.google.hr/books?id=P\\_XGPgAACAAJ](https://books.google.hr/books?id=P_XGPgAACAAJ)
- [111] Hornik K., Stinchcombe M., White H., 1989, *Neural Networks*, 2, 359, *Multilayer feedforward networks are universal approximators*
- [112] Csaji B., 2001, M.S.Thesis, Dept. Science, Eotvos Lorand Univ., Budapest, Hungary, *Approximation with artificial neural networks*
- [113] Kumerički K., Müller D., Passek-Kumerički K., Schäfer A., 2007, *Physics Letters B*, 648, 186, *Deeply virtual compton scattering beyond next-to-leading order: The flavor singlet case*
- [114] Vinnikov A. V., 2006, *Code for prompt numerical computation of the leading order GPD evolution*
- [115] Bertone V., Dutriex H., Mezrag C., Morgado J. M., Moutarde H., 2022, *Eur. Phys. J. C*, 82, 888, *Revisiting evolution equations for generalised parton distributions*
- [116] Berthou B., et al., 2018, *Eur. Phys. J. C*, 78, 478, *PARTONS: PARTonic Tomography Of Nucleon Software: A computing framework for the phenomenology of Generalized Parton Distributions*
- [117] Freund A., McDermott M., 2002, *Phys. Rev. D*, 66, 079903, *Erratum: Next-to-leading order evolution of generalized parton distributions for desy hera and hermes [phys. rev. d 65, 056012 (2002)]*
- [118] Müller D., 2006, *Physics Letters B*, 634, 227, *Next-to-next-to-leading order corrections to deeply virtual compton scattering: the non-singlet case*
- [119] Braun V. M., Manashov A. N., Moch S., Schoenleber J., 2020, *JHEP*, 09, 117, *Two-loop coefficient function for DVCS: vector contributions*
- [120] Braun V. M., Manashov A. N., Moch S., Schönleber J., 2021, *Phys. Rev. D*, 104, 094007, *Axial-vector contributions in two-photon reactions: Pion transition form factor and deeply-virtual compton scattering at nnlo in qcd*
- [121] Braun V. M., Ji Y., Schoenleber J., 2022, *Phys. Rev. Lett.*, 129, 172001, *Deeply Virtual Compton Scattering at Next-to-Next-to-Leading Order*
- [122] Gross D. J., Wilczek F., 1974, *Phys. Rev. D*, 9, 980, *Asymptotically free gauge theories. ii*
- [123] Georgi H., Politzer H. D., 1974, *Phys. Rev. D*, 9, 416, *Electroproduction scaling in an asymptotically free theory of strong interactions*
- [124] Floratos E., Kounnas C., Lacaze R., 1981, *Nuclear Physics B*, 192, 417, *Higher order qcd effects in inclusive annihilation and deep inelastic scattering*
- [125] Belitsky A., Müller D., Niedermeier L., Schäfer A., 1999, *Nuclear Physics B*, 546, 279, *Evolution of non-forward parton distributions in next-to-leading order: singlet sector*
- [126] Müller D., Polyakov M. V., Semenov-Tian-Shansky K. M., 2015, *JHEP*, 03, 052, *Dual parametrization of generalized parton distributions in two equivalent representations*
- [127] Hwang D., Müller D., 2008, *Physics Letters B*, 660, 350, *Implication of the overlap representation for modelling generalized parton distributions*
- [128] Kumerički K., Müller D., 2010, *Nuclear Physics B*, 841, 1, *Deeply virtual compton scattering at small  $x_b$  and the access to the  $gpd h$*
- [129] Aid S., et al., 1996, *Nuclear Physics B*, 470, 3, *A measurement and qcd analysis of the proton structure function  $f_2(x, q^2)$  at hera*
- [130] Aktas A., et al., 2005, *Eur. Phys. J. C*, 44, 1, *Measurement of deeply virtual compton scattering at HERA*

- [131] Aaron F., et al., 2009, *Physics Letters B*, 681, 391, *Deeply virtual compton scattering and its beam charge asymmetry in  $e\pm p$  collisions at her*
- [132] Chekanov S., et al., 2003, *Physics Letters B*, 573, 46, *Measurement of deeply virtual compton scattering at her*
- [133] Chekanov S., et al., 2009, *JHEP*, 05, 108, *A Measurement of the  $Q^{*2}$ ,  $W$  and  $t$  dependences of deeply virtual Compton scattering at HERA*
- [134] Aaron F. D., et al., 2010, *JHEP*, 05, 032, *Diffraction Electroproduction of rho and phi Mesons at HERA*
- [135] Chekanov S., et al., 2007, *PMC Phys. A*, 1, 6, *Exclusive rho0 production in deep inelastic scattering at HERA*
- [136] Goloskokov S. V., Kroll P., 2010, *Eur. Phys. J. C*, 65, 137, *An Attempt to understand exclusive pi+ electro-production*
- [137] Goloskokov S. V., Kroll P., 2011, *Eur. Phys. J. A*, 47, 112, *Transversity in hard exclusive electroproduction of pseudoscalar mesons*
- [138] Schilling K., Wolf G., 1973, *Nuclear Physics B*, 61, 381, *How to analyse vector-meson production in inelastic lepton scattering*
- [139] Brodsky S. J., Frankfurt L., Gunion J. F., Mueller A. H., Strikman M., 1994, *Phys. Rev. D*, 50, 3134, *Diffraction lepton production of vector mesons in qcd*
- [140] Alexeev M. G., et al., 2021, *Eur. Phys. J. C*, 81, 126, *Spin density matrix elements in exclusive  $\omega$  meson muoproduction*
- [141] Dembinski H., et al., 2023, *scikit-hep/iminuit*, doi:10.5281/zenodo.8249703, <https://doi.org/10.5281/zenodo.8249703>
- [142] James F., Roos M., 1975, *Comput. Phys. Commun.*, 10, 343, *Minuit: A System for Function Minimization and Analysis of the Parameter Errors and Correlations*
- [143] Kumerički K., Müller D., 2016, *EPJ Web Conf.*, 112, 01012, *Description and interpretation of DVCS measurements*
- [144] Diehl M., Kugler W., 2008, *Physics Letters B*, 660, 202, *Some numerical studies of the evolution of generalized parton distributions*
- [145] Freund A., McDermott M., 2002, *Phys. Rev. D*, 65, 074008, *Next-to-leading order qcd analysis of deeply virtual compton scattering amplitudes*
- [146] Shuvaev A. G., Golec-Biernat K. J., Martin A. D., Ryskin M. G., 1999, *Phys. Rev. D*, 60, 014015, *Off-diagonal distributions fixed by diagonal partons at small  $x$  and  $\xi$*
- [147] Martin A. D., Nockles C., Ryskin M. G., Shuvaev A. G., Teubner T., 2009, *Eur. Phys. J. C*, 63, 57, *Generalised parton distributions at small  $x$*
- [148] Shuvaev A., 1999, *Phys. Rev. D*, 60, 116005, *Solution of the off-forward leading logarithmic evolution equation based on the gegenbauer moments inversion*
- [149] Radyushkin A. V., 1998, *Phys. Rev. D*, 59, 014030, *Double distributions and evolution equations*
- [150] Radyushkin A. V., 1999, *Phys. Lett. B*, 449, 81, *Symmetries and structure of skewed and double distributions*
- [151] Forte S., Garrido L., Latorre J. I., Piccione A., 2002, *JHEP*, 05, 062, *Neural network parametrization of deep inelastic structure functions*
- [152] Rojo J. C., 2006, Other thesis ([arXiv:hep-ph/0607122](https://arxiv.org/abs/hep-ph/0607122))
- [153] Giele W. T., Keller S. A., Kosower D. A., 2001, *Parton Distribution Function Uncertainties*
- [154] Ball R. D., Del Debbio L., Forte S., Guffanti A., Latorre J. I., Rojo J., Ubiali M., 2010, *Nuclear Physics B*, 838, 136, *A first unbiased global nlo determination of parton distributions and their uncertainties*
- [155] Riedmiller M., 1994, *Computer Standards & Interfaces*, 16, 265, *Advanced supervised learning in multi-layer perceptrons — from backpropagation to adaptive learning algorithms*
- [156] Kumericki K., Mueller D., Schafer A., 2011, *JHEP*, 07, 073, *Neural network generated parametrizations of deeply virtual Compton form factors*

- [157] Defurne M., et al., 2017, *Nature Commun.*, 8, 1408, *A glimpse of gluons through deeply virtual compton scattering on the proton*
- [158] Benali M., et al., 2020, *Nature Phys.*, 16, 191, *Deeply virtual Compton scattering off the neutron*
- [159] Kumerički K., Müller D., Murray M., 2014, *Phys. Part. Nucl.*, 45, 723, *HERMES impact for the access of Compton form factors*
- [160] Kumericki K., Müller D., 2016, *EPJ Web of Conferences*, 112, 01012, *Description and interpretation of dvcs measurements\**
- [161] Penttinen M., Polyakov M. V., Goeke K., 2000, *Phys. Rev. D*, 62, 014024, *Helicity skewed quark distributions of the nucleon and chiral symmetry*
- [162] Moutarde H., Sznajder P., Wagner J., 2019, *Eur. Phys. J. C*, 79, 614, *Unbiased determination of DVCS Compton Form Factors*
- [163] Kumericki K., Liuti S., Moutarde H., 2016, *Eur. Phys. J. A*, 52, 157, *GPD phenomenology and DVCS fitting: Entering the high-precision era*
- [164] Pisano S., et al., 2015, *Phys. Rev. D*, 91, 052014, *Single and double spin asymmetries for deeply virtual compton scattering measured with clas and a longitudinally polarized proton target*
- [165] Jo H. S., et al., 2015, *Phys. Rev. Lett.*, 115, 212003, *Cross sections for the exclusive photon electroproduction on the proton and generalized parton distributions*
- [166] Defurne M., et al., 2015, *Phys. Rev. C*, 92, 055202, *E00-110 experiment at jefferson lab hall a: Deeply virtual compton scattering off the proton at 6 gev*
- [167] Moutarde H., Sznajder P., Wagner J., 2018, *Eur. Phys. J. C*, 78, 890, *Border and skewness functions from a leading order fit to DVCS data*
- [168] Vanderhaeghen M., Guichon P. A. M., Guidal M., 1999, *Phys. Rev. D*, 60, 094017, *Deeply virtual electroproduction of photons and mesons on the nucleon: Leading order amplitudes and power corrections*
- [169] Goloskokov S. V., Kroll P., 2008, *Eur. Phys. J. C*, 53, 367, *The Role of the quark and gluon GPDs in hard vector-meson electroproduction*
- [170] Ball R. D., et al., 2015, *JHEP*, 04, 040, *Parton distributions for the LHC Run II*
- [171] Ketkar N., 2017, *Introduction to pytorch*. Apress, Berkeley, CA, pp 195–208, doi:10.1007/978-1-4842-2766-4\_12, [https://doi.org/10.1007/978-1-4842-2766-4\\_12](https://doi.org/10.1007/978-1-4842-2766-4_12)

# Curriculum vitae

Marija Čuić was born on November 26<sup>th</sup> 1995 in Zagreb, Croatia. She went to the "IV. gimnazija, Zagreb", where she was enrolled in a bilingual Croatian-English classroom. She finished her secondary education in 2014, after which she enrolled into the integral undergraduate and graduate study of Physics, which she completed in 2019 with a Master's thesis titled "Towards a field theory on quantized spaces" under the supervision of dr. sc. Danijel Jurman, earning the title Master of Science in Physics. In the same year she enrolled into a doctoral study program Elementary Particle Physics at the University of Zagreb, Faculty of Science, Department of Physics and was hired as a research and teaching assistant by the Ministry of Science and Education at the same department. During her time as a teaching assistant, she gave auditory and practical exercises in Elementary Particle Physics 1 and 2 since 2019, Physical Cosmology from 2019 to 2022, and Quantum Physics from 2022. She participated in "The strong interaction at the frontier of knowledge" Horizon 2020 project. Aside from her teaching duties, Marija has been a member of the department council as an assistant representative since 2022, a member of the faculty council since 2021, a member of the student council from 2021 to 2023, where she served as president in the year 2022/2023. She was in the organizing committee of the PhD Student Symposium of the Faculty of Science in 2020 and 2021, and a member of the organizing committee of the REVESTRUCTURE workshop in 2023. Her native language is Croatian, she is fluent in English and German, and has elementary proficiency in Spanish.

## Invited talks and seminars

- *Recent advances in GPD and CFF extraction from hard exclusive processes*, Towards improved hadron femtography with hard exclusive reactions 2023, August 7-11 2023, JLab, USA
- *Multichannel GPD and CFF extraction from hard exclusive processes*, JLab cake seminar, July 2 2023, JLab, USA

- *Multichannel GPD extraction at LO and NLO at high energy*, REVESTRUCTURE workshop, July 10-12 2023, Zagreb, Croatia
- *CFF and GPD extraction from multi-channel fits*, International Workshop on Hadron Structure and Spectroscopy 2023, Jun 25-28 2023, Prague, Czech Republic
- *GPD studies with hard exclusive processes*, QCD Evolution Workshop 2023, May 22-26 2023, Orsay, France
- *Impact of Neutron DVCS Measurements on Extraction of Compton Form Factors*, International workshop on CLAS12 physics and future perspectives at JLab, March 21-24 2023, Paris, France
- *GPD studies with hard exclusive processes*, 3DPartons Week, October 26-28 2022, Orsay, France
- *Exclusive Production at large  $Q^2$* , Opportunities with JLab Energy and Luminosity Upgrade, September 26-30 2022, Trento, Italy
- *World Inside of a Proton* Women in Science, popularization workshop, May 7th 2022, Zagreb, Croatia

## Refereed publications

### Submitted

- 2 Čuić M., Duplančić G., Kumerički K., Passek-Kumerički K., accepted for publication in JHEP, *NLO corrections to the deeply virtual meson production revisited: impact on the extraction of generalized parton distributions*

### Published

- 1 Čuić M., Kumerički K., Schäfer A., 2020, [Phys. Rev. Lett.](#), 125, 232005, *Separation of quark flavors using deeply virtual compton scattering data*